A Novel Analytical Model for Predicting 3D Positron Emitter Distributions for PET-Based Range Verification in Carbon Ion Therapy

Tianxue Du

München 2026

A Novel Analytical Model for Predicting 3D Positron Emitter Distributions for PET-Based Range Verification in Carbon Ion Therapy

Tianxue Du

Dissertation
an der Fakultät für Physik
der Ludwig–Maximilians–Universität
München

vorgelegt von
Tianxue Du
aus Huaibei, China

München, den 30.01.2026

Erstgutachter: Prof. Dr. Katia Parodi

Zweitgutachter: PD. Dr. George Dedes

Tag der mündlichen Prüfung: 05.03.2026

Zusammenfassung

Die Strahlentherapie spielt eine zentrale Rolle in der Krebsbehandlung, und die Teilchentherapie hat sich aufgrund ihrer überlegenen Dosiskonformität im Vergleich zur konventionellen Photonenstrahlentherapie als fortschrittliche Behandlungsmodalität etabliert. Unter den verschiedenen Teilchenmodalitäten bieten Kohlenstoffionen ausgeprägte physikalische und biologische Vorteile. Gleichzeitig ist die Kohlenstoffionentherapie jedoch besonders empfindlich gegenüber Reichweitenunsicherheiten, da bereits geringe Abweichungen in der Strahlreichweite zu einer Unterdosierung des Tumors oder zu einer unnötigen Bestrahlung des umliegenden gesunden Gewebes führen können. Die Positronen-Emissions-Tomographie (PET) stellt einen geeigneten Ansatz zur in vivo Reichweitenverifikation dar, bei dem gemessene PET-Signale typischerweise mit vorhergesagten β^+-Aktivitätsverteilungen verglichen werden, die aus Positronen-Emitter-Verteilungen (PED) abgeleitet sind. Zur Vorhersage der PED werden häufig Monte-Carlo-Simulationen (MC) eingesetzt, deren hoher Rechenaufwand jedoch eine routinemäßige klinische Anwendung einschränkt. Dies motiviert die Entwicklung schneller und zuverlässiger alternativer Vorhersagemethoden.

Ziel dieser Arbeit ist die Entwicklung und umfassende Validierung eines analytischen Frameworks zur Vorhersage dreidimensionaler PED sowie der entsprechenden β^+-Aktivitätsverteilungen in der Kohlenstoffionentherapie, um ein recheneffizientes und klinisch anwendbares Werkzeug für die PET-basierte Reichweitenverifikation bereitzustellen.

Zu diesem Zweck wurde ein analytisches Framework zur PED-Vorhersage entwickelt, das einen verbesserten eindimensionalen analytischen Ansatz mit einem dreidimensionalen Ausbreitungskern kombiniert, der vom Pencil-Beam-Algorithmus (PBA), wie er üblicherweise in der Dosisberechnung verwendet wird, inspiriert ist. Ein zuvor vorgeschlagener eindimensionaler analytischer Ansatz zur Vorhersage von PED aus Tiefendosisprofilen für Kohlenstoffionen wurde weiterentwickelt, indem verfeinerte Modellierungsfunktionen eingeführt und zusätzliche Positronen-Emitter berücksichtigt wurden. Darüber hinaus wurde eine Abbildungsstrategie entwickelt, um longitudinale Heterogenitätseffekte in der PED der Projektilfragmente angemessen zu berücksichtigen. Auf Basis des verbesserten eindimensionalen Modells wurde ein PBA-basiertes Framework etabliert, das durch die Integration von Materialinformationen und lateralen Ausbreitungsparametern die vollständige dreidimensionale PED-Vorhersage in heterogenen Medien ermöglicht.

Der analytische Ansatz wurde zunächst durch in-silico-Studien anhand von MC-Simulationen validiert, wobei sowohl mehrere Schichtphantome als auch realistische, aus Patientendaten abgeleitete Computertomographie-Geometrien untersucht wurden. Zur

Reichweitenbewertung lagen die Unterschiede zwischen den distalen Abfallpositionen der vorhergesagten und simulierten eindimensionalen PED-Profile für alle Validierungsfälle unter 0,8 mm. Die Übereinstimmung zwischen vorhergesagten und simulierten dreidimensionalen PED wurde mittels globaler Gamma-Index-Analyse unter Anwendung der Kriterien 2 %/2 mm und 1 %/1 mm bewertet. Für die Patientengeometrien wurden Durchlassraten von über 95 % für das 1 %/1 mm-Kriterium erzielt. Diese Ergebnisse belegen die Fähigkeit des Ansatzes, dreidimensionale PED sowohl hinsichtlich der Reichweite als auch der Amplitude mit hoher Genauigkeit vorherzusagen.

Anschließend wurde der analytische Ansatz anhand realer klinischer Fälle validiert, bei denen ein Offline-PET/CT-Monitoring eingesetzt wurde. Vier Patienten, die am Heidelberg Ion Beam Therapy Center mit Kohlenstoffionen behandelt wurden, wurden ausgewählt, und deren Bestrahlungspläne sowie CT-Bilder dienten als Grundlage für MC-Simulationen und die analytische Vorhersage der β^+-Aktivitätsverteilungen. Die analytisch vorhergesagten Aktivitätsverteilungen, die aus den simulierten Dosisverteilungen mithilfe des analytischen Ansatzes abgeleitet wurden, wurden sowohl mit den simulierten Ergebnissen als auch mit den gemessenen Offline-PET-Daten verglichen. Die analytischen und MC-basierten Aktivitätsverteilungen zeigten eine gute Übereinstimmung in der Reichweite mit mittleren Abweichungen von unter 0,5 mm sowie in der Amplitude mit einem mittleren normierten quadratischen Mittelwertfehler von unter 2 %. Die zwischen den gemessenen PET-Signalen und den analytisch vorhergesagten Aktivitätsmustern ermittelten Reichweitenverschiebungen stimmten mit publizierten Ergebnissen überein.

Darüber hinaus wurde eine erste Validierung unter Verwendung von In-Beam-PET-Daten durchgeführt, die in einem Polymethylmethacrylat-Phantom aufgenommen wurden, welches vom National Institutes for Quantum Science and Technology in Chiba bereitgestellt wurde. Erste Vergleiche zeigten ausgeprägte Abweichungen im frühesten Akquisitionszeitfenster (0–60 s nach der Bestrahlung), die hauptsächlich auf ungenaue Vorhersagen kurzlebiger Positronen-Emitter zurückgeführt wurden. Zur Abschwächung dieses Effekts wurden isotopenspezifische Skalierungsfaktoren eingeführt. Nach Anwendung dieser Korrekturen wurde für die meisten Fälle eine gute Übereinstimmung zwischen analytischen Vorhersagen und Messungen sowohl hinsichtlich der longitudinalen Reichweite als auch der lateralen Aktivitätsprofile erzielt, insbesondere zu späteren Akquisitionszeitpunkten, wobei die Reichweitenverschiebungen unter 2 mm lagen. Dennoch sind weitere Verfeinerungen der Modellparameter auf Basis verbesserter MC-Simulationen oder direkt aus experimentellen Messdaten erforderlich.

Insgesamt wurde in dieser Arbeit ein analytisches Framework zur schnellen und präzisen Vorhersage von Positronen-Emitter-Verteilungen und entsprechenden β^+-Aktivitätsverteilungen in der Kohlenstoffionentherapie entwickelt und validiert, das im Vergleich zu vollständigen Monte-Carlo-Simulationen eine Rechenbeschleunigung um mindestens einen Faktor von 40 erreicht. Durch die Nutzung der in analytischen Dosisberechnungsmodellen für Kohlenstoffionen üblicherweise eingesetzten Pencil-Beam-Algorithmen ermöglicht der vorgeschlagene analytische Ansatz eine unkomplizierte Integration in Behandlungsplanungssysteme und erleichtert damit seine Überführung in die routinemäßige klinische Anwendung.

Abstract

Radiotherapy plays an important role in cancer treatment, and particle therapy has emerged as an advanced modality due to its superior dose conformity compared to conventional photon radiation therapy. Among particle modalities, carbon ions offer distinct physical and biological advantages. However, carbon ion therapy is sensitive to range uncertainties, as small deviations in beam range can lead to tumor underdosage or unnecessary radiation exposure to surrounding healthy tissue. Positron emission tomography (PET) monitoring is one viable approach for in vivo range verification, in which measured PET signals are typically compared with predicted β^+-activity distributions derived from positron emitter distributions (PED). Monte Carlo (MC) simulations are commonly used to predict PED, but their computational cost limits routine clinical applicability. This motivates the development of fast and reliable alternative prediction methods.

The objective of this thesis is the development and comprehensive validation of an analytical framework for predicting 3D PED and corresponding β^+-activity distributions in carbon ion therapy, enabling a computationally efficient and clinically applicable tool for PET-based range verification in carbon ion therapy.

To this end, an analytical framework for PED prediction was developed by combining an improved 1D analytical approach with a 3D spreading kernel inspired by the pencil beam algorithm (PBA) commonly used in dose calculation. A previously proposed 1D analytical approach for predicting PED from depth dose profiles for carbon ions was further revised by introducing finer modelling functions and considering additional positron emitters (PEs). In addition, a mapping strategy was developed to better handle longitudinal heterogeneity effects in projectile PED. Based on the improved 1D model, a PBA-based framework was established to enable full 3D PED prediction in heterogeneous media by integrating material information and lateral spreading parameters.

The analytical approach was first validated through in-silico studies against MC simulations for several slab phantoms as well as realistic computed tomography (CT) scans from patient data. For range assessment, the differences between distal fall-off positions of predicted and simulated 1D PED profiles were below 0.8 mm for all validation cases. The agreement between predicted and simulated 3D PED was evaluated using global gamma index analysis with the 2%/2 mm and 1%/1 mm criteria. For patient cases, the passing rates for 1%/1 mm criteria were above 95%. These results demonstrated the capability of this approach to predict 3D PED with good accuracy in terms of range and magnitude.

Next, the analytical approach was validated using real clinical cases where offline

PET/CT monitoring was employed. Four carbon ion therapy patients treated at the Heidelberg Ion Beam Therapy Center were selected, and their treatment plans and CT images were used for MC simulations and analytical prediction of β^+-activity distributions. The analytically predicted activity distributions, derived from the simulated dose distributions with the analytical approach, were then compared with both simulated results and measured offline PET data. The analytical and MC activity distributions demonstrated a good match in range with mean deviations less than 0.5 mm, and in amplitude with mean normalized root mean square error less than 2%. Range shifts between the measured PET signals and the analytical activity patterns were evaluated and found to be consistent with published results.

In addition, a preliminary validation was performed using in-beam PET data acquired in a polymethylmethacrylate phantom provided by the National Institutes for Quantum Science and Technology in Chiba. Initial comparisons revealed pronounced discrepancies in the earliest acquisition window (0–60 s after irradiation), which were primarily attributed to inaccurate predictions of short-lived PEs. To mitigate this effect, isotope-dependent scaling factors were introduced. After applying these corrections, good agreement between analytical predictions and measurements was achieved for most cases in terms of both longitudinal range and lateral activity profiles, especially at later acquisition times, with range shifts below 2 mm. Nevertheless, further refinement of the model parameters based on improved MC simulations or directly on experimental measurement data will be required.

Overall, this thesis developed and validated an analytical framework for fast and accurate prediction of PED and β^+-activity distributions in carbon ion therapy, achieving a computational speed-up of at least a factor of 40 compared to full MC simulations. By leveraging the PBAs commonly used in analytical carbon ion dose engines, the proposed analytical approach enables a straightforward integration into treatment planning systems, thereby facilitating its translation into routine clinical practice.

Contents

List of Figures

List of Tables

List of Abbreviations

1D	One-dimensional
2D	Two-dimensional
3D	Three-dimensional
BAMS	Beam and Application Monitoring System
BEV	Beam's-eye-view
BGO	Bismuth germanate
CNAO	Centro Nazionale di Adroterapia Oncologica
CT	Computed tomography
CTV	Clinical target volume
DNA	Deoxyribonucleic acid
DOI	Depth of interaction
FOV	Field of view
FWHM	Full width at half maximum
GPU	Graphics processing unit
GSI	GSI Helmholtz Centre for Heavy Ion Research
HIMAC	Heavy Ion Medical Accelerator
HIT	Heidelberg Ion Therapy Center
HU	Hounsfield unit
IDD	Laterally integrated depth dose
IDPED	Laterally integrated depth positron emitter distribution
LEM	Local effect model
LET	Linear energy transfer
LINAC	Linear accelerator
LOR	Line of response
MC	Monte Carlo
MKM	Microdosimetric kinetic model
MLS	Most-likely-shift

NRMSE	Normalized root mean square error
PBA	Pencil beam algorithm
PE	Positron emitter
PED	Positron emitter distribution
PET	Positron emission tomography
PG	Prompt gamma
PHA	Pulse height analyzer
PMMA	Polymethylmethacrylate
PMT	Photomultiplier tube
QAR	Organ at risk
QGSP_BIC	Geant4 physics list
QST	National Institutes for Quantum Science and Technology
R80	Distal position of the 80% level
RBE	Relative biological effectiveness
RF	Radio frequency
RMSD	Root-mean-square error
RT	Radiotherapy
SC	Superconducting
SEB	Secondary-electron bremsstrahlung
SiPM	Silicon photomultiplier
TOF	Time-of-flight
TPS	Treatment planning system

1

Introduction

Cancer, a disease in which abnormal cells grow uncontrollably and can spread to other parts of the body (a process called metastasis), poses a major public health and economic burden globally. These abnormal cells arise from genetic mutations, which can result from an inherited condition or environmental factors such as tobacco, obesity, viruses, radiation and carcinogenic chemicals. About 1 in 5 people develop cancer in their lifetime. In 2022, there were close to 20 million new cases of cancer worldwide alongside 9.7 million cancer deaths, and new annual cancer cases are predicted to exceed 35 million by 2050, representing a 77% increase from the 2022 level [Bray et al., 2024].

Multiple cancer treatment modalities exist such as surgery, radiotherapy (RT), chemotherapy, hormone therapy and immunotherapy. Among these, RT, which utilizes ionizing radiation to damage the DNA of cancerous cells leading to cellular death, is currently one of the common treatment options. Approximately half of cancer patients receive RT, either alone or in combination with surgery and chemotherapy for a wide range of cancers [Yap et al., 2016]. The history of RT dates back to the discovery of X-ray by Wilhelm Röntgen in 1895, shortly followed by its first clinical application for cancer treatment in 1896 [Grubbé, 1933]. Since then, the field of RT has undergone tremendous developments. Improvements in diagnostic imaging, treatment planning, and treatment delivery techniques have greatly enhanced the accuracy and precision of treatments, enabling more effective targeting of cancerous tissues while sparing surrounding healthy tissues [Chandra et al., 2021].

In 1946, a half-century after the discovery of X-ray, Robert Wilson described the energy deposition characteristics of protons in therapeutic energy range and proposed the possible clinical application of particle beams [Wilson, 1946]. The energy deposited at a given depth increases as the particle slows down, primarily due to the velocity dependence of the stopping power, resulting in a sharp increase in dose (the amount of radiation energy absorbed per unit mass of matter) near the end of the particle range, known as the Bragg peak (see Figure 1.1). Unlike X-rays (photons), which deposit most of their energy upstream and

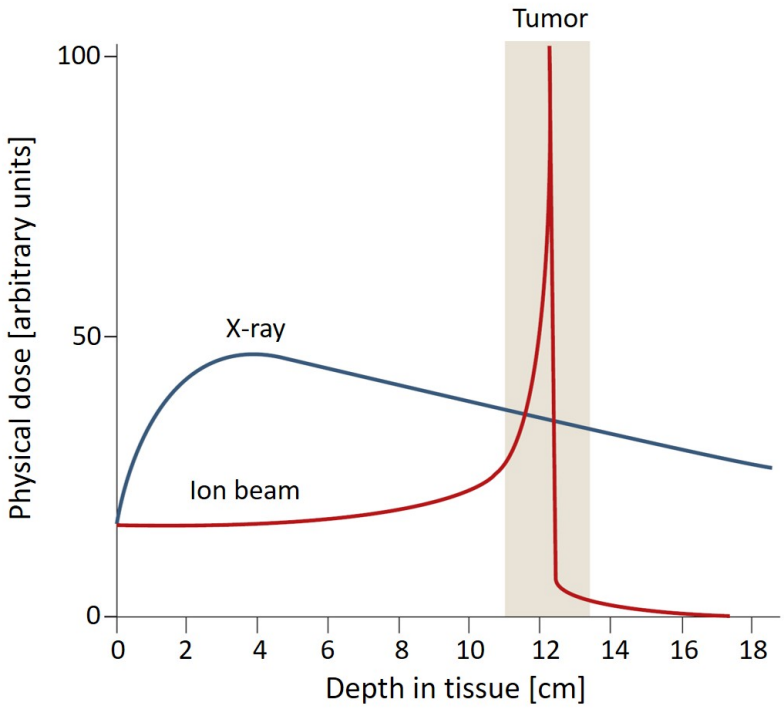

Figure 1.1: Comparison of depth dose distributions in tissue for X-rays and charged particles. Figure from [Durante and Loeffler, 2010]

downstream of the tumor in surrounding healthy tissues, charged particles deposit most of their energy precisely at the Bragg peak (see Figure 1.1). This distinct characteristic offers a significant advantage by minimizing the unwanted irradiation of healthy tissues. In the subsequent years, particle therapy with proton and heavier ions such as ^{12}C was extensively investigated by research facilities and later integrated as hospital-based particle therapy centers [Halperin, 2006]. While protons exhibit a increased relative biological effectiveness (RBE) of approximately 1.1, carbon ions offer additional radiobiological advantages owing to a differential RBE that increases toward the Bragg peak, making them particularly attractive for clinical applications [Durante and Loeffler, 2010]. In recent years, there has been increased investment in the establishment of particle therapy centers worldwide. According to the latest update from the Particle Therapy Cooperative Group (PTCOG) in December 2025, proton therapy is currently available in 24 regions with a total of 129 operational centers, while carbon ion therapy is available in 7 countries, including Germany, Japan and China, with 17 operational centers and five additional facilities in the planning or construction phase [PTCOG, 2026].

With an increasing number of patients undergoing particle therapy, further improvements in treatment quality becomes increasingly essential. One of the critical factors influencing treatment quality is range uncertainties, which refers to uncertainties in the ion stopping position and thus in the Bragg peak location. It can be caused by anatomical changes

occurring during fractionated treatments, in which the dose is delivered over multiple sessions, as well as by variations in daily patient positioning. These range uncertainties may result in an underdosage of the tumor or an overdosage of the healthy tissues, highlighting the importance of accurate range verification. Positron emission tomography (PET), which relies on the imaging of the positron emitting (β^+ decay) nuclei ensuing from nuclear interactions of the incoming beam with the irradiated tissue, is so far the most extensively clinically investigated approach for this purpose [Enghardt et al., 2004, Moglioni et al., 2022, Parodi et al., 2023, Kraan et al., 2024b]. However, because the PET signal is not directly proportional to the delivered dose, the measured activity cannot be directly compared to dose distribution. Monte Carlo (MC) simulations have been typically employed to predict β^+-activity, and their comparison to the actual PET measurements allows for treatment verification [Pönisch et al., 2004, Enghardt et al., 2004, Parodi et al., 2007a,c, Bauer et al., 2013, Fiorina et al., 2018]. Despite their accuracy, MC simulations are computationally intensive and time-consuming. To overcome these computational challenges, analytical methods were initially proposed as a viable alternative to MC methods to predict β^+-activity distributions, with early developments primarily focusing on proton therapy. Parodi and Bortfeld [2006] developed an analytical filtering method to calculate activity based on the convolution of MC simulated dose with specific filter functions. This method was later extended by Attanasi et al. [2011] and subsequently integrated into an in-house treatment planning system (TPS) by Frey et al. [2013] and in the research version of a commercial TPS by Pinto et al. [2020]. Additionally, Miyatake and Nishio [2013] developed an analytical activity pencil beam algorithm based on experimental data of β^+-activity in thick targets. In recent years, fast MC tools using GPU acceleration have been developed to address the computational shortcomings of MC codes, with first applications focusing on proton therapy, both for dose calculation [Jia et al., 2012, Wan Chan Tseung et al., 2015, Choi et al., 2018] and PET-based range verification [McNamara et al., 2022, Borys et al., 2022]. However, while considerable progress has been made in applying fast MC techniques to proton therapy, their application in carbon ion therapy, particularly to PET based range verification, remain comparatively limited [Qin et al., 2017, Qi et al., 2021, Lysakovski et al., 2024]. Hence, given these persisting limitations and the need for computational efficiency in PET-based verification for carbon ion therapy, analytical methods specifically focused on predicting the more complex β^+-activity in carbon ion therapy have been proposed. For example, an experimental-based approach was proposed to predict positron emitter distributions (PED) by linear superposition of measured positron emitter yields from different reference materials [Priegnitz et al., 2012]. Helmbrecht et al. [2016] then extended this approach to 3D PED calculations, revealing, however, limitations in the validity of the lateral description of the beam for secondary particles and the prediction of the projectile fragments distribution. Another 1D analytical approach suggested by Hofmann et al. [2019] predicts PED based on dose profiles using built-in modeling functions. Their approach adapted a filtering approach originally designed for proton therapy [Parodi and Bortfeld, 2006] to be applicable for carbon ion therapy. This approach, however, was primarily investigated in 1D or quasi-3D scenarios, i.e., simply handled as a collection of 1D distributions [Vasic et al., 2024].

In this thesis, a dedicated computational framework has been proposed, developed and

thoroughly investigated for 3D PED prediction to facilitate PET-based range monitoring in carbon ion therapy. The proposed framework consists of two key components: a 1D PED prediction approach and a 3D spreading kernel. The 1D prediction approach incorporates and extends the previously developed analytical approach by Hofmann et al. [2019], while the 3D spreading kernel is conceptually analogous to the dose calculation technique utilized by the pencil beam algorithm (PBA). Comprehensive validation of this approach has been conducted through in-silico studies and clinical comparisons using offline and in-beam PET measurement data from collaborating institutions.

The thesis is organized as follows. Chapter 2 presents the fundamentals of particle therapy, discussing the underlying physical and radiobiological principles, clinical implementation, and the uncertainties in particle therapy. Existing techniques for in vivo range verification are also introduced. Chapter 3 focuses on PET-based range monitoring, covering the principles and fundamentals, offline and in-beam PET methodologies, and presenting the clinical implementation of PET-based range monitoring. Chapter 4 describes the methods used in this thesis to calculate the 3D PED in carbon ion therapy, namely, MC simulation and the novel analytical approach. After summarizing the MC settings used throughout the thesis, the chapter reviews previous analytical models, identifies their limitations, and introduces the corresponding improvements developed in this work. The formulation of the 3D spreading kernel is finally presented. Chapter 5 evaluates the analytical approach through in-silico validation, comparing analytical predictions against MC simulations. Chapter 6 provides clinical validation using patient offline PET measurement data. Chapter 7 shows another validation using in-beam PET data of phantom studies. Finally, Chapter 8 summarizes the key conclusions derived from this work and provides future perspectives.

2

Fundamentals of particle therapy

Particle therapy is an external beam irradiation cancer therapy using protons or heavy ions (typically carbon ions). Unlike the conventional radiotherapy using X-rays, it exploits the distinct physical and biological properties of these particles to achieve precise and effective tumor irradiation. This chapter presents the physical and biological basis of particle therapy, the clinical implementation, and the uncertainties in particle therapy.

2.1 Interactions of heavy charged particles with matter

In the context of particle therapy, the particles of interest refer to charged particles heavier than electrons, for example, protons and carbon ions. This section therefore focuses on the interactions of heavy charged particles with matter. In the therapeutic energy range, three primary interaction mechanisms are of particular relevance: first, inelastic Coulomb collisions with atomic electrons; second, elastic nuclear scattering on atomic nuclei; and third, nuclear interactions with atomic nuclei. These interactions lead to modifications of the incident charged particles in terms of energy loss and change of direction, transfer of energy to matter, resulting in energy deposition, generation of secondary particles and possible alteration of the primary particles.

2.1.1 Inelastic Coulomb collisions with atomic electrons

Inelastic Coulomb collisions with the bound atomic electrons are the principal process through which charged particles lose energy along their trajectory in the material. These interactions either create atomic ionization, where an electron is ejected from the atom, or excitation, where the electron is raised to a higher bound state, and a small deflection of the

incident charged particles. The occurrence of frequent, small energy losses along the path of charged particles in matter leads naturally to the concept of stopping power, defined as the average energy loss, dE, per unit distance, dx, along the track of the particle. The collision stopping power for a singly charged particle heavier than an electron is described by the Bethe-Bloch formula, which is valid at energies above approximately 1 MeV/n (Megaelectronvolt per nucleon) [Bethe, 1930, Bloch, 1933, Attix, 2008]:

$$-\frac{dE}{dx} = 2\pi N_a r_e^2 m_e c^2 \rho \frac{Z}{A}\frac{z^2}{\beta^2}\left[\ln\left(\frac{2m_e c^2\gamma^2\beta^2 T_{max}}{I^2}\right) - 2\beta^2 - 2\frac{C}{Z} - \delta\right] \tag{2.1}$$

where N_a is Avogadro's number, r_e is the classical electron radius, $m_e c^2$ is the rest mass energy of the electron, ρ is the mass density of absorbing material, Z is the atomic number of absorbing material, A is the atomic weight of absorbing material, z is the charge of incident particle, $\beta = v/c$ the particle velocity in units of c, the Lorentz factor $\gamma = 1/\sqrt{1-\beta^2}$, the mean ionization potential I, T_{max} is the largest possible energy transfer in a single collision with a free electron, $2C/Z$ and δ describe the shell and density effect correction, respectively. The shell correction becomes relevant at low particle velocities, where the assumption of free electrons breaks down and the finite binding energies of atomic electrons, particularly those in inner shells, reduce the energy transfer to the medium. The density effect correction accounts for the reduction in stopping power at high particle energies due to dielectric polarization of the medium, which weakens the effective electric field acting on distant electrons.

An example of the mass collision stopping power $(-\frac{1}{\rho}\frac{dE}{dx})$ of different ions in "tissue soft"[I] defined by ICRU [1984] is shown in Figure 2.1 as a function of the particle energy. For incident ions at therapeutic energies in the order of 100 MeV/n, the stopping power increases with decreasing energy due to the dominant $1/\beta^2$ dependence in Eq. (2.1). As the energy decreases further to approximately 0.1-1 MeV/n, the stopping power arrives to the maximum and then decreases, where the Lindhard–Scharff–Schiøtt theory provides the appropriate description [Lindhard et al., 1963]. The evolution of stopping power suggests that when the heavy charged particle is almost at the end of its path its capacity to ionize increases rapidly, giving rise to the Bragg peak, whose width and shape are also influenced by range straggling and nuclear interactions, as discussed later.

From the perspective of matter, energy losses of charged particles through inelastic collisions correspond to energy "gains" by the medium, resulting in atomic excitation or ionization. To quantify the amount of energy imparted to matter, a macroscopic quantity, absorbed dose, is defined as the mean energy dϵ deposited by ionizing radiation in a given mass of material dm [ICRU, 1998]:

$$D = \frac{\mathrm{d}\epsilon}{\mathrm{d}m} \tag{2.2}$$

The unit of absorbed dose is Gray (Gy) which is 1 Joule per kilogram (J kg^{-1}). The dose absorbed in a thin layer of an absorber material with mass density ρ is given by a

[I] "tissue soft" refers to the ICRU four-component tissue-equivalent material, with a density of 1.0 g/cm^3 and a mean excitation energy of 74.9 eV, composed by hydrogen (10.12%), carbon (11.10%), nitrogen (2.60%), and oxygen (76.18%).

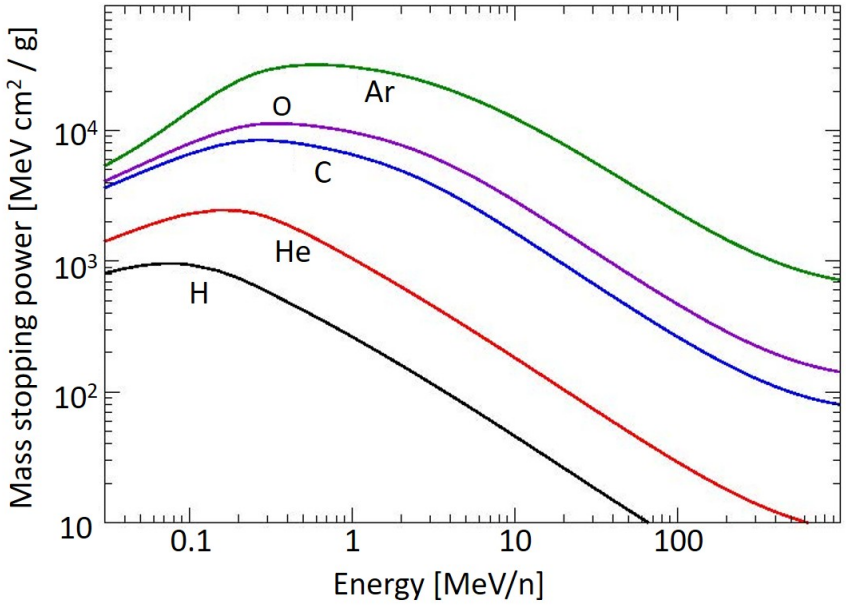

Figure 2.1: Mass stopping powers as a function of energy for the ions H, He, C, O, and Ar in the material "tissue soft" which is defined by ICRU [1984]. Figure from [Lühr et al., 2012]

.

combination of the fluence Φ (the total number of particles that pass through a unit area) and the stopping power:

$$D[Gy] = 1.6 \times 10^{-9} \times \frac{\mathrm{d}E}{\mathrm{d}x}[\mathrm{keV}/\mu\mathrm{m}] \times \Phi[\mathrm{cm}^{-2}] \times \frac{1}{\rho}[\mathrm{cm}^3/\mathrm{g}] \tag{2.3}$$

2.1.2 Elastic nuclear scattering

When a charged particle passes close to an atomic nucleus at a distance much smaller than the atomic radius, the Coulomb interaction occurs primarily with the nuclear charge rather than with bound electrons. Such interactions deflect the particle trajectory but cause negligible energy loss, and are therefore considered elastic. Most collisions involve a distant interaction of the particle with a nucleus; the nuclear charge is partially screened by the atomic electrons, and the incident particle experiences only a small deflection. The cumulative effect of these numerous small-angle deflections along the particle path is referred to as multiple Coulomb scattering. This phenomenon has been studied extensively, notably by Moliere [1947] and Highland [1975]. The angular distribution of charged particles after traversing a thin foil can be approximated by a Gaussian distribution, with the mean

scattering angle given by Highland's expression [Highland, 1975]:

$$\bar{\theta}_0 = 14.1 \frac{z}{pv} \sqrt{\frac{L}{L_R}} \left(1 + \frac{1}{9} \log \frac{L}{L_R}\right) \tag{2.4}$$

where z, p and v are the charge number, momentum and velocity of the incident particle, respectively; L is the thickness of the scatterer; L_R[II] is the radiation length characteristic of the scattering material, which increases as the atomic number of the target material decreases. The dependence of multiple scattering on an inverse power of the kinetic energy of ions according to Eq. (2.4) explains the progressive broadening of an ion beam as it penetrates matter and loses energy. Moreover, multiple-scattering processes are less pronounced for heavier ions compared to protons, due to the greater mass of the former. Figure 5.6 illustrates the above two features.

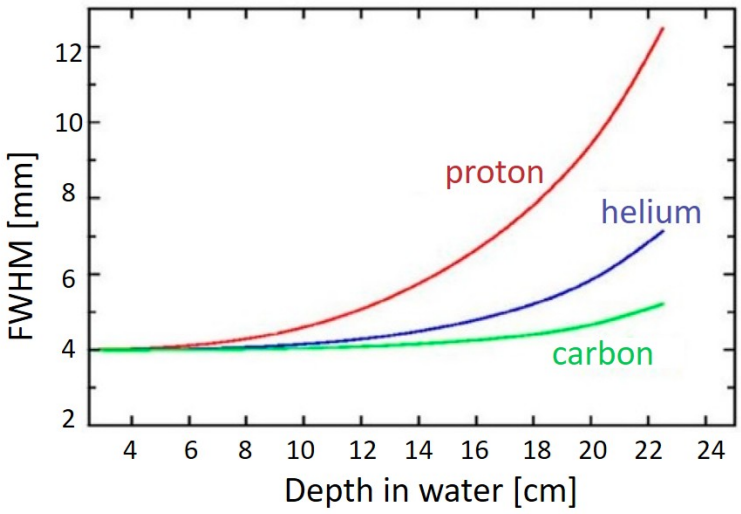

Figure 2.2: Full width at half maximum (FWHM) of beams of protons, helium and carbon ions as a function of depth in water. Figure from [Wickert et al., 2022]

.

2.1.3 Nuclear reactions with atomic nuclei

In addition to electromagnetic interactions, charged particles may also undergo inelastic interactions with atomic nuclei governed by the nuclear force, i.e., nuclear reactions. These interactions lead to an exponential attenuation of the primary ion fluence $\Phi(z)$ in depth according to

$$\Phi(z) = \Phi_0 \exp\left(-N\sigma_{tot} z\right) \tag{2.5}$$

[II]It is defined as the mean length (in cm) into the material at which the energy of an electron is reduced by the factor 1/e.

where Φ_0 is the initial ion beam fluence, N is the density of target nuclei, σ_{tot} is the total reaction cross-section and z is the thickness of the absorber.

For protons, nuclear reactions like (p,n), (p,d) and others can occur, leading to the disappearance of the incident protons and the production of secondary particles including neutrons, recoil nuclei and radioactive isotopes.

For heavier ions, nuclear reactions are commonly described by the abrasion–ablation model when colliding with target nuclei [Hüfner et al., 1975, Gaimard and Schmidt, 1991]. The initial abrasion stage corresponds to the removal of nucleons from the overlapping region of the colliding nuclei, followed by an ablation stage in which the excited pre-fragments de-excite via statistical emission of light particles and γ-rays. This process is illustrated in Figure 2.3, which highlights the roles of projectile overlap, the shearing away of nucleons from the projectile–target overlap region during the collision (abrasion), and the de-excitation of fragments (ablation). It is worth knowing that proton collisions can

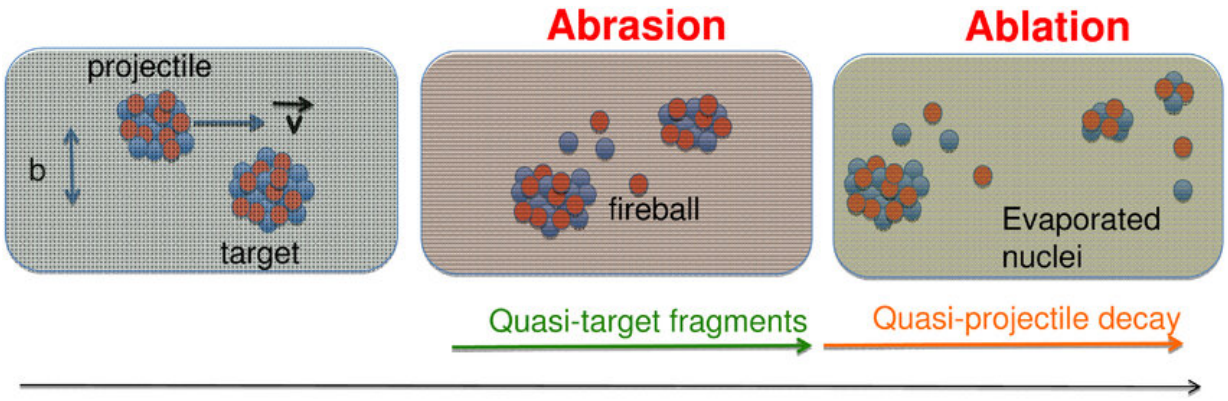

Figure 2.3: The abrasion-ablation model for nucleus-nucleus collisions. Figure from [Durante and Paganetti, 2016]

.

only produce target fragmentation, whereas in heavier ion collisions, both the projectile and the target can undergo fragmentation. Projectile fragments approximately preserve the direction and velocity of the incident ions since the majority of the collisions are statistically at relatively large distances (so called peripheral collisions), and thereby continue traveling forward with velocities close to that of the incident ion. In contrast, target fragments arise from nuclei in the traversed medium that participate in the interaction, often leaving behind excited remnants that subsequently de-excite and almost stay at rest.

Inelastic nuclear interactions also affect the lateral penumbra of charged particle beams. Secondary (or of any superior order) charged particles emerge from the collision at a small but non-negligible angle to the direction of the incident particle and create a halo of dose around the beam that broadens with depth. This halo is often approximated by a second (or third) broader Gaussian distribution, around the narrower one due to the previously described multiple Coulomb scattering.

In addition to the processes influencing the dose deposition, heavy charged particles

can also produce some radioactive isotopes in the body due to the nuclear interactions, such as positron emitters. This creates the possibility of monitoring the stopping point of the projectile ions by detecting the signals ensuing from these secondary products of the irradiation.

2.1.4 Range and depth-dose curve

Charged particles lose energy in a quasi-continuous fashion along their tracks in matter until they come to rest. This means that charged particles have a finite and reasonably well-defined range. A quantity for describing this behavior is the so-called continuous-slowing-down-approximation (CSDA) range, defined as

$$R_{CSDA}(E_0)_{=} \int_0^{E_0} \left(\frac{dE}{dx}\right)^{-1} dE \tag{2.6}$$

This represents the average path length traveled by a charged particle with kinetic energy E_0 before coming to rest. For heavy charged particles, whose trajectory is nearly rectilinear, the projected range R is very close to R_{CSDA}.

It is important to note that stopping power is an average value for the energy loss per unit distance. The amount of energy loss in each interaction has a probability distribution, leading to a phenomenon known as energy-loss straggling. The energy straggling directly translates into a straggling of the residual range and leads to a broadening of the Bragg-peak. In practice, energy and particularly range straggling for clinical ion beams can be assumed to have nearly Gaussian distributions. In addition, nuclear interactions influence the Bragg-peak shape by attenuating the primary particle fluence.

The laterally integrated depth–dose curve for a beam of heavy charged particles is known as the Bragg curve. Figure 2.4 illustrates Bragg curves of protons, helium and carbon ions, and the depth-dose curve of photons (X-rays). Multiple-scattering processes are less important for heavier ions compared to protons, due to the greater mass of the former. As a result, both range straggling and lateral scattering are reduced, producing steeper lateral and distal dose gradients for heavier ion beams compared with protons. In contrast to protons, nuclear interactions of heavier ions with matter cause projectile fragmentation. These fragments are mainly produced close to the Bragg peak and some of them have a greater range than that of the primary ion. Consequently, Bragg curves of heavier ions exhibit a characteristic dose tail extending beyond the Bragg peak (see the blue and green curves in Figure 2.4).

The pronounced Bragg peak allows for highly localized dose deposition at the tumor site while sparing surrounding healthy tissues. In clinical applications, tumors extend over a finite volume rather than a single depth. To deliver a uniform dose across the entire target, Bragg peaks of different energies and heights are superimposed to form a spread-out Bragg peak (SOBP). This approach enables homogeneous irradiation of the tumor volume while preserving the sharp distal fall-off.

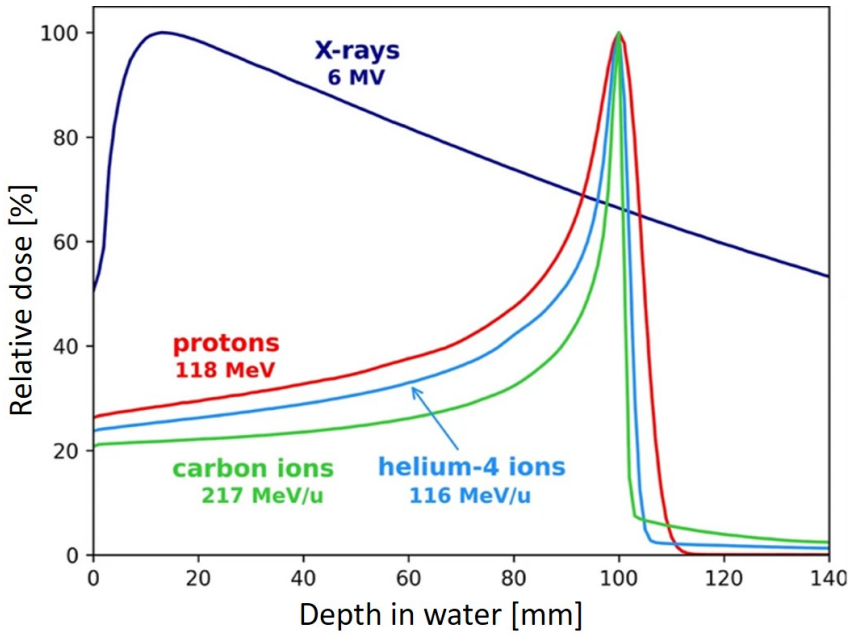

Figure 2.4: Depth-dose curves of X-rays, protons, helium and carbon ions. Figure from [Piacentini et al., 2024].

2.2 Radiobiological properties of ion beams

Exposure of biological tissues to ionizing radiation initiates a cascade of physical and chemical processes that ultimately cause cell death. Ionization and excitation of cellular molecules lead to biological damage both by direct ionization of critical biomolecules and indirectly through the production of highly reactive free radicals, primarily via the radiolysis of water. They react with other nearby molecules, thereby transferring chemical damage to them. While many molecular structures within the cell can be damaged, most such lesions are quickly repaired and have limited impact on viability. DNA, however, represents the most critical target, as its integrity is essential for the regulation of cellular function. Radiation-induced DNA damage constitutes the major pathway leading to reproductive cell death, either through mitotic failure or apoptosis.

The severity of biological damage depends not only on the absorbed dose but also on the quality of the radiation and the cell type. Linear energy transfer (LET) is a well-established concept [Kellerer, 1970] for quantifying radiation quality. LET is defined as the quotient of the $d\varepsilon$ by dl, where $d\varepsilon$ is the average energy locally imparted to the medium by a charged particle of specified energy in traversing a distance of dl, i.e.,

$$L_\Delta = \left.\frac{d\varepsilon}{dl}\right|_\Delta \tag{2.7}$$

The subscript Δ refers to the word "locally" in the definition and indicates the cutoff limit of energy transfer, and the unit of LET is kiloelectron volts per micrometer. Any

energy transfer greater than this cutoff limit will not be considered local. L_∞ indicates that all possible energy transfers have been included, and this unrestricted LET is equivalent to collisional stopping power (see Eq. (2.1)). Among the particles of interest in particle therapy, protons are classified as low-LET radiation producing sparse ionization along their tracks. In contrast, heavier ions are high-LET radiation, generating larger density of energy transfer events to the medium per particle track.

The differing biological consequences of radiation qualities are generally expressed through the relative biological effectiveness (RBE), which is defined as the ratio of the dose of a reference radiation (usually X-rays) to the dose of the radiation under study required to achieve the same biological effect [ICRU, 1979]:

$$\mathrm{RBE} = \left.\frac{\text{dose of reference radiation}}{\text{dose of radiation under investigation}}\right|_{iso-effect} \tag{2.8}$$

The concept of the biological dose is then introduced as the product of the physical absorbed dose and the RBE. This quantity represents the effective dose experienced by tissue and provides the basis for prescription and evaluation in particle therapy. In this way, clinical experience from photon therapy, such as dose levels associated with local tumor control, can be directly translated into the framework of particle therapy.

There are several variables related to RBE. Figure 2.5 shows the relationship between LET and RBE: RBE increases with LET up to an optimal range, after which it decreases due to "overkill" effects where excessive ionization density wastes energy without increasing cell kill. Besides LET, RBE varies with other factors, including dose per fraction, cell type and biological end-points [Jäkel, 2008].

Summarizing available data from numerous cell experiments and in vivo studies with protons, Paganetti et al. [2002] concluded that the RBE of protons is approximately 1.1 with small variation with depth, and this fixed RBE value is used for clinical applications of proton beams. Unlike protons, the RBE of heavier ions cannot be described by a single fixed value because it varies markedly along the beam path, increasing toward the distal edge where the LET is highest, and also varies within the target volume. Several bio-mathematical models have been developed and employed clinically to calculate heavier ions RBE (mainly carbon ions) [Stewart et al., 2018]. The Japanese centers started with the semi-empirical Kanai model which incorporated fast neutron RBE [Kanai et al., 1999], and switched more recently to the microdosimetric kinetic model (MKM), which links cell survival to the stochastic distribution of energy deposition on the micrometer scale, using microdosimetric quantities to describe how track structure influences biological response [Hawkins, 2003]. In Europe, the local effect model (LEM) was used since the GSI pilot project. Its main assumption is that the biological effect of ion beams can be predicted from photon dose–response relationships combined with the local spatial pattern of energy deposition along ion tracks [Scholz et al., 1997]. This model has evolved over the years to the latest version LEM-IV [Elsässer et al., 2010]. In recent years, there has been a rapidly growing body of studies investigating the RBE of carbon ions [Frese et al., 2012, Mein et al., 2020, Flint et al., 2024] and the differences among these models are quite considerable

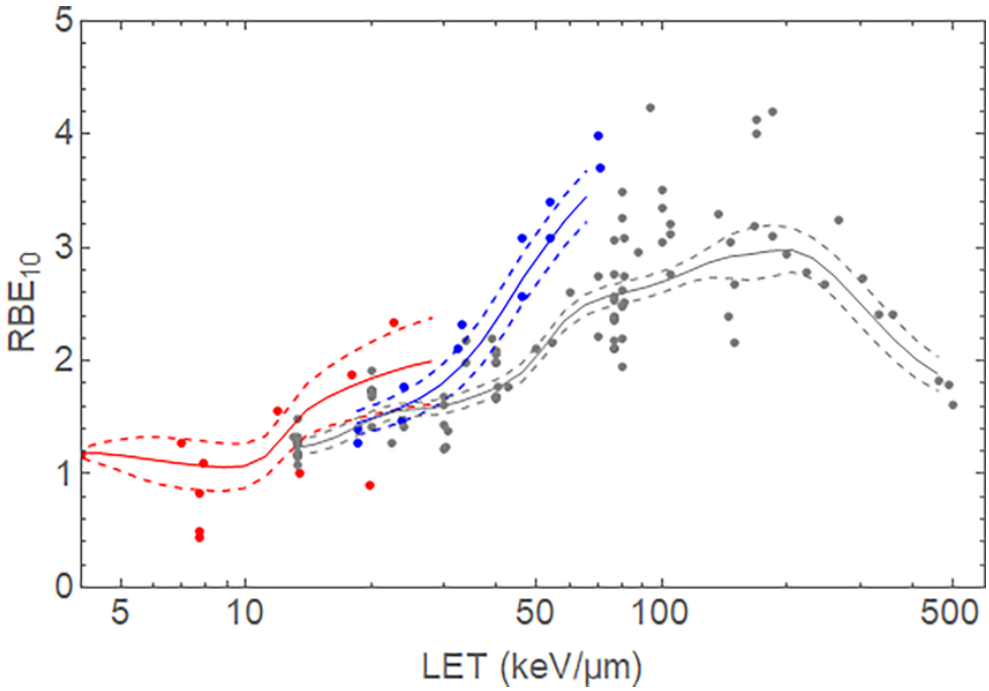

Figure 2.5: RBE at 10% survival fraction (RBE_{10}) as a function of LET. The RBE is depicted for different ions and energies (red protons, blue helium ions and gray carbon ions). Figure from [Helm and Fournier, 2023].

[Stewart et al., 2018]. As current RBE models have largely evolved independently in Europe and Asia, with limited integration of clinical trial data across regions, a more comprehensive and globally consistent framework for the use of RBE in carbon ion therapy would be highly desirable. Notably, several studies have already worked toward LEM–MKM translation and mapping to facilitate comparison of prescriptions, constraints, and clinical experience across centers [Fossati et al., 2012, Grosshagauer et al., 2022, Góra et al., 2024].

2.3 Clinical implementation of particle therapy

At present, the particles clinically used in particle therapy centers are largely limited to protons and carbon ions [PTCOG, 2026], whereas other particles, such as helium ions, oxygen ions, or multi-ion beams, are still confined to the research stage or early clinical trials [Tommasino et al., 2015, Mairani et al., 2022, Ikawa et al., 2025, Takei et al., 2025]. In general, to achieve sufficient treatment depth in patients, protons require a range of energies between a lower energy of ∼50-70 MeV and an upper energy of 200-250 MeV, while carbon ions require energies of 80-430 MeV/n (or, somewhat less preferable, 400 MeV/n in some cases). The production of particles to these therapeutic energies is accomplished using accelerators. Once extracted, the ion beams undergo a series of beam handling operations in the beam transport system before being delivered in the treatment room for therapy.

From the perspective of the medical staff, treatment execution relies on treatment planning and patient positioning, which are supported by the treatment planning system and patient positioning system, respectively. This chapter therefore presents the essential components of the "ions from source to tumor" process, including accelerators, beam transport and delivery, treatment planning and patient positioning.

2.3.1 Accelerators

The cyclotron and synchrotron have remained the two types of accelerators currently utilized in particle therapy. The seventeen facilities under operation employing carbon ions ions are using a synchrotron. For protons, synchrotrons, cyclotrons and synchrocyclotrons are employed clinically [PTCOG, 2026]. Although other types of accelerators, such as linear accelerators (LINAC) [Amaldi et al., 2009], laser-driven proton acceleration [Ceccotti et al., 2007, He et al., 2025], do exist or are being developed, these are not yet used in clinic and will not be introduced in this section.

Cyclotron and synchrocyclotron

The charged particle beam path in a simple cyclotron is shown in Figure 2.6. An oscillating radio frequency (RF) electric field is created between D-shaped electrodes (Dee). The charged particles are injected into the center of the cyclotron and accelerated by the electric field between the electrodes. When the beam leaves the electric field region, it enters the magnetic field region and is progressively bent over 180° and reenters the electric field region at the correct time to be accelerated in the opposite direction. Due to the magnetic field confinement and the increasing energy given to the charged particles by the RF field, they follow a spirally shaped orbit of a few hundred turns to the outer radius of the magnet from where they are extracted and sent into the beam line. In a classical cyclotron, the angular frequency of the electric field ω is given by

$$\omega = \frac{qB}{m}, \tag{2.9}$$

Where is q is the charge of the particle, B is the magnetic field, and m is the mass of the particle. This makes the assumption that the particle is classical, and does not experience relativistic phenomena. These effects start to become significant when v, the velocity of the particle, becomes greater than $\approx \frac{c}{3}$. To correct for this, the relativistic mass is used instead of the rest mass; thus, the Lorentz factor γ multiplies the mass, such that

$$\omega = \frac{qB}{m\gamma}, \tag{2.10}$$

where

$$\gamma = \frac{1}{\sqrt{1 - \frac{v^2}{c^2}}}. \tag{2.11}$$

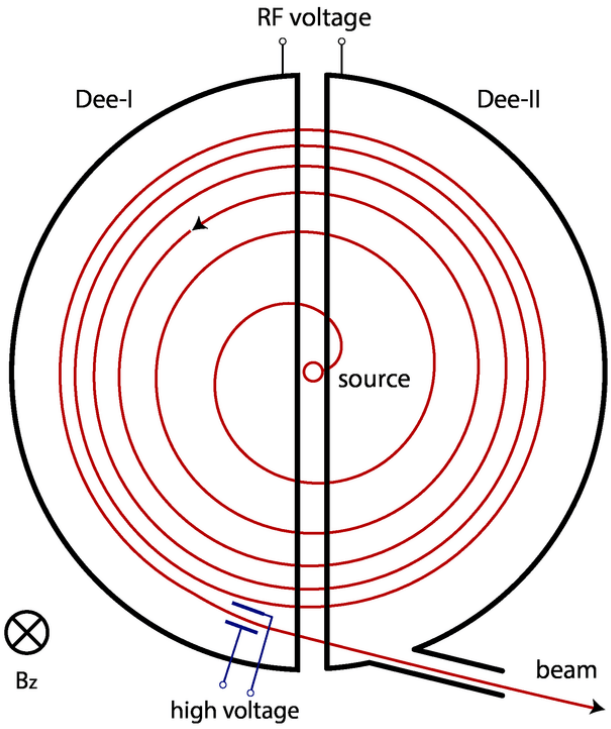

Figure 2.6: Pictorial description of a classical cyclotron in top view. Figure from [Seidel, 2021].

This can be achieved by a varying frequency of the accelerating RF field to remain synchronized with the particle revolution frequency. For protons, the frequency sweep is repeated at a rate of 500–1,000 Hz. During each sweep, a group of protons is accelerated from source to extraction, generating a pulse of extracted protons. Since such small cyclotrons operate in this 500–1,000 Hz pulsed beam intensity mode, they are called synchrocyclotrons.

The world first treatments using protons were performed with a synchrocyclotron at the Lawrence Berkeley Laboratory (LBL) in 1954. Shortly thereafter, proton therapy was introduced to treat patients at other institutions, including the Gustav Werner Institute in Sweden in 1957 and the Harvard Cyclotron Laboratory in the USA in 1961, both employing cyclotrons. By the 1990s, cyclotrons for proton therapy were with a typical diameter of five meters and a weight of 200 tons [Flanz et al., 1995]. As it can be advantageous to reduce the size of a cyclotron, superconducting (SC) magnets were employed in the cyclotrons in 2001 for the first time [Schillo et al., 2001], and the diameter was reduced to 3.5 meters and a weight of 100 tons. Nowadays, many proton therapy facilities have SC cyclotrons in operation [PTCOG, 2026]. Compared to cyclotrons, relatively few proton therapy facilities currently employ synchrocyclotrons; however, synchrocyclotrons are commonly adopted in single-room proton therapy facilities, and their use is expected to increase in the near future as many such facilities are currently under construction [PTCOG, 2026].

Synchrotron

A schematic of a classical synchrotron is shown in Figure 2.7. The synchrotron consists of a closed ring of dipole (bending) and quadrupole (focusing) magnets and one or more RF cavities, into which the beam is injected from an external source. The beam then circulates around the ring repeatedly through the accelerating RF structure. In order to keep the beam within the closed ring, both the magnetic field strength and the RF frequency must be synchronously increased as the beam energy increases. Thus, the beam is contained within the ring as its energy increases. When the beam reaches the desired energy, it is extracted. Generally, the advantage of synchrotrons is that they have greater energy flexibility, smaller energy spread, and lower power consumption.

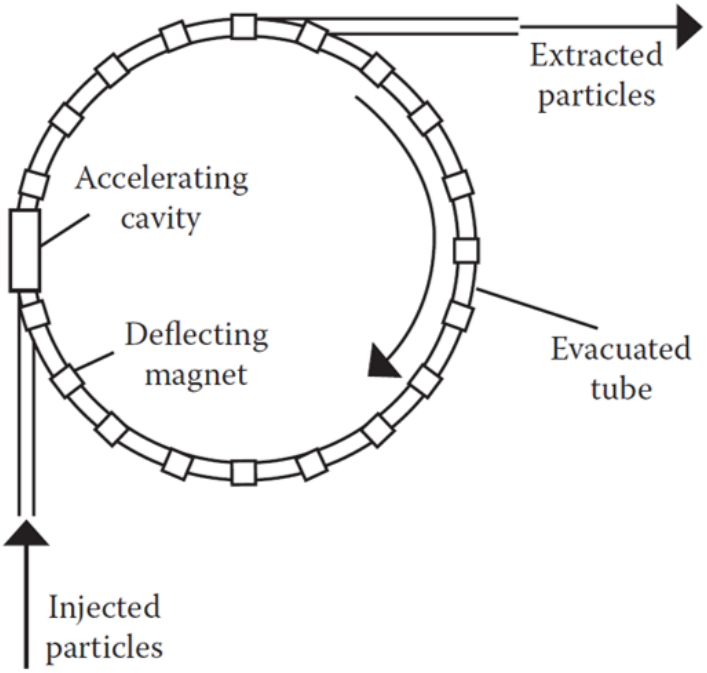

Figure 2.7: Schematic of a classical synchrotron in top view. Figure from [Ma and Lomax, 2012].

For protons, the ring has a typical diameter of 6–8 meters. Recent developments have focused on compact designs, with ring diameters reduced through the use of improved magnets, optimized beam optics, and streamlined injector systems. Examples include the "Radiance 330" synchrotron, installed at McLaren (Flint, MI) and Massachusetts General Hospital (Boston, MA) [Balakin et al., 2021], and compact synchrotrons developed by Hitachi, the first of which began clinical operation in Hokkaido in 2014 [Umezawa et al., 2013]. Advances in power efficiency, faster magnetic field ramping, and novel injection technologies have further reduced treatment times and power consumption. These improvements are aimed at making synchrotron-based proton therapy more compact, cost-effective, and competitive with cyclotron-based systems.

For carbon ion therapy, synchrotrons have been indispensable as cyclotrons capable of accelerating heavy ions become prohibitively large, heavy, and complex to construct and operate. The first synchrotron dedicated to therapeutic carbon ions was developed at the Heavy Ion Medical Accelerator (HIMAC) of the National Institutes for Quantum Science and Technology (QST, formerly NIRS) in Chiba, Japan [Sato et al., 1995]. This synchrotron generates the maximum carbon ion beam energy of 800 MeV/n, and has a diameter of about 40 meters [Sato et al., 1995]. The Helmholtz Centre for Heavy Ion Research (GSI) in Darmstadt, Germany, became the birthplace of carbon ion therapy in Europe [Kraft et al., 1995]. In GSI, the SIS-18 synchrotron, which have a circumference of 216 meters, was employed for the first clinical carbon ion treatment, producing the maximum carbon ion beam energy of 430 MeV/n [Kraft et al., 1995]. The research and experience of these pioneers lay the groundwork for subsequent synchrotron-based facilities worldwide. Since then, designs have evolved to reduce the size of the synchrotrons, leading to the design of the Heidelberg Ion Therapy Center (HIT) in Germany [Haberer et al., 2004]. The synchrotron in HIT has a diameter of 20 meters and can accelerate carbon ions to 430 MeV/n. HIT has pioneered techniques such as field-regulation of synchrotron magnets, achieving cycle-time reductions of about 30%, which is particularly significant for carbon ion treatments [Feldmeier et al., 2012]. Following them, more synchrotron-based carbon ion therapy facilities have been established since 2010, including the Centro Nazionale di Adroterapia Oncologica (CNAO) in Italy, the Shanghai Proton and Heavy Ion Center (SPHIC) in China, and MedAustron in Austria. Later on, NIRS has started the still ongoing development of the "SuperMinimac", a compact carbon ion synchrotron with SC magnets and a reduced diameter of just 7 meters, compared to the conventional 25 meters [Iwata, 2016]. Most recently, Rossi et al. [2022] established a European Collaboration to investigate superconducting magnets for next-generation heavy ion therapy in the frame of the European H2020 HITRIplus program. Vretenar and Benedetto [2024] introduce the Next Ion Medical Machine Study (NIMMS) for investigating the feasibility of a compact superconducting synchrotron for heavy ion therapy. These innovations highlight the central role of synchrotrons in carbon ion therapy and the ongoing efforts to improve their compactness, efficiency, and beam control.

2.3.2 Energy selection and Beam transport systems

The delivery of particles from the accelerator to the target (tumor) requires a series of dedicated devices and systems, and their configuration depends on the type of accelerator employed. In synchrotron-based facilities, the extracted beam can be directly accelerated to the desired energy and is then transported to the treatment room via the beam transport system. In contrast, cyclotrons and synchrocyclotrons generate beams at a fixed energy. To obtain the required beam energies, energy selection systems are indispensable. After energy analysis, the beam transport system guides the particles to the treatment room. Energy selection and beam transport systems thus constitute the most critical components bridging the accelerator and the target, and an overview of both systems will be presented in this section.

Energy selection systems

As mentioned above, beams extracted from synchrotrons can be delivered directly at the required energy with a very small energy spread (∼0.1%). In contrast, (synchro)cyclotrons can only provide beams at a fixed energy. Therefore, the beam needs to be accelerated to a sufficiently high energy before being extracted, subsequently its energy will be reduced to the desired value by an energy selection system.

In most cases, the beam is directed on a degrader to reduce its energy. The degrader consists of a low-Z (light) material with adjustable thickness placed in the beam path. Light materials are preferred in order to minimize multiple scattering (cf. Eq. (2.4)), with graphite compressed to high density being a common choice. For proton therapy, the required clinical energy range is typically 70–250 MeV. To reach the lowest energies, a degrader with a thickness of about 20 cm is needed. Various designs exist, including stacks of flat plates or adjustable wedges. It is important to note that while the degrader reduces the beam energy, it also increases the beam size and beam divergence due to multiple scattering. Moreover, statistical variations in the particle path length through the degrader broaden the energy spectrum of beam.

To control the beam shape, collimators are placed downstream to remove particles scattered out of the acceptance of the subsequent beam transport system. This typically includes a "beam-size defining" collimator positioned directly after the degrader and a "divergence defining" collimator placed further downstream. To ensure a well-defined beamline acceptance, these collimators should be as short as possible but thick enough to stop particles. Materials such as copper, brass, steel, or lead are commonly used. Finally, a beam analysis system consisting of magnets and slits selects the desired beam energy and energy spread (i.e., momentum and momentum spread) before the beam is injected into the transport line.

As synchrotron-accelerated beams exhibit very small energy spreads, low-energy proton beams (below 110 MeV) and carbon ion beams produce extremely sharp Bragg peaks. From a therapeutic perspective, a homogeneous SOBP needs to be created by superimposing a series of beams at different energies. However, sharp Bragg peaks make this goal more difficult to achieve. Therefore, suitable ripple filters or range shifters are often employed to deliberately increase a bit the energy spread of beam, thereby prevent ripples in the SOBP with a reasonable number of superimposed beam energy components.

Beam transport systems

The beam transport system between the energy selection system and the treatment rooms typically uses standard beam optics. It includes a common beam transport line consisting of bending and focusing magnets and beam analysis elements. The bending magnets deflect the beam along a curved trajectory, thereby steering the beam along the desired transport path. The focusing magnets act like a mirror, reversing the direction of the dispersion created by the upstream bending magnet so that the following bending magnet brings the dispersion back to zero. By arranging multiple magnets in sequences, the beam size and

divergence are kept within the acceptance, and the beam is delivered to the scheduled treatment room.

Inside the treatment room, the beam is transported to either an isocentric gantry or a fixed beamline, which then transports the beam to the treatment delivery nozzle. For gantries that have less than 360° rotation, for example, 180°, combinations of gantry rotations and robotic couch movements can be utilized to achieve multiple coplanar and non-coplanar beam entry angles and, accordingly, optimized treatment plans. Fixed beam treatment rooms can have either one horizontal beamline or a combination of a horizontal beamline and another fixed beamline at a certain angle (e.g., vertical or oblique) to the horizontal beamline, with all beamlines having the same isocenter.

2.3.3 Treatment delivery techniques

Based on the prescribed dose distribution for the target volume, the beam is then delivered to the target. Currently, two types of delivery techniques are available. The first technique, called passive scattering, uses scatterers in the nozzle to spread the beam laterally. In the longitudinal dimension of the dose distribution rotating modulators or ridge filters are used to create a region of uniform depth dose across the target (a homogeneous 3D dose cube). To further shape the field, a patient–specific collimator is used to shape the field laterally to conform to the maximum beams-eye-view extent of the target volume, while a range compensator is used to correct for patient surface irregularities and density heterogeneities in the beam path, thereby protecting the normal tissues distal to the target [Chu et al., 1993]. Figure 2.8(a) shows the schematic of the passive scattering (wobbling) method and also illustrates its downside of the unnecessary dose to the proximal edge of the tumor. In the wobbling technique, two steering magnets deflect the pencil beam to trace a circular path, after which a single scatterer spreads the beam laterally to produce a uniform irradiation field.

The second type of beam delivery technique is pencil beam scanning, also referred to as spot scanning or raster scanning. In spot scanning, the beam is switched off while it is repositioned to the next spot, while in raster scanning the beam remains on and continuously sweeps across the field. For this technique, two pairs of scanning magnets located at the nozzle entrance are used to position spots in the lateral dimension of the target volume, and by changing the beam energy the spots can cover the longitudinal dimension of the target volume [Pedroni et al., 1995] (see Figure 2.8(b)). As mentioned in Section 2.3.2, energy changes in scanning techniques depend on the accelerator: energy can be changed directly in a synchrotron, while it changes with an energy selection system when a cyclotron is employed.

The advantages of passive scattering includes its simplicity and robustness. It is less sensitive to organ motion as it delivers a broad, uniform field at once, with the only time-dependent process being the SOBP modulation if used. However, it requires multiple beam-modifying devices such as scatterers, modulators, collimators, and compensators, which increase secondary radiation exposure (especially neutrons), potentially elevating the risk of secondary cancers [Jarlskog and Paganetti, 2008]. Moreover, as mentioned above,

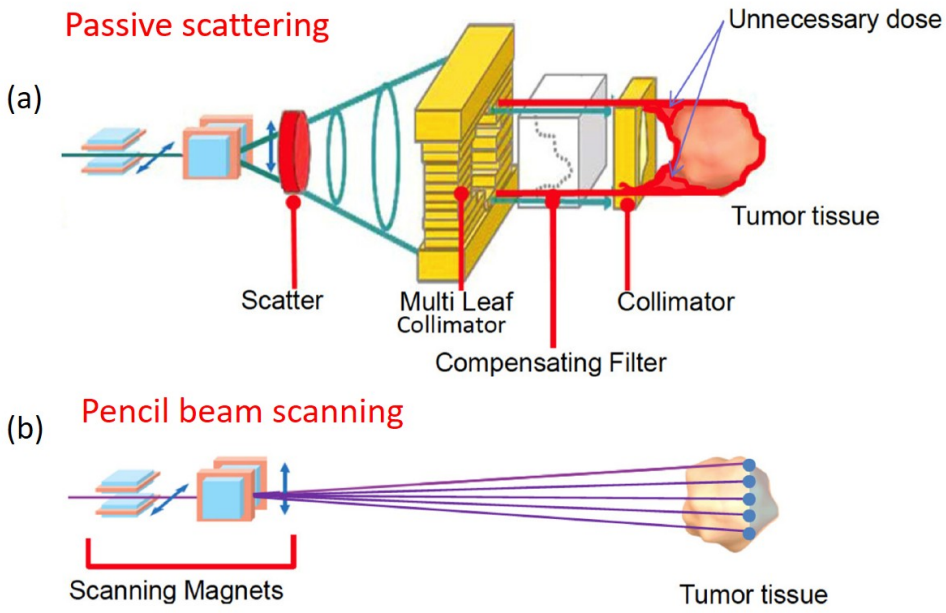

Figure 2.8: The two types of treatment delivery techniques: passive scattering (wobbling method) (a) and pencil beam scanning (b) techniques. Figure adapted from [Durante and Paganetti, 2016].

passive scattering provides less conformal dose distributions, often leading to unnecessary dose deposition in normal tissues (cf. Figure 2.8(a)).

Pencil beam scanning enables superior dose conformity and sub-millimeter targeting accuracy. By varying both spot intensity and energy, it achieves intensity-modulated particle therapy (IMPT), sparing healthy tissues more effectively. It also significantly reduces the production of stray radiation. On the downside, this technique is more complex, requiring precise verification of beam position and intensity for each spot, as small deviations can distort the planned dose distribution due to the sharp dose gradients of individual pencil beams. In other words, it is sensitive to organ motion and range uncertainties, which can increase the risk of overdosage in adjacent organs at risk (OAR) and underdosage in target tumor.

Since the development of pencil beam scanning technique in the mid-1990s [Pedroni et al., 1995], its use has steadily increased, and today the number of facilities equipped with scanning techniques are more than those with scattering techniques [PTCOG, 2026].

2.3.4 Treatment planning

Treatment planning is the process of transforming the prescription provided by the radiation oncologist into a deliverable treatment, a task carried out with the aid of a computerized treatment planning system (TPS). Its primary goal is to deliver a high dose to the tumor while respecting the dose constraints imposed on critical structures, with the patient

geometry typically derived from computed tomography (CT) images expressed in Hounsfield units (HU). At the core of a TPS lies the dose calculation algorithm, with the PBA and MC simulation being the most widely used approaches. Both methods will be introduced in the following sections.

Pencil beam algorithms

The PBA presented here is mainly based on the work of [Schaffner et al., 1999] and [Soukup et al., 2005] where the scanning technique was employed for proton therapy.

In PBA, the dose of a pencil beam is described by the laterally integrated depth dose (IDD) in water and by its lateral spread characteristics. The underlying physics of the lateral spread originates from multiple scattering and nuclear interactions occurring as the beam traverses the medium. This spread is typically modeled by Gaussian distributions, whereby a double or triple Gaussian parameterization is often employed to more accurately reproduce the dose distribution in the off-axis regions caused by multiple scattering and nuclear interactions [Pedroni et al., 2005, Schwaab et al., 2011, Kusano et al., 2007, Inaniwa et al., 2014]. The parameters of the Gaussian distribution can be determined through theoretical models such as Molière or Fermi–Eyges multiple scattering theory [Deasy, 1998], empirical formulas (e.g., [Kanematsu, 2009]) or by fitting to dose distributions obtained from experimental measurements [Pedroni et al., 2005] or MC simulations [Parodi et al., 2013].

When a beam traverses a heterogeneous medium (e.g., patient anatomy), typically only the material information along the central axis of the beam is traced and considered. In this way, the heterogeneous medium is simplified into a series of laterally infinite, homogeneous slabs composed of the same material as that traversed along the central axis. The water-equivalent range is then calculated along the central axis and the lateral spread is modeled by Gaussian distributions. However, this approach does not account for the heterogeneities located lateral to the beam axis. Therefore, PBA requires dedicated approaches to handle lateral heterogeneities. Commonly applied methods include the ray-casting method [Schaffner et al., 1999] and beam splitting methods [Schaffner et al., 1999, Soukup et al., 2005, Kanematsu et al., 2009].

The principle of the ray-casting method is to uniformly and densely distribute many rays parallel to the beam central axis over the cross-section of the beam spot. In this way, every voxel irradiated by the beam is intersected by at least one ray, and the water-equivalent depth of that voxel can be calculated according to the material traversed by the corresponding ray. The method is applicable to parallel beams with small angular divergence and therefore tends to perform better for heavier ions such as carbon than for protons. However, this approach neglects the dose distribution behind material interfaces that arise from angular spread in the phase space and from multiple scattering (see Figure 2.9) [Schaffner et al., 1999].

In beam splitting, a single beam is splitted into smaller sub-pencil beams, which are weighted according to the fluence of the original spot (see Figure 2.10). Since sub-pencil beams have smaller size, the error introduced by neglecting lateral heterogeneities is reduced.

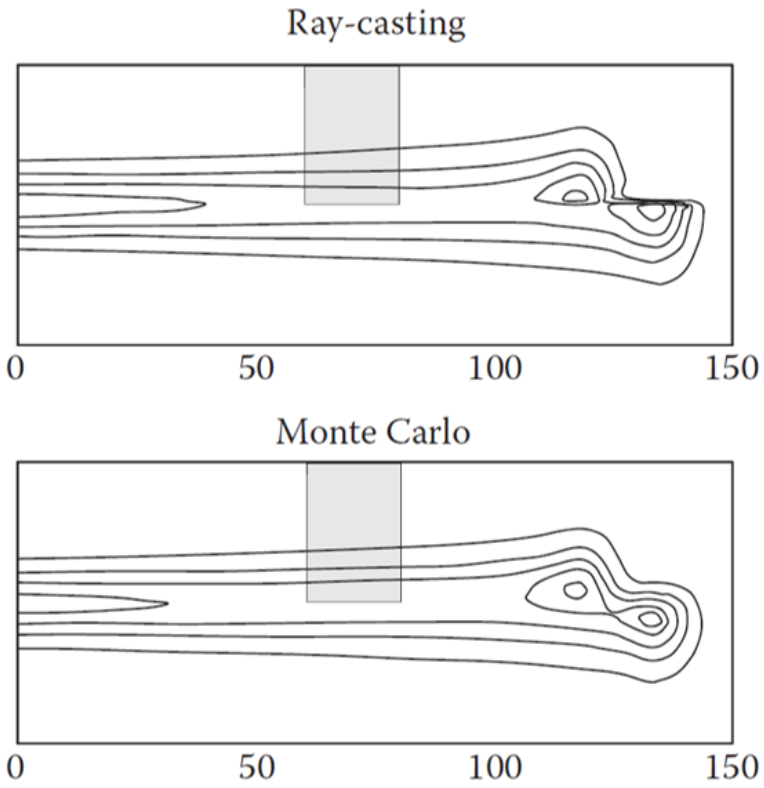

Figure 2.9: Comparison of dose distribution calculated by ray-casting and MC methods for a single proton pencil beam whose central axis is passing directly along a bone-water interface. Note the shearing of the Bragg peak behind the density heterogeneity due to the ray-casting approach and the smoother separation of the Bragg peak predicted by the MC method. Figure adapted from [Schaffner et al., 1999].

Obviously, the more sub-pencil beams are created, the higher the accuracy of the dose calculation, but this also comes at the cost of increased computational time. Therefore, determining an appropriate splitting strategy is beneficial. Schaffner et al. [1999] first proposed a splitting method tailored to proton pencil beam scanning, and subsequently Soukup et al. [2005] introduced an adaptive splitting approach, in which spots are divided such that the spacing of the sub-spots matches the voxel size of the geometry. Later, Kanematsu et al. [2009] proposed a dynamic splitting method for carbon ions that accounts for downstream inhomogeneities, thereby addressing the problem that beam splitting is arbitrary in granularity and will be insufficient or excessive, globally or locally in individual cases.

Monte Carlo methods

The MC method is a powerful computational technique that uses repeated random sampling to obtain the statistical properties of some phenomenon. In particle therapy, MC methods

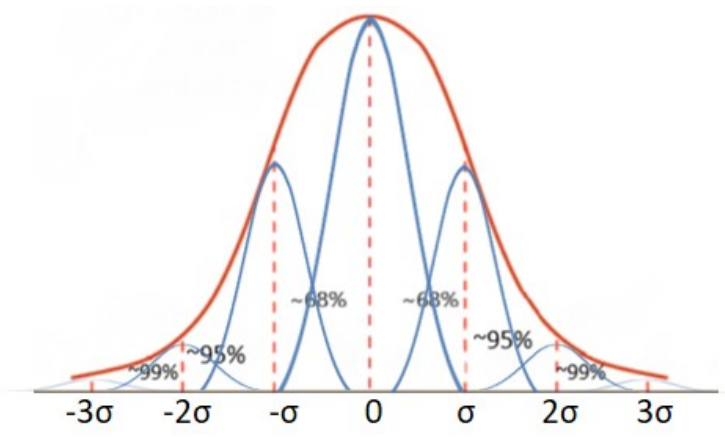

Figure 2.10: Decomposition of a pencil beam into a set of smaller sub-pencil beams.

are implemented to simulate physics processes across various materials, track particles trajectories in 3D, and incorporate essential radiobiological effects. As a result, MC methods have been widely used not only for dose calculations but also for the design and commissioning of novel clinical facilities, shielding and radiation protection, and prediction and interpretation of data for range monitoring strategies [Muraro et al., 2020].

The MC method is often referred to as the gold standard. Compared to analytical algorithms, MC simulations achieve higher accuracy because the history of each individual particle is simulated. However, the computation time is typically much higher than that of analytical algorithms. The results of MC simulations depend on factors such as the number of simulated particles (with larger numbers reducing statistical uncertainty), the chosen physics models, and the accuracy of nuclear interaction cross sections.

One of the MC tools presently used in particle therapy is Geant4 [Agostinelli et al., 2003], the successor of the Geant series of software toolkits developed by CERN using C++. On top of Geant4, two medical MC toolkits TOPAS and GATE have been developed [Perl et al., 2012, Jan et al., 2004]. Other options, such as FLUKA [Böhlen et al., 2014] and Monte Carlo N-Particle eXtended (MCNPX) [Waters et al., 2007], are also widely employed in research and clinical contexts.

Current commercial TPS, such as Eclipse (Varian Medical Systems, Palo Alto, CA) and RayStation (RaySearch Laboratories, Stockholm, Sweden) have embedded a MC algorithm for dose calculation, currently only available for protons, which is also used for treatment plan optimization. In RayStation, the proton MC algorithm is furthermore implemented on the GPU, speeding up MC simulations significantly.

2.4 Range uncertainties in particle therapy

Particle therapy offers superior dose conformity and better sparing of OAR compared to radiotherapy using photons. Both advantages are related to the finite range of a particle

beam in patients. However, even a few millimeters of range uncertainty can lead to underdosage in the target volume or overdosage of a nearby OAR. Therefore, it is essential to understand the sources of range uncertainties and to incorporate them into the planning process for a robust optimized treatment. Besides, in vivo imaging techniques for range verification can help to understand the true uncertainties during the treatment, thereby supporting validation and quality assurance of particle therapy.

2.4.1 Sources of range uncertainties

The sources of range uncertainties can be divided into two groups: those causing uncertainties in the range calculation in the TPS and those causing discrepancies between prescribed dose and delivered dose [McGowan et al., 2013].

Uncertainties in the TPS

As mentioned before, patient geometry in the TPS is typically derived form the corresponding CT data in HU. HUs can be converted into elemental composition of materials for MC simulations [Schneider et al., 2000] or into stopping power of tissue relative to water for analytical algorithms [Schneider et al., 1996, Schaffner and Pedroni, 1998]. There are uncertainties in the HU values themselves and the conversion from HUs to tissue properties, which are reflected in uncertainties in range. The CT imaging errors can come from noise and CT artifacts. For protons, it has been reported to be approximately ±0.5% [Durante and Paganetti, 2016]. In addition, the stopping power conversion method introduces range uncertainties has been reported to be up to 1.8% for bone and 1.1% for soft tissues translating into a range uncertainty of 1–3 mm [Schaffner and Pedroni, 1998], whereas uncertainties in elemental composition conversion causes tissue I value uncertainties on the order of 10–15%, introducing an additional range uncertainty of approximately 1.5% [Paganetti, 2012]. The issues are very similar for heavier ions. Some novel CT imaging techniques have been proposed to reduce uncertainties in the conversion process. Dual energy CT, employing CT scanners capable of scanning a patient with two different X-ray energies, provides relative electron density and effective atomic number of materials which enables a better relative stopping power estimation and thereby reduces range uncertainties in proton and carbon ion therapy [Hünemohr et al., 2014]. In addition. active research is undertaken into the development of ion-based CT (for both protons and heavier ions), in which the energy loss of ions passing through a patient is directly measured. This approach enables direct determination of stopping power inside the patient and thereby eliminates the need for conversion from HUs to stopping power [Poludniowski et al., 2015, Rinaldi et al., 2014].

The dose calculation algorithms used in TPS can themselves introduce range uncertainties [Durante and Paganetti, 2016]. Analytical algorithms, such as PBA, have inherent limitations when dealing with complex geometries. For example, increased scattering in complex geometries can lead to range degradation, while this effect is not considered in analytical algorithms. As mentioned in the previous section, to address lateral inhomogeneities,

PBA employ strategies such as ray-casting or beam splitting. Although these methods improve accuracy, they remain approximations and may be insufficient in situations with complex geometries, particularly at interfaces parallel to the beam direction. In contrast, MC simulations explicitly model each particle transport, providing more reliable dose calculations in cases with pronounced multiple scattering and large material heterogeneity.

Uncertainties in the dose delivery

One important source of range uncertainties in dose delivery is organ motion including interfractional motion and intrafractional motion. Interfractional motion refers to anatomical or positional changes that occur between treatment fractions, e.g., gradual anatomical changes such as weight loss or tumor shrinkage, or changes in patient setup. Intrafractional motion, on the other hand, occurs within a single treatment fraction, and mainly includes respiration, cardiac motion and bowel movements. These motions may displace the target or upstream tissue, thereby shifting radiological path length along the beam path. Their influence in particle therapy can result in severe underdosage of the clinical treatment volume (CTV) and overdosage of normal tissues. Besides, in pencil beam scanning, the interplay effect between beam motion and organ motion can impact dose homogeneity and thus lead to local underdosage (or overdosage) in the CTV, and could also lead to unwanted hot spots in QARs [Dowdell et al., 2013].

To mitigate such uncertainties, a variety of management strategies have been developed for use before and during treatment. Immobilization and in-room image guidance are routinely applied to achieve precise bony or soft-tissue setup at the beginning of each fraction. 4D CT can be employed at the planning stage to generate a treatment plan that guarantees delivery of the prescribed dose throughout a respiratory cycle [Engelsman et al., 2006]. Robust optimization methods that account for setup and range uncertainties in the planning process further improve treatment resilience in the presence of motion and anatomical changes. While respiratory gating and rescanning are available during delivery to reduce the impact of motion [McGowan et al., 2013].

2.4.2 In vivo range verification approaches

The above approaches help to manage and reduce the potential range uncertainties, but they do not provide an ultimate verification of the dose actually delivered. To this end, in vivo range verification is highly desirable. Various methods, such as PET, prompt gamma (PG) monitoring, ionoacoustics and secondary-electron bremsstrahlung (SEB), have been proposed to monitor the beam range during or after treatment. These techniques allow for not only validating the actual treatment delivery but also enabling subsequent treatment adaptations.

Positron emission tomography

PET monitoring is one of the most established approaches for in vivo verification in particle therapy. It exploits positron-emitting isotopes such as ^{15}O, ^{13}N, and ^{11}C that are generated through nuclear interactions during irradiation with stable ion beams. By detecting in coincidence the photon pairs from the annihilation of the positron emitted in β^+ decay, PET provides spatial information that can be correlated to the beam range with millimeter accuracy. PET monitoring will be discussed in detail in the following chapter.

Prompt gamma monitoring

PG monitoring exploits the fact that PG rays are emitted almost instantaneously during nuclear fragmentation reactions along the ion beam path. Unlike PET, which relies on the delayed decay of positron emitters, PG signals are not influenced by physiological or physical processes taking place after emission, and thus provide a more direct correlation with the actual beam range during irradiation.

Min et al. [2006] performed the first experiments to measure the correlations between (1D) PG distributions and the distal fall-off regions in proton therapy. Figure 2.11 shows a clear correlation between the maximum of the PG distributions and the Bragg peaks, e.g., within 1–2 mm at 100 MeV. Following that, Testa et al. [2009] then performed the

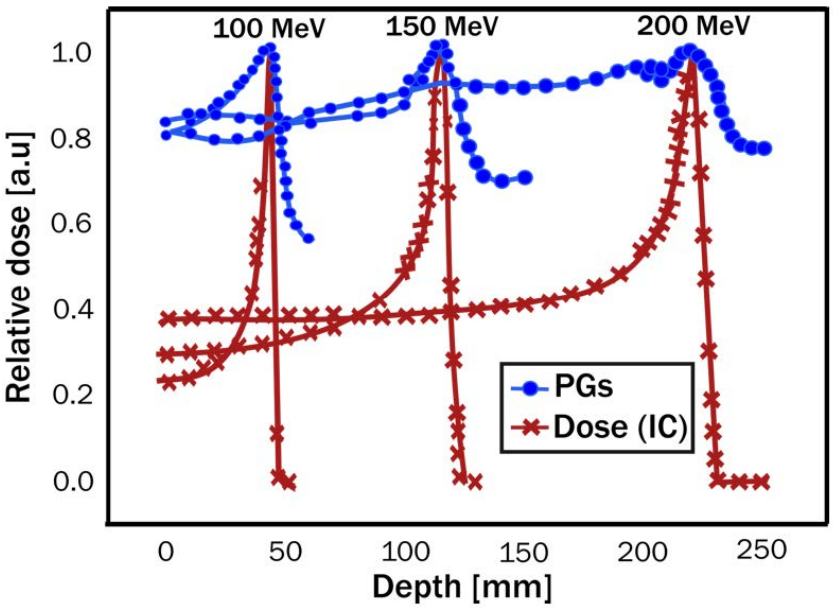

Figure 2.11: For proton energies of 100, 150 and 200 MeV, the measured depth-dose is correlated with the PG distribution. For high energies (150 MeV and 200 MeV) the sharpness of the PG in the distal fall-off is reduced due to the background of high energy neutrons. Figure adapted from [Min et al., 2006].

first experiments in carbon ions (^{13}C). In the subsequent years, PG monitoring has made remarkable progress toward translation into the clinic. The first clinical studies reported successful PG monitoring in proton treatments with both passive scattering and pencil beam scanning techniques [Richter et al., 2016, Xie et al., 2017, Berthold et al., 2023, Bertschi et al., 2023]. Its application to carbon ion therapy remains comparatively less mature and is currently being explored in ongoing projects, such as those at CNAO [Idrissi et al., 2024], where lower prompt-gamma statistics and higher background levels pose additional challenges. These studies on PG monitoring can pave the way for a higher level of real-time verification of particle therapy.

Ionoacoustics

Ionoacoustics is an emerging in vivo range verification technique that relies on the detection of acoustic waves generated by rapid local tissue heating and expansion during ion energy deposition in case of pulsed beams. Since this thermoacoustic effect is directly linked to dose deposition, and naturally enhanced at the Bragg peak, ionoacoustics theoretically provides a more straightforward correlation with range and dose than nuclear-based approaches.

Pioneering attempts in the 1990s demonstrated the feasibility of detecting acoustic signatures from proton beams with hydrophones placed on the patient skin [Hayakawa et al., 1995]. With the adoption of modern pencil beam scanning and compact synchrocyclotron accelerators, which offer short, high-intensity pulses ideal for acoustic generation, the method has gained renewed attention. Recent phantom experiments have shown sub-millimeter accuracy for range verification (see Figure 2.12) [Lehrack et al., 2017, Lascaud et al., 2021, Schauer et al., 2022, 2023], and simulation studies suggest that millimeter precision may be achievable in realistic clinical conditions by using multiple detectors and triangulation [Jones et al., 2018, Yu et al., 2021, Jiang et al., 2022]. The main advantages of ionoacoustics are its direct correlation with dose, its potential for real-time monitoring, and its relatively simple and cost-effective instrumentation, particularly when combined with conventional ultrasound imaging for anatomical coregistration [Parodi and Assmann, 2015]. On the other hand, the method faces challenges, including acoustic signal attenuation in heterogeneous tissues and the need for optimized beam time structures to maximize signal generation, as well as dedicated low-frequency, high sensitivity and broad band with instrumentation.

Although still at an early stage of development compared with PET or PG monitoring, ionoacoustics holds promise as a unique and practical tool for quasi real-time, anatomy-coregistered range and dose verification, with potential applications in challenging anatomical sites such as the prostate, liver, and breast where inter and intrafractional organ motion is a major concern.

Secondary-electron bremsstrahlung

SEB imaging relies on electromagnetic interactions and detects low-energy photons emitted by secondary electrons generated during ion energy loss. Phantom studies have demonstrated SEB imaging for both protons [Yamaguchi et al., 2016] and carbon ions [Yamaguchi et al.,

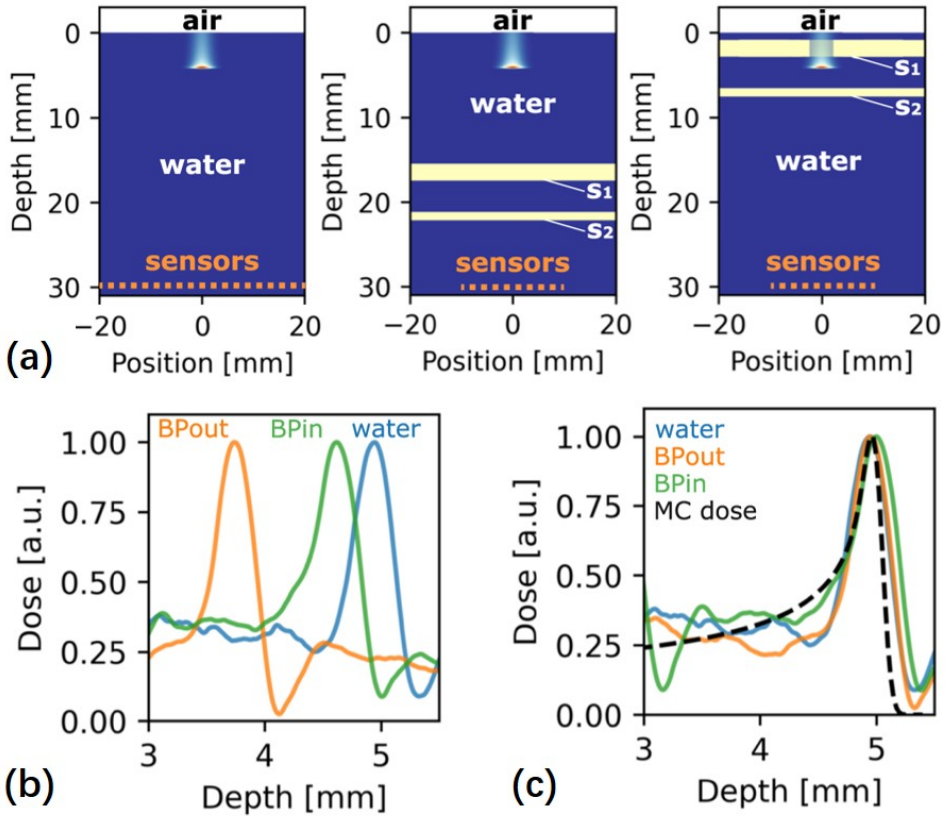

Figure 2.12: Top: (a) schematic representation of the setup used for the ionoacoustic measurements with a proton beam of 22 MeV in water (left), as well as with a silicone phantom positioned such that the proton beam stops before the silicone phantom (middle, "BPout") and inside the silicone phantom (right, "BPin"). The ionoacoustic signals were detected using a focused piezoelectric ultrasound transducer, which was scanned perpendicular to the proton beam axis to mimic a linear array of sensors. Bottom: comparison of the laterally integrated acoustic pressures in water (blue), with BPout (orange) and BPin (green), (b) assuming a homogeneous medium for the reconstruction and (c) after correcting for the speed of sound, compared to the MC dose (black dashed line). The relative error on the Bragg peak position is lower than 0.5%. Figure adapted from [Lascaud et al., 2021].

2018] and shown a correlation between the measured SEB signal and the beam range. In addition, a recent patient CT–based simulation study investigated the feasibility of SEB imaging as an in vivo range verification tool for proton therapy [Yabe et al., 2025]. However, research on SEB-based monitoring is still comparatively limited and at an earlier stage than PET, PG, and ionoacoustic techniques, and experimental imaging in clinical situations has not yet been achieved.

3

PET range monitoring in particle therapy

As mentioned in Section 2.4.2, PET enables the in vivo range verification better by exploiting the positron emissions induced during therapeutic irradiation. However, the electromagnetic processes underlying the dose distribution differ fundamentally from the nuclear mechanisms underlying the production of positron emitters. Consequently, the PET-based range verification entails a comparison of the measured positron annihilation with predicted PET images, or equivalently a positron emitter distribution (PED), which can be obtained through computational approaches such as MC simulations or analytical methods. The workflow is illustrated in Figure 3.1: starting from the treatment planning (TP) data, the β^+-activity distribution can be predicted. The calculated activity is then compared to the actual PET measurement of the given fraction in order to verify the correct application of the irradiation. If relevant deviations are found corrections in the TP are requested, otherwise the irradiation is continued in the next fraction.

The two complementary aspects of PET-based range verification are therefore PET measurements and computational PED prediction. This chapter primarily focuses on the first aspect, describing the physical rationale of PET monitoring, the fundamentals of PET imaging, and its clinical implementation. A brief overview of the computational methods for PED prediction is also included for completeness, while detailed descriptions of the methods (both MC and analytical) applied in this study are provided in the next chapter.

3.1 Rationale of PET monitoring

3.1.1 β^+ decay and annihilation

Positron emitters (PEs) are radionuclides that undergo β^+ decay. In the process of β^+ decay, a positron along with a neutrino ν are emitted and a proton in the nucleus is converted to

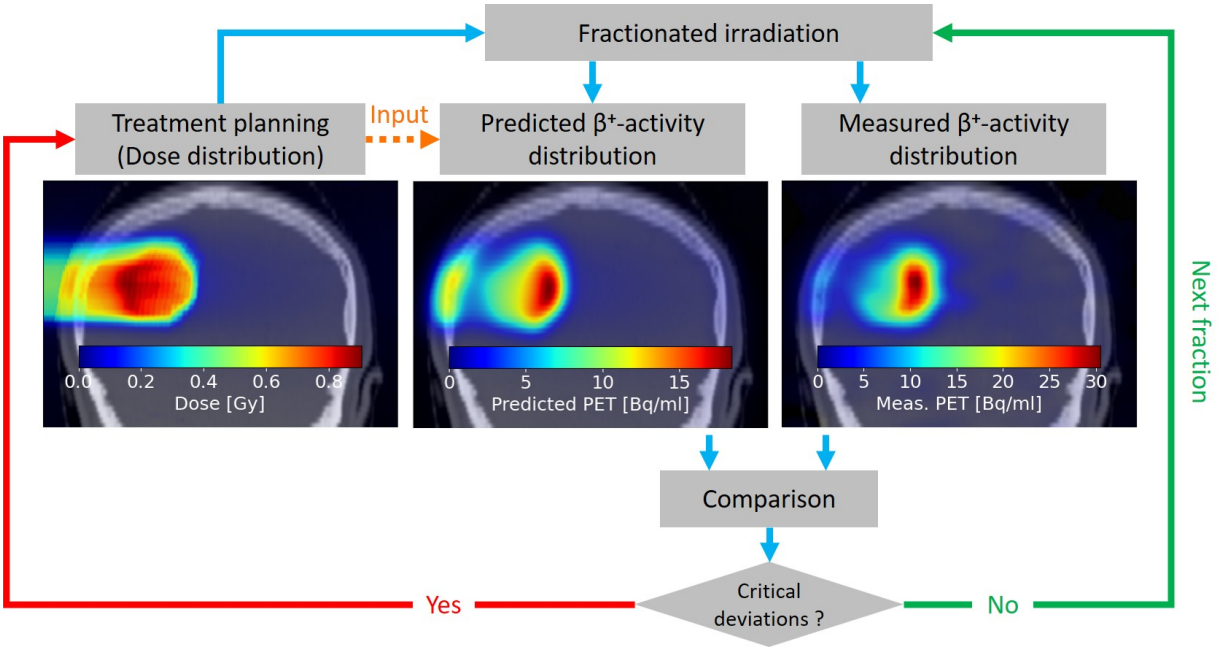

Figure 3.1: Depiction of the PET-based treatment verification workflow. Patient treatment planning (TP) data is used as input for a prediction of the β^+-activity distribution in the patient. Then a comparison of the predicted distribution with the measured PET data of the fraction is performed in order to verify the treatment.

a neutron.

$$ {}^{1}_{1}p^{+} \rightarrow {}^{1}_{0}n + {}^{0}_{1}\beta^{+} + \nu \tag{3.1} $$

The general equation for positron decay from an atom is:

$$ {}^{A}_{Z}X \rightarrow {}^{A}_{Z-1}Y + {}^{0}_{1}\beta^{+} + \nu + Q\ (+e^{-}) \tag{3.2} $$

where Q denotes the decay energy. The proton-rich atom X achieves stability by converting a proton to a neutron, with the positron carrying away the positive charge.

The β^+ activity follows a decay law in the form of an exponential function. The determination of the decay law can start from the concept of the decay constant λ of a radionuclide, which refers to the decay probability per unit time of the radionuclide. The number of radionuclides undergoing decay dN at a moment is given by

$$ dN = -\lambda N\, dt \tag{3.3} $$

Thus, the remaining number of radionuclides $N(t)$ follows the exponential decay law:

$$ N(t) = N(0)\, e^{-\lambda t} \tag{3.4} $$

where $N(0)$ is the number of radionuclides initially.

The half-life of the radionuclide $T_{1/2}$, which is the time it takes for half of the radionuclide present to decay, is thereby given by

$$T_{1/2} = \frac{\ln 2}{\lambda} \tag{3.5}$$

Besides, the rate of the decay of the radionuclide at any instant t, called the activity of the radionuclide, is

$$A(t) = \lambda N(t) \tag{3.6}$$

and the unit for activity is the becquerel (Bq).

After emission from the nucleus, the positron loses kinetic energy primarily through inelastic collisions with surrounding atomic electrons (see Section 2.1.1). Once essentially at rest, it combines with an electron, leading to annihilation. The annihilation most commonly produces two photons of 511 keV (the rest-mass equivalent of electron and positron) emitted in opposite directions to conserve momentum (annihilation into more than two photons is also possible but occurs with much lower probability). However, in reality, many photon pairs are not emitted strictly at 180° due to non-zero momentum when the positron and electron annihilate. PET is based on the principle of coincidence detection of the two 511-keV photons arising from PEs, which will be discussed in detail later.

3.1.2 Production of positron emitters in particle therapy

PEs can be produced through the nuclear reactions between the projectiles and target nuclei in particle therapy (see Section 2.1.3). The irradiation-induced PEs in human body are diverse, as summarized in Table 3.1. Due to the composition of the tissue, the target PEs produced are mainly carbon and oxygen isotopes. Among them, short-lived isotopes are particularly relevant for PET imaging performed during or immediately after treatment (in-beam PET), whereas longer-lived isotopes become more important for PET acquisitions carried out after the treatment session (offline and in-room PET).

Table 3.1: List of the PEs produced in hadron therapy and their half-life.

PE	^{15}O	^{14}O	^{11}C	^{10}C	^{13}N	^{12}N	^{17}F	^{30}P	^{38}K
Half-life	2.03 min	70.6 s	20.38 min	19.3 s	9.97 min	11 ms	1.07 min	2.49 min	7.63 min

It should be noted that in proton therapy, incident protons can only produce target fragments, while in carbon ion therapy, projectile and target nuclei can both fragment. This fundamental difference is reflected in the activity distributions (or PED). For protons, nuclear interactions generate target fragments that remain nearly at rest, leading to an activity profile that is flat or slightly increasing with depth. As the projectile energy falls below the reaction threshold near the Bragg peak, the activity exhibits a pronounced fall-off. By contrast, in carbon ion therapy, the flat contribution from target fragments is superimposed by the activity originating from projectile fragments, most notably ^{11}C. Since these projectile fragments are produced with nearly the same velocity as the incident ions

and have a comparable residual range, they give rise to a characteristic activity maximum just proximal to the Bragg peak. Additionally, long-range secondary particles such as protons can still induce target fragmentation distal to the Bragg peak, further shaping the overall activity profile. The above features of β^+-activity induced by protons and carbon ions are displayed in Figure 3.2.

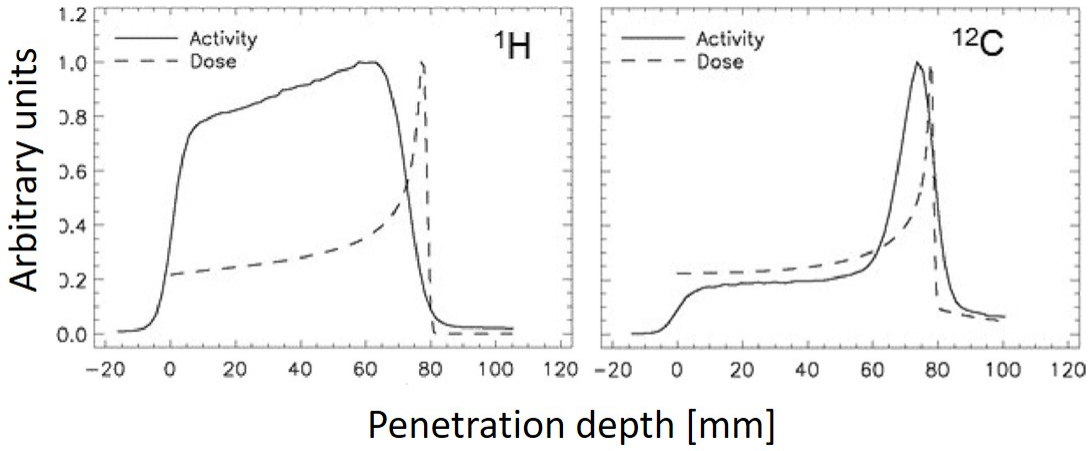

Figure 3.2: Depth distributions of calculated dose (dashed line) and measured β^+-activity (solid line) for proton (left) and ^{12}C (right) ions impinging in polymethylmethacrylate (PMMA). Figure adapted from [Parodi et al., 2023].

3.2 Fundamentals of PET imaging

3.2.1 Scintillation detectors in PET

As discussed in Section 3.1.1, the annihilation of a positron produces two photons of 511 keV emitted in the opposite directions. PET is based on the detection of two photons in coincidence using solid scintillation detectors. These solid detectors emit scintillation or flashes of light after absorbing γ-rays or X-rays. The optical photons are then converted to an electrical pulse or signal traditionally by a photomultiplier tube (PMT). The pulse is amplified by a linear amplifier, sorted by a pulse height analyzer (PHA), and finally registered as a count.

The 511-keV photons interact with detectors material by photoelectric absorption or Compton scattering. In both cases, the interaction excites the atoms of the detector to higher energy states, which subsequently decay to the ground state by emitting optical photons. The number of optical photons and the time of the scintillation decay vary with the detector material. A high-light-output detector produces a well-defined pulse and results in better energy resolution, while a shorter decay time enhances the efficiency of the detector at high count rates.

A conventional PMT converts the optical photons produced in the detector to electrical pulses. It is a vacuum glass tube containing a photocathode at one end, several dynodes in the middle, and an anode at the other end. A high voltage is applied between the photocathode and the anode, with incremental voltage difference between successive dynodes. The end of photocathode is fixed onto the detector. Scintillation photons strike the photocathode, releasing photoelectrons which are accelerated toward the first dynode. Each electron hits the surface of the dynode, releasing multiple secondary electrons that are in turn accelerated toward the next closest dynode. The process of multiplication continues until the last dynode is reached, producing an avalanche of electrons that is finally collected at the anode. The resulting current pulse is then amplified by an amplifier to a detectable pulse, which is then analyzed for its size by the PHA, and finally delivered to a recorder or computer for storage or to a monitor for display. Figure 3.3 shows the schematic of a PMT detector in the top panel.

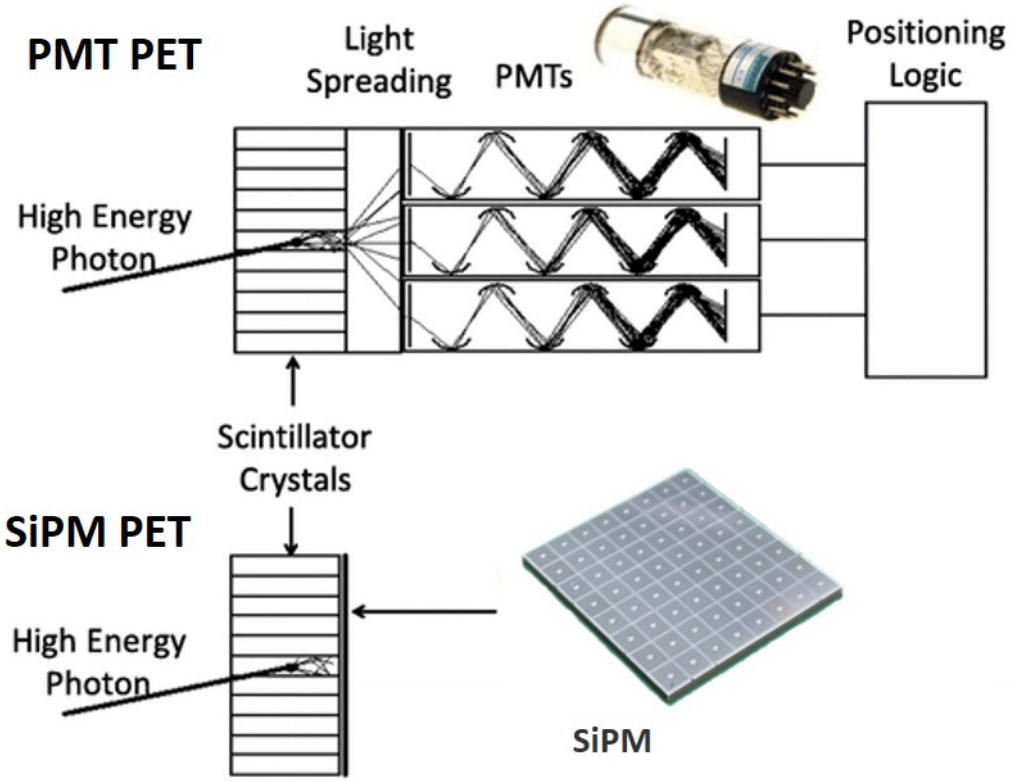

Figure 3.3: Comparison of PMT PET detector and SiPM PET detector. Figure adapted from [Zhang et al., 2018].

In recent years, silicon photomultipliers (SiPMs) have emerged as a promising alternative to conventional PMTs [Roncali and Cherry, 2011]. SiPMs are single-photon-sensitive devices composed of pixels of single-photon avalanche diodes (SPADs) implemented on a silicon

substrate. They offer several advantages, including compact size, potentially low production costs and insensitivity to magnetic fields [Roncali and Cherry, 2011]. Figure 3.3 displays an example of a SiPM-based detector, showing its size much more compact than the above PMT detector. In addition, SiPMs provide excellent intrinsic time resolution and high photon-detection efficiency [Seifert et al., 2013]. More recently, a number of clinical PET systems employing SiPM readout have been commercialized by manufacturers [Singh, 2024].

3.2.2 Characteristics of PET scanners

With continuous development, PET scanners have undergone significant evolution. The very first PET scanner was designed as a pair of coincident radiation detectors in 1953 [Sweet, 1953]. Later, in 1969, a PET scanner with a dual planar array of detectors was developed [Burnham et al., 1970]. In the following years, more advanced PET scanners employing a hexagonal array of detectors and full or partial rings of detectors were subsequently developed and introduced into clinical practice [Ter-Pogossian et al., 1975, Townsend et al., 1993, DeGrado et al., 1994]. Today, the geometry of PET scanners has become increasingly diverse to meet specific clinical needs, for example, hemispherical designs for brain imaging [Yoshida et al., 2020] or elliptical and D-shaped configurations for cardiac imaging [Akamatsu et al., 2021]. In addition, recent efforts have focused on the development of long axial field of view (FOV) systems that retain a conventional cylindrical geometry, enabling total body imaging with greatly improved sensitivity and reduced acquisition time [Spencer et al., 2021, Prenosil et al., 2022, Dai et al., 2023]. Despite these variations in design, the fundamental of PET imaging, i.e., the detection of two annihilation photons in coincidence, remains unchanged, and these different scanner types share some common performance characteristics. In this section, the performance characteristics of PET scanners, including time resolution, energy resolution, and sensitivity, are presented with reference to the classical full-ring PET configuration.

Timing resolution

The timing resolution of a PET detector reflects the uncertainty in measuring the arrival time of photons on an event-by-event basis. Good timing resolution is essential for accurately identifying photon pairs originating from a single annihilation event. Within the FOV of the scanner, the two coincident photons may travel different distances before interacting with the detectors, and additional variability arises from the light emission time in detectors, which depends on its decay constant. These factors lead to a time difference between the two signals induced by the detected photon pair, which needs to be accounted for by introducing a coincidence time window. Obviously, a large time difference (poor time resolution) requires a wider window to detect most of the valid coincidence events, whereas fast scintillators with short decay time help to reduce the time difference and improve the time resolution. In practice, the lower limit of the coincidence window is determined by the scanner geometry. For a whole-body PET system with a diameter of about 100 cm, the maximum distance difference can be the scanner diameter (about 100 cm) which

corresponds to a time difference of 3–4 ns. As a result, the coincidence window cannot be less than this. From the other aspect, the time difference can be reduced with scintillators that have short decay time. For a fast scintillator such as BaF_2 (barium fluoride) with a decay time of 0.6 ns, the coincidence window is therefore restricted primarily by geometry rather than scintillator performance.

While a wider coincidence window increases the chance of detecting true events, it also allows more random coincidences, i.e., false coincidences from unrelated photons that arrive within the same window (see Figure 3.4). Their rate is proportional to both

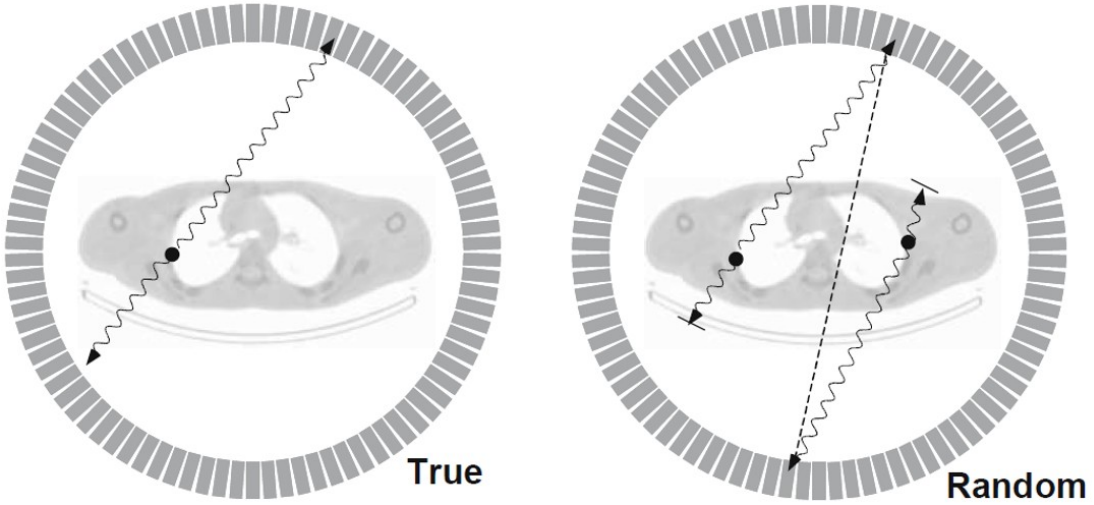

Figure 3.4: True and random coincidences in a PET scanner. In a true coincidence, the photon pair are detected and the line of response (LOR) contains the spot of annihilation. In a random coincidence, two independent photons are accidentally attributed to the same annihilation event, leading to an incorrect LOR (dashed line). Figure from [Bailey et al., 2005].

the square of the activity in the FOV and the width of the coincidence window. As a result, random coincidences increase rapidly at high activity levels, degrading image contrast and signal-to-noise ratio if not corrected. In addition, intrinsic radioactivity in PET detectors, arising primarily from the decay of ^{176}Lu in lutetium-based scintillators, produces background events that increase the random coincidence rate and limit image quality, particularly in high-sensitivity PET imaging. Although correction methods exist, they propagate additional noise into the reconstructed image, making prevention preferable. Thus, using fast scintillators with good timing resolution allows the coincidence window to be narrowed, minimizing random coincidences while preserving sensitivity. Moreover, excellent timing resolution enables time-of-flight (TOF) PET, where differences in photon arrival times are exploited to localize the annihilation event along the line of response (LOR), further improving image quality [Surti and Karp, 2016].

Energy resolution

The energy resolution of a PET detector reflects its ability to distinguish between different energy deposition events. In scintillation detectors, this performance depends on both the light output of the scintillator and its intrinsic energy resolution. Good energy resolution is essential for improving image contrast as it enables to reject scatter coincidences. Scatter coincidences are true coincidences from single annihilation events, but where one or both the photons undergo Compton scattering in the FOV before entering the detectors (see Figure 3.5). These scattered events lead to mispositioned LORs, thereby misrepresenting

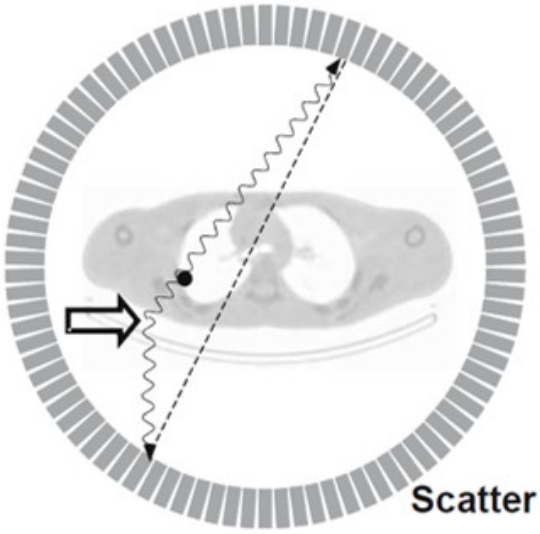

Figure 3.5: In a scatter coincidence, one or both the emitted photons undergo Compton scattering before detection, thereby leading to a mispositioned LOR (dashed line). Figure from [Bailey et al., 2005].

the true events and degrading the image contrast. Since scattered photons have less energy than 511 keV, many scatter coincidences can be excluded from the dataset by setting tight energy windows around the 511 keV photopeak. Detectors with good energy resolution allow a narrow energy window, thus lead to a more extensive and accurate rejection of scatter coincidences and ultimately enhanced image contrast.

However, not all scatter events can be removed since some scattered photons still fall within the energy window. Consequently, additional scatter-correction techniques which estimate the distribution of scattered radiation are often used to remove it and improve image quality.

Sensitivity

The sensitivity of a PET scanner reflects its ability to detect coincident photons emitted within the FOV and is mainly determined by the scanner geometry and the stopping efficiency of its detectors for 511 keV photons. Geometrical factors such as small ring

diameter and large axial FOV increase sensitivity by covering a larger solid angle. On the detector aspect, high stopping power is crucial for capturing photons, which depends on the density and effective atomic number of the detector material. Materials like bismuth germanate (BGO) offer excellent stopping power, enabling a high detection efficiency and thereby improving signal-to-noise ratio of reconstructed images. However, BGO suffers from its slow scintillation decay, resulting in poor timing resolution. Consequently, modern PET scanners tend to employ LSO and Lutetium–yttrium oxyorthosilicate (LYSO), which provide superior timing performance at the cost of a somewhat reduced stopping power and the presence of intrinsic radioactivity from ^{176}Lu. As a compromise, materials like GSO have also been explored, offering moderate stopping power and timing performance without intrinsic radioactivity.

In addition, a high stopping power for the crystal (together with a proper detector arrangement) also helps the reduction of parallax error. A photon enters a detector and travels a short distance before depositing all its energy. Typically detectors do not measure this point, known as the depth-of-interaction (DOI) in the crystal, and this point is projected to the entrance surface of the detector which leads to increasing errors in LOR for smaller radii geometries and off-axis emissions (Figure 3.6). For photons entering the

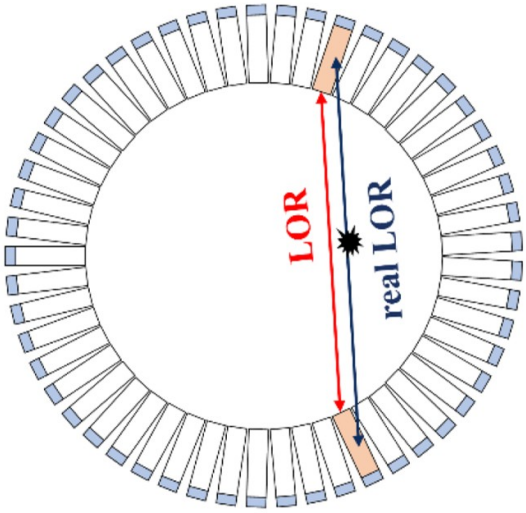

Figure 3.6: Parallax error in the LOR due to the unknown DOI of the photons within the detectors. Figure from [Yu et al., 2022].

detectors at oblique angles, this projected position can produce significant deviations from the real position, leading to a blurring of the reconstructed image, known as the parallax effect. This effect is more evident at large radial distances from the scanner central axis. Thinner crystals can shorten the DOI and thus reduce parallax effects, but they also reduce sensitivity, creating a trade-off. This has driven the development of detectors capable of DOI measurement include the multilayer [Ito et al., 2010a], dual-ended readout [Ren et al., 2014], and light-sharing methods [Ito et al., 2010b]. These technologies aim to decouple sensitivity from resolution losses, paving the way for high-performance PET systems.

3.2.3 PET Image Reconstruction

Reconstruction algorithms in PET aim to recover the three-dimensional distribution of annihilation events from the measured projection data. Analytic methods assume noise-free data and seek a direct mathematical inversion from projections to the image. The most common analytic method is the filtered backprojection (FBP) method [Herman, 1995]. FBP first applies an analytical inversion of the projection data using 1D Fourier transform and a high-pass (ramp) filter to compensate for blurring introduced by backprojection. Then, it takes inverse Fourier transform to obtain the filtered projection and backprojects it. While computationally efficient, FBP is sensitive to statistical noise and artifacts, particularly under low-count conditions or when incomplete data are available, which limits its applicability in treatment verification PET imaging.

In modern systems, reconstruction is most often performed using iterative algorithms. These methods estimate the activity distribution that is most consistent with the measured coincidence data, assuming Poisson counting statistics. The maximum-likelihood expectation–maximization (MLEM) algorithm [Shepp and Vardi, 2007] iteratively refines the reconstructed image to maximize the likelihood of the measured data but converges slowly and becomes noisy with iterations. The ordered-subset expectation–maximization (OSEM) algorithm [Hudson and Larkin, 1994], divides the projection data into subsets to achieve faster convergence without compromising image quality. In addition, incorporating TOF information into reconstruction localizes events along each LOR, improving signal-to-noise ratio and convergence, especially valuable in large patients or low-count scenarios [Merlin et al., 2018, Conti and Bendriem, 2019].

Iterative reconstruction methods are particularly well suited for low-count PET acquisitions, as they incorporate statistical weighting and system modeling to suppress noise and enhance contrast. This characteristic makes them especially relevant in PET-based range verification in particle therapy, where the irradiation-induced positron activity is several orders of magnitude lower than in conventional diagnostic PET [Enghardt et al., 2004].

3.3 Clinical application of PET range monitoring

3.3.1 PET imaging system configurations

In clinical practice of particle therapy, PET image acquisition for treatment verification relies on PET scanners installed within the treatment room or in adjacent PET imaging rooms. Depending on the arrangement of the scanner relative to the irradiation site and the time of image acquisition with respect to treatment delivery, three PET configurations are distinguished: offline PET, in-room PET, and in-beam PET.

Offline PET

In offline PET configurations, the patient walks or is transported to a dedicated imaging room after treatment, where a commercial PET/CT scanner is typically used. The combined

PET/CT setup allows for co-registration of activity and anatomical images since patient repositioning introduces potential misalignment relative to the treatment planning CT. The offline approach is technically less demanding, and better image quality can be achieved with a full-ring detector geometry configuration. However, the time delay between irradiation and PET acquisition (up to 30 min) causes a significant reduction in signal due to radioactive decay (particularly of short-lived isotopes such as ^{10}C and ^{15}O) and biological washout.

The earliest clinical trial of offline PET was conducted at the Hyogo Ion Beam Treatment Center in Japan using a commercial PET/CT scanner (SET-2300W, Shimadzu Corporation) for proton therapy [Hishikawa et al., 2002]. However, no comparison with a predicted PET distribution was performed in that study. A subsequent pilot study at Massachusetts General Hospital (MGH) was preformed with a PET/CT scanner (Siemens Biograph Sensation 16) located in the radiology department, approximately a 10-minute walk from the treatment facility [Parodi et al., 2007c]. In this work, the expected PET distribution was obtained from CT-based MC calculations complemented by functional information, and a good spatial correlation together with a quantitative agreement within 30% was observed between the measured and predicted activity distributions [Parodi et al., 2007c]. This first work was followed up by Knopf et al. [2011] with more patient cases. Other notable offline PET investigations have been carried out, including studies at the University of Florida Proton Therapy Institute [Hsi et al., 2009].

Later, HIT conducted the large-scale clinical trial to verify both proton and carbon ion treatments using a full-ring PET/CT scanner (Siemens Biograph mCT 40) installed in a dedicated room adjacent to the treatment rooms [Combs et al., 2012]. The PET scanner consisted of four detector rings, each containing 48 detector blocks with 13×13 crystals having a dimension of $4 \times 4 \times 20$ mm^3 each, with a FOV of 21.8 cm (axial) × 60.5 cm (transaxial). The use of lutetium oxyorthosilicate (LSO) detector crystals with high scintillation light yield and fast scintillation light decay enabled a narrow coincidence time window and the application of TOF PET techniques. The image reconstruction was preformed iteratively by a 3D-OSEM algorithm considering the local detector response and the TOF information [Bauer et al., 2013]. For post-irradiation imaging, patients were either walked or transported via a dedicated shuttle system from the treatment room to the adjacent PET/CT suite immediately after irradiation. Before scanning, patients were re-immobilized using the same fixation devices as during beam delivery (e.g., thermoplastic masks for head-and-neck cases) to ensure spatial consistency with the planning CT. For liver patients, re-immobilization was avoided due to the complex setup; instead, they were immobilized once in the PET/CT room, transported in the same position to the treatment room for irradiation, and then returned for post-treatment PET imaging. The offline PET workflow has enabled precise, routine post-irradiation PET monitoring at HIT, achieving an overall range verification accuracy of a few millimeters [Bauer et al., 2013, Nischwitz et al., 2015].

In-room PET

To minimize the post-treatment delay, in-room PET systems are positioned within the treatment room but off the beam axis. After irradiation, the treatment couch is rotated or translated into the scanner FOV, allowing image acquisition to start within 2–3 minutes after irradiation while short-lived nuclides are still abundant. Thus, the overall signal intensity would be significantly higher than in the offline scenario. Moreover, this configuration also reduces biological washout and positioning uncertainties compared to offline PET.

A representative example is the mobile NeuroPET scanner (Photo Diagnostic Systems, Inc.), which was adapted by MGH for in-room operation [Zhu et al., 2011]. A small bore full-ring scanner was employed, providing whole-volume imaging with improved count statistics and reduced acquisition time, usually around five minutes [Zhu et al., 2011]. However, since the imaging must still occur after treatment, the clinical workflow is temporarily interrupted. Moreover, while in-room PET improves temporal accuracy, short-lived isotope decay and biological washout remain limiting factors. Despite these challenges, in-room PET opens new possibilities for personalized and adaptive particle therapy, such as verification of individual fields in multi-field irradiations and near real-time adaptive treatment monitoring.

In-beam PET

In-beam PET enables image acquisition during irradiation without interrupting the clinical workflow and is thus considered the optimal solution for in vivo treatment verification. However, one of the main technical difficulties is filtering out data acquired during particles extraction, as the strong beam-induced background noise floods the PET detectors and leads to excessive random coincidence events [Enghardt et al., 2004]. Consequently, in-beam PET is particularly well suited to synchrotron-based facilities, where beam pauses (inter-spill) naturally allow PET data acquisition with reduced background, whereas at cyclotron-based facilities continuous beam delivery typically requires more sophisticated random suppression methods to enable online PET measurements [Kraan et al., 2014].

The PET system is integrated in-situ near the treatment couch, allowing for direct monitoring of the irradiation process without moving the patient. This configuration requires a dedicated system architecture that avoids interference with the treatment setup, beamline components, and safety procedures. By collecting events in parallel with beam delivery, in-beam PET avoids the impact of patient repositioning and minimizes biological washout and count statistics. The count statistics increase during irradiation and start to decrease only after beam termination, resulting in a better signal compared to offline and in-room acquisitions.

The first clinical in-beam PET prototype was installed at GSI in the 1990s [Pawelke et al., 1997, Enghardt et al., 2004]. Around 440 patients treated with scanned carbon ion beams, primarily with head and neck tumors, have been daily imaged. The system was constructed from components of the Siemens ECAT EXACT PET scanner made of BGO scintillators and PMTs. Its configuration was designed as a dual-head detector arrangement mounted above and below the patient couch to avoid interference with the horizontal

beamline. At GSI, discontinous pencil beams are delivered, and the collection of counts is during the beam pauses and continues after treatment.

Subsequent systems have been developed for both proton and carbon ion therapy. At the proton therapy center in Kashiwa, Japan, a planar in-beam PET system (Hamamatsu Photonics) was mounted directly on the rotating gantry [Nishio et al., 2010]. CNAO in Pavia, Italy, implemented the INSIDE project (INnovative Solutions for In-beam DosimEtry in hadron therapy), featuring a dual-head planar PET system combined with a tracker for detecting secondary charged fragments [Bisogni et al., 2017]. This system utilizes lutetium fine silicate (LFS) crystals coupled to SiPMs, offering excellent time and energy resolution and a compact geometry suitable for clinical integration. The acquisition is performed all along the treatment during both irradiation (spill) and inter-spill. As the in-spill data were found to be of insufficient quality, they only use the inter-spill data together with a short time of after-beam data [Moglioni et al., 2022, Kraan et al., 2024b] similar to the earlier GSI studies.

More recently, at HIMAC, the world first open-type 3D PET (OpenPET) system has been developed for in-beam monitoring. In the conventional dual-head geometries, resolution is degraded along the axis perpendicular to the detector heads. The OpenPET system introduces a full-ring PET geometry with an open FOV to mitigate the problem, allowing beam access to the patient while maintaining a large number of LORs.

Two main OpenPET configurations have been realized: the dual-ring OpenPET (DROP) [Yamaya et al., 2008] and the single-ring OpenPET (SROP) [Tashima et al., 2012]. The DROP design splits the detector ring axially to create an open FOV imaged through oblique LORs between the two rings, while the SROP is designed as a single cylindrical detector truncated by two oblique planes with higher sensitivity and a reduced number of detectors than the earlier DROP. To implement the SROP using block detectors, two arrangement methods were investigated: (1) a slant-ellipsoid (SE) type, in which ellipsoidal rings are arranged along the bedside and (2) an axial-shift (AS) type, in which detectors are axially shifted along the plane tilted against the axial direction. These two types arranged with DOI detectors were compared by simulation and found no significant difference in image quality [Kinouchi et al., 2011]. Both designs were sequently realized in small prototype systems [Yoshida et al., 2013, Tashima et al., 2016]. Although the imaging performance was similar, the AS-type SROP geometry was found to be more compact and easier to manufacture than the SE-type SROP geometry, which requires ellipsoidal block rings. Later, a human-scale OpenPET system based on the AS-type SROP geometry was developed [Tashima et al., 2020]. Figure 3.7 shows the configurations of the DROP and AS-type SROP systems.

The human-scale SROP employs DOI detectors using Zr-doped gadolinium oxorthosilicate (GSOZ) crystals with DOI to mitigate parallax errors and preserve spatial resolution within the open geometry. Each scintillator was sized in crystals of $2.8 \times 2.8 \times 7.5$ mm^3, and the DOI block consisted of an array of $16 \times 16 \times 6$ crystals. PMTs are used instead of SiPMs to ensure radiation tolerance under ion beam exposure, with digitizer electronics positioned 15 m away from the irradiation field to prevent radiation damage. The image reconstruction is preformed iteratively by a 3D-OSEM algorithm with the DOI information.

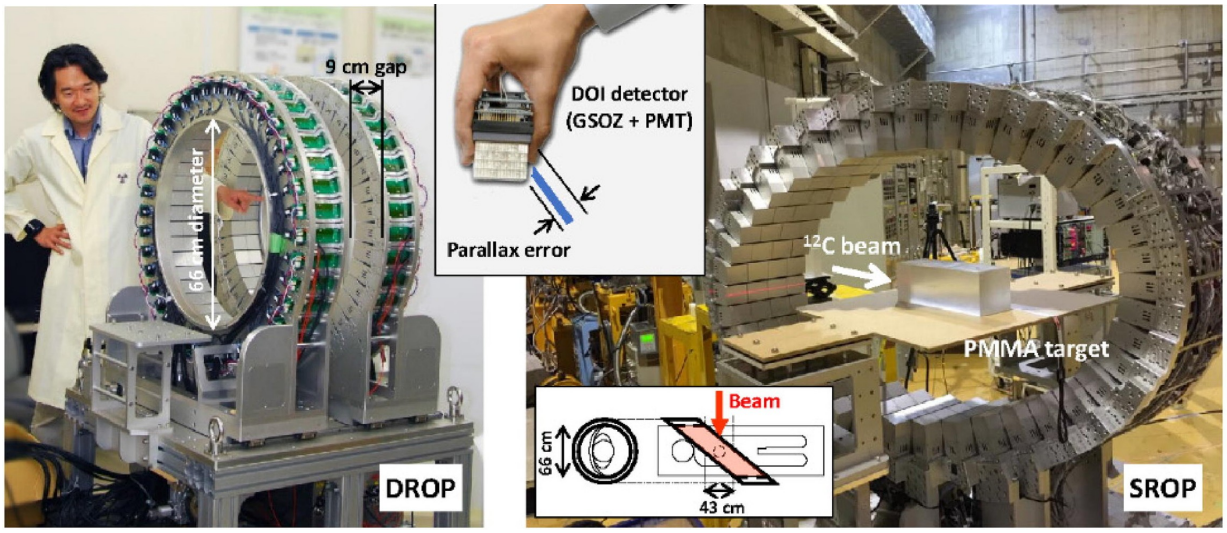

Figure 3.7: Configurations of dual-ring OpenPET (DROP) and single-ring OpenPET (SROP). Figure adapted from [Parodi et al., 2023].

This human-scale SROP have been successfully tested at HIMAC in in-beam imaging studies with phantoms and animals [Tashima et al., 2020]. Subsequently, it has been installed in the clinical treatment room [Tashima et al., 2023] and is being used for clinical trials [Tashima et al., 2024], and representing one of the most advanced implementations of in-beam PET to date. The in-beam PET data used in this work were acquired with the SROP system.

3.3.2 General computational methods for β^+-activity prediction

MC simulations

As presented in Section 2.3.4, MC methods are widely used in radiation physics and medical physics including dose calculations, the design and commissioning of novel clinical facilities, etc. In the context of PET-based range monitoring, MC methods are employed to predict β^+-activity, and comparing it to the measurement allows for treatment verification [Parodi et al., 2007c, Bauer et al., 2013, Fiorina et al., 2018].

Before MC methods are employed to predict PED in patient, careful commissioning of the MC is needed to first produce the dosimetric data in water, therefore, the modeling of the clinical beam configuration is necessary. Beam modelling can be realized by explicitly implementing the clinical beamline geometry or by using a phase space approach (see details in Section 5.2.1). Subsequently, MC simulations of PED in patient are performed with the necessary input information. The properties of the incident beam, i.e., energy, beam size, lateral position and number of primaries for each scanned spot, are acquired from the treatment plan. The patient anatomical geometry is derived from the underlying CT data, which are segmented into the tissue mass density and elemental composition [Parodi et al., 2007c]. In addition, in order to enable a consistent range prediction as in the TPS,

stopping power values of tissue, as derived from the HU values, relative to water should be kept consistent with those used by the TPS [Bauer et al., 2013]. Based on these inputs, the dose distribution and the distribution of considered positron emitters are obtained by MC simulations using appropriate scoring functions, typically defined on the same voxel grid as the underlying CT geometry.

A subsequent post-processing step is required to convert the predicted PED into the activity distribution expected to be measured during PET acquisition. This conversion is typically performed using analytical models that account for various factors influencing the detected activity, including potential activity loss during the delay between irradiation and imaging, physical decay during acquisition, biological washout in different tissues, and the spatial resolution of the scanner [Parodi et al., 2007c, Bauer et al., 2013, Min et al., 2013]. For in-beam PET, the biological washout can be neglected due to the short acquisition time during irradiation.

Analytical methods

Because MC simulations are computationally intensive and time-consuming, analytical methods were developed to efficiently predict β^+-activity distributions, with early efforts mainly focused on proton therapy and later on carbon ion therapy. A brief overview of these analytical methods has been presented in Chapter 1.

Machine learning

More recently, machine learning (ML) approaches have been explored as an alternative to analytical models for predicting the nonlinear relationship between dose and PED. These methods leverage data-driven learning to implicitly capture the underlying physics of β^+-activity formation without explicit analytical parameterization. Li et al. [2019] and Liu et al. [2019] applied neural network architectures such as feedforward and recurrent neural networks (RNNs) to establish mappings between simulated activity and dose profiles, demonstrating robust generalization across different beam energies and anatomical conditions. Ma et al. [2020] proposed a generative adversarial network (DiscoGAN) framework that integrates activity data with anatomical and stopping-power information from CT images to enhance predictive accuracy. Overall, ML-based frameworks offer a promising direction for fast and patient-specific prediction of dose and range verification.

4

Computation of 3D PED in carbon ion therapy

This chapter details the two approaches used in this study to calculate the PED in carbon ion therapy: MC simulation and the analytical method developed in this study. Section 4.1 introduces the MC toolkit and basic simulation settings employed throughout this study. The MC simulations used later to validate the analytical method follow these settings, but case-specific parameters, such as phantom geometries and beam configurations, differ between validation cases and are therefore described in the corresponding validation chapters rather than here. The rest of the chapter is devoted to the development of the analytical method, which represents the core contribution of this study and is presented in detail in Section 4.2.

4.1 Monte Carlo simulation settings

In this study, Geant4 version 10.07.p04 was used to simulate the production of PEs by carbon ion irradiation. To run a Geant4 simulation, several aspects of the simulation process had to be defined, including the system geometry, the materials involved, the generation of particles, the physics models and the storage of events and tracks. For modeling the hadronic physics processes (i.e., interactions between hadrons and matter), the physics model QGSP_BIC (quark-gluon string precompound, binary light ion cascade package) was selected in all the simulations. This choice was based on the findings of [Chacon et al., 2019, 2024], who concluded that the BIC model of Geant4 provided the best overall fit in positron-emitting fragment yield of the experimental ^{12}C beam measurements. Besides, the electromagnetic processes were modeled by the default standard electromagnetic physics list.

Multiple MC simulations were conducted in this work for different purposes, including

the generation of reference data to parameterize the analytical model and the validation of the proposed model. To generate reference data, simulations were initially performed in a cylindrical phantom of a homogeneous reference material. The so-called reference material consists of six elements (H, C, N, O, P and Ca) which contribute to the main production of PEs in human tissue, and its properties are shown in table 5.1. Mono-energetic and mono-directional carbon ion pencil beams with initial lateral sigma σ_0 of 3 mm hit perpendicularly at the geometric center of the flat surface of the cylindrical phantom, propagating along the cylinder axis, as shown in Figure 4.1. 36 independent simulations were carried out, one

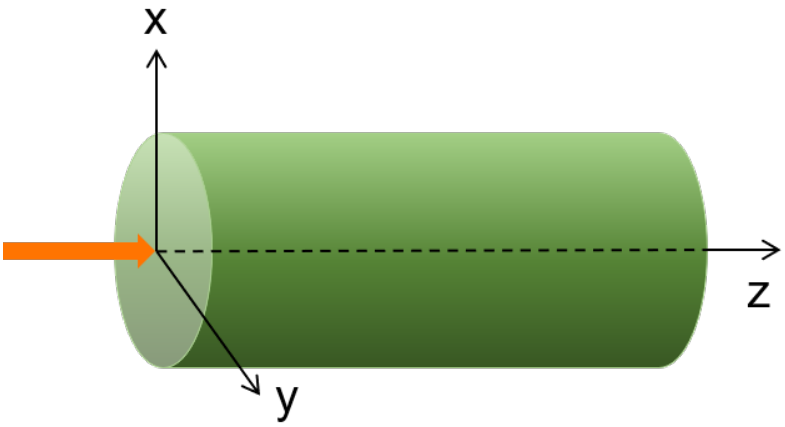

Figure 4.1: Scheme of the MC simulations for generating reference data: A carbon ion pencil beam with initial lateral sigma σ_0 of 3 mm hit perpendicularly at the geometric center of the flat surface of the cylindrical phantom filled with the reference material, propagating along the z axis.

for each initial energy from 80 to 430 MeV/n in 10 MeV/n increments, each using 5×10^8 carbon ion primaries. The dose and number of PEs were scored with cylindrical scoring using 0.2 mm radial binning and 0.5 mm binning in depth. MC simulations performed at 250 MeV/n, chosen as the representative beam energy within the therapeutic range, show that PEs generated from the fragmentation of phosphorus (^{30}P) and calcium (^{38}K) in the reference material are only about 2% of the total PE yield. Because this share is significantly smaller than the contributions from other target nuclei, ^{30}P and ^{38}K are not considered in this study. Ultimately, five isotopes ^{11}C, ^{10}C, ^{15}O, ^{13}N and ^{14}O, which are the most relevant PEs in carbon ion therapy [Pönisch et al., 2004] were considered and scored in the initial simulations and all the subsequent simulations.

For the validation cases, the corresponding phantom configurations and beam setups are specific to each scenario and will be described in detail in the relevant sections.

Table 4.1: The reference material properties

Mass density	Electron density	Mass abundances (%)					
($g{\cdot}cm^{-3}$)	(10^{20} cm^{-3})	H	C	N	O	P	Ca
1.54	4.71	2	31	26	38	1	3

4.2 Development of the analytical approach

The analytical approach developed in this work for predicting 3D PED in carbon ion therapy builds upon a 1D analytical PED prediction approach and a PBA kernel for 3D spreading. The 1D approach incorporates and extends a previously proposed 1D analytical method by Hofmann et al. [2019]. The original 1D approach demonstrated the feasibility of modeling PED profiles based on the dose profiles in carbon ion therapy. This method was later evaluated using patient data by Vasic et al. [2024], which revealed its limitations in dealing with highly heterogeneous geometries, such as those involving air cavities. To address these limitations, this work introduces several improvements to the original 1D approach, including improved modeling functions, the consideration of more PEs channels, and a novel mapping process for handling longitudinal heterogeneity effects in projectile PED. The enhanced 1D analytical method is then integrated into a PBA framework to enable 3D PED prediction. To clearly position the novel contributions introduced in this work, a brief review of the previous 1D method and its limitations is provided in Section 4.2.1. The improvements on the 1D method in Section 4.2.2. In Section 4.2.3 the framework based a PBA for 3D PED prediction is presented.

4.2.1 Review of the previous 1D analytical models

A filtering approach for proton therapy

A filtering approach was initially proposed by Parodi and Bortfeld [2006] to predict positron emitter activity $P(z)$ along depth z in proton therapy by convolving the dose distribution $D(z)$ with a filter kernel $f(z)$.

$$P(z) = D(z) * f(z) = \int_{-\infty}^{\infty} D(z')f(z - z')\,dz'. \tag{4.1}$$

The filter kernel $f(z)$ is described in terms of one or more so-called $\tilde{Q}_\nu$ functions that are a convolution of a Gaussian with a power-law function. The filter parameters are refined by fitting the convolution of the filter kernel with dose distributions at different energies to the PED profiles obtained from MC simulations. For each interaction channel of the primary proton with a target nucleus resulting in a positron emitter, one filter is created in the reference space.

Furthermore, this method is generalized to heterogeneous media considering both the different residual ranges across different materials and the contribution of different reaction

channels to the total PE density. A path length operator $\mathcal{F}$ converts the penetration depth z in a specific medium into the reference-material-equivalent depth $z_{ref,eq}$.

$$\mathcal{F} : z \rightarrow z_{ref,eq} = \int_0^z \frac{\rho_{el}(z)}{\rho_{el,ref}} dz \tag{4.2}$$

where $\frac{\rho_{el}(z)}{\rho_{el,ref}}$ is the electron density of the material at depth z relative to the electron density of the reference material. After transformation of the depth dose distribution in real space by the operator $\mathcal{F}$ into the reference space of reference material, the convolution of the dose distribution with filter kernels $f(z)$ is applied in the homogeneous reference space. Resulting distributions are transformed back to real space using the inverse operator $\mathcal{F}^{-1}$. After that, the material influence on the strength of PED is considered by multiplying weighting factors $g_j(z)$ according to the tissue composition at each depth. This local factors $g_j(z)$ are defined as:

$$g_j(z) = \left[\frac{w_j(z) \cdot \rho(z)}{w_{j,ref} \cdot \rho_{ref}}\right] \left[\frac{\rho_{el,ref} \cdot \rho(z)}{\rho_{el}(z) \cdot \rho_{ref}}\right] \tag{4.3}$$

where $w_j(z)/w_{j,ref}$ is the weight fraction of the target nucleus j at depth z relative to the weight fraction of the same target nucleus in the reference material, and $\rho(z)/\rho_{ref}$, $\rho_{el}(z)/\rho_{el,ref}$ are the mass and electron density of the material at depth z relative to the one of the reference material, respectively. The normalization factor in the first bracket accounts for the activation dependence on the nuclear density. The second factor introduces a correction for the energy deposition. Finally, the total positron emitter distribution is calculated by

$$P(z) = \sum_{j=1}^{N} g_j(z) \mathcal{F}^{-1} \left[\mathcal{F}(D(z)) * f_j(z)\right] \tag{4.4}$$

A previous 1D analytical approach for carbon ion therapy

Hofmann et al. [2019] applied the convolution framework to carbon ion therapy. They found that the calculated filter was strongly energy-dependent and did not reproduce the PED when applied to other energies, as illustrated in Figure 4.2. Instead, they used the convolved profiles P to predict the distal fall-off position of PED, while the rest of PED was constructed using parameterized modeling functions. It is important to note that, in this context, the term PED refers to 1D depth PED profiles.

In the work of Hofmann et al. [2019], MC simulations from Geant4 version 10.02.p02 are used [Agostinelli et al., 2003] to calculate the PED in phantoms as reference data. For the modelling of physical processes, the physics list QGSP_BIC_HP (quark-gluon string precompound, binary light ion cascade, high precision neutron package (NeutronHP)) is chosen. Two PEs, ^{11}C and ^{15}O, were considered and tracked. In carbon ion therapy, PEs originate not only from the fragmentation of the target nuclei in the media but also from the fragmentation of the projectile particles themselves. For instance, ^{11}C can be produced as a fragment of both the projectile carbon ion and a target nucleus, while ^{15}O is exclusively

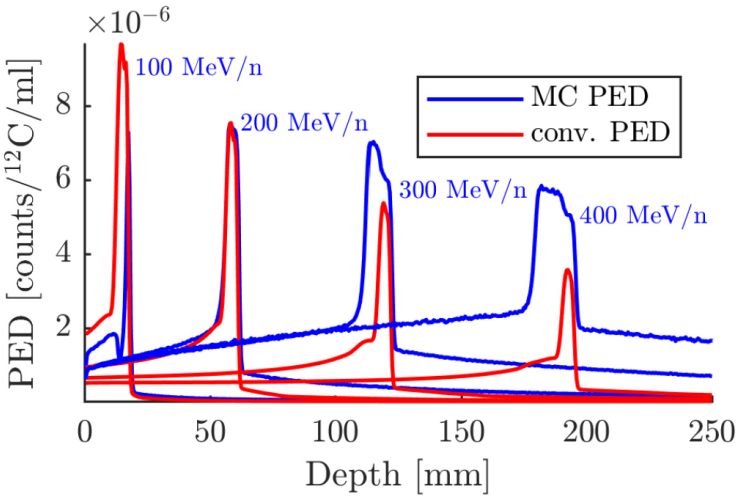

Figure 4.2: ^{11}C distributions from interactions between primary ^{12}C ions and carbon nuclei targets. A filter designed for 200 MeV/n carbon ions impacting the reference material is applied to the depth dose distributions at various carbon ion energies (100 MeV/n, 200 MeV/n, 300 MeV/n, and 400 MeV/n). However, the resulting convolved profiles P (red) do not correspond with the Monte Carlo (MC) simulated ^{11}C distributions (blue) at 100 MeV/n, 300 MeV/n, and 400 MeV/n. Figure from [Hofmann et al., 2019].

generated from target fragmentation. Since projectile fragments and target fragments exhibit different spatial and kinetic characteristics, it is necessary to separate projectile and target contributions in PED modeling. To achieve this, they introduced a method to separate ^{11}C into $^{11}C_{proj}$ and $^{11}C_{tar}$ based on the kinetic energy difference before and after the nuclear interaction. Fragments with kinetic energy above the 70% of the kinetic energy of initial projectile at the time of interaction are considered to be projectile fragments, while those with an energy below the threshold are considered to be target fragments. Figure 4.3 shows the kinetic energies of ^{11}C after nuclear interactions of projectile particles ^{12}C with target nuclei in MC simulations against the kinetic energy of the projectile at the time of interaction and justifies the separation criterion. This separation leads to the two typical PED in carbon ion therapy: PED_{tar}, a broad build-up and tail from positron emitters created mainly from target nuclei that stay at their site of production; and PED_{proj}, a peak close to the Bragg peak position where the positron emitters formed from the projectile particle come to rest. Thus, PED_{tar} and PED_{proj} were calculated separately by modeling functions, as summarized below. The total PED was then obtained by summing the two components.

- Modelling PED of $^{11}C_{proj}$ in the reference material

The modeling approach proposed by Hofmann et al. [2019] determines first the peak region then the profiles, which is described as follows. The distal limit of the peak region is first predicted by the 10% distal fall-off position of convolved profiles P. The proximal

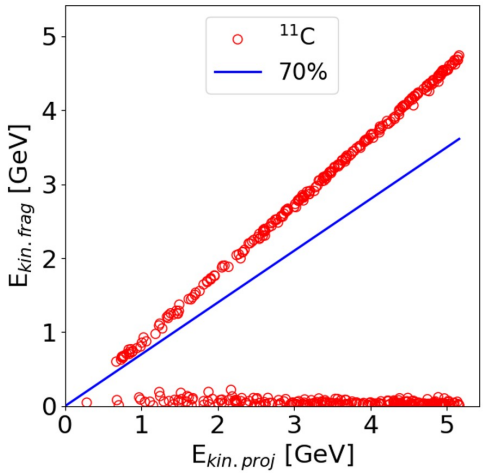

Figure 4.3: Kinetic energy distributions for ^{11}C versus projectile particles ^{12}C with 70% threshold. Figure adapted from [Hofmann et al., 2019].

limit is then determined by the ratio $\frac{A_f}{A_p}$ of the incident primary particle range, with A_p and A_f being the mass numbers of the primary particle and the fragments, respectively. The incident particle range is determined by the 80% distal fall-off position of depth dose. Finally, the analytical function predicting the PED profile for each subspecies of $^{11}C_{proj}$, noted as i, that is to be mapped into the peak region is given by

$$\mathrm{PED}_{i,proj}(E,z) = \{h_i(E) \cdot \Phi_{^{12}C}(z)\} * G(z), \tag{4.5}$$

where $h_i(E)$ is an energy-dependent scaling factor in the form of a fourth-degree polynomial to account for the height of the PED peak, $\Phi_{^{12}C}(z)$ is the fluence loss correction for ^{12}C and the Gaussian function $G_i(z)$ accounts for energy loss fluctuations with empirically determined width σ_G of 1.2 mm.

An example of PED of $^{11}C_{proj}$ generated from the interactions of ^{12}C ion beams of initial kinetic energies of 100, 200, 300 and 400 MeV/n with carbon ($Z_t = 6$) and oxygen ($Z_t = 8$) target nuclei is shown in Figure 4.4. The modelling results show good agreement with the MC results.

- Modelling PED_{tar} in the reference material

The PED for target PEs are described as having a build-up part before the Bragg peak followed by a distal tail after the Bragg peak, which are parameterized by different analytical functions [Hofmann et al., 2019]. In the build-up region, PEs are created in interactions from the projectile with the target nuclei and the number of PE increases along the depth due to interactions of secondary particles with the target nuclei in the media. The build-up part b for each target PE subspecies i is represented by the following equation:

$$\mathrm{P}_{i,b}(z) = P_{i,b,max}\left[1 - \alpha_i \exp\left(-c_i z\right)\right] \tag{4.6}$$

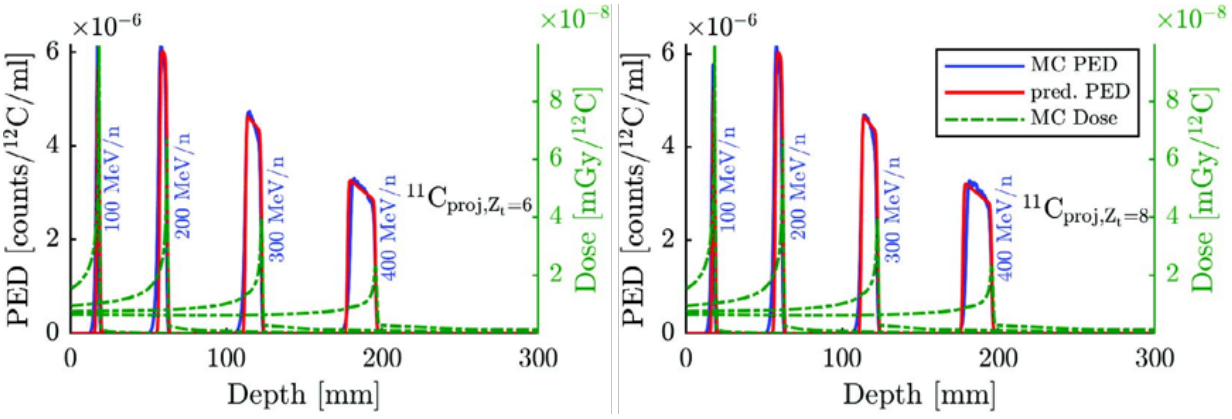

Figure 4.4: PED for the $^{11}C_{proj}$ generated from the interactions of ^{12}C ion beams of initial kinetic energies of 100, 200, 300 and 400 MeV/n with carbon (left) and oxygen (right) target nuclei in the reference material. The MC simulated PED are shown in dashed and the analytical PED are shown in solid lines. Figure adapted from [Hofmann et al., 2019].

where $P_{i,b,max}$ refers to the theoretical maximum number of produced PEs at large depths, α_i is determined by the number of PEs at the entrance of the phantom, and c_i is a factor considering the build-up rate.

In the region after the Bragg peak, the number of the secondary particles declines resulting in a distal tail and is modeled by:

$$\mathrm{P}_{i,t}(E,z) = \beta_i E^3 \frac{1}{z} \tag{4.7}$$

where β_i is a scaling parameter and E is the initial kinetic energy. The gap between the end of the build-up function (maximum position of convolved P) and beginning of tail (10% distal fall-off position of the convolved P) is interpolated linearly.

An example of PED of target PEs, $^{11}C_{tar}$, ^{15}O, for energies between 100 MeV/n and 400 MeV/n is shown in Figure 4.5. The modelling results show good agreement with the distal fall off positions compared to the MC results, indicating that the method are well-suited for predicting the range of PED_{tar}. However, noticeable discrepancies can be observed in the build-up region, especially at lower energies. As discussed in Hofmann et al. [2019], the parameterization of the build-up part was designed to be applicable across all energies (i.e., energy independent), which comes at the cost of reduced accuracy, most notably at lower energies. This finding suggests that further refinement of the modeling function, with explicit consideration of energy dependence, would help improve overall prediction accuracy.

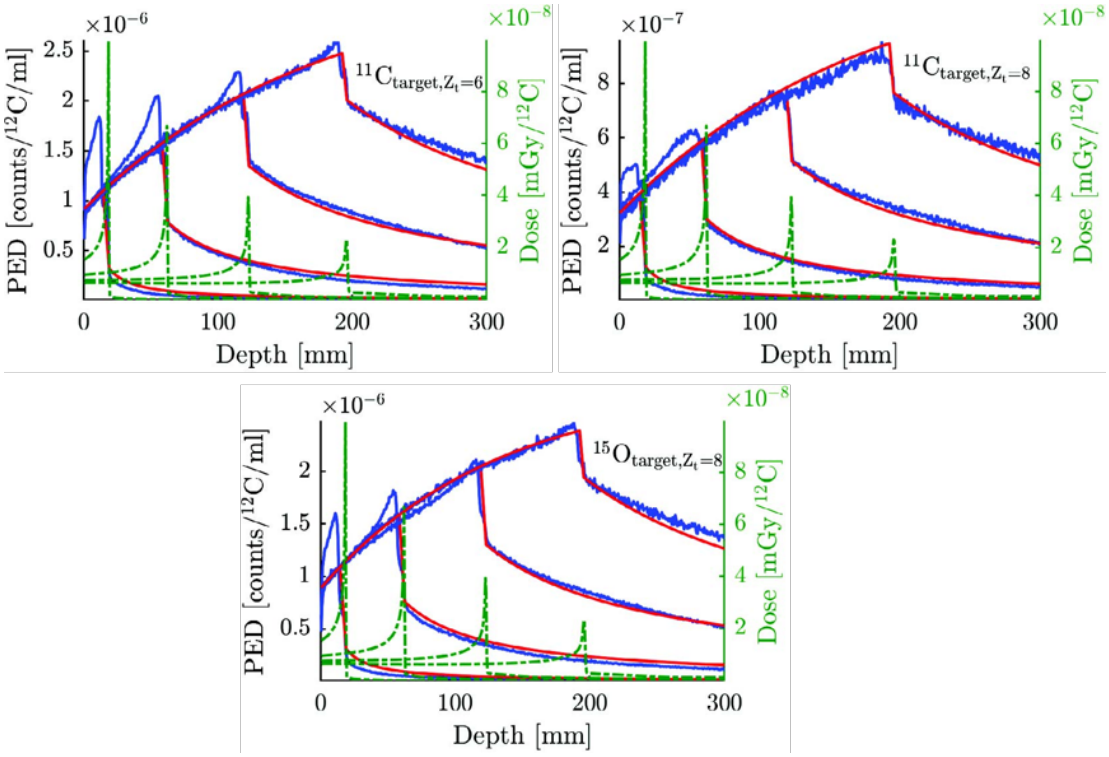

Figure 4.5: PED for the $^{11}C_{target}$ (top) and ^{15}O (bottom) generated from the interactions of ^{12}C ion beams of initial kinetic energies of 100, 200, 300 and 400 MeV/n with carbon (top left) or oxygen (top right) target nuclei in the reference material. The MC simulated PED are shown in dashed and the analytical PED are shown in solid lines. Figure adapted from [Hofmann et al., 2019].

- Heterogeneity effect

This approach is generalized to inhomogeneous media following the same methodology as the one proposed by Parodi and Bortfeld [2006]. A path length operator $\mathcal{F}$ (Eq. (4.2)) and its inverse operator serve the conversion between the penetration depth z in a specific medium and the reference-material-equivalent depth $z_{ref,eq}$. The material effect on target PED can be taken into account by multiplying a local factor $g_j(z)$ (cf. the factor in the first bracket of Eq. (4.3)) to adjust the weight of different production channels [Parodi and Bortfeld, 2006], where j refers to the target nuclei involved in the production channel of the PE subspecies i.

As for the projectile PED, Hofmann et al. [2019] first accounted for material effect along the beam path where projectile PEs were initially produced and then mapped projectile PEs into their stopping interval (the peak region). The analytical function for the projectile PED profile considering the material effect that is to be mapped into the peak region is given by:

$$\mathrm{PED}_{i,proj}(E,z) = \{h_i(E) \cdot g_j(z) \cdot \Phi_{^{12}C}(z)\} * G(z), \tag{4.8}$$

In their implementation, a linear mapping relationship was established between the production region (where projectile PEs are generated) and the stopping region (where they eventually come to rest). The predicted PED given by Eq. (4.8) was then mapped into the stopping interval. Finally, the PED value at each depth within the stopping interval was determined by uniform interpolation.

Evaluation and identified limitations

Hofmann et al. [2019] investigated this analytical method for homogeneous and inhomogeneous slab phantoms, considering both pencil beam and spread-out Bragg peak scenarios. They achieved a mean relative error (MRE) below 4% in all tested cases and a distal fall-off position that matched well with maximum deviations of 0.6 mm for homogeneous and 1.3 mm for inhomogeneous phantoms, compared to MC simulated results. The predicted distributions from the analytical approach in comparison to the ones from MC simulations are displayed in Figure 4.6 for a spread out Bragg peak (242 MeV/n–290 MeV/n and 230 MeV/n–280 MeV/n) in the reference material and a slab phantom, respectively.

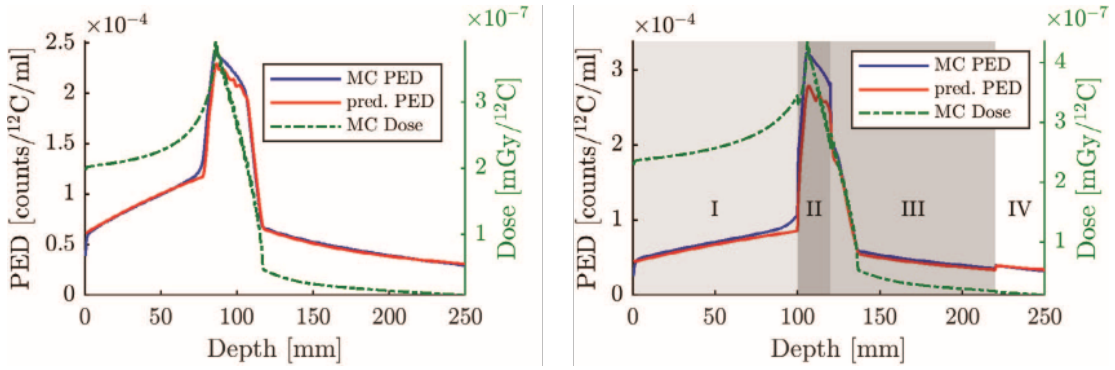

Figure 4.6: ^{12}C ions with energies between 230 MeV/n and 280 MeV/n impinge on the homogeneous reference material (left) and ^{12}C ions with energies between 242 MeV/n and 290 MeV/n impinge on a slab phantom (right) where different materials are indicated with different gray values in background (I: water, II: bone, III: PMMA, IV: reference material). PED profiles show the sum of ^{11}C and ^{15}O distributions. MC simulated PED and dose are shown in solid blue and dashed green, respectively. The analytical PED is shown in solid red. Figure adapted from [Hofmann et al., 2019].

Vasic et al. [2024] then explored the performance of the method using one patient CT data provided by the LMU Klinikum Großhadern. Three cases with focus on cranial anatomies were studied and used to verify the analytical prediction algorithm against MC simulations, which performed in Geant4 version 10.02.p02 using the QGSP_BIC_HP physics list. The first case is a more homogeneous brain irradiation case, whereas the second and the third cases are more heterogeneous anatomies including numerous air cavities in the head and neck region. In the simulation, 200 MeV/n carbon ions, forming a square field of $50 \times 50\ mm^2$, impinged on three different regions of a patient and PEs (^{11}C and ^{15}O) and

dose were scored in the voxelized geometry of the patient. The analytical PED was then calculated based on the dose distribution and the material properties of the voxels lines along the beam direction. The comparison between the analytical and MC-simulated PED was evaluated using the MRE. The MRE was calculated for each longitudinal profile within the field, and the average MRE along with its standard deviation was reported to quantify the overall agreement. Additionally, shifts between the analytical and simulated PED were evaluated using the difference between their 80% distal fall-off positions.

During their investigation, they found the height of the analytical PED in the peripheral regions of the field was underestimated. This was explained as an intrinsic limitation of the 1D approach in areas with non-uniform fluence [Vasic et al., 2024] (see Figure 4.7). To avoid this issue from misleading the MRE analysis, a mask was chosen to discard peripheral voxels with the condition that the maximum PED at the peak of the prediction differs more than 20% from the one in MC.

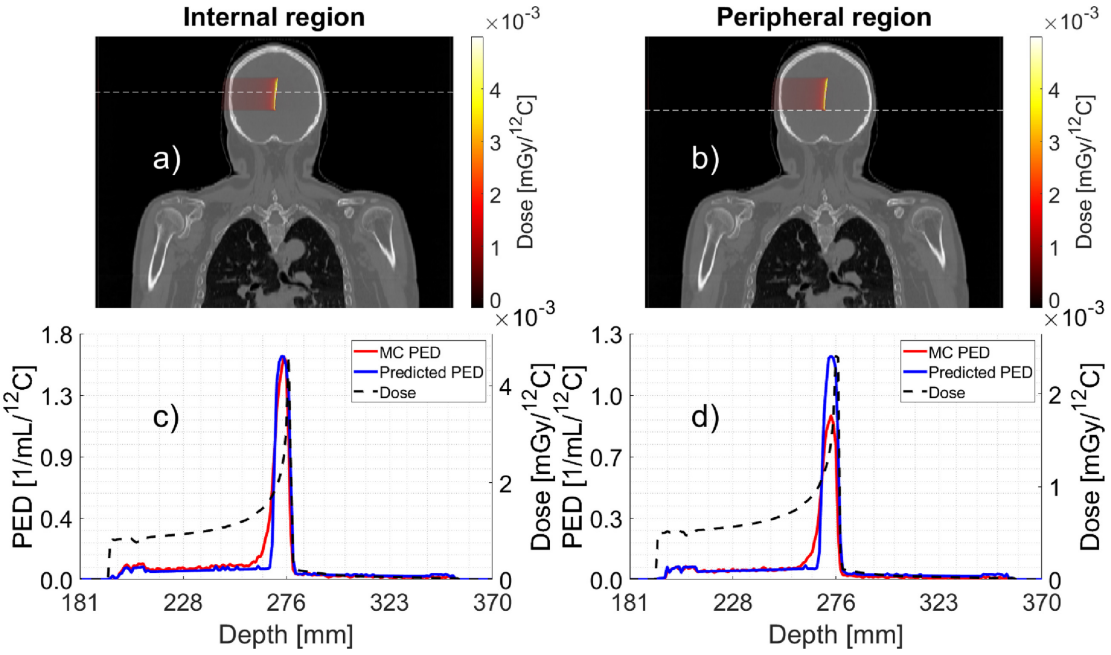

Figure 4.7: The maximum PED_{pred} along voxel line of interest was compared with the maximum PED_{MC} simulated along the same voxel line. (a) and (c) represent PED_{pred} and the PED_{MC} in the internal slice of the field distribution, i.e., around the beam axis. (b) and (d) represent PED_{pred} and the PED_{MC} in the peripheral region, i.e., at large distances from the central beam axis where the field is no more homogeneous. It can be seen that the prediction is higher than the simulated data in the regions peripheral to the field distribution. The dashed black lines represent the dose along the analyzed slice. Data were taken from the analysis of data for in-silico irradiation of the brain region in the patient CT. Figure from [Vasic et al., 2024].

In the brain case, the PED_{pred} agreed well with PED_{MC} for all voxel lines within the chosen mask, yielding a mean MRE of $0.88 \pm 0.07\%$. In the first head and neck

case, which features air cavities located proximal to the PED peak, notable discrepancies between PED_{pred} and PED_{MC} were observed, primarily in the shape of the distribution (see Figure 4.8), with a mean MRE of $1.06 \pm 0.47\%$. For both the brain and the first head and neck cases, the distal fall-off positions were predicted within an average deviation of 1 mm.

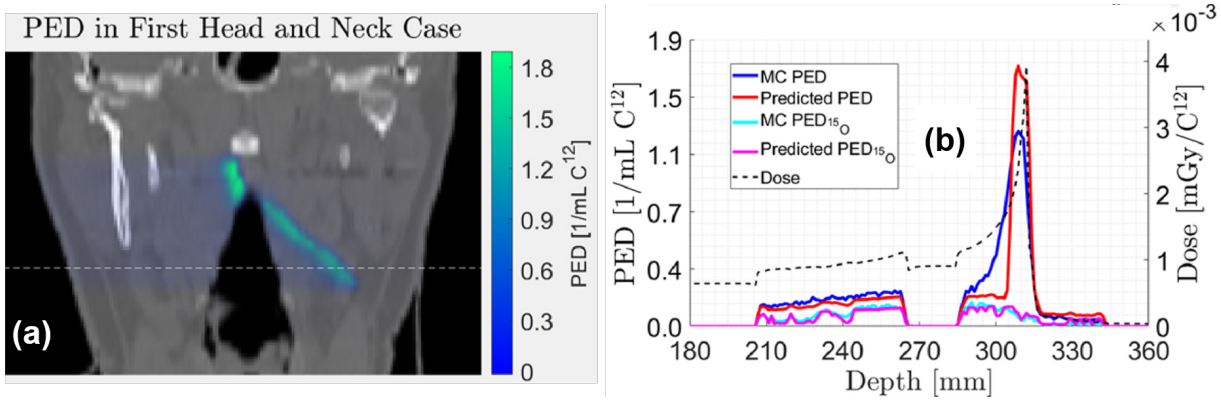

Figure 4.8: Results of the first head and neck case. (a) shows a CT slice in coronal view of the patient with the total analytical PED (^{15}O and ^{11}C). The white dashed line represents the voxel line considered for (b). (b) shows the contribution of dose, ^{15}O and the total PED along the voxel line shown in (a). Figure adapted from [Vasic et al., 2024].

In the second head and neck case, where the presence of more complex air cavities made it difficult to predict the shape of PED. Here, an obvious disagreement of PED was found particularly in the anatomical regions where the tissue density drops drastically (see Figure 4.9), leading to a mean MRE of $1.59 \pm 0.83\%$ and an average shift of -1.44 ± 3.06 mm. Detailed analysis showed that the main source of error in the two head-and-neck cases came from the PED for $^{11}\text{C}_{proj}$. This highlights a limitation of the 1D approach in predicting projectile PED for cases with high inhomogeneities and underlines the need for further improvements.

Vasic et al. [2024] re-examined the prediction of PED_{proj} and identified a potential optimization on the prediction of its distal limit. In the previous formulation, the distal limit was determined by the 10% distal fall-off position of convolved profiles P [Hofmann et al., 2019]. Vasic et al. [2024] demonstrated that changing this percentage, denoted here as K, can reduce the range deviation. As they observed that the distance between the maximum dose and the air cavity strongly influenced the prediction accuracy, they divided the voxel lines into two categories for further analysis: "Cavity close" voxel lines where the cavity lies within 5 mm of the dose maximum, and "Cavity far" voxel lines, where this distance exceeds 5 mm. For the all three cases studied, they optimized K separately for each cavity-distance group. For example, in the two head-and-neck cases, changing K in a range of 45%-65% for the "Cavity close" groups reduced a mean shift to below 0.5 mm (solid blue lines in Figure 4.10). In the "Cavity far" groups, choosing K in a range of 15–30% brought the mean shift close to zero (solid red lines in Figure 4.10). Overall,

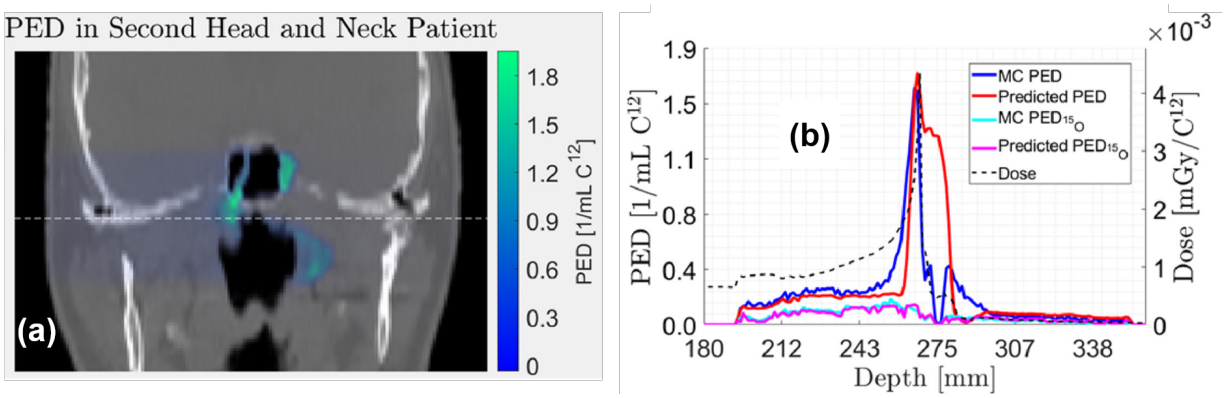

Figure 4.9: Results of the second head and neck case. (a) shows a CT slice in coronal view of the patient with the total analytical PED (^{15}O and ^{11}C). The white dashed line represents the voxel line considered for (b). (b) shows the contribution of dose, ^{15}O and the total PED along the voxel line shown in (a). Figure adapted from [Vasic et al., 2024].

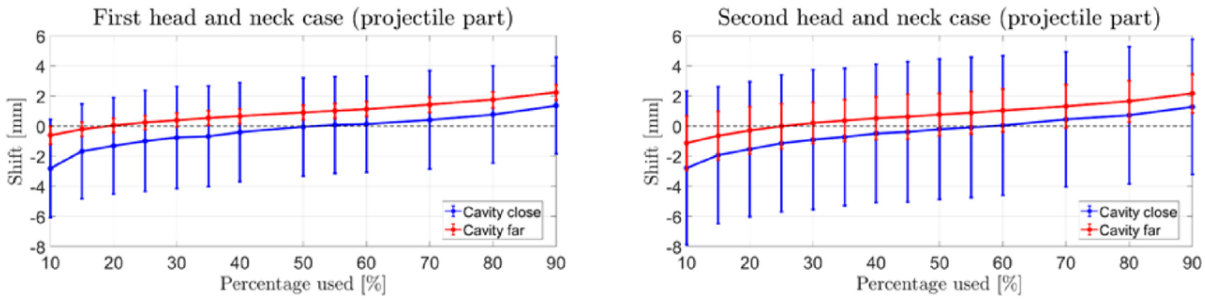

Figure 4.10: Shift at 80% distal fall-off of distributions for $^{11}C_{proj}$, versus percentage (K parameter) used to estimate the distal fall-off position. Data where the maximum dose is delivered close to the air cavity (blue solid line) and far from the air cavity (red solid line) are separated. Left and right graphs report data analyzed for the first and the second head and neck cases, respectively. PED_{proj} is analytically predicted changing the K parameter of the filtered PED which is used to determine the position of the fall-off region. Data is shown as error bars where the central point is the average shift and the error corresponds to the standard deviation. Figure adapted from [Vasic et al., 2024].

applying a K value between 20% and 25% yielded the shift closer to zero in all cases for this particular patient.

- Limitations of the 1D approach and potential improvements

Here the limitations of the Hofmann's 1D approach and outline possible improvements are summarized. First, Hofmann et al. [2019] considered only two major PEs, while additional PEs could be included in future work. Besides, Figure 4.5 shows that the modeled PED_{tar} curves deviate in the build-up region. This arises because the parameterization of the

build-up was made energy-independent to ensure applicability across all energies, which inevitably reduces accuracy. Introducing an explicit energy dependence into the modeling function could therefore enhance the accuracy of prediction.

Subsequently, Vasic et al. [2024] found that the 1D method underestimated the PED amplitude in peripheral regions of the irradiation field. This exposed a limitation of constructing a 3D PED by predicting 1D PED for each voxel line (a quasi-3D approach). This points to the need for a genuine 3D extension of the model. Moreover, Vasic et al. [2024] observed large discrepancies in the prediction of PED_{proj} in highly heterogeneous media. To mitigate this, they adjusted the parameter K (which defines the distal fall-off positions) for different anatomical scenarios and demonstrated that this tuning can improve the prediction accuracy. However, their study fixed the beam energy and retained the filter functions from Hofmann et al. [2019], leaving open the question of whether the optimal K values identified would apply across other energies or alternative filter sets (e.g., if new PEs are added, new filters need to be build). In practice, K would likely to be re-optimized for new scenarios. Furthermore, the material effect on PED$proj$ remains an open issue. In the original mapping procedure of Hofmann et al. [2019], the material properties at the stopping position of projectile PEs is not properly taken into account. For instance, if the stopping region includes an air cavity its very low stopping power should allow projectile fragments to traverse the cavity, yielding an almost zero PED in this air cavity region. But the original mapping relationship would assign numerous projectile PEs into the cavity region, producing an unrealistically high PED (see Figure 4.9). Future work must therefore incorporate a dedicated material-effect correction for PED_{proj}.

4.2.2 Enhanced 1D analytical approach with proposed improvements

This subsection presents an enhanced 1D analytical approach that addresses the shortcomings of Hofmann et al. [2019]'s model. The proposed improvements include (i) incorporating additional PEs, (ii) implementing energy-dependent parameterizations to improve build-up accuracy, (iii) introducing a material-effect correction for projectile PED. The enhanced 1D analytical approach then serves as the foundation for the full 3D extension presented later in this chapter. It is important to note that throughout this work, the 1D analytical approach predicts the laterally integrated depth positron emitter distributions (IDPED), the same quantity calculated by Hofmann et al. [2019]'s model while simply named as PED. In Section 4.2.2, the term IDPED will be used to specify this quantity unambiguously.

Five PEs and their subspecies

As the five PEs ^{11}C, ^{10}C, ^{15}O, ^{13}N were considered in the MC simulations (see Section 4.1), the same PEs should be included in the analytical method as well. Among the five PEs considered, ^{11}C and ^{10}C can be produced via both projectile and target fragmentation, while the others are exclusively generated from target fragmentation. The fragments with low kinetic energy originate from target nuclei, whereas those with high kinetic energy

correspond to fragments of projectile particles. Therefore, ^{11}C and ^{10}C were categorized into the target and projectile contributions based on their kinetic characteristics, denoted as $^{11}C_{target}$, $^{11}C_{proj}$, $^{10}C_{target}$ and $^{10}C_{proj}$ using 70% threshold for ^{11}C [Hofmann et al., 2019] and 50% threshold for ^{10}C. The justification and comparison of these thresholds for ^{11}C and ^{10}C are illustrated in Figure 4.3 and Figure 4.11, respectively. Consequently, a total of seven types of PEs were considered: five target PEs ($^{11}C_{target}$, $^{10}C_{target}$, ^{15}O, ^{13}N and ^{14}O) and two projectile PEs ($^{11}C_{proj}$ and $^{10}C_{proj}$).

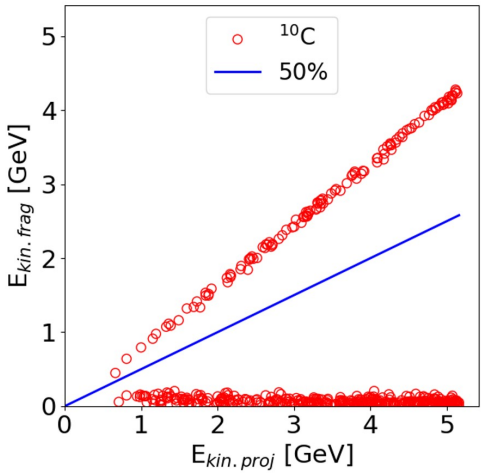

Figure 4.11: Kinetic energy distributions for ^{10}C versus projectile particles ^{12}C with 50% threshold.

Since PEs can be generated from different target nuclei and thus make the prediction of PED material-dependent, Further subdivision was performed for each PEs according to their target nuclei. Target nuclei can only produce target PEs with atomic numbers less than or equal to their own. The resulting subdivision is displayed in Table 4.2.

Table 4.2: Subdivision of different PEs according to their target nuclei.

Target nucleus	**PEs**						
	$^{11}C_{proj}$	$^{10}C_{proj}$	$^{11}C_{target}$	$^{10}C_{target}$	^{15}O	^{13}N	^{14}O
H	√	√					
C	√	√	√	√			
N	√	√	√	√		√	√
O	√	√	√	√	√	√	√
P	√	√					
Ca	√	√					

Building IDPED for target and projectile PEs

The construction of IDPED for each subspecies of PEs follows closely that described by Hofmann et al. [2019] (see Section 4.2.1) but with improved modeling functions.

- IDPED of target PEs

The IDPED of the five target PEs, generated in the reference material, are described as having a build-up part followed by a distal part [Hofmann et al., 2019]. An example of the IDPED for the $^{11}C_{target}$ is shown in Figure 4.12. An analytical function, comprising the

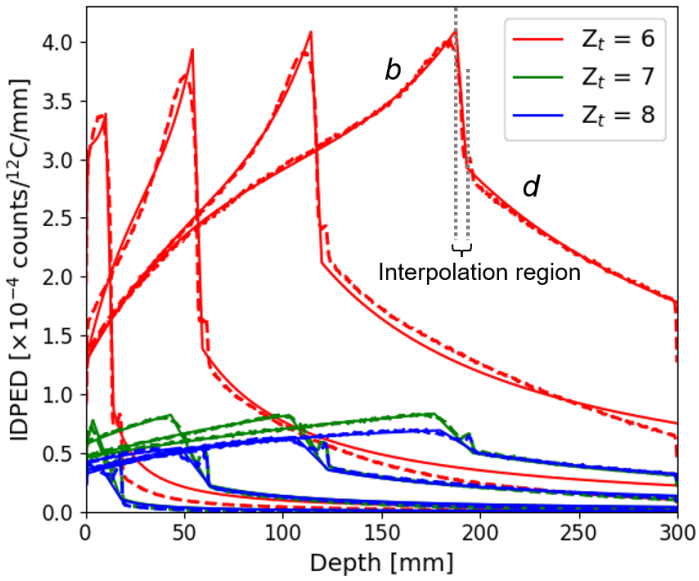

Figure 4.12: IDPEDs for the $^{11}C_{target}$ generated from the interactions of ^{12}C ion beams of initial kinetic energies of 100, 200, 300 and 400 MeV/n with carbon (red), nitrogen (green) and oxygen (blue) target nuclei in the reference material. The MC simulated IDPEDs are shown in dashed and the analytical IDPEDs are shown in solid lines. Two gray vertical lines separate the red solid line, representing the analytical IDPEDs for $^{11}C_{target}$ with carbon target of 400 MeV/n, into three regions: the build-up region b, the interpolation region and the distal region d, from left to right. A discontinuity is observed in the distal fall-off regions of the dashed lines, suggesting a transition in the nuclear models within Geant4.

sum of two exponential terms, was used to describe the build-up part b for each target PE subspecies i:

$$\mathrm{IDPED}_{i,b}(E,z) = A_i\left[1-\alpha_i\exp\left(-c_{1,i}z\right)\right] + B_i\left[\exp\left(c_{2,i}z\right)-1\right], \tag{4.9}$$

where the first one describes a less steep build-up and the other one compensates for the rapid growth in the area just before the Bragg peak, A_i is the theoretical maximum number

of produced PE at large depth from the less steep build-up, α_i is determined by the number of PE at the entrance of phantom, $c_{1,i}$ is considered as the build-up rate, B_i is determined by the difference in the number of PE at the end of build-up predicted by the first exponential term and the one obtained from MC simulation, and $c_{2,i}$ represents the rate of the rapid growth. For different PE subspecies, the form of the analytical functions could be adjusted according to their distribution profiles. For the most complicated case, α_i, $c_{1,i}$ and $c_{2,i}$ can be energy-dependent factors; this applies, for example, to the IDPED of $^{11}C_{target}$ from carbon target nuclei, as shown in Figure 4.12. In the simplest cases, only the first term with an energy-independent factor $c_{1,i}$ is sufficient.

For the distal part d of IDPED, a power function correlated with the initial kinetic energy E of the carbon ion beam was proposed:

$$\mathrm{IDPED}_{i,d}(E,z) = \beta_i E^3 \frac{1}{z^{n_i}}, \tag{4.10}$$

where a scaling factor β_i and the power of function n_i depend on the type of PE denoted as i and are both energy-independent.

The end position of the build-up and the initial position of the distal part of each IDPED were determined by different distal fall-off positions of the convolved profiles P by Eq. (4.1). The percentages of distal fall-off with respect to the maximum of P were determined based on the best agreement with MC simulated data. These percentages were energy-independent but varied among each subspecies of PEs. As shown in Figure 4.12, the IDPED profiles increase until the end of the build-up, followed by the distal tails which begin several millimeters later. The gap between the end of build-up part and beginning of distal part is interpolated linearly.

The IDPEDs for the five targets generated from different target nuclei in the reference material from MC simulations and the analytical modelling are shown in Figure 4.13.

- IDPED of projectile PEs

The modeling approach for projectile IDPED generated in the reference material, except those generated from target hydrogen nuclei, follows closely what was described by Hofmann et al. [2019] (see Eq. (4.5)). The analytical IDPED of four energies are shown in solid lines in Figure 4.14, with a comparison to the simulated results in dashed lines.

Since the IDPED for $^{11}C_{proj}$ and $^{10}C_{proj}$ from target hydrogen nuclei, i.e., the yellow dashed profiles shown in Figure 4.14, have a longer build-up than for the other target nuclei, the aforementioned function, Eq. (4.5), is not suitable for their modeling. Instead, a Landau distribution empirically was found to provide a better fit, even though this choice was driven by fit quality rather than by a specific physical interpretation. The modeling function is provided below:

$$\mathrm{IDPED}(E,z) = \{k(E) \cdot Landau(\mu,\eta)\} * G(z), \tag{4.11}$$

where $k(E)$ is an energy-dependent scaling parameter in the form of a three-degree polynomial, μ is the maximum position of the Landau distribution determined by the maximum

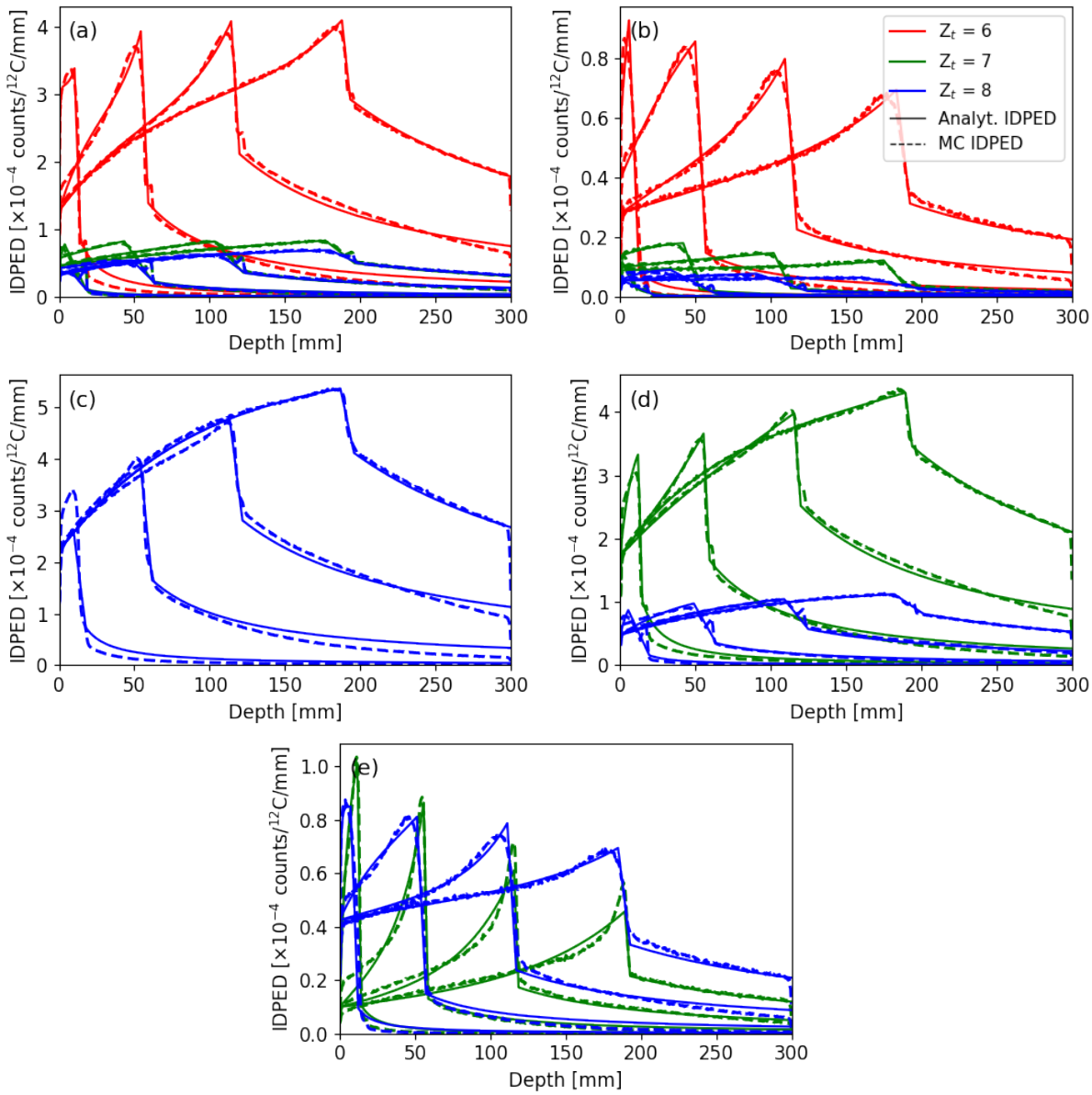

Figure 4.13: IDPEDs for the five target PEs, $^{11}C_{target}$ (a), $^{10}C_{target}$ (b), ^{15}O (c), ^{13}N (d) and ^{14}O (e) generated from the interactions of ^{12}C ion beams of energies of 100, 200, 300 and 400 MeV/n with different target nuclei in reference material. MC simulated IDPEDs are shown in dash and analytical IDPEDs are shown in solid.

position of convolved profiles P, η is the width parameter of the Landau distribution, which shows a linear correlation to the 80% distal fall-off position of IDD, and a Gaussian term $G(z)$ accounts for energy loss fluctuations. The fitting results are shown by the yellow solid

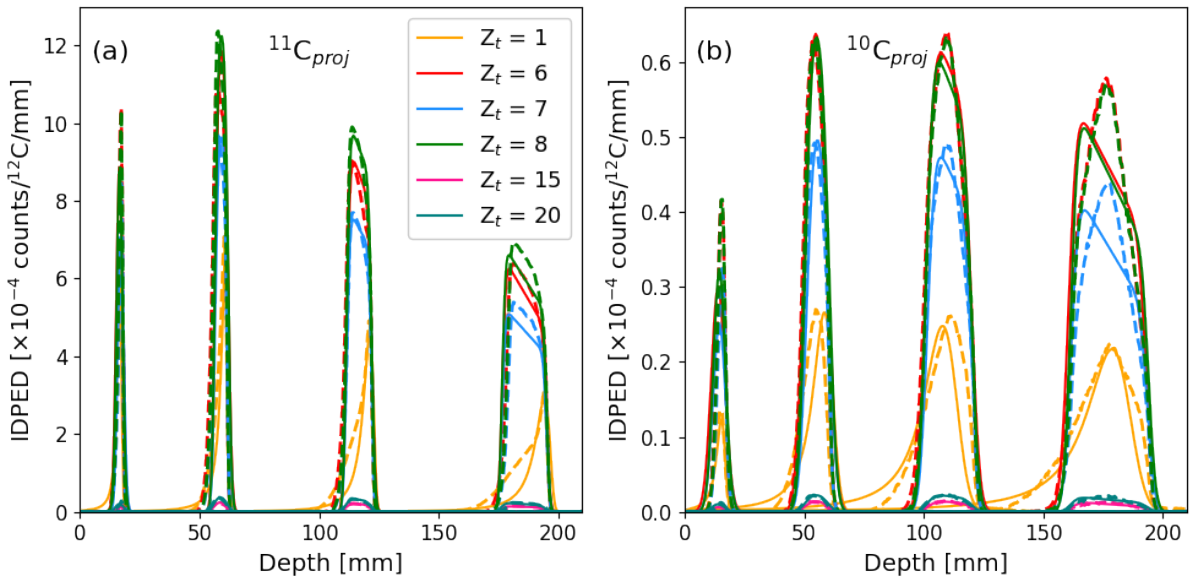

Figure 4.14: IDPEDs for the two projectile PEs, (a) $^{11}C_{proj}$, (b) $^{10}C_{proj}$ generated from the interactions of ^{12}C ion beams of initial kinetic energies of 100, 200, 300 and 400 MeV/n with the six different target nuclei in the reference material. The MC simulated IDPEDs are shown in dashed lines and the analytical IDPEDs are shown in solid lines.

profiles in Figure 4.14.

Longitudinal heterogeneity effect

As described in Section 4.2.1, to predict PED in heterogeneous media, adaptations are required to account for the different residual ranges across different materials and the contribution of different reaction channels to the total PE density.

The first adjustment involves converting the penetration depth z in a heterogeneous medium into the reference-material-equivalent depth $z_{ref,eq}$. Similar to the operator defined in Eq. (4.2), the depth conversion used in the study is defined as

$$\mathcal{F} : z \rightarrow z_{ref,eq} = \int_0^z SPR(z)dz \tag{4.12}$$

Here, $SPR(z)$ represents the stopping power ratio, defined as the stopping power in the medium at depth z relative to that in the reference material, calculated using the stopping power for heavy charged particles defined by Tsoulfanidis [2021] as follows:

$$SPR\,(z) = \frac{\rho_{el}(z)}{\rho_{el,ref}} \left(\frac{\ln\left(\frac{2mc^2}{I(z)}\beta^2\gamma^2\right) - \beta^2}{\ln\left(\frac{2mc^2}{I_{ref}}\beta^2\gamma^2\right) - \beta^2} \right) \tag{4.13}$$

where $\rho_{el}(z)/\rho_{el,ref}$ is the electron density of the material at depth z relative to the electron density of the reference material, mc^2 is the rest energy of electron, equal to 0.511 MeV, $I(z)$ and I_{ref} are the mean excitation energies of the material at depth z and the reference material, respectively, $\gamma = (E + Mc^2)/Mc^2$ where E is the particle kinetic energy in MeV and M is the particle rest mass, and $\beta = \sqrt{\gamma^2 - 1}/\gamma$. In our case, E is set as the initial energy of carbon ion primaries and M is the rest mass of a carbon ion.

The second adaptation stems from the effect of the irradiated material on the generation of PED. For both target PEs and projectile PEs, the irradiated material influences their production. Additionally, for projectile PEs, it is necessary to consider the impact of the traversed material on their stopping process. This distinction arises from the different generation processes of target PEs and projectile PEs. Target PEs are generated and stop at the same position, while projectile PEs travel a certain distance within the medium after their production. Therefore, the material effects on target PED and projectile PED were considered separately.

The material effect on target PED can be taken into account by multiplying a local factor $g_j(z)$ to adjust the weight of different production channels, which is same as in Eq. (4.8), where j refers to the target nuclei involved in the production channel of the PE subspecies i.

Here a scaling factor is sought to establish, denoted as ζ, for the projectile PED based on its formation process, where projectile PEs are produced at a certain depth and stop at another further downstream. In a discrete voxel-based space, this process is equivalent to associating each voxel where projectile PEs eventually come to rest (stopping voxels) with the voxels that originally produced them (producing voxels). A linear relationship between the production depth z of projectile fragments ($^{11}\mathrm{C}_{proj}$ or $^{10}\mathrm{C}_{proj}$) and their stopping position R_f was established by Hofmann et al. [2019] under the assumption that projectile fragments inherit the same velocity as the primary ^{12}C ions:

$$R_f = \frac{A_{proj}}{12} R_0 + \frac{12 - A_{proj}}{12} z \tag{4.14}$$

where R_0 is the range of the primary carbon ions, A_{proj} refer to the mass number of fragments (11 or 10). Consider a scenario in Figure 4.15: a carbon ion beam impinges horizontally on a medium filled with a homogeneous reference material, going from left to right. Assuming that N voxels from the entrance surface produce projectile PEs, and these PEs ultimately stop in K voxels. Based on the above Eq. (4.14), we have that the projectile PEs generated at the entrance ($z = 0$, voxel P_1) stop at $S_1 = \frac{A_{proj}}{12} R_0$, and those generated at the the maximum depth ($z = R_0$, voxel P_N) stop immediately at $S_K = P_N$, as shown in Figure 4.15. All intermediate production voxels are then mapped linearly to stopping voxels, each stopping voxel sequentially includes the contribution of N/K producing voxels.

The construction of the above mapping relationship is only valid in a homogeneous medium, where the relationship between the residual ranges of the projectile PEs and their production positions is linear [Hofmann et al., 2019]. However, when the medium is no

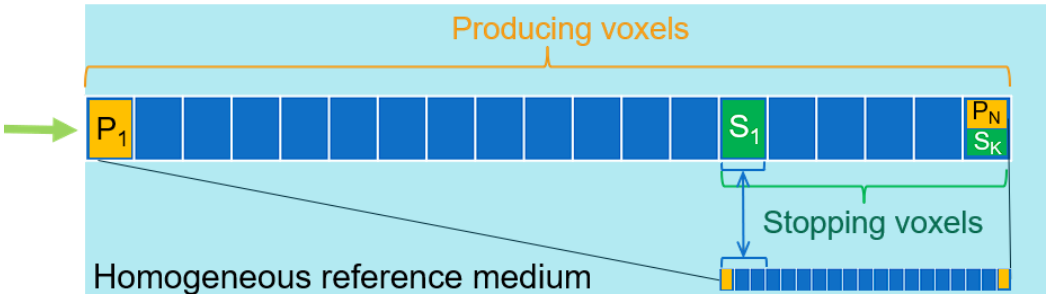

Figure 4.15: A carbon ion beam impinges horizontally on a homogeneous medium filled with the reference material. The central ray traverses voxels from P_1 to P_N and the generated projectile PEs stops in the voxels from S_1 to S_K. The producing interval containing N producing voxels are compressed to match the stopping interval containing K stopping voxels, as illustrated in the lower part of the figure. The mapping is established by sequentially matching the subinterval of each stopping voxel with the subinterval of the corresponding compressed producing voxels, ensuring that the subintervals are of equal length. For example, the projectile PEs in the stopping voxel S_1 corresponds to them produced in producing voxels from P_1 to $P_{N/K}$, and so on.

longer homogeneous, the linear relationship no longer holds, and the mapping relationship between stopping voxels and producing voxels is no longer uniform.

To address this, it was necessary to convert the heterogeneous space into the homogeneous reference material space by Eq. (4.12) first, as shown in Figure 4.16(a). The steps to establish the mapping relationship are as follows:

1. The first step involves determining the producing and stopping intervals. When the projectile IDPED in the reference space is constructed (see Section 4.2.2), the stopping interval can be easily determined by the positions where the projectile IDPED is non-zero. The production interval commences at the entrance surface and is assumed to share the same end of the stopping interval. These intervals, when associated to the inhomogeneous medium that has been converted to the reference space, determine the numbering for the producing and stopping voxels. As shown in Figure 4.16(b), we determined M producing voxels and L stopping voxels.

2. Next step is to establish the mapping relationship between the producing and stopping voxels. Essentially, the mapping process compresses the producing interval to match the length of the stopping interval, as shown in Figure 4.16(b). Each subinterval of a stopping voxel is then sequentially matched with the corresponding subinterval of the compressed producing voxels, ensuring equal lengths. Noting the path length of a stopping voxel s (for $s \in [1, \mathrm{L}]$) in the reference space is denoted as $l_{STOP,s}$, the subinterval which the k-th stopping voxel belongs to is $\left[\sum_{s=1}^{k-1} l_{STOP,s}, \sum_{s=1}^{k} l_{STOP,s}\right]$. Noting the path length of a producing voxel p is $l_{PROD,p}$ (for $p \in [1, \mathrm{M}]$), then the numbering set of producing voxels I, which are mapped to the k-th stopping voxel,

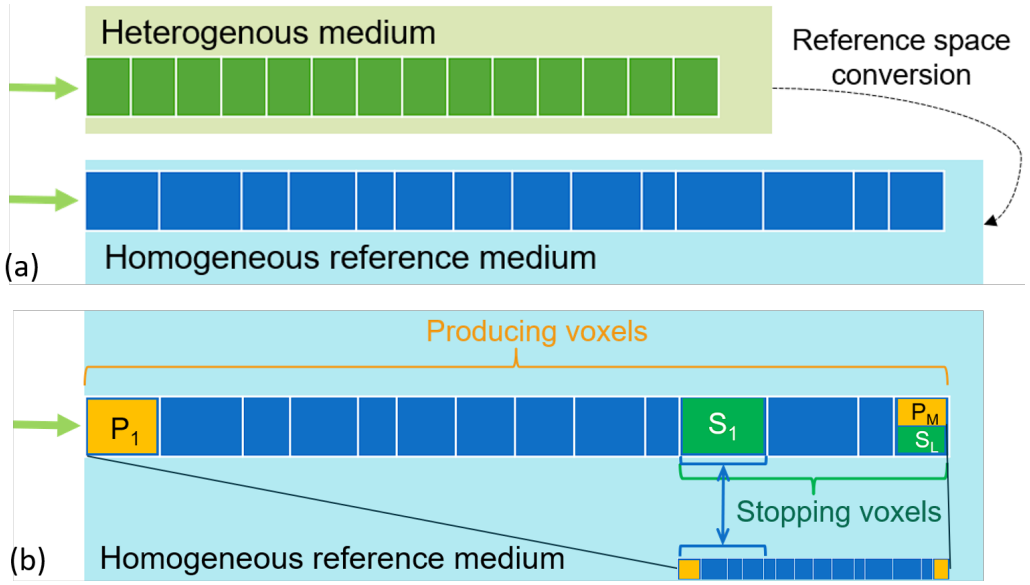

Figure 4.16: The upper figure of (a) shows a carbon ion beam shooting horizontally a heterogeneous medium and the voxels its central ray goes through. The path length of the traced ray in each voxel is converted into homogeneous reference space by Eq. (4.12). The regular voxels in heterogeneous medium are converted into homogeneous reference medium, with different lengths stretched to the estimated equivalent path lengths, as shown in the bottom figure of (a). (b) remains a consistent reference space conversion result with (a). Assuming the ion beam energy is the same as in Figure 4.15, the producing and stopping intervals remain the same, while the numbering of producing and stopping voxels changes. The central ray traverses voxels from P_1 to P_M and the generated projectile PEs stops in the voxels from S_1 to S_L. The mapping process follows the same principle as in Figure 4.15: the producing voxels are compressed to match the length of the stopping interval. Each subinterval of a stopping voxel is then sequentially matched with the subinterval of certain compressed producing voxels, ensuring equal lengths.

satisfies the following condition:

$$\forall m \in I, \sum_{s=1}^{k-1} l_{STOP,s} <= a \sum_{p=1}^{m} l_{PROD,p} < \sum_{s=1}^{k} l_{STOP,s} \tag{4.15}$$

where a is the ratio between the length of stopping interval to the one of producing interval in reference space, equal to K/N, the ratio between the number of stopping voxels and the number of producing voxels in a homogeneous reference medium, as shown in Figure 4.15. By repeating the above process for all subintervals of each stopping voxel, the mapping relationship between stopping voxels and producing voxels is established.

The mapping associates each stopping voxel with corresponding producing voxels in the

heterogeneous space, with the projectile PEs in a stopping voxel equal to the sum of the projectile PEs from the mapped producing voxels. For example, the projectile PED via the interactions with target nucleus j at the k-th stopping voxel, denoted as $\mathrm{PED}_{STOP,k,j}$, is estimated as the accumulation of projectile PED of its mapped producing voxels m from the same target nucleus j, denoted as $\mathrm{PED}_{PROD,m,j}$, as shown in the equation below:

$$\mathrm{PED}_{STOP,k,j} = \sum_{m \in I} \mathrm{PED}_{PROD,m,j} \tag{4.16}$$

where I is the numbering set of producing voxels mapped to the k-th stopping voxel. As the material effect on the production of PED is accounted by multiplying the local factor (4.4), we have:

$$\mathrm{PED}_{PROD,m,j} = g_{j,m}\, \mathrm{PED}^{*}_{PROD,m,j} \tag{4.17}$$

where $g_{j,m}$ is the g factor at the m-th producing voxel, which accounts for the amount of target nuclei j in the material of the m-th producing voxel relative to the reference material, and $\mathrm{PED}^{*}_{PROD,m,j}$ is the projectile PED that is expected to be produced from the target nucleus j at the m-th producing voxel transformed in the reference space. Substituting Eq. (4.17) into Eq. (4.16), we get:

$$\mathrm{PED}_{STOP,k,j} = \sum_{m \in I} g_{j,m}\, \mathrm{PED}^{*}_{PROD,m,j} \tag{4.18}$$

We introduce the scaling factor ζ for projectile PED at the k-th stopping voxel produced from the target nucleus j based on its definition:

$$\zeta_{j,k} = \frac{\mathrm{PED}_{STOP,k,j}}{\mathrm{PED}^{*}_{STOP,k,j}}, \tag{4.19}$$

where $\mathrm{PED}^{*}_{STOP,k,j}$ is the projectile PED produced from target nucleus j at the reference-material-equivalent depth of the k-th stopping voxel in reference medium. Given Eq. (4.18), Eq. (4.19) can be reformulated as:

$$\zeta_{j,k} = \frac{\sum_{m \in I} g_{j,m}\, \mathrm{PED}^{*}_{PROD,m,j}}{\mathrm{PED}^{*}_{STOP,k,j}}, \tag{4.20}$$

As we deduced previously the mapping relationship in the case of homogeneous reference medium shown in Figure 4.15, we have:

$$\mathrm{PED}^{*}_{STOP,k,j} = \sum_{m \in I'} \mathrm{PED}^{*}_{PROD,m,j} \tag{4.21}$$

where I' is the numbering set of producing voxels mapped to the stopping voxel in the case of homogeneous reference medium, with its quantity equal to N/K. Applying Eq. (4.21) to Eq. (4.20), we have:

$$\zeta_{j,k} = \frac{\sum_{m \in I} g_{j,m}\, \mathrm{PED}^{*}_{PROD,m,j}}{\sum_{m \in I'} \mathrm{PED}^{*}_{PROD,m,j}}, \tag{4.22}$$

Here we made an approximation that $\mathrm{PED}^{*}_{PROD,m,j}$ is constant for m in I and I' as the yields of projectile PEs across the nearby producing voxels in the homogeneous reference medium are close. Consequently, we can simplify Eq. (4.22) to:

$$\zeta_{j,k} = \frac{\sum_{m\in I} g_{j,m}\,\mathrm{PED}^{*}_{PROD,m,j}}{\sum_{m\in I'} \mathrm{PED}^{*}_{PROD,m,j}} \approx \frac{\sum_{m\in I} g_{j,m}}{N/K} = a\sum_{m\in I} g_{j,m}, \tag{4.23}$$

Equation (4.23) can be further generalized to any depth z where the projectile PED locates:

$$\zeta_j(z) = a\sum_{m\in I} g_{j,m} \tag{4.24}$$

with I the numbering set of producing voxels mapped to the voxel at depth z by Eq. (4.15).

A simple thought experiment shows how the ζ_j factor works for the stopping voxels filled with air: Because such a stopping voxel has negligible stopping power, hardly any producing voxels satisfy the mapping condition determined by Eq. (4.15) and the numbering set I is thus empty. As a result, $\zeta_j = 0$, and the predicted PED in this stopping voxel will be scaled to zero.

4.2.3 3D extension based on a PBA framework

A dedicated framework based on a PBA was developed to construct 3D PED, which is shown in Figure 4.17. This framework required a similar input structure to the PBA used by Soukup et al. [2005] for 3D dose computation, including IDPED, parametrization of the lateral properties of PED along the depth, and phantom and beam information.

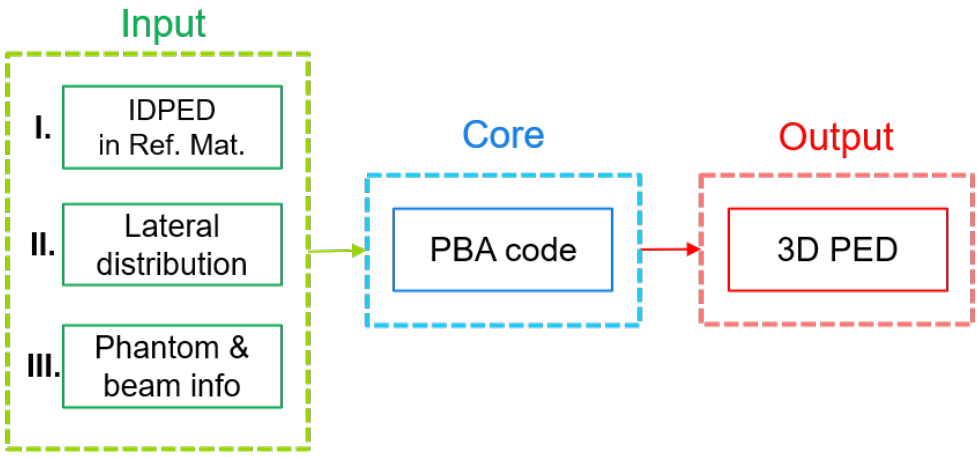

Figure 4.17: The computational framework for calculating 3D PED.

- IDPED was derived using analytical functions detailed in Section 4.2.2 combined with a filtering approach on IDD at corresponding energies in the reference material.

The parameters of these analytical functions were predefined using IDD and IDPED data from the MC simulations in the reference material described in Section 4.1. In a future practical applications within a TPS, the IDD in the reference material could be obtained from the 3D dose distribution per ion beam spot.

- Lateral properties of PED were parameterized by fitting the MC-calculated lateral distributions of PEs in the reference material along the penetration depth, using either a single Gaussian or double Gaussian function. Details of this parametrization will be provided in Section 4.2.3.
- Phantom information consist of mass density, electronic density, mass fractions of elements, and material mean excitation energy for each voxel. Beam information requires incident direction, position, energy, and beam spot size.
- The proposed PBA is able to deal with the longitudinal and lateral heterogeneities effects for PED. The methods for coping with the longitudinal heterogeneity is explained in detail in Section 4.2.2. The ray-casting method [Schaffner et al., 1999, Siggel et al., 2012] is used for dealing with lateral heterogeneity effects.

Parametrization of lateral distribution

The lateral PED is parameterized using Gaussian distributions, similar to the approach typically done for parametrization of dose distributions in particle therapy. A single Gaussian distribution given by

$$\mathrm{PED}(E,z,r) = \mathrm{IDPED}(E,z)\frac{1}{2\pi\sigma\left(E,z\right)^2}e^{-\frac{r^2}{2\sigma(E,z)^2}}, \tag{4.25}$$

where r is the radial distance to the beam central axis, was utilized to fit simulated projectile PED lateral profiles aiming to deduce the σ value along depth z, with a sampling resolution of 0.5 mm in depth. Figure 4.18 displays the fitting results against the simulated lateral PED in semi-logarithmic scale for projectile PEs using the single Gaussian function.

A double Gaussian parametrization method similar to the one proposed by Parodi et al. [2013] was adopted to better account for the lateral off-axis contributions of target PED. The double Gaussian distribution was defined by the following equation:

$$\mathrm{PED}(E,z,r) = \mathrm{IDPED}(E,z)\left(\frac{1-w\left(E,z\right)}{2\pi\sigma_1\left(E,z\right)^2}e^{-\frac{r^2}{2\sigma_1(E,z)^2}} + \frac{w\left(E,z\right)}{2\pi\sigma_2\left(E,z\right)^2}e^{-\frac{r^2}{2\sigma_2(E,z)^2}}\right) \tag{4.26}$$

where the σ_1 and σ_2 represent the narrow and broad Gaussian components with related weights $1-w$ and w, respectively.

The lateral PED data display fluctuations at larger radial distances, as exemplified in Figure 4.19 (b) and (e), owing to low statistics at large off-axis distances. To mitigate this, a threshold has been implemented, defining the fitting region to enclose 99.75% of the total area in the radius-weighted distribution $r \cdot \mathrm{PED}(E,z,r)$, to eliminate data points with significant fluctuation, similar to Parodi et al. [2013].

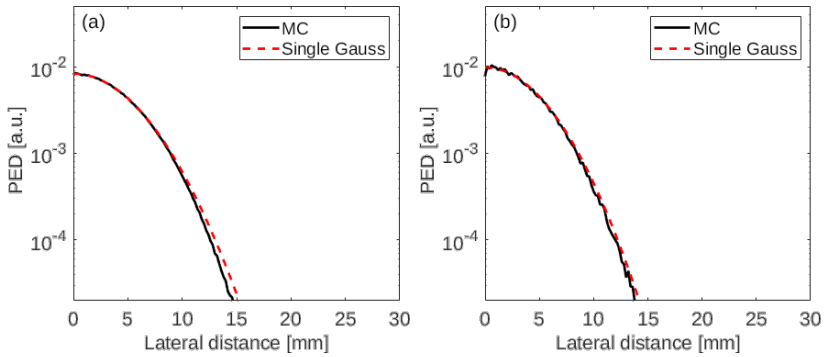

Figure 4.18: Example of MC simulated lateral PED of $^{11}C_{proj}$ (a), $^{10}C_{proj}$ (b) for carbon ion irradiation ($E = 250$ MeV/n, $\sigma_0 = 3$ mm) in reference material at depth of 8.5 cm shortly before the Bragg peak (located at ca. 9.3 cm) with corresponding single Gauss fit results.

The fitted area was normalized by IDPED values at the sampled depth. The resulting sigma parameters were corrected by quadratic subtraction of the initial beam width σ_0 as in Parodi et al. [2013]. In practice, the final sigma values are then obtained by quadratically adding the actual entrance beam width instead of the value of 3 mm used to build the reference data.

3D PED calculation

The distribution of a PE isotope in a voxel with its center coordinate (x, y, z) by a single pencil beam with initial energy E along the z-axis was determined by the following equation:

$$\mathrm{PED}(E, x, y, z) = \left(\sum_j \begin{cases} g_j(x, y, z) & \text{if target PE} \\ \zeta_j(x, y, z) & \text{if projectile PE} \end{cases} \mathrm{IDPED}_j(E, z_{ref,eq}) \right) \cdot G(E, z_{ref,eq}, r) \tag{4.27}$$

The factors g_j and ζ_j are defined by Eq. (4.4) and Eq. (4.24) for target and projectile PEs, respectively. Here a ray-casting technique [Schaffner et al., 1999] is used to derive the reference-material-equivalent depth $z_{ref,eq}$ by tracing a ray parallel to the beam central axis traversing the voxel and to simultaneously determine the mapping relationship for projectile PEs. IDPED is built by the analytical method presented in Section 4.2.2. The function G represents a single Gaussian term for projectile PEs and a double Gaussian term for target PEs with off-axis distance r.

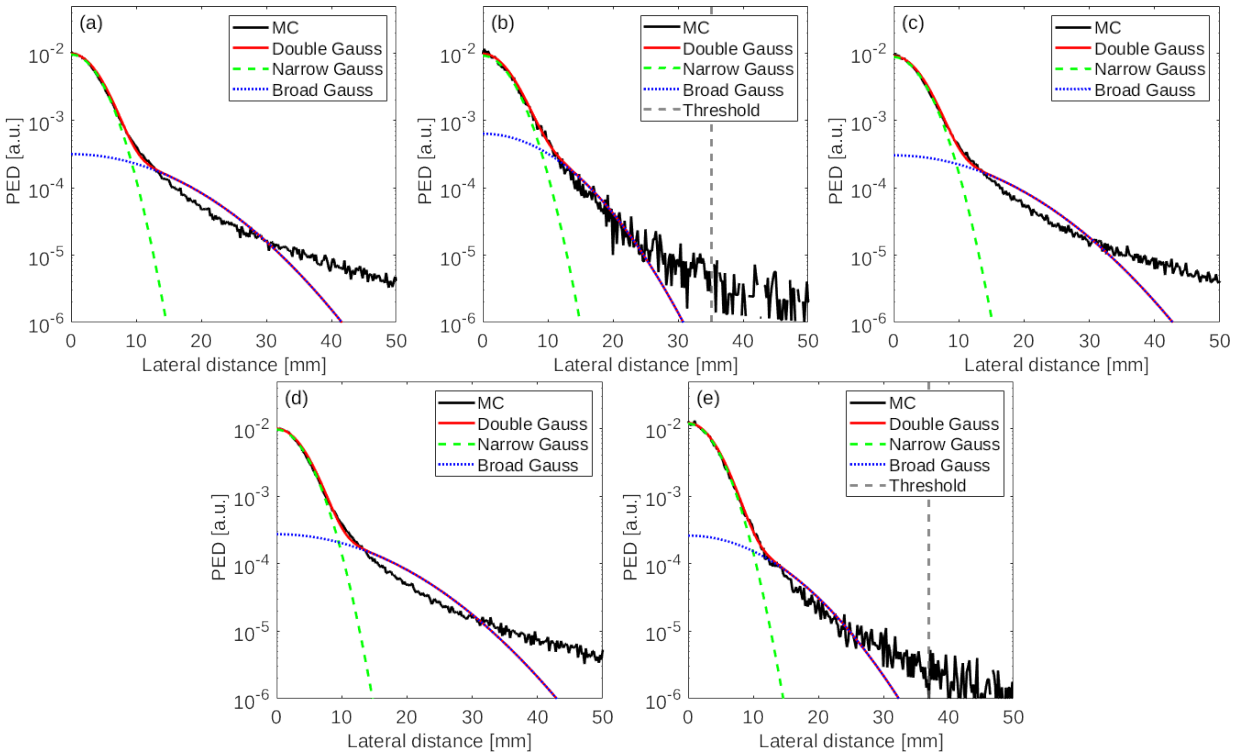

Figure 4.19: Example of simulated lateral PED of target PEs $^{11}C_{target}$ (a), $^{10}C_{target}$ (b), ^{15}O (c), ^{13}N (d), ^{14}O (e) for carbon ion irradiation ($E = 250$ MeV/n, $\sigma_0 = 3$ mm) in the reference material at a depth of 8.5 cm shortly before the Bragg peak (located at ca. 9.3 cm) with corresponding double Gauss fit. The vertical dashed line in (b) and (e) shows the threshold beyond which the right part is eliminated before fitting.

5

In-silico validation

This chapter presents two in-silico validation studies in which predictions from the analytical approach are compared with full blown MC simulations. The first validation, described in Section 5.1, uses mono-energetic carbon ion pencil beams incident on slab phantoms composed of carefully selected materials. Section 5.2 then examines a more realistic scenario in which several pencil beams extracted from four treatment plans hit geometries derived from the corresponding patient CT data. Although complete treatment plans are not considered in this section, this validation study incorporates realistic beams with momentum spectra and complex anatomical heterogeneities, thereby laying the groundwork for subsequent validation with complete treatment plans and the PET measured data. All simulations employed the same Geant4 version 10.07.p04, the QGSP_BIC physics list, and the isotope scoring described in Section 4.1.

5.1 Validation with slab phantoms

5.1.1 Slab-phantom design and beam configuration

Two slab phantoms filled with bone, brain, PMMA, water and reference material with their properties shown in Table 5.1 were employed to validate sequentially the longitudinal and lateral heterogeneity correction, as shown by mass density values in Figure 5.1. The chosen geometries have large longitudinal or lateral density gradient and distinguished element components in order to amplify the heterogeneity effects. Simulations were performed using single monoenergetic, mono-directional pencil beams hitting perpendicularly the phantom surface from left to right. The beams comprised 5×10^8 ions each, with an initial kinetic energy ranging from 100 MeV/n to 400 MeV/n and an initial Gaussian distribution with σ between 2 mm and 5 mm.

Table 5.1: Material properties of the investigated phantoms

Material	Reference	Brain	Bone	Water	PMMA
Mass density (g·cm^{-3})	1.54	1.04	1.85	1.00	1.19
Electron density (10^{23} cm^{-3})	4.71	3.45	5.91	3.34	3.87
Mass abundances					
Hydrogen (H)	2%	11%	6%	11%	8%
Carbon (C)	31%	15%	28%	-	60%
Nitrogen (N)	26%	2%	3%	-	-
Oxygen (O)	38%	71%	41%	89%	32%
Phosphorus (P)	1%	-	7%	-	-
Calcium (Ca)	3%	-	15%	-	-

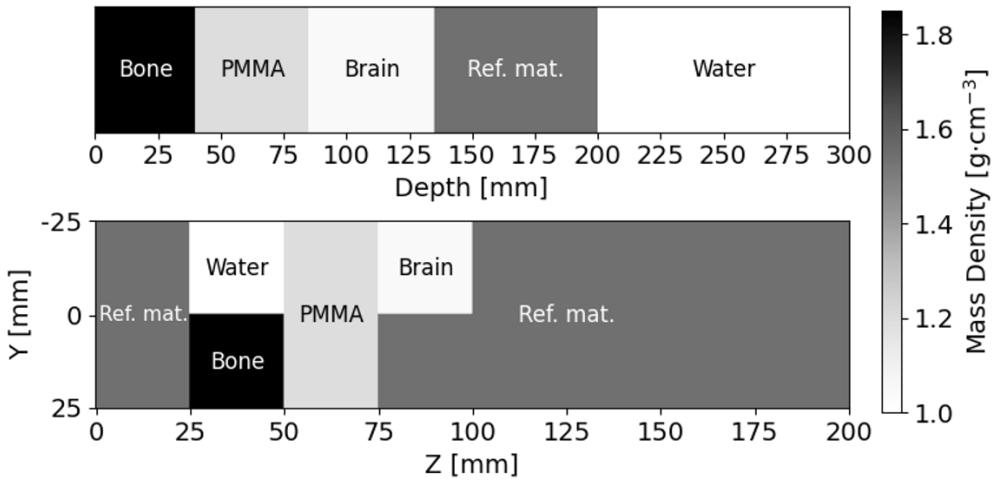

Figure 5.1: A 3D phantom with 1D longitudinal heterogeneities (top), filled with materials of strongly varying compositions, was used to validate the effects of longitudinal heterogeneity on PED, and a 3D phantom composed of different materials with both lateral (y-axis) and longitudinal (z-axis) heterogeneities (bottom) was used to validate the lateral heterogeneity effect on PED.

5.1.2 Analytical and MC PED comparison in slab phantoms

Figure 5.2 shows the IDPEDs for $^{11}C_{target}$ and $^{11}C_{proj}$ from the interactions of a carbon ion beam at 300 MeV/n with different target nuclei in the slab phantom shown in Figure 5.1 (top), as calculated by MC simulation and analytical prediction. The differences between total analytical and simulated IDPEDs for $^{11}C_{target}$ and $^{11}C_{proj}$ were quantified using the normalized root-mean-square error (NRMSE), which yielded 2.77% and 3.61%, respectively. These values were normalized to the difference between the maximum and minimum of the

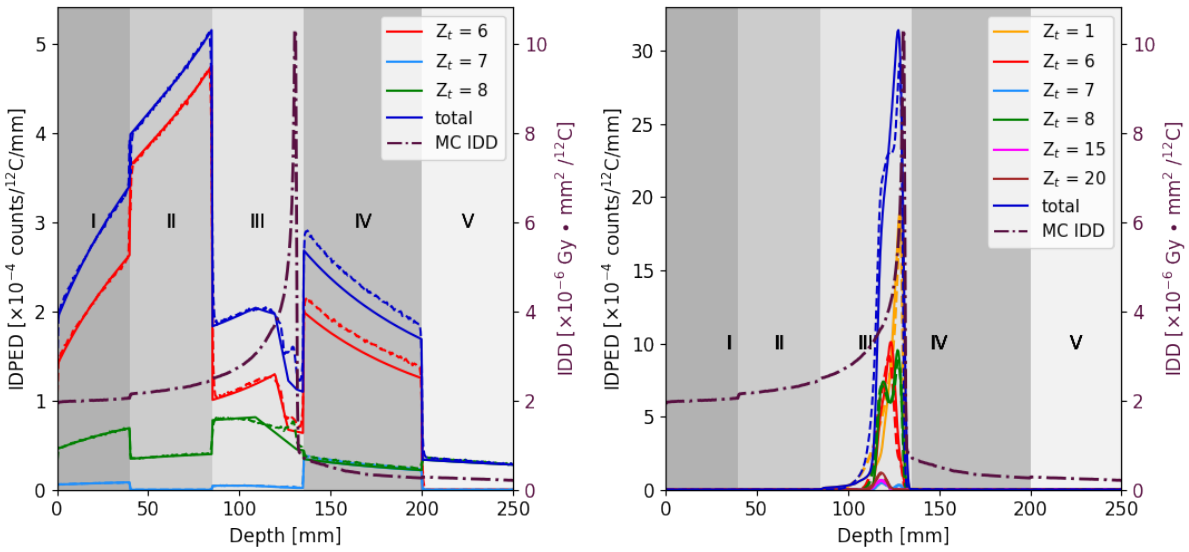

Figure 5.2: IDPEDs for $^{11}C_{target}$ (left) and $^{11}C_{proj}$ (right) from a ^{12}C ion beam at 300 MeV/n impinging on the phantom shown in Figure 5.1 (top) (I: bone, II: PMMA, III: brain, IV: reference material, V: water), calculated by MC simulation and analytical prediction shown in dash and solid lines, respectively. IDPEDs from different target nuclei and total IDPEDs are shown in different colors. The MC simulated IDDs are shown by dash-dotted lines.

MC simulated IDPEDs. In the left figure, the build-up part of the IDPED for $^{11}C_{target}$ locates at regions I, II, and III with the analytical and simulation results closely aligning. The tails of IDPED appear in the end of region III and subsequent regions. In region IV, the analytically predicted IDPED of carbon target nuclei (red solid lines) is lower than the simulated one. This discrepancy was introduced by the modeling function, Eq. (4.10), and can also be observed in Figure 4.12 at the analytical tail profile of the data for the initial 300 MeV/n beam energy. The right figure displays the IDPED profiles for $^{11}C_{proj}$ generated from the six target nuclei in the phantom. The IDPED of hydrogen target nucleus (in orange), predicted using a Landau distribution as the modeling function, is sufficiently close to the simulation results in both the distal fall-off position and the amplitude, with a NRMSE of 3.51%. In particular, the profile of oxygen as the target nucleus (in green) has a double peak, illustrating the impact of heterogeneity on projectile PEs. As discussed in Section 4.2.2, the distribution of projectile PEs is influenced by both the material at its generation locations and the materials it traverses. Thus, the overall heterogeneity of regions I, II, and III results in its double peak even though the IDPED is located in the homogeneous region III. The analytical predictions employing the proposed ζ factor, Eq. (4.24), closely match the simulation results, with an NRMSE of 3.61% for the total $^{11}C_{proj}$ yield.

Figure 5.3 illustrates the total IDPEDs for all the PEs considered from a carbon ion beam at 100, 200, 300 and 400 MeV/n in the 1D heterogeneous slab phantom determined by MC simulation and analytical prediction. The respective NRMSE values were 2.14%, 3.82%, 2.91%, and 2.33%, indicating good agreement between the analytical and simulated IDPEDs across different energies in the heterogeneous phantom. This consistency suggests the effectiveness of the IDPED modeling and the longitudinal heterogeneity correction. The range of the different beams was estimated from the distal position of the 80% PED level (R80), as shown in Table 5.2. The submillimeter shifts between the MC and analytical IDPED predictions highlight the accuracy of the modeling also in longitudinally heterogeneous media.

Table 5.2: R80 values for the MC and analytical IDPEDs shown in Figure 5.3, along with their relative shifts between MC simulations and analytical predictions. R80 was determined after applying linear interpolation to achieve a refined bin size of 0.01 mm. The error of R80 was estimated by combining contributions from the refined bin size and the error introduced by linear interpolation, which arises from the curvature of the original depth-IDPED curve between data points.

Energy [MeV/n]	100	200	300	400
$R80_{MC}$ [mm]	14.00 ± 0.01	52.87 ± 0.01	129.63 ± 0.02	199.96 ± 0.06
$R80_{Analytical}$ [mm]	14.04 ± 0.01	53.65 ± 0.02	129.61 ± 0.02	199.97 ± 0.05
Shift [mm]	0.04 ± 0.01	0.78 ± 0.02	-0.02 ± 0.03	0.01 ± 0.08

Figure 5.4 presents the two-dimensional PED for carbon ion beams with four different initial σ values at different impinging kinetic energies in the presence of lateral heterogeneity. The accuracy of analytical predictions compared to simulation results was assessed using global gamma index analysis with 10% maximum threshold, employing the 2%/2 mm and 1%/1 mm criteria. The passing rates of the 2%/2 mm criteria were 99.40%, 99.19%, 98.61% and 94.24% for energies from low to high, respectively. For the stricter 1%/1 mm criteria, they were 92.46%, 93.95%, 93.38% and 84.29%, respectively. The overall high passing rates underline the efficacy of the 3D PED prediction method, which utilizes the ray-casting technique to address lateral heterogeneity. Noticeable differences are observed in the distal region of the PED, particularly for the cases of 300 and 400 MeV/n: here the analytical results show clearer boundaries at beam center, while simulation results do not. This is because particles undergo scattering, causing blurring at the lateral edges, whereas the ray-casting method can only consider heterogeneity in a straight-line propagation manner, making the edges clearer [Schaffner et al., 1999]. Nevertheless, considering that heavy ions exhibit relatively minor scattering, the deviations introduced by the ray-casting method are deemed to be acceptable.

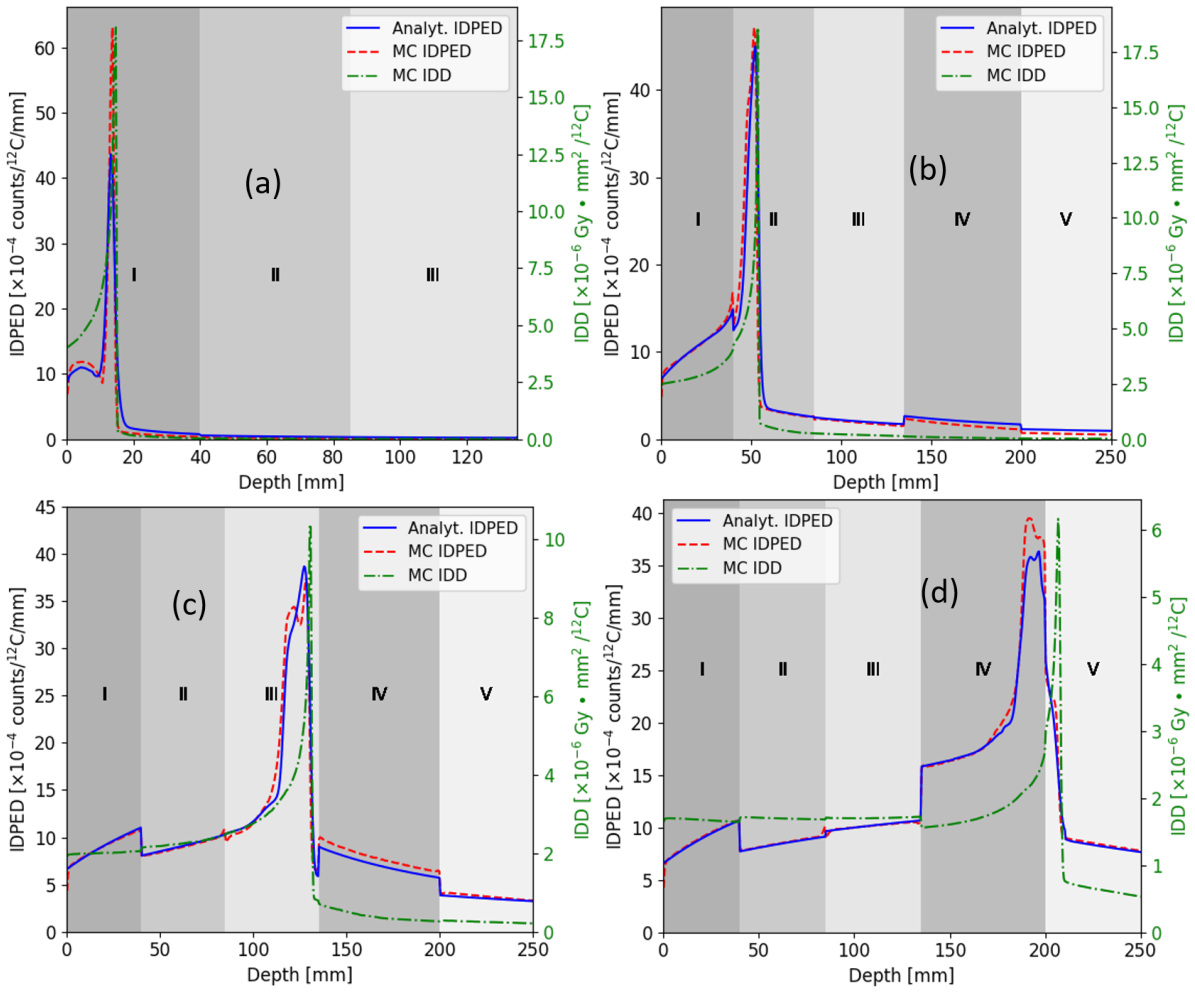

Figure 5.3: IDPEDs for total PEs from a ^{12}C ion beam at 100 MeV/n (a), 200 MeV/n (b), 300 MeV/n (c) and 400 MeV/n (d) hitting the slab phantom shown in Figure 5.1 (top) (I: bone, II: PMMA, III: brain, IV: reference material, V: water), calculated by MC simulation and analytical prediction shown in red dashed and blue solid lines, respectively. The MC simulated IDD are shown by dash-dotted lines.

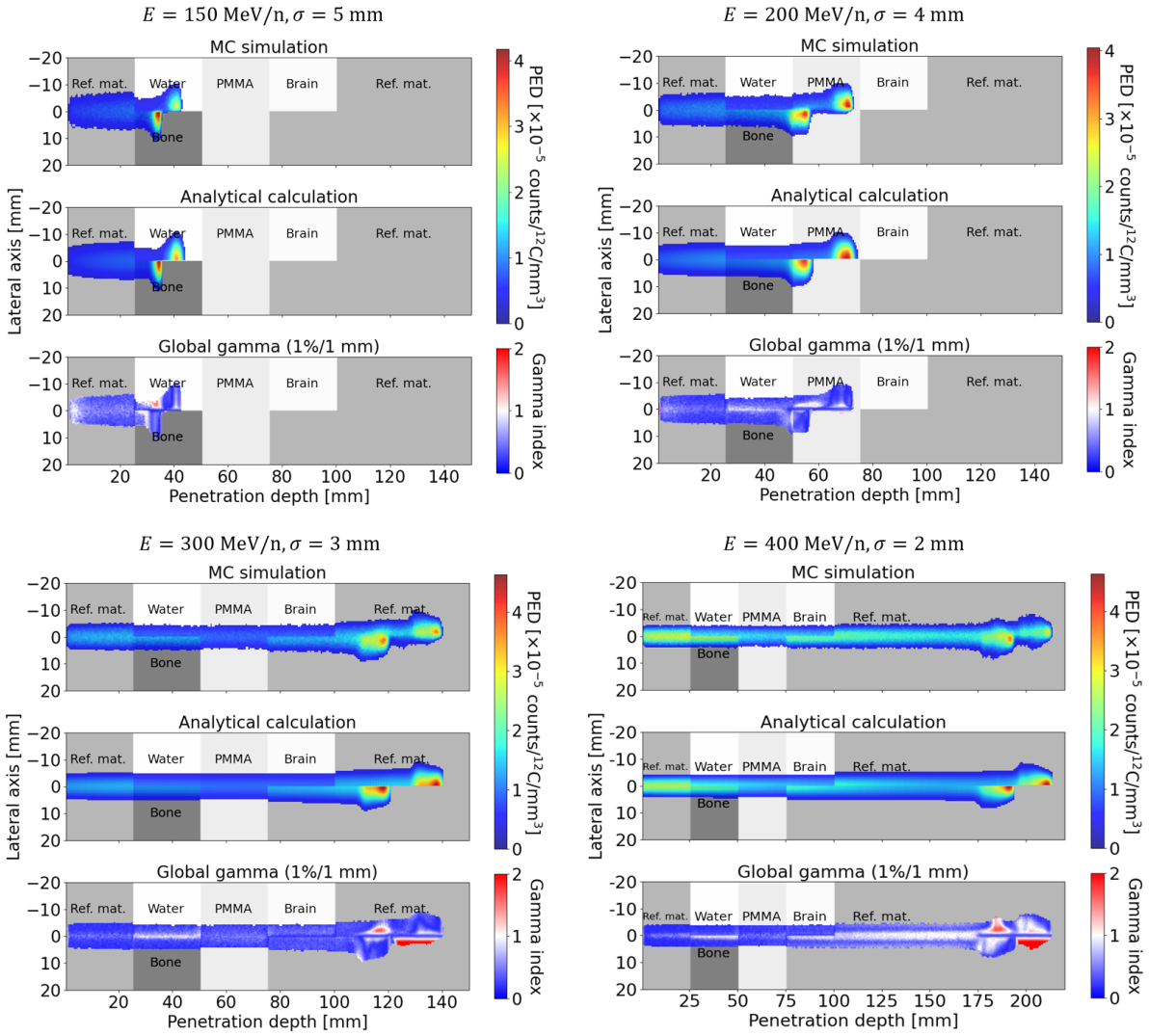

Figure 5.4: Total PED for a Gaussian ^{12}C ion beam with σ = 5 mm at 150 MeV/n (left top), σ = 4 mm at 200 MeV/n (right top), σ = 3 mm at 300 MeV/n (left bottom), σ = 2 mm at 400 MeV/n (right bottom), hitting the 3D heterogeneous phantom shown in Figure5.1 (bottom). Each subfigure shows 2D PED calculated by MC simulation and the analytical method, with rainbow wash representation for the PED and a blue-white-red gradient colormap with gamma index map (using 1%/1 mm criteria), both overlaid on the grayscale representation of the phantom.

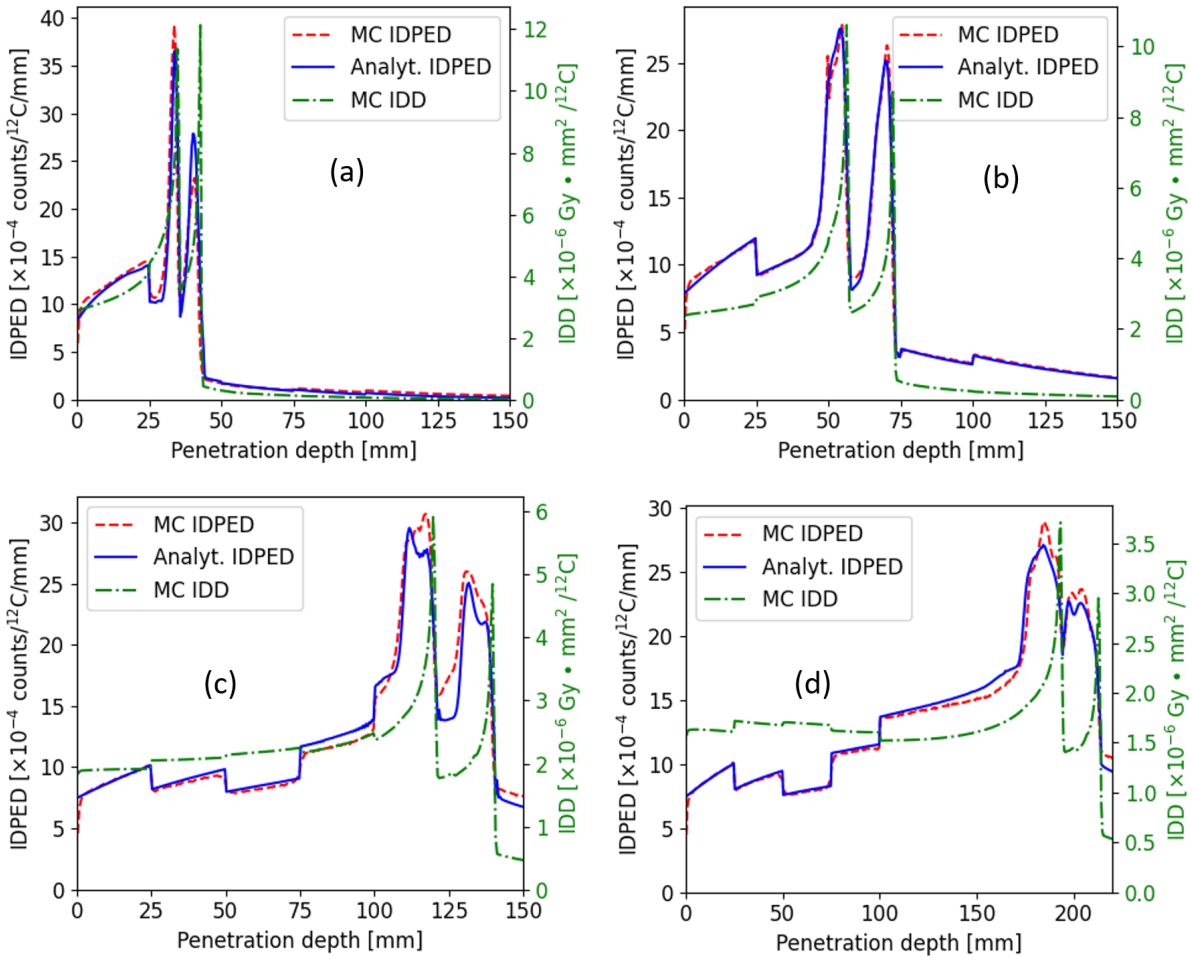

Figure 5.5: (a-d) show IDPEDs of the four cases of Figure 5.4 for initial beam energies of 150, 200, 300 and 400 MeV/n and different initial σ values, respectively. The MC simulated IDPEDs are shown in dashed red lines, while analytical IDPEDs are depicted by solid blue lines. The MC simulated IDDs are displayed with dash-dotted green lines.

Figure 5.5 depicts the simulated and analytical IDPEDs, along with the simulated IDDs. The double peaks observed correspond to the mixed range of the laterally varying maximum penetration of the beam in the heterogeneous phantom, as visible in Figure 5.4. The R80 values of both peaks of the IDPEDs were determined for range assessment, as detailed in Table 5.3, showing submillimeter shifts between MC simulations and analytical predictions for all cases.

Table 5.3: R80 values of the double peaks of the MC and analytical IDPEDs shown in Figure 5.5, along with their relative shifts between MC simulations and analytical predictions. R80 values and their errors were determined by the same method described in Table 5.2.

Energy [MeV/n]	150		200	
	Peak 1	Peak 2	Peak 1	Peak 2
$R80_{MC}$ [mm]	34.41 ± 0.02	41.57 ± 0.03	55.71 ± 0.03	71.46 ± 0.02
$R80_{Analytical}$ [mm]	34.78 ± 0.05	41.62 ± 0.01	55.85 ± 0.01	71.45 ± 0.01
Shift [mm]	0.37 ± 0.05	0.05 ± 0.03	0.16 ± 0.03	-0.01 ± 0.02
Energy [MeV/n]	300		400	
	Peak 1	Peak 2	Peak 1	Peak 2
$R80_{MC}$ [mm]	119.42 ± 0.01	138.44 ± 0.05	192.77 ± 0.02	211.46 ± 0.08
$R80_{Analytical}$ [mm]	119.41 ± 0.02	138.66 ± 0.03	193.50 ± 0.46	211.67 ± 0.02
Shift [mm]	-0.01 ± 0.02	0.22 ± 0.06	0.72 ± 0.46	0.21 ± 0.08

Figure 5.6 depicts normalized lateral profiles of the total PED reported in Figure 5.4 at varying depths, calculated with MC simulations and the analytical method. The y-axis is scaled logarithmically. Generally, the curves exhibit a good match. At shallower depths, the total PED consists only of target PED, and the lateral distribution of target PED is represented by a combination of narrow and broad Gaussian components, as shown in Eq. (4.26). It can be seen in profiles at these shallower depths (in red and green), particularly in Figure 5.6(b-d), that the distribution at the center was formed by the narrow Gaussian, with a small contribution at the lateral off-axis location described by the broad Gaussian. The lateral profiles at depths with lateral heterogeneity (in green) show varying amplitudes on either side as a result of the heterogeneity. The profiles at distal depths (in blue or in green for Figure 5.6(a)) correspond to the locations of the second peaks in Figure 5.5, having the main contribution from projectile PED. The main differences are near the beam center, where MC profiles show a smooth transition, while the analytical one has a distinct falloff. This difference mirrors the explanation for discrepancies in the distal region shown in Figure 5.4.

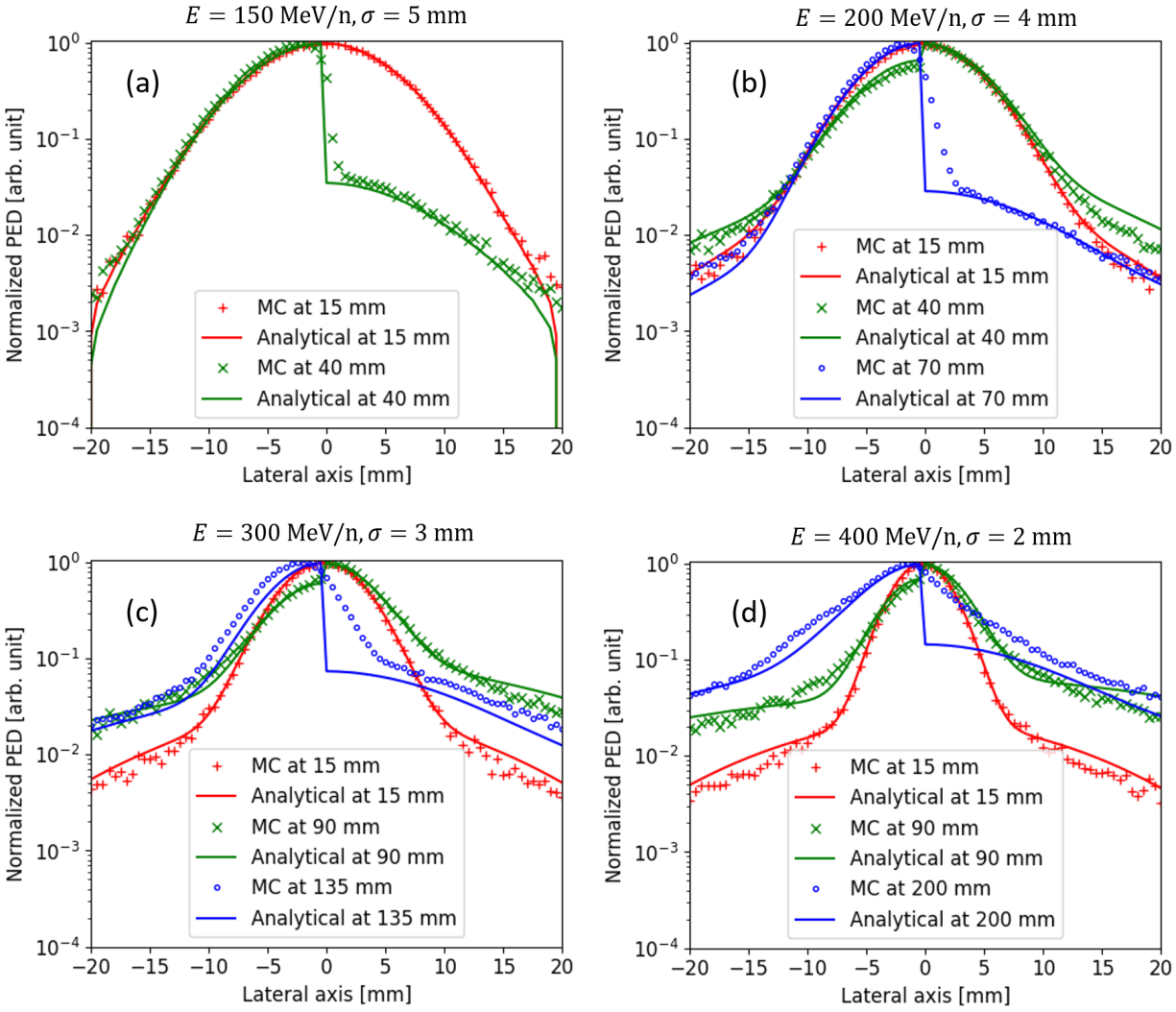

Figure 5.6: (a-d) show normalized lateral profiles of PED on a semi-logarithmic scale for the four cases depicted in Figure 5.4 at initial kinetic beam energies of 150, 200, 300 and 400 MeV/n and different initial sigmas, respectively, with semi-logarithmic scale for improved display. The profiles were obtained at 15 mm, corresponding to the reference material region at the beginning, at 40 mm in (a, b) and 90 mm in (c, d) with lateral inhomogeneity, and at 70 mm in (b), 130 mm in (c) and 200 mm in (d) for the distal depth. For (a), the profile at 40 mm represents both the depth with lateral inhomogeneity and the distal depth.

5.2 Validation with patient CT data derived geometries

5.2.1 Geometry generation and beam modeling using phase space

Four representative beam spots from HIT treatment plans for indications of brain, neck, liver, and sacrum tumors [Bauer et al., 2013, 2014] were simulated using the corresponding patient CT data, covering nominal ^{12}C ion beam energies of 170–370 MeV/n and FWHM spot sizes of 5–10 mm in air at isocenter. The input patient geometry properties including the tissue mass densities and elemental composition weights were deduced from HU based on the conversion approach proposed by [Schneider et al., 2000, Parodi et al., 2007c] and the mean excitation energy of tissue was determined internally by Geant4. Simulations were performed based on the spots settings in the treatment plans with 2.5×10^8 ions per spot.

For consistency to the treatment plans performed at HIT, the modeling of the beam delivery follows the one described in [Parodi et al., 2010] with the detailed beamline model of Parodi et al. [2013]. Due to confidential issues with their beamline geometry, an explicit implementation of the beam model is not available for external users. To provide a solution for this problem, Tessonnier et al. [2016] created phase space files containing the characteristics (charge, mass, energy, coordinates and direction cosines) of every particles (primary carbon ions and secondaries) at the end of the beamline, for each of the available initial beam energies. In this work, those phase space files were applied to sample primary carbon ions event-by-event, thereby preserving the beam delivery model behavior and intrinsic momentum spread of beam spots. The following parts detail how the phase space files are integrated into the Geant4 code.

Figure 5.7 shows the schematic of the beamline with the vacuum window, the Beam and Application Monitoring System (BAMS), composed of two multiwire proportional chambers and three ionization chambers that are monitoring the beam, and the ripple filter used to broaden the narrow Bragg peaks of carbon ions. The carbon ion beam initial size in vacuum can be 2.5, 5, 7.5, and 9.5 mm (FWHM), reflecting four different foci used at HIT. The phase space was calculated for an infinitely narrow ("zero-width") beam propagating through the beamline and the scoring plane was defined at a plane perpendicular to the beam direction after the ripple filter (about 102 cm upstream the isocenter). It should be noted that the beamline configuration illustrated in [Tessonnier et al., 2016] did not include a ripple filter, and in that case the phase space was scored at the exit of the BAMS, about 112 cm upstream of the isocenter. However, in the clinical application of carbon ions at HIT a ripple filter was present in the beamline, and Tessonnier et al. [2016] also generated phase-space data including the ripple filter. The latter configuration was adopted in this work.

In order to perform MC transport of the pencil beam ions from a treatment plan using the phase space, the following steps are performed:

1. Extract the information of the beam spot to be simulated from the treatment plan

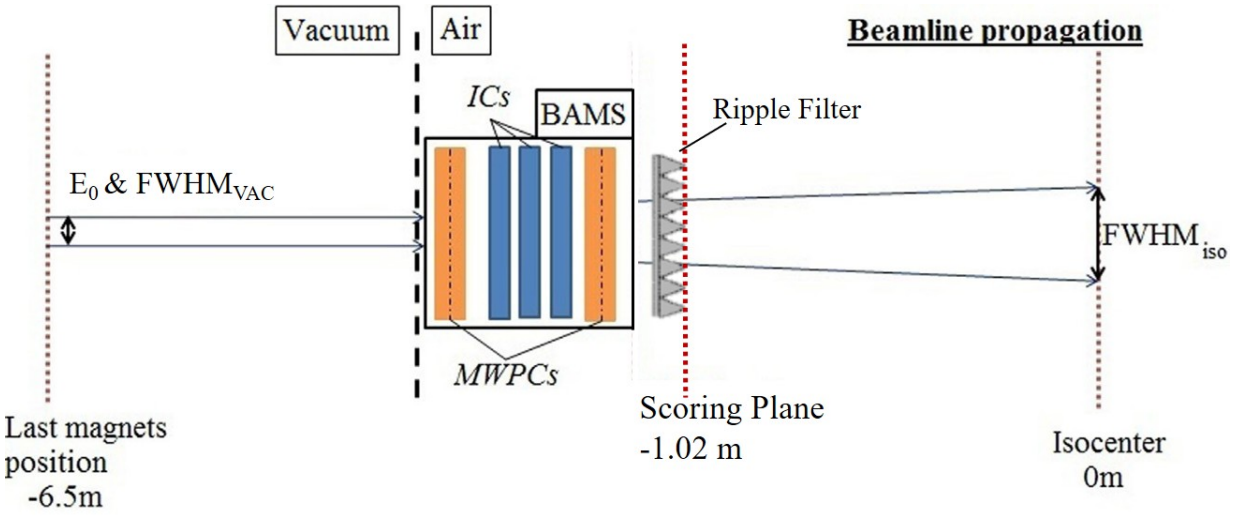

Figure 5.7: Schematic of the HIT beamline for a beam with an initial energy E_0 and an initial focus FWHM_{vac}. Figure adapted from [Tessonnier et al., 2016]

including the beam size at isocenter, the nominal energy, the planned position at isocenter $(X'_{\mathrm{iso}}, Y'_{\mathrm{iso}})$. Although the beam initial size in vacuum is not given explicitly in the treatment plan, it can be inferred from the beam size at isocenter based on a foci table provided by HIT.

2. Read the phase space file (only for the primaries) of the current energy and select randomly a certain amount of primaries data which will be handled as the primary history to be read sequentially, one per event.

3. For each primary loaded from the primary history, the PS coordinates $\left(X_{\mathrm{PS}}, Y_{\mathrm{PS}}\right)$ are read. These coordinates are then added to, respectively, two distinct positions $(X_{\mathrm{Vac}}, Y_{\mathrm{Vac}})$ randomly sampled from a Gaussian distribution with the FWHM size corresponding to the expected Gaussian size of the beam in vacuum for the selected focus (see the left panel of Figure 5.8), to obtain the final position of the particle to be transported:
$$(X_{\mathrm{Plane}}, Y_{\mathrm{Plane}}) = (X_{\mathrm{PS}} + X_{\mathrm{Vac}},\ Y_{\mathrm{PS}} + Y_{\mathrm{Vac}}).$$

4. To direct the particle towards the chosen spot, the entire phase–space distribution is rotated from the central-axis reference $(X_{\mathrm{iso}}, Y_{\mathrm{iso}})$ to the new coordinates $(X'_{\mathrm{iso}}, Y'_{\mathrm{iso}})$. This transformation yields updated exit coordinates $(X'_{\mathrm{Plane}}, Y'_{\mathrm{Plane}})$ and new direction cosines $\mathbf{d}'$, ensuring that the particle targets the planned position on the isocenter plane (see the right panel of Figure 5.8).

The above procedure generates the particle positions and directions in the IEC GANTRY coordinate system (see Figure 5.9(a)), whose origin is located at the isocenter. Because the patient representations are constructed from the CT data defined in a DICOM patient-based

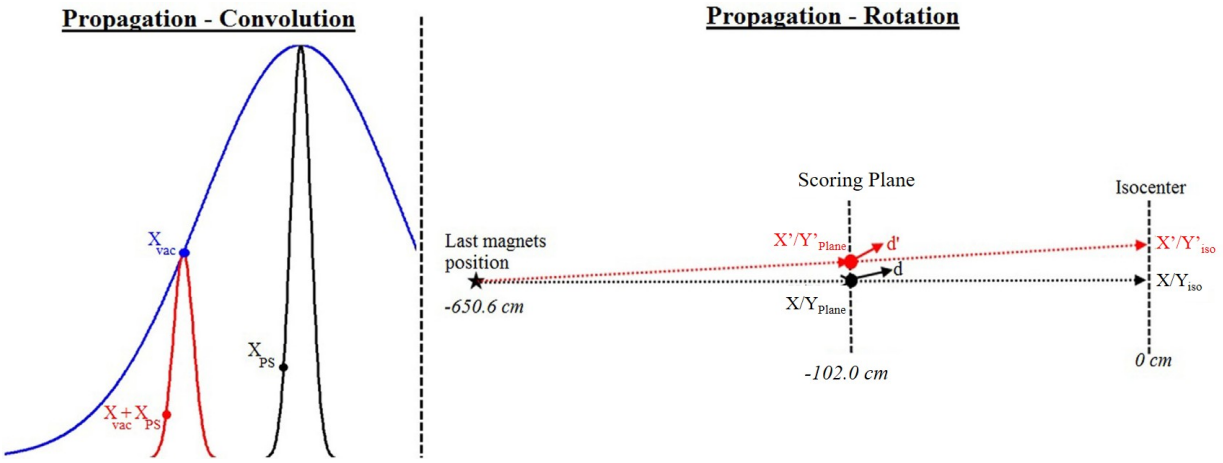

Figure 5.8: Propagation process. Left panel: the new position $X_{\text{Plane}}/Y_{\text{Plane}}$ (shown in red) is obtained by adding the original position on the phase space $X_{\text{PS}}/Y_{\text{PS}}$ (shown in black) to the selected position on the Gaussian in vacuum $X_{\text{Vac}}/Y_{\text{Vac}}$ (shown in blue); Right panel: rotation of the beam to the expected position $X'_{\text{iso}}/Y'_{\text{iso}}$ at isocenter. This is achieved by transforming the $X_{\text{Plane}}/Y_{\text{Plane}}$ position on the scoring plane with a direction cosine $\mathbf{d}$ to the new $X'_{\text{Plane}}/Y'_{\text{Plane}}$ position on the scoring plane with the direction cosines $\mathbf{d}'$ in order to reach the $X'_{\text{iso}}/Y'_{\text{iso}}$ position at isocenter. Figure adapted from [Tessonnier et al., 2016].

coordinate system, it is needed to perform a conversion of the two different coordinate systems to align beam sources and the patient CT. Figure 5.9 illustrates three IEC coordinate systems and their relationships.

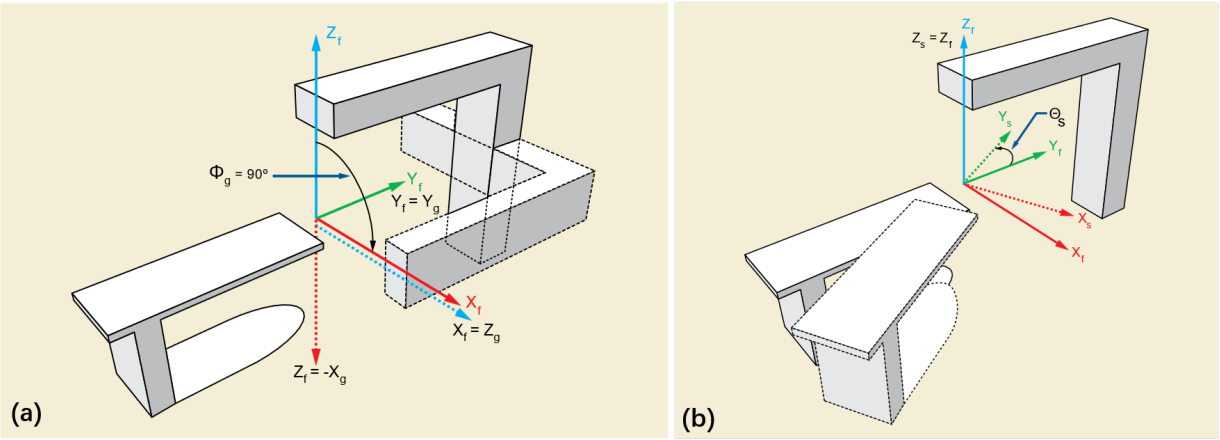

Figure 5.9: IEC FIXED (f), GANTRY (g) and PATIENT SUPPORT (s) coordinate systems for a horizontal fixed beam-line, with the X, Y, Z axes shown red, green, and blue, respectively. Figure from [NEMA, 2009].

- The Y-axis of both IEC FIXED and IEC GANTRY points towards the gantry bearing,

and the Z-axis in IEC FIXED is always pointing upwards. With Y and Z-axes defined, the X-axis of IEC FIXED is also given.

- The IEC GANTRY system is obtained by rotating the IEC FIXED about its Y-axis by the "gantry angle" Φ_g (right-hand convention) (see Figure 5.9(a)).
- The IEC PATIENT SUPPORT is obtained by rotating the IEC FIXED around its Z-axis by the "patient support angle" Θ_s (right-hand convention) (see Figure 5.9(b)).

Both Φ_g and Θ_s are provided in the treatment plan files. As IEC GANTRY and IEC PATIENT SUPPORT share IEC FIXED as their common parent system, their transformations can be linked and built through IEC FIXED. Figure 5.10 shows how the the

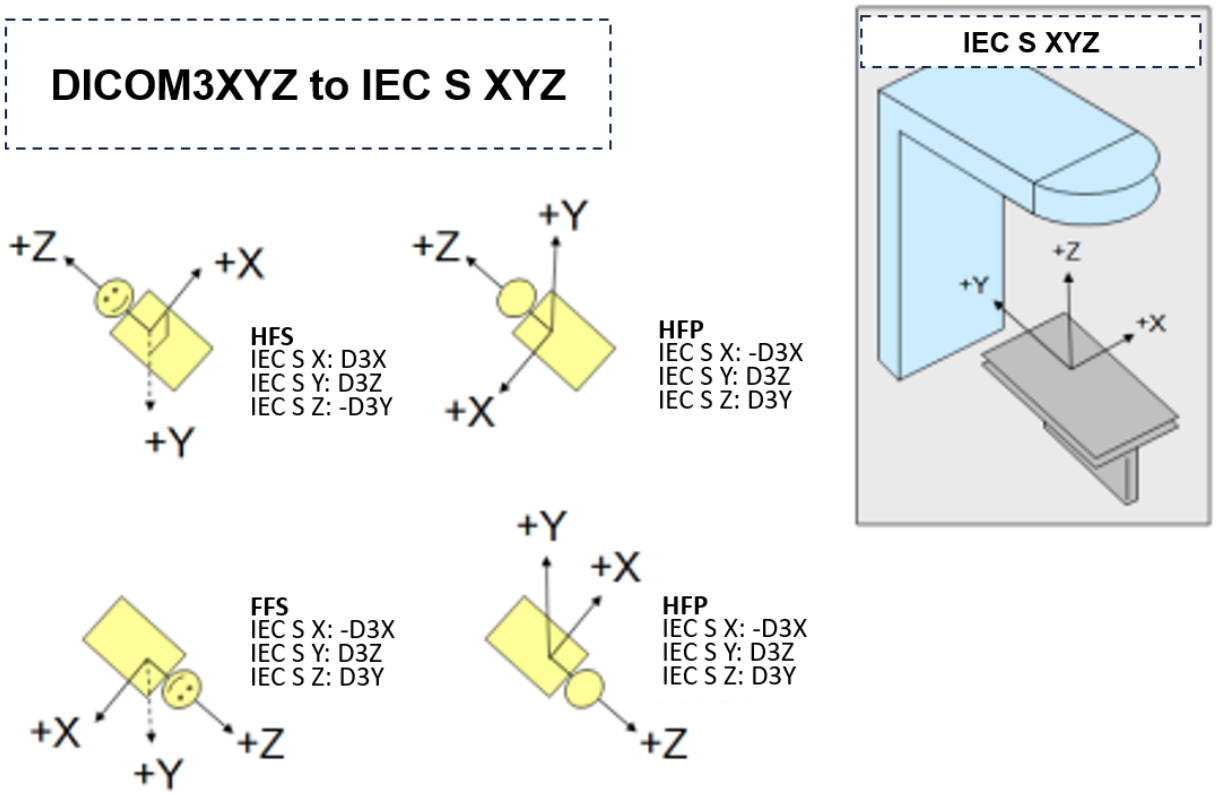

Figure 5.10: The relationships between the IEC S (PATIENT SUPPORT) system and DICOM patient coordinate systems with different patient orientations. Figure adapted from [Dec, 2021].

DICOM patient coordinate system relates to the IEC PATIENT SUPPORT system. The required transformation depends on the patient orientation. For example, when the patient orientation is HFS (Head First Supine: The patient is lying flat on their back, facing up, with the head positioned toward the front of the equipment.), the IEC PATIENT SUPPORT system must be rotated by $-90°$ about its X-axis (the right-hand rule) to align its axes with

those of the DICOM system. In addition, the origin of the DICOM system may differ from the isocenter which is specified in the DICOM coordinate system, thus a corresponding translation of the origin is also needed to complete the conversion from IEC PATIENT SUPPORT to DICOM patient system.

An additional conversion step may be necessary, depending on how the phantom is implemented in the code. For example, the code may set the upper-left voxel of the first CT slice as the origin of its coordinate system, or it may place its origin at the geometric center of the phantom; the internal X, Y, and Z axes may differ from the DICOM patient system. Consequently, an adjustment from the DICOM patient system to the coordinate system defined by the code is usually required. Fortunately, the CT DICOM dataset provides all the information needed for this task: the isocenter coordinates, the first-corner position, the CT image orientation vectors, the voxel size, and the number of voxels. Using these parameters, one can compute the required translation and rotation to align the DICOM system with the phantom coordinate system used by the code.

After completing the coordinate system conversion described above, the beam sources and the corresponding patient CT are co-registered in a common coordinate system. With this prerequisite satisfied, it is possible to run the MC simulations for individual beam spot from a treatment plan on the patient CT. The same procedure will be employed in the next chapter, where full treatment plan simulations are performed.

5.2.2 Analytical and MC PED comparison in anatomical geometries

Figure 5.11(a-d) shows PED for four beam spots extracted from HIT treatment plans [Bauer et al., 2013, 2014] for tumor locations in the brain, neck, liver, and sacrum, respectively, calculated by MC simulation and the analytical approach. The nominal energies of the four beam spots are approximately 190 MeV/n, 170 MeV/n, 260 MeV/n, and 370 MeV/n, respectively, with their beam sizes (expressed as full width at half maximum, FWHM) around 5 mm, 7 mm and 10 mm in the latter two cases, respectively. The comparison between simulated and analytical PED was done by global gamma index analysis with 1% maximum threshold (as suggested by Kraan et al. [2024a] to include more valid voxels), using the 2%/2 mm and 1%/1 mm criteria. The gamma index map using 1%/1 mm criteria is depicted in the third column of Figure 5.11 for a selected slice. Across all cases, the largest PED discrepancies were found in the distal regions of the gamma index map, which correspond to the locations around the PED peak. The passing rates for the 2%/2 mm criteria were 99.97%, 100%, 99.87% and 99.92% respectively. For the stricter 1%/1 mm criteria, they were 98.96%, 99.61%, 96.25% and 97.82%, respectively. The high passing rates for both the 2%/2 mm and the stricter 1%/1 mm criteria demonstrate good agreement between the simulated results and predictions.

Figure 5.12 shows the IDPEDs and IDDs of the four beam spots calculated by integrating the 3D PED perpendicular to their incident directions. The R80 values for the MC and analytical IDPEDs, exhibiting shifts below 1 mm, are shown in Table 5.4.

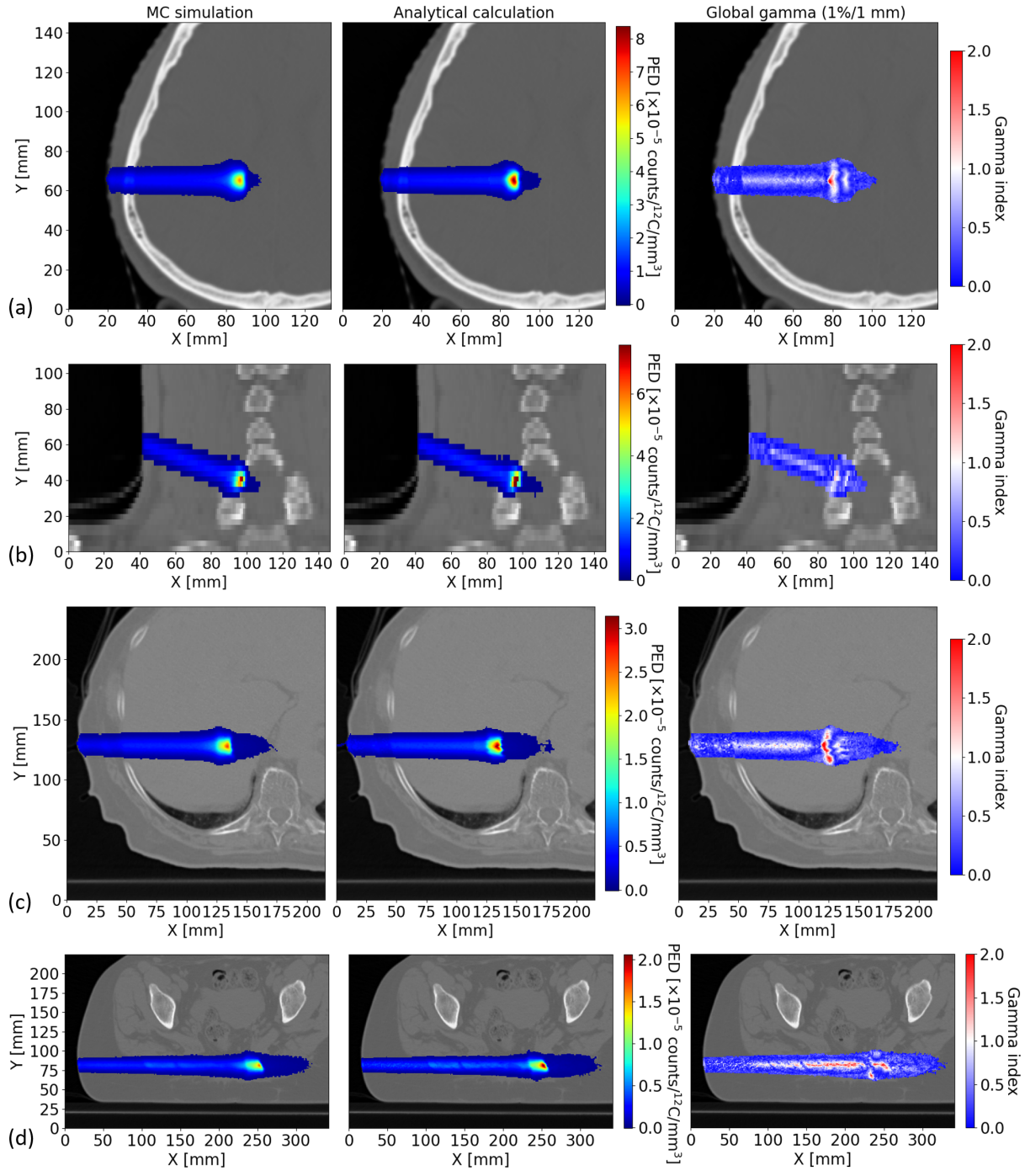

Figure 5.11: (a-d) display PED of four beam spots extracted from treatment plans for tumors located in the brain, neck, liver, and sacrum, respectively, calculated by MC simulation (left) and the analytical method (middle), along with gamma index maps (right), using 1%/1 mm criteria, overlaid on the correspondent planning CT images.

Table 5.4: R80 values for the MC and analytical IDPEDs shown in Figure 5.12, along with their relative shifts between MC simulations and analytical predictions. R80 values and their errors were determined by the same method described in Table 5.2.

Cases	Brain	Neck	Liver	Sacrum
$R80_{MC}$ [mm]	70.71 ± 0.01	62.02 ± 0.01	129.14 ± 0.01	238.04 ± 0.01
$R80_{Analytical}$ [mm]	70.57 ± 0.01	62.09 ± 0.01	129.51± 0.01	238.82 ± 0.02
Shift [mm]	-0.14 ± 0.01	-0.07 ± 0.01	0.37 ± 0.01	0.78 ± 0.02

5.3 Discussion

This chapter demonstrated the feasibility of the analytical approach by in-silico studies. Validation with heterogeneous phantoms and patient CTs, using beams with varying initial kinetic energies and initial sizes, showed good agreement with MC simulations, confirming the accuracy of the analytical approach for PED and range prediction in complex scenarios. It should be noted that gamma-index analysis, originally developed for dose comparisons, was used to provide a convenient 3D metric for comparing PED and yielded high passing rates; however, it may not be adequate for measured PET data, which are spatially inhomogeneous and subject to scanner-dependent reconstruction artifacts. Next work shown in the later chapter therefore explores alternative metrics when benchmarking against measured PET data.

Minor deviations between the analytical fitting process and the MC reference appear in Figure 4.12, 4.14 and 4.19. The largest deviations occur in the $^{10}C_{proj}$ depth curves in Figure 4.14 because the empirical function optimized for $^{11}C_{proj}$ was reused for convenience for $^{10}C_{proj}$ without refinement. This simplification was made because the contribution of $^{10}C_{proj}$ to the total PET distributions is small, both in terms of yield (less than one-tenth of $^{11}C_{proj}$ over the therapeutic energy range) and the short half-life (only 19.3 s). To quantify the impact of this approach, the analytical IDPED in Figure 5.3 was recalculated by replacing the modeled $^{10}C_{proj}$ curves with the MC results, and the improvements were very limited (ΔNRMSE < 0.002, Δshift < 0.01 mm). For offline/in-room PET the influence is even smaller because of the almost complete radioactive decay in the time elapsed between irradiation and imaging. In Figure 4.12 the deviations are confined to the tail beyond the distal fall-off, well past the depth that determines the range, so they should not affect range verification. Figure 4.19 shows that the double-Gaussian function fits the lateral profile well. The remaining discrepancies are confined to the off-axis region where the amplitude is about 10^{-4}, i.e., two orders of magnitude smaller than the central peak, and are therefore deemed acceptable. If higher accuracy is required, a triple Gaussian can be adopted to fit the lateral distributions.

Although the results presented in this chapter are promising, they are based on the assumption that MC simulations can accurately replicate actual measured distributions. However, variations in different physics models within Geant4 have shown deviations in

the prediction of positron emitter production, sometimes diverging from experimental data [Chacon et al., 2019, Bolst et al., 2017, Chacon et al., 2024]. Therefore, the accuracy of the analytical method is limited by the simulation accuracy of the MC platform. For PEs from target fragmentation, such as ^{15}O, experimental yield data could be utilized to improve the analytical modeling. However, for PEs generated through both projectile and target fragmentation, such as ^{11}C, it still relies on MC-based data, as their separation is not easily achievable with experimental data. To address this, ongoing research is focused on improving physics models used in MC simulations [Dudouet et al., 2014, Mancini-Terracciano et al., 2019, Horst et al., 2019, Sato et al., 2022].

A yield approach for 3D PED calculations in carbon ion therapy was proposed by Helmbrecht et al. [2016]. Herein, the range shifts between the IDPEDs calculated by the analytical method versus MC simulations are less than 0.8 mm in all validation cases, while in Helmbrecht et al. [2016] the range differences in some cases reached values up to 1.5 mm, when comparing predicted and simulated distributions. Besides, Helmbrecht et al. [2016] acknowledged their limitations in predicting projectile PED as they only took the material of stopping voxels into account while neglected the production of projectile PE along the path of the beam. My approach addressed this issue with the proposed mapping process. Moreover, in their approach, the lateral properties of the beam were described theoretically by means of the Moliere's scattering theory, which omitted the contribution from secondaries. In contrast, my method derives the lateral distribution of PED through Gaussian fitting of PED obtained from MC simulations, including secondaries. This ensures that the lateral broadening of PED accounts for contributions from both the primary and secondary fluence.

Since Helmbrecht et al.'s approach builds on a 1D approach proposed by Priegnitz et al. [2012], a comparison with the refined 1D approach is also possible. In Priegnitz et al. [2012] the NRMSE (normalized to the maximum) showed errors below 12% in general when comparing predicted and measured distributions in inhomogeneous targets. Herein, the NRMSE (normalized to the difference between the maximum and minimum of the MC simulated IDPED) were below 4% for the validation cases using the 1D heterogeneous phantom, as shown in Figure 5.3. This normalization approach is stricter, as the difference between the maximum and minimum is typically smaller than the maximum value alone. This results in a smaller denominator, causing normalized errors to be more pronounced. Another distinction between the work presented and the work of Priegnitz et al. [2012] and Helmbrecht et al. [2016] is that their methods rely on experimental yield data, so they avoided any potential inaccuracies in the MC-based data introduced by physics models or cross section data. However, their methods require extensive experimental campaigns and are affected by the detector response, as well as by unavoidable uncertainties in distinguishing different isotope contributions through decay fitting of measured activity. In fact, in Helmbrecht et al. [2016], the yield database for calcium carbonate was also determined by MC simulation due to rare beam time. In contrast, MC-based data are easily generated and can be validated on a lower number of measured data with respect to purely experimental approaches. Moreover, while MC simulations are limited by uncertainties of the physical models and cross section data, they will also benefit from their continuous

advancements.

The in-silico studies presented in this chapter demonstrate that the analytical method agrees well with MC simulations under controlled conditions. An evaluation in clinical-like scenarios is now required. In the next chapter, both the MC and analytical approaches will be applied to complete treatment plans and compare the resulting predictions directly with measured PET data, providing a comprehensive validation of the method under realistic clinical conditions.

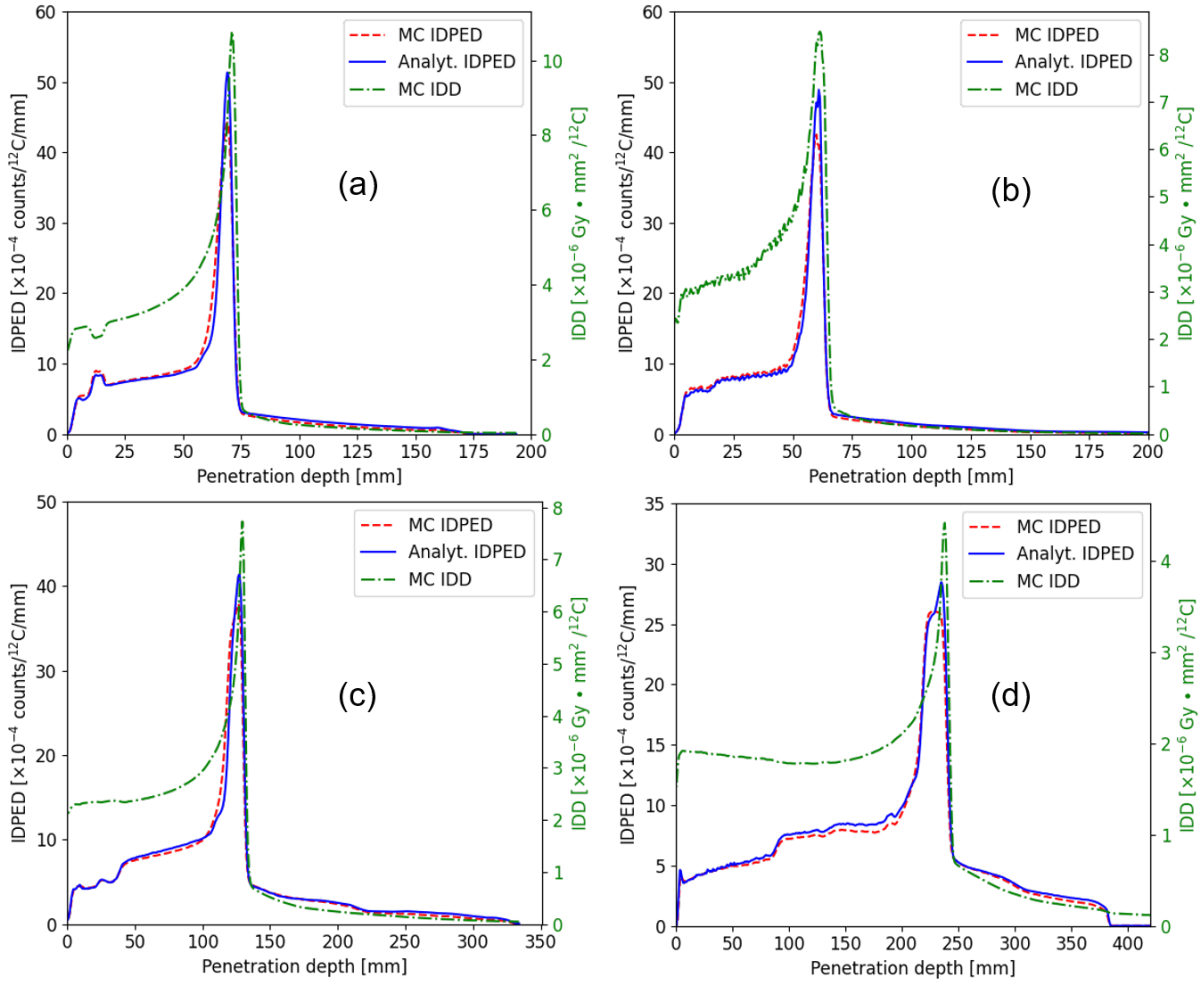

Figure 5.12: (a-d) show the IDPEDs of the four beam spots for the brain, neck, liver, and sacrum cases, respectively, which was calculated by integrating the PED perpendicular to their incident directions. The MC simulated IDPEDs are shown in dashed red lines and the analytical IDPEDs are depicted in solid blue lines. The MC simulated IDDs are displayed with dash-dotted green lines.

6

Clinical validation with patient offline PET data

In Chapter 5, in-silico validation studies of the 3D analytical approach were presented, demonstrating good agreement with MC simulations. In this chapter, the analytical approach is further validated under real clinical conditions by comparing its predictions with both MC simulations and offline PET measurements for several patient cases.

In Section 6.1, the selection of four patients treated with carbon ions at HIT is first presented. The MC simulation method, which generates the MC-simulated dose distribution and PED, and the analytical approach, which predicts the PED based on the MC-simulated dose, are described. The activity calculation from PED is then presented. Furthermore, a longitudinal shift evaluation method is used. In Section 6.2, both range and amplitude comparisons between analytical and simulated results are performed as a prerequisite for the subsequent range comparison between analytical and measured results. Finally, in Section 6.3 the results are summarized and discussed.

6.1 Material and methods

6.1.1 Subject selection

Four patients undergoing carbon ion therapy at HIT were selected for this study [Bauer et al., 2013, Kurz et al., 2016]. The cohort included one patient with a brain tumor (BR), one with a head&neck tumor (HN), one with a liver tumor (LIV), and one with a pelvic tumor (PEL). Offline PET monitoring was employed for treatment verification. Each patient received pencil beam scanning irradiation in the treatment room, followed by PET/CT scanning in a separate room equipped with a commercial PET/CT scanner (see Section 3.3.1 for further details on the PET system). More details on the patient workflow and

data acquisition are described in [Bauer et al., 2013]. The anonymized HIT clinical datasets used for this study include the treatment planning CT (TP-CT) images, treatment plans, PET images and FLUKA MC simulated dose-to-water distributions. An overview of the patient cases is provided in Table 6.1.

Table 6.1: Details of the clinical datasets used in this study: one brain tumor BR, one head/neck tumor HN, one liver tumor, LIV and one pelvic tumor PEL. Treatments details include energy range, number of ions to be delivered according to the plan ('IonsTP'), the irradiation time (t_{irr}), the time between end of irradiation and PET imaging (Δt), the PET-imaging duration (t_{PET}).

Patient ID	Energy [MeV/n]	IonsTP	t_{irr} [min:s]	Δt [min:s]	t_{PET} [min:s]
BR	89-208	0.53E09	03:58	08:15	30:00
HN	98-210	1.02E09	06:10	05:29	30:00
LIV	209-315	8.77E09	29:03	12:03	30:00
PEL	219-430	8.40E09	14:28	09:26	30:00

Note: The long treatment time for the LIV case was due to respiratory gating. The PEL patient received two separate treatment plans delivered on alternating days to ensure full target coverage. Only one of these plans is presented in this study, and this single-field plan naturally exhibits limited dose coverage, which is reflected in the corresponding dose images.

6.1.2 PED calculation by MC and analytical methods

MC PED calculation based on treatment plans

MC simulations were conducted using Geant4 version 10.07.p04 and the QGSP_BIC physics list to obtain dose (both dose-to-tissue and dose-to-water) and PED spot by spot based on patient-specific treatment plans and CT-derived geometry. The simulated dose-to-tissue distributions were used as the input for the following analytical prediction, whereas the dose-to-water distributions were used for comparison with the FLUKA MC results from HIT. The scoring of PEs followed the procedure described in Section 4.1.

To enable an appropriate comparison with measurement data from HIT, the simulation settings have to accurately reproduce HIT scanned ion beam delivery. Fortunately, the relevant FLUKA MC modeling had already been implemented for producing the input of the analytical planning system [Parodi et al., 2012] and the full MC framework was used in routine clinical workflows [Bauer et al., 2014]. To allow meaningful comparisons with experimental data, consistency between the present MC and HIT MC simulations was guaranteed by replicating the clinical beam configuration and matching the CT-range calibrations across different CT acquisition protocols. Specifically, the clinical beam configuration was replicated using input phase-space data [Tessonnier et al., 2016] generated with the FLUKA MC code, which incorporated the detailed beamline model described

in Parodi et al. [2013]. The CT-to-material conversion method followed the stoichiometric calibration of [Schneider et al., 2000, Parodi et al., 2007b]. The employment of the phase space files into the Geant4 code has been detailed in Section 5.2.1.

An additional correction was applied to the internal Geant4 SPR calculation of CT-derived materials to ensure consistency to the clinically used CT-SPR calibration curves (depending on anatomical site). The SPR is defined as the ratio of the stopping power of carbon ions in a material to that in water at a specific energy. These corrections were implemented by tuning the mean excitation potential (I) of CT-derived materials to match the CT-SPR tables used at HIT at the energy of 120 MeV/n. The resulting CT-I lookup tables were then built and incorporated into the Geant4 MC simulations. Details of the construction of the lookup table are presented in the following part. Finally, the consistency was validated by comparing the Geant4 simulated dose-to-water of the four patient cases with the FLUKA MC results from HIT. It is important to note that the same FLUKA MC engine was also employed to generate the clinical TPS database (SyngoPT, Siemens and RayStation, RaySearch Lab) at HIT [Parodi et al., 2012, Bauer et al., 2014].

CT to stopping power calibration

The SPR values of materials directly affect the prediction of ion beam range in both the MC simulations and analytical calculations. As CT images are expressed in HU, which reflect the photon attenuation properties of tissues rather than their ion stopping powers, SPR values derived from the elemental composition of CT-based materials may therefore be biased. Such discrepancies may lead to inaccurate ion beam range predictions. At HIT, different CT-SPR calibration tables are used clinically to ensure the accurate range predictions. In this work, the corrections of SPR were implemented by tuning I value of CT-derived materials to match the CT-SPR tables used at HIT at the energy of 120 MeV/n.

Because the SPR values provided by HIT are defined as the ratio of the stopping power of carbon ions in a material to that in water, it is necessary to first calibrate the stopping power in water before calibrating the stopping power of CT-derived materials. To this end, HIT provides reference IDD in water for carbon ions at nominal energies of approximately 100, 200, 300, and 400 MeV/n. They were used as benchmark data for calibrating the I value of water. Specifically, using the Geant4 MC code with the phase space data as input, carbon ion beams of the same nominal energies were simulated in water (with a mass density set to 1.0 g/cm^3) to determine the IDD, and in each simulation the I value of water was adjusted to determine the optimal match to the HIT reference IDD. An I-value range between 75 eV and 85 eV in 1 eV increment was investigated. Figure 6.1 shows the resulting normalized IDD curves in water at a nominal energy of approximately 300 MeV/n for I values of 75, 80 and 85 eV, together with the corresponding HIT reference IDD curve at the same energy. For the four energies, the R80 positions of the simulated IDDs (for each tested I value) and those of the HIT reference curves were extracted. By performing a polynomial fit of the water I values and the simulated R80 positions, and identifying the intersection with the HIT R80 value, an estimate of the optimal I value for water was

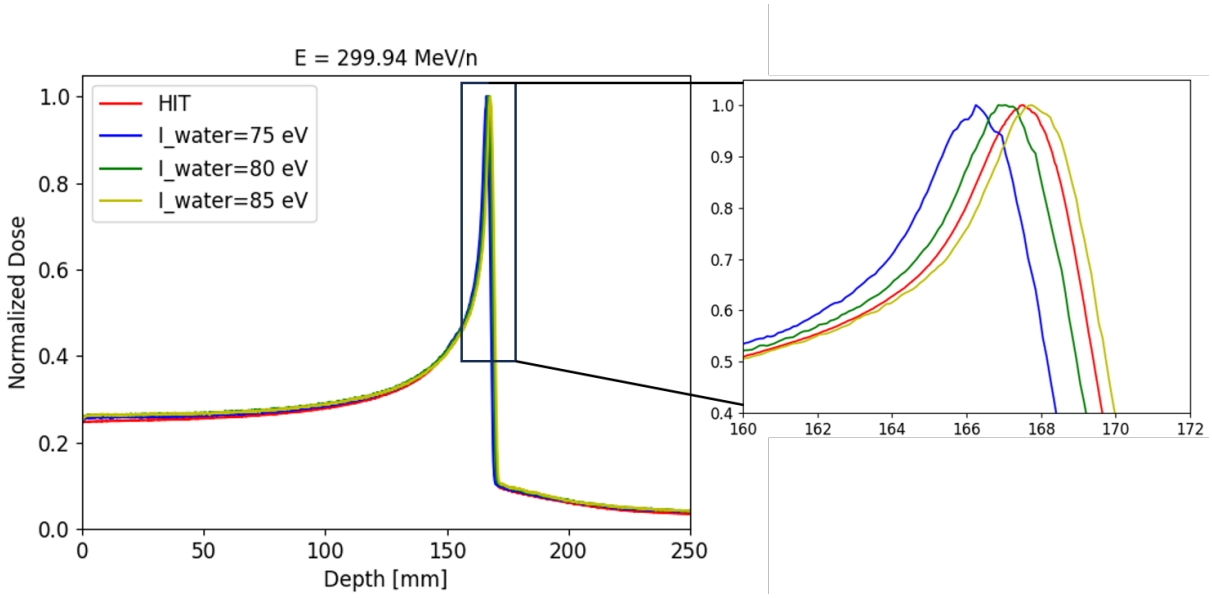

Figure 6.1: Geant4 simulated IDD curves for different I values and HIT IDD curve in water at a nominal energy of 299.94 MeV/n.

obtained (see Figure 6.2). Across the four energies, the optimal I value was found to be 82 eV.

After implementing this calibrated water I value in the Geant4 code, the I values of the CT-derived materials were subsequently tuned so that the SPR values calculated internally in Geant4 matched those provided in the HIT CT–SPR calibration tables. Figure (6.3) shows the tuned I values as a function of HU values compared to the initial I values internally calculated by Geant4. Finally, a consistency check was performed by comparing the SPR values with the ratios of Bragg peak positions in water and HU-specific materials obtained from Geant4 simulations at a beam energy of 120 MeV/n (see Table 6.2). The good agreement between SPR values and the Bragg peak ratios confirms the reliability of the CT–SPR calibration procedure and validates the resulting HU-I lookup table. This calibrated HU-I table was used in both Geant4 MC and analytical methods for the PED calculation based on the treatment plans.

Table 6.2: Comparison of HIT SPR values and ratios of simulated Bragg peak positions for different HU materials at 120 MeV/n

Materials	Water	HU = -500	HU = 1000	HU = 2000
I [eV]	82	105.7	87.84	234.94
Bragg peak [mm]	35.75±0.05	71.35±0.05	23.65±0.05	20.15±0.05
HIT SPR	1	0.5004	1.5122	1.7849
Ratio of Bragg peak	1	0.5000±0.0008	1.5116±0.0038	1.7742±0.0051

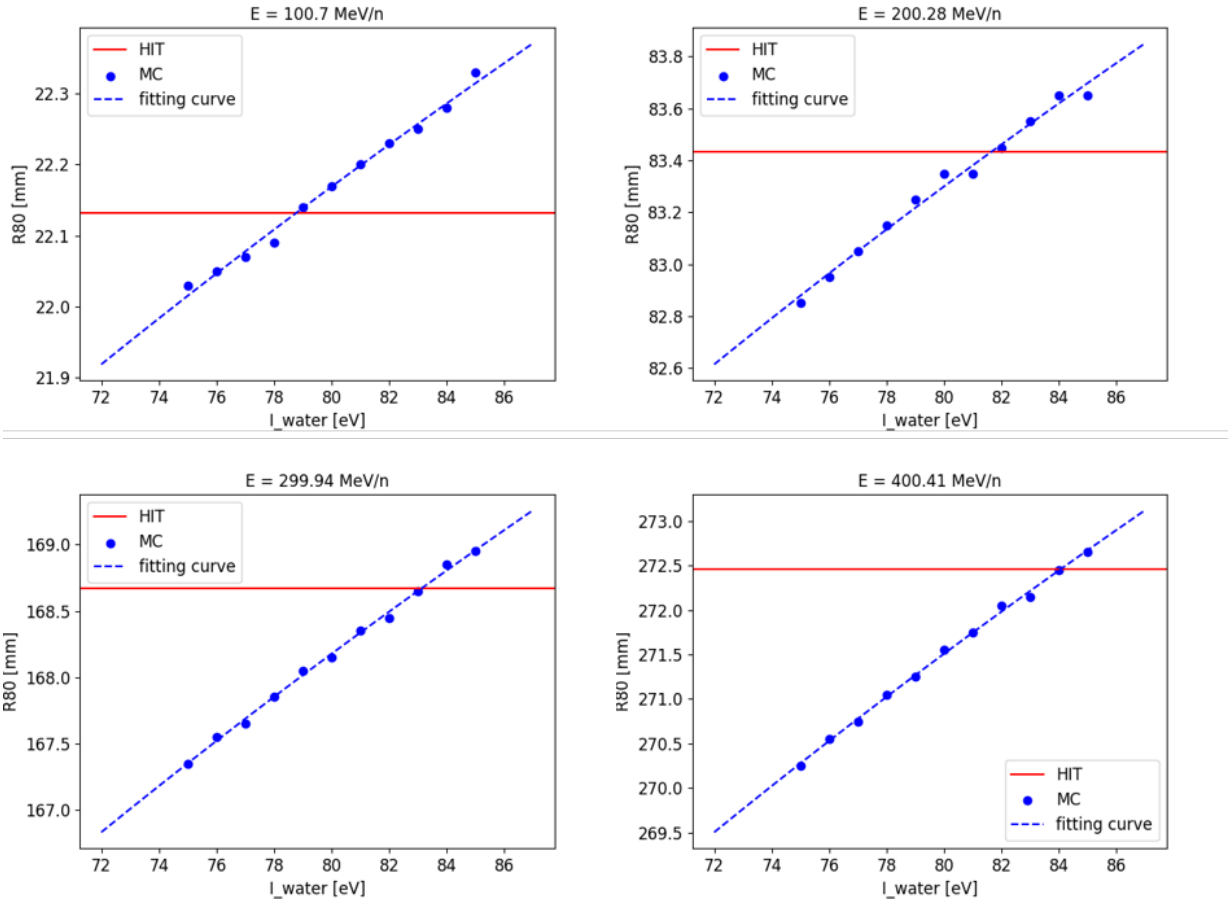

Figure 6.2: Polynomial fit of I values versus R80 values by Geant4 and the HIT R80 value.

Analytical PED calculation based on treatment plans

The construction and pre-calculation of the analytical approach framework has been presented in Section 4.2. In practical applications, the analytical algorithm only requires the corresponding 3D dose-to-tissue distributions and the beam and patient information. The analytical prediction begins by reading the 3D dose-to-tissue distribution of a single spot. In this study, the dose distribution for each beam spot in the treatment plans was first calculated through Geant4 MC simulations. This 3D dose distribution was converted to a 3D dose in the reference material by tracing each beam ray to obtain its depth–dose profile and converting it to the corresponding equivalent depth in the reference material. The resulting dose distribution was then laterally integrated to generate the reference IDD. Next, the IDPEDs of the five target PEs and two projectile PEs generated from different target nuclei in the reference material were then built based on the reference IDD built before. The same CT-to-material conversion method as that used in the MC simulations was applied to build the material information of the patient anatomy, including the mass density, electron density, and mass abundances. The I value of material was got from

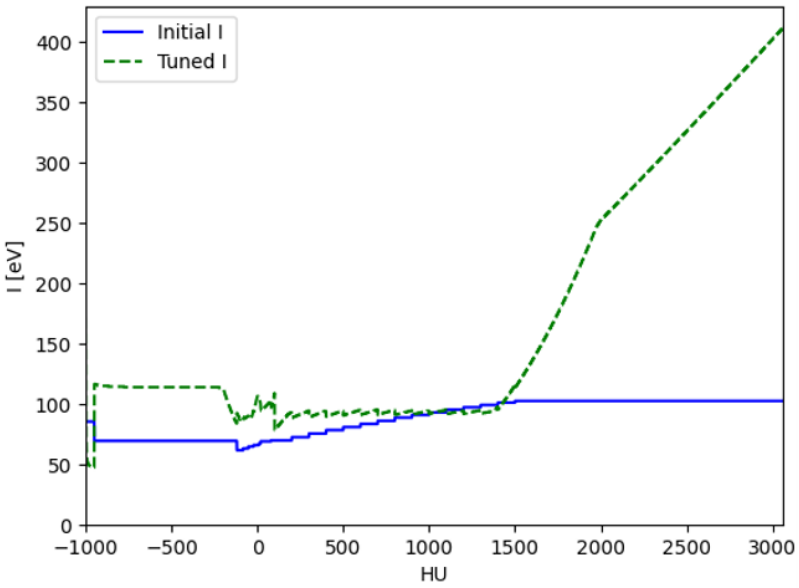

Figure 6.3: Tuned and initial I values as a function of HU values.

the same CT-I lookup table employed in the MC simulations. Finally, using predefined parametrization of the lateral properties of PED, along with beam parameters including the initial beam size and energy, the algorithm spreads the IDPED into 3D PED, accounting for the phantom heterogeneity.

In the context of this work, the dose-to-tissue distributions were calculated using MC simulations, which served as the required input of the analytical approach. However, when the analytical approach is deployed and commissioned in the clinical workflow, the dose-to-tissue per spot can be retrieved from the TPS without any need for MC simulations. If the TPS provides dose-to-water rather than dose-to-tissue, the same conversion procedure described above can be applied, except that only the dose values need to be rescaled from water to the reference material according to the corresponding mass stopping power ratio.

6.1.3 β^+ activity calculation for offline PET

To compute the activity pattern from the analytical or simulated PED, it is necessary to account for both the time course of measurement (cf. Table 6.1) and the biological washout PEs. The PEs are generated during the irradiation and may undergo radioactive decay during irradiation, the subsequent patient transport, or the PET measurement. In addition to the physical decay, the activity distribution is affected through the biological washout which depends primarily on tissue perfusion. Following the model described in [Mizuno et al., 2003, Parodi et al., 2007c], tissue is segmented according to CT Hounsfield units into regions of low, intermediate, or normal perfusion, though only the slow component of washout is considered here, given the relatively large time delays between irradiation and imaging (Δt). Each tissue region is assigned a distinct biological decay constant λ_{bio} and

a relative fraction M_s of the slow-decay component, with parameter values also reported in [Mizuno et al., 2003, Parodi et al., 2007c] and later used also in the HIT clinical PET study [Bauer et al., 2013]. Taking these factors into account, an expected activity pattern $\langle A(r)\rangle$ averaged over the PET imaging time t_{PET} can be calculated according to [Parodi et al., 2007c, Bauer et al., 2013] by:

$$\langle A(r)\rangle = \mathrm{G}(r) \cdot \sum_j \left[\mathrm{M}_s(r)\mathrm{PED}_j(r) \cdot \frac{\left[1-\exp\left(-_{phys,j}\cdot t_{irr}\right)\right]}{t_{irr}} . \exp\left(-\lambda_{tot,j}(r)\cdot\Delta t\right) \cdot \frac{\left[1-\exp\left(-\lambda_{tot,j}(r)\cdot t_{\mathrm{PET}}\right)\right]}{\lambda_{tot,j}(r)\cdot t_{\mathrm{PET}}} \right] \quad (6.1)$$

where $\mathrm{G}(r)$ is the three-dimensional Gaussian point spread function modeling the spatial resolution of the PET scanners, $PED_j(r)$ is the PED for the j-th PE calculated by either the simulation or the analytical prediction, and λ_{tot} is the total decay constant given by the sum of λ_{bio} and the physical decay constant λ_{phys}.

6.1.4 Data analysis

Consistency between the present simulations and those from HIT was first verified by comparing the simulated dose-to-water of the four patient cases with MC results from HIT through gamma analysis. Next, the analytically predicted PET results were compared with both MC simulated results and measured data to verify the capability of the analytical approach for range verification in clinical scenarios.

1D activity profiles along the selected line in beam direction for each case were plotted to illustrate the magnitude and range of the analytical, simulated and measured activity. To assess the longitudinal shifts, 1D activity profiles were extracted along the beam direction for each (x, y) in the transverse plane from the two 3D distributions to be compared and employed a most-likely-shift (MLS) method, as detailed in the following section. Additionally, the activity yield differences between the analytical and MC profiles were evaluated using the NRMSE.

Most-Likely-Shift method

The MLS method was originally proposed by Frey et al. [2014] for offline PET-based treatment monitoring and widely used in in-vivo PET verification [Zhang et al., 2021, Moglioni et al., 2022]. For each pair of coordinates (x, y) in the transverse plane, it takes 1D activity profiles along the beam direction from the two 3D activity distributions to be compared and calculates the most likely shift δ_{MLS} that minimizes the difference between a distal fall-off segment of the two profiles:

$$\delta R_{\mathrm{MLS}} = \arg\min_{\delta_{\mathrm{MLS}}} \left(\sum_{z_{\min}}^{z_{\max}} \left| A_{\mathrm{ref}}(z) - A_{\mathrm{pred}}\left(z - \delta_{\mathrm{MLS}}\right) \right| \right) \quad (6.2)$$

where A_{ref} and A_{pred} represent the reference (i.e., simulated or measured) and the analytically predicted activity profiles, respectively. The method applied follows exactly as described in Frey et al. [2014]. The parameters $z_{\min}$ and $z_{\max}$ define the distal region of interest: $z_{\max}$

is the maximum depth between the 50% dose fall-off and the 20% activity fall-off, and $z_{\min}$ ranges from the location of the activity maximum and one voxel upstream of $z_{\max}$. Moreover, only those profiles with an integrated activity of at least 20% of the highest integrated activity were considered, so that low activity profiles, known for being less reliable [Frey et al., 2014, Min et al., 2013], are excluded from analysis. For a detailed description, the reader is referred to Frey et al. [2014].

6.2 Results

Figure 6.4 shows MC-simulated dose-to-water distributions from the present simulations and from HIT for all patient cases. Gamma index passing ratios of 99.97%, 99.92%, 99.50% and 99.35% (1%/1 mm criteria) for the BR, HN, LIV and PEL cases, respectively, demonstrate good consistency of simulations between the Geant4-based platform and HIT data, enabling the use of the simulated dose of each spot for the analytical predictions.

Figure 6.5 shows results for the BR case. Comparing the analytical/MC-simulated results before and after washout effect correction (Figure 6.5(a) vs. (c)/(b) vs. (d)) shows that most activity initially formed in the brain was washed away, leading to local activity maxima mainly in the bone and distal tumor. Figure 6.5(e) shows the measured PET image where the local maximum in the bone (ca. 8 Bq/ml) is much lower than the one in the distal tumor (ca. 30 Bq/ml), mainly contributed by the stopping projectile PEs. 1D profiles extracted along the white line will be displayed later and reveal both peaks.

Figure 6.6 shows results for the HN case. A similar washout effect can be observed for the HN case when comparing (a) with (c) and (b) with (d), where the activity in soft tissue decreases and the main activity is located at the distal region in front of the spinal cord. The measured PET likewise exhibits a local maxima in this distal region, mainly contributed by the projectile PEs (see Figure 6.6(e)).

Figure 6.7 and 6.8 show results for the LIV and PEL cases, respectively. In Figure 6.7, two parallel irradiation fields were used. Again, a comparison of the analytical and MC results before and after washout correction indicates that activity initially formed in the liver was largely reduced, leaving local activity maxima in the entering fat region and distal tumors. These features also appear in the measured PET image (Figure 6.7(e)). Similarly, in Figure 6.8, the washout effect reduces activity in muscle tissue, with the main activity remaining in body fat and the distal region. Figure 6.8(e) exhibits the local activity maxima at the distal region similar to those in (c) and (d), but shows the noisiest measured PET result among the four cases.

For all the four cases, analytical predicted PET images closely match simulated results in shape and amplitude based on Figure 6.5, 6.6, 6.7 and 6.8. However, differences to the measured PET images are observed, with a similar level of disagreement for both analytical and simulated results, primarily due to inaccuracies in the washout effect correction and noise in measured PET data [Bauer et al., 2013, Frey et al., 2014, Kurz et al., 2016]. Nevertheless, the maxima positions among the analytical, simulated, and measured PET images remain qualitatively well aligned.

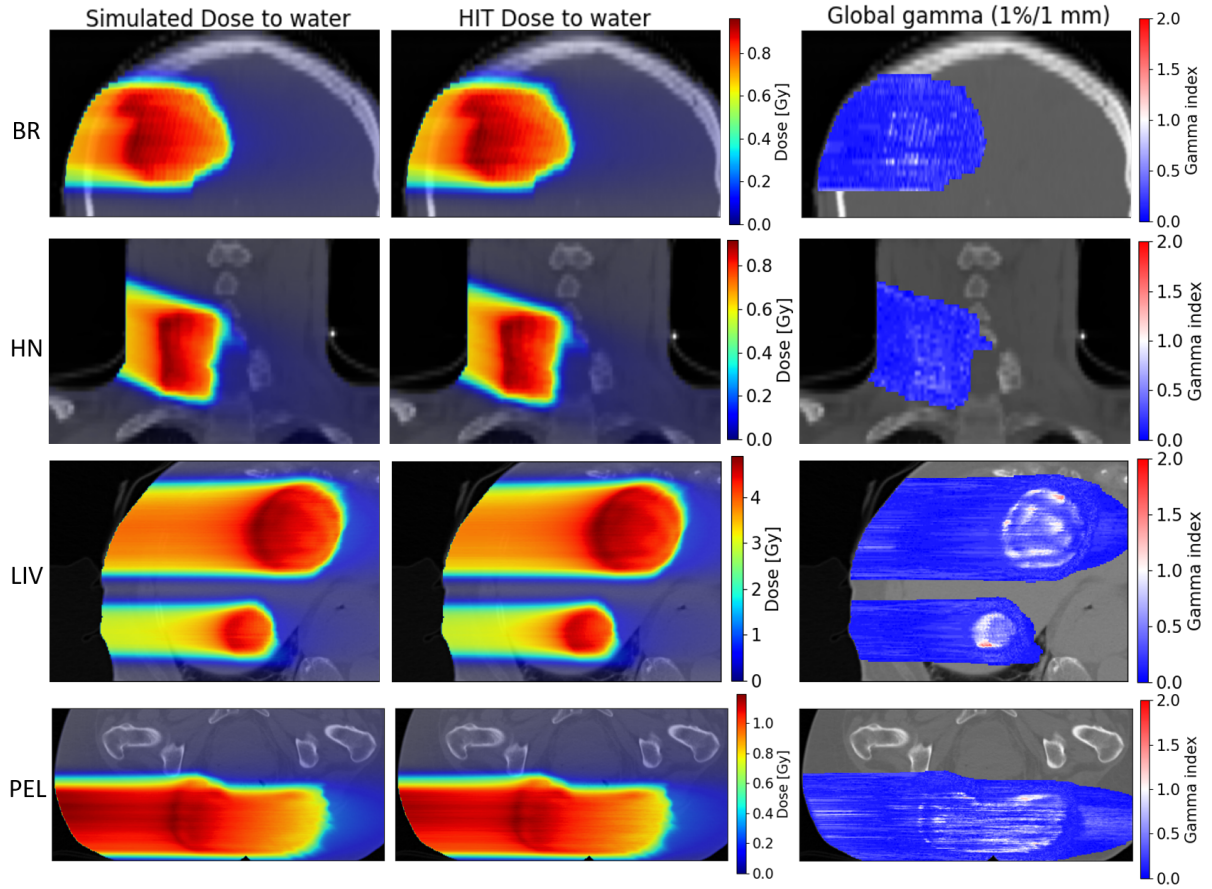

Figure 6.4: Consistency check of dose-to-water between the present Geant4 MC and HIT FLUKA MC simulations. Dose-to-water distributions of the BR, HN, LIV and PEL cases from top to bottom, calculated using the Geant4-based platform developed for this work (left) and by HIT (middle), along with gamma index maps (right), using 1%/1 mm criteria, overlaid onto the corresponding planning CT images.

To confirm this observation, 1D activity profiles were extracted along the white lines shown in Figure 6.5, 6.6, 6.7 and 6.8. A quantitative comparison of selected activity profiles with corresponding CT values is shown in Figure 6.9. For the brain case (Figure 6.9(a)), analytical and MC simulated PET profiles show excellent agreement in shape and amplitude, with consistent peak positions in the bone and distal regions compared to measurements. The measured activity in the tumor volume is significantly higher than expected, which suggests an overestimated washout correction in the tumor volume. For the head/neck case (Figure 6.9(b)), the analytical prediction underestimates the distal activity peak relative to the MC simulation. This discrepancy can be attributed to the pronounced tissue heterogeneity at that region, as evident from the CT profile. Spatial agreement is observed between the predicted and measured activity gradients near the spinal cord structure. For the liver case (Figure 6.9(c)), analytical and MC simulated PET

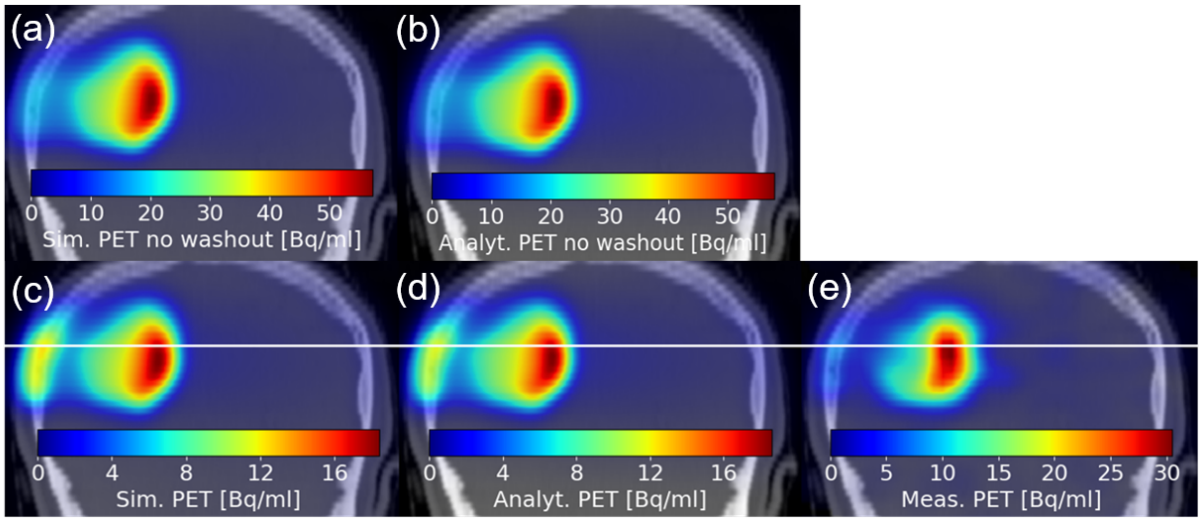

Figure 6.5: Results for the BR case displayed in coronal view. Geant4 MC-simulated PET images are shown in (a) and (c); analytical PET images in (b) and (d); measured PET in (e). (a) and (b) are displayed PET without washout correction, whereas (c) and (d) include washout correction. The white lines in (c-e) indicate where the profiles along the beam direction were extracted.

profiles also show strong agreement, with a minor discrepancy in the distal fat region behind the air cavity. Three peaks in the entering fat region, at the tumor, and in the distal fat region are observed in both analytical and measured profiles, and they share close peak positions. For the pelvic case (Figure 6.9(d)), analytical and MC simulated PET profiles again demonstrate excellent agreement in shape and amplitude. It is hard to identify peaks from the noisy measured profile, while one peak can be identified in the analytical profile and its distal fall-off closely corresponds to the distal fall-off of the highest peak in the measured profile.

The MLS method presented in Section 6.1.4 was used to quantify the range deviation between the analytical activity distribution and the simulated or measured results in beam's-eye-view (BEV). Figure 6.10 shows the range differences between the analytical and the simulated activity distributions in BEV by the MLS method for the BR, HN, LIV and PEL cases from left to right.

The mean range differences and their root-mean-square error (RMSD) were calculated, as listed in the first row of Table 6.3. The range deviation between the analytical and simulated activity distributions in all four cases remain below 0.5 mm, with all RMSD values under 1 mm. It demonstrates excellent range agreement between the analytical predictions and the MC simulations for the four cases. The activity yield differences between the analytical and MC profiles are evaluated using NRMSE. The third row of Table 6.3 shows the mean NRMSE values and corresponding RMSD values. The HN and PEL cases exhibit slightly higher mean NRMSE, mainly due to the complex heterogeneities and larger noise in PET images caused by stronger tissue attenuation and reduced photon detection in

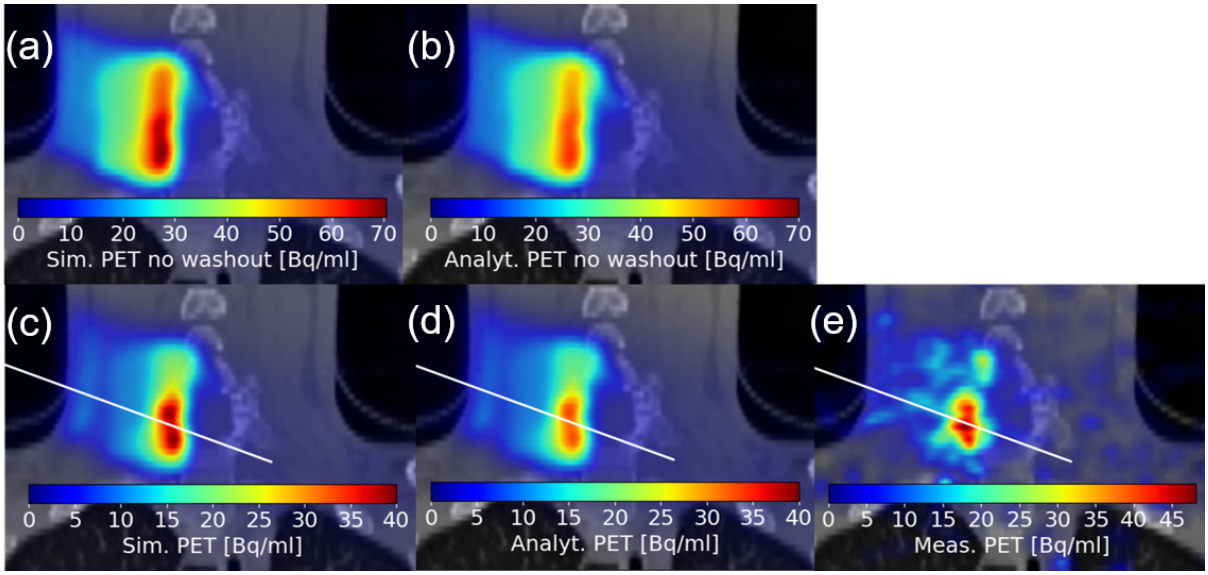

Figure 6.6: Results for the HN case displayed in coronal view. Geant4 MC-simulated PET images are shown in (a) and (c); analytical PET images in (b) and (d); measured PET in (e). (a) and (b) are displayed PET without washout correction, whereas (c) and (d) include washout correction. The white lines in (c-e) indicate where the profiles along the beam direction were extracted.

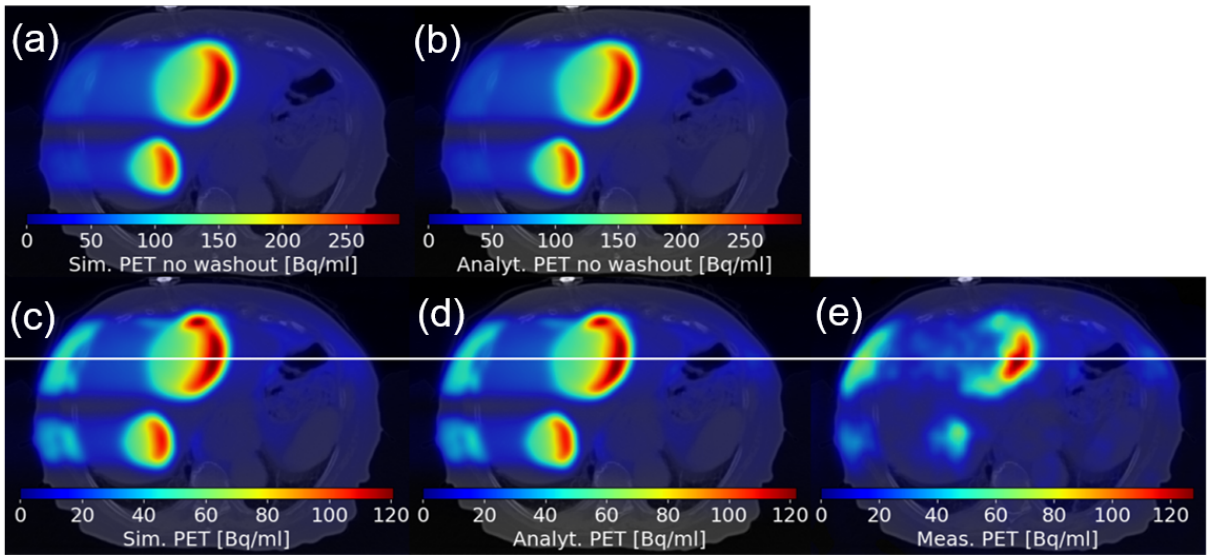

Figure 6.7: Results for the LIV case displayed in axial view. Geant4 MC-simulated PET images are shown in (a) and (c); analytical PET images in (b) and (d); measured PET in (e). (a) and (b) are displayed PET without washout correction, whereas (c) and (d) include washout correction. The white lines in (c-e) indicate where the profiles along the beam direction were extracted.

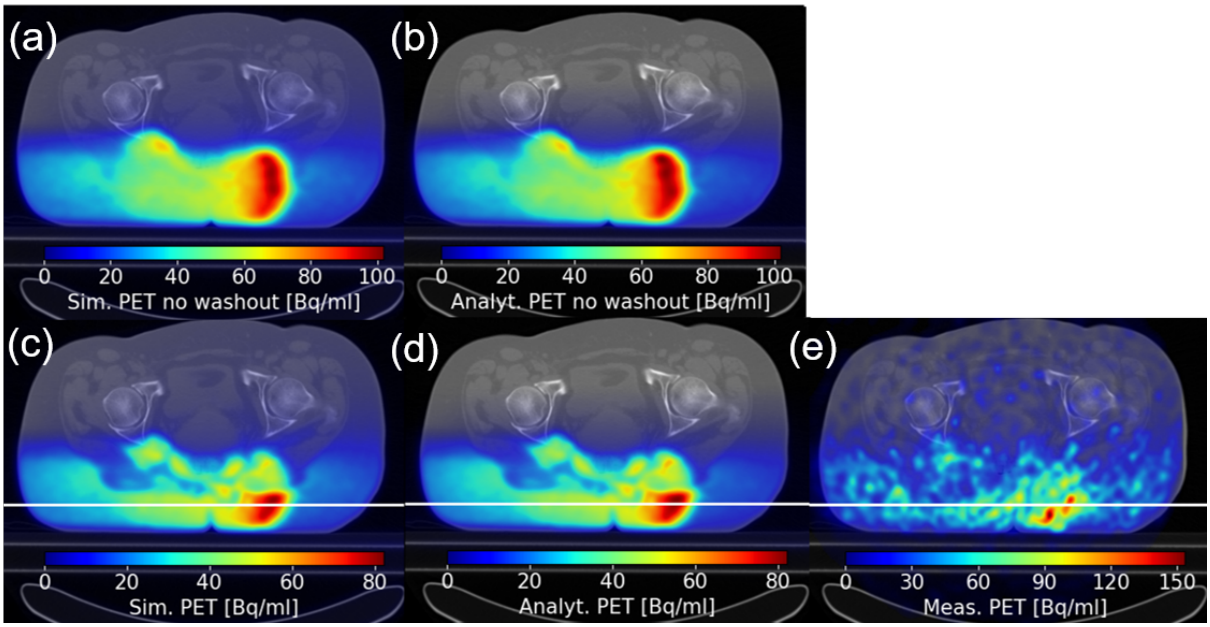

Figure 6.8: Results for the PEL case displayed in axial view. Geant4 MC-simulated PET images are shown in (a) and (c); analytical PET images in (b) and (d); measured PET in (e). (a) and (b) are displayed PET without washout correction, whereas (c) and (d) include washout correction. The white lines in (c-e) indicate where the profiles along the beam direction were extracted.

head-and-neck and pelvic regions. Overall, the mean NRMSE values ranged between 1–2% and the RMSD values are below 1%, demonstrating that the analytical approach predicts the distribution amplitudes with a comparable accuracy as the MC simulations.

Figure 6.11 shows the range differences between the analytical and the measured activity distributions in BEV by the MLS method for the BR, HN, LIV and PEL cases from left to right. For the HN and PEL cases, the shift maps show numerous regions with large shifts of -10 to -20 mm, compared to BR and LIV cases. This is primarily due to the greater statistical noise and fluctuations in the measured PET data for HN and PEL (cf. Figures 6.6(e) and 6.8(e)). The MLS method compares a dynamically selected distal segment of the measured profile to the corresponding segment of the analytical profile. When the measured data are noisy, the resulting shape mismatch can be too large for a realistic MLS to exist. The mean range differences and their RMSD are listed in the second row of Table 6.3. Overall, the mean deviations are within ± 3 mm excluding the PEL case. Figure 6.11 highlights several regions where the shifts between the analytical prediction and the measured PET exceed ± 10 mm: positive shifts along the right edge of BR, negative shifts along the left side of HN, positive shifts at the upper part of LIV, and for PEL, positive shifts on the left side and negative shifts on the right, top, and bottom edges. A definitive explanation of these large shift regions would require a dedicated deformable-registration analysis between the planning CT and the CT acquired on the day of the PET/CT, which

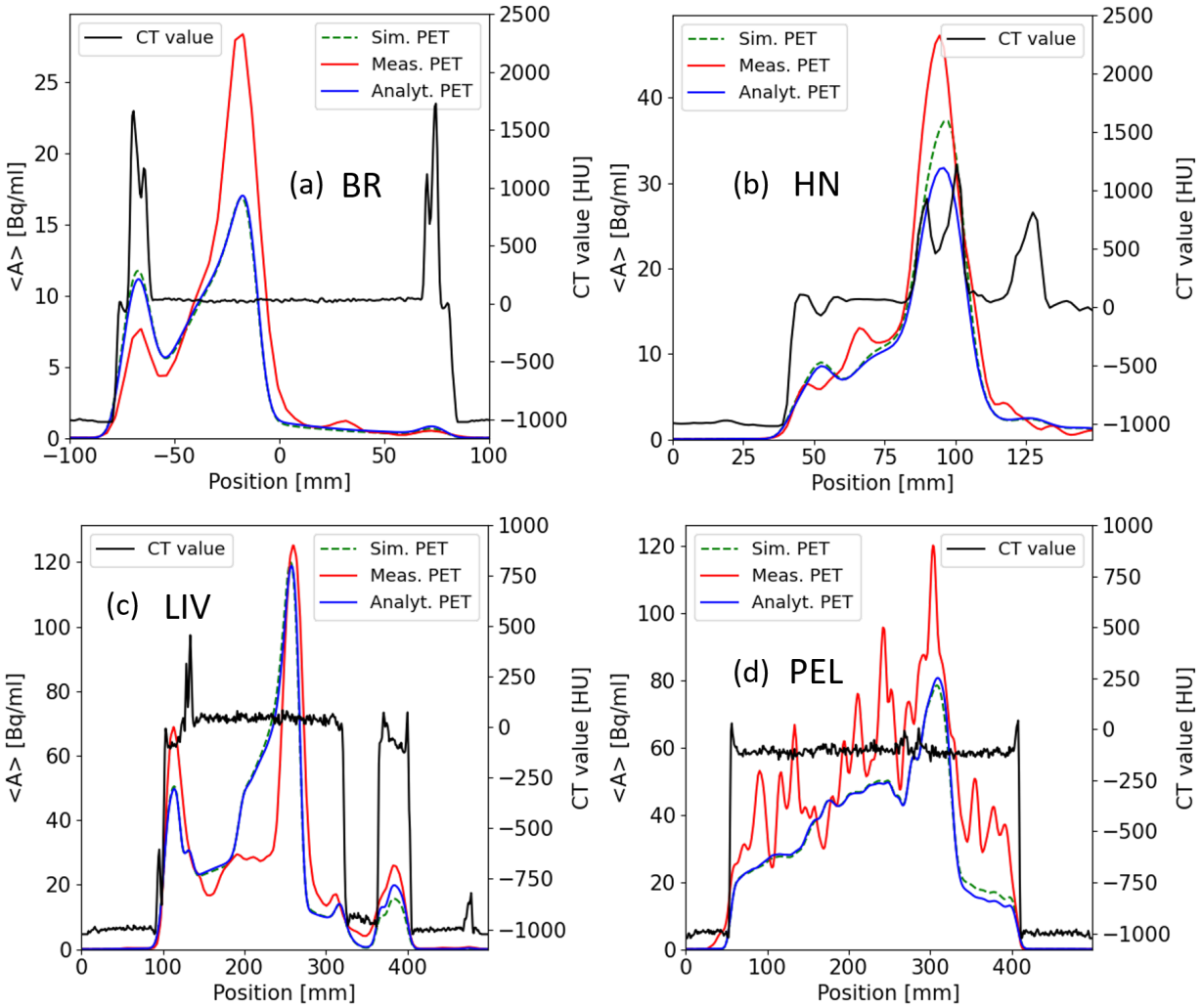

Figure 6.9: Selected depth activity-profiles along the white lines in Figure 6.5-6.8 with corresponding CT values are shown in (a)–(d) for the BR, HN, LIV, and PEL cases, respectively.

is beyond the purpose of the present validation study. Nevertheless, same or similar cases have been reported in previous PET-based range-verification studies (e.g., [Bauer et al., 2013]), and their relevant findings and explanations will be discussed in the Section 6.3.

6.3 Discussion

This work validated an in-house developed analytical approach for in-vivo PET verification in carbon ion therapy using four patients cases in real clinical conditions. The validation followed a multi-stage strategy. First, the present MC simulations were tuned to reproduce the HIT MC, which is considered the gold standard and also underlies the TPS at HIT.

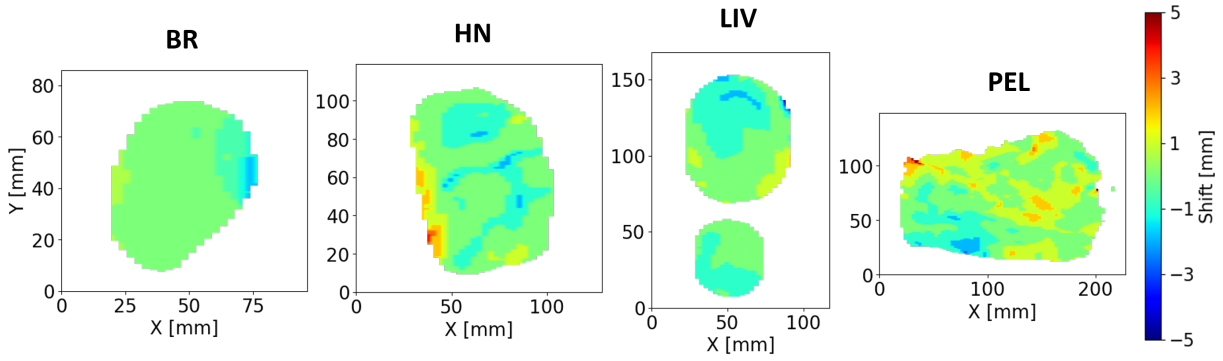

Figure 6.10: Range shift maps for BR, HN, LIV and PEL from left to right. Analytical and simulated distributions are compared.

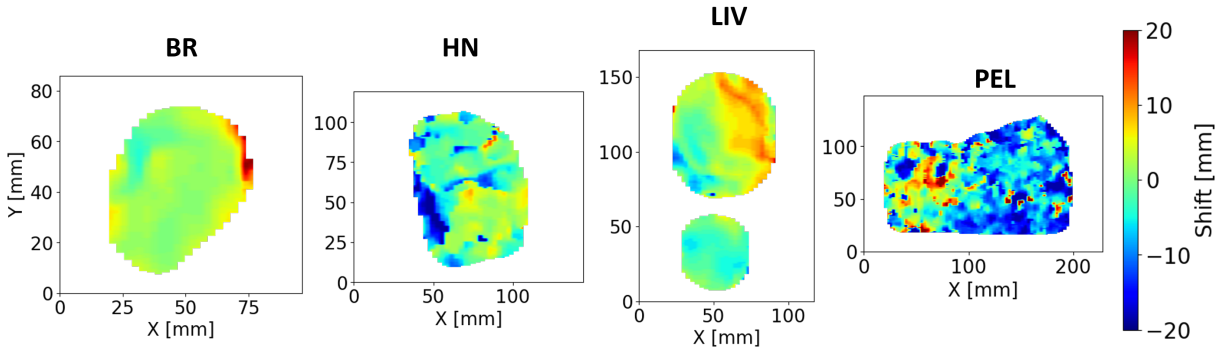

Figure 6.11: Range shift maps for BR, HN, LIV and PEL from left to right using the MLS method. Analytical and measured distributions are compared.

Next, the consistency between the present MC and the HIT MC dose-to-water was verified. Once validated, the MC simulations were used as the gold-standard reference to assess the analytical predicted PET images, given that the analytical predictions were based on MC-simulated dose-to-tissue distributions and the parameters of the approach were derived by fitting MC-calculated data (Section 4.2).

The good agreement between the analytical predictions and MC simulations (with mean longitudinal shifts ≤ 0.5 mm and mean NRMSE values $\leq 2\%$) confirms that the analytical method accurately predicts PED in terms of both range and amplitude. The longitudinal shifts between the analytical predictions and measured data were subsequently evaluated. A direct investigation of the reason of shifts between analytical predictions and measured PET images was beyond the scope of this work, as these patient data had already been analyzed in previous PET-based range verification studies at HIT. Therefore, these studies for the interpretation of such deviations are referred below.

Bauer et al. [2013] reported the same BR and HN cases. Rather than analyzing range shift maps, the study compared activity profiles along the beam direction, similar to

Table 6.3: Mean range differences (Shifts) and mean NRMSE with corresponding RMSD values for BR, HN, LIV, and PEL. The gray rows refer to analytical vs. simulated distributions; the white rows refer to analytical vs. measured distributions.

	BR	HN	LIV	PEL
Shifts [mm]	-0.11 ± 0.40	-0.08 ± 0.77	-0.35 ± 0.67	0.25 ± 0.88
	2.36 ± 3.23	-2.29 ± 6.10	1.57 ± 4.88	-5.46 ± 8.71
NRMSE [%]	1.25 ± 0.51	1.54 ± 0.44	1.25 ± 0.48	2.04 ± 0.83
	-	-	-	-

Note: NRMSE is not reported for the analytical vs. measured comparison due to the higher noise level in measured PET profiles.

that shown in Figure 6.9, and found good spatial agreement between the predicted and measured activity and deemed them a proper beam delivery. Moreover, Nischwitz et al. [2015] investigated 10 patients with primary glioblastoma and reported two representative cases in detail. The first case featured a small, relatively homogeneous tumor. Its range shift map showed overall low range deviation with a few large deviations (ca. 10 mm) along the left edge and yielded an average MLS of 1.9±2.2 mm. The second case was a large tumor of complex, irregular shape with a central necrosis and surrounding oedema. The range shift map revealed a broader region of pronounced shifts (upper-left) and a mean MLS of 6.4±5.2 mm. Nischwitz et al. [2015] concluded that the beam range in homogeneous tumors was more accurate than in inhomogeneous ones, which explained the larger shift of their second case. Besides, Nischwitz et al. [2015] noted that being below the used safety margins of commonly 3-5 mm, allow a solid prediction of the beam range. The present BR case with few large shifts at the upper-left edge has a mean MLS of 2.36±3.23 mm, which falls into this interval. This result supports the reliability of the range prediction and also confirming a proper beam delivery, as also concluded by [Bauer et al., 2013].

Kurz et al. [2016] reported the same LIV case. A 5–20 mm region of over-range in Figure 6.11(LIV) was also noted in the corresponding range shift map. This deviation was attributed to slight differences in the patient's outer contour on the treatment day, in addition to residual motion despite the application of an abdominal press [Kurz et al., 2016]. In addition, Kurz et al. [2016] reported a mean MLS of 1.56±4.57 mm between measured data and simulation which closely aligns with the result of 1.57±4.88 mm in this work. The similar range shift map and nearly identical mean MLS value confirm the accuracy of the range prediction for the LIV case.

Frey et al. [2014] reported one pelvic case (different from the present PEL), and a pronounced continuous over-range region was displayed in their range shift map which was confirmed to be an overshoot due to the anatomic changes between planning CT and PET/CT. This resulted in a mean MLS of 4.26±11.25 mm. As a consequence, the simulation was redone based on the CT obtained from the PET/CT scan after the treatment. The pronounced over-range region disappeared, and the corresponding MLS analysis showed

a good conformity of the two distributions, yeilding a mean MLS of 0.71±8.34 mm. In comparison, the range shift map for the PEL case shows large shift regions that are relatively scattered across the field, without any continuous and pronounced area. Given that the PET image for PEL is already the noisiest among the four cases (see Figure 6.8(d)), it is impossible to rule out a significant influence of image noise associated with low counting statistics and/or inaccuracies in the biological washout model on the observed range differences.

A different approach for 3D PED calculations in carbon ion therapy based on a database of PET yields measured in phantoms was proposed and validated with a patient case by Helmbrecht et al. [2016]. A thorough comparison was previously made in [Du et al., 2025] and showed that the analytical method provided better range prediction than [Helmbrecht et al., 2016]'s approach. However, a key advantage of their technique is that it relied on experimental yield data and avoided any potential inaccuracies in the MC-based data introduced by physics models or cross-section data. From this perspective, the analytical method is limited by the accuracy of MC simulations needed for but would also benefit from ongoing advancements in physics models and cross-section databases [Mancini-Terracciano et al., 2019, Horst et al., 2019, Sato et al., 2022, Gao et al., 2023].

The analytical method achieves accurate range predictions compared to full-blown MC simulations with a higher computational speed. Although the code is a proof-of-principle version and can be further optimized, it already performs about 40 times faster than CPU-based MC tools [Du et al., 2025]. In addition, it relies on a traditional pencil beam algorithm and employs a data structure similar to that used by standard TPS, facilitating straightforward integration into clinical workflows. As demonstrated for proton therapy using a filtering-based approach [Frey et al., 2013, Pinto et al., 2020], this method can potentially enable range predictions shortly after the end of treatment in offline PET monitoring. Moreover, the analytical method allows for fine tuning of the predicted yields by applying an isotope-specific scaling factor once the MC engine is calibrated to a given facility or experimental yield data become available.

As Frey et al. [2014] noted and this study also demonstrated, inaccuracies in the biological washout model and image noise from low counting statistics also lead to range discrepancies between measurements and predictions. Ongoing research on biological washout in animals [Helmbrecht et al., 2013, Ammar et al., 2014, Toramatsu et al., 2018, 2022, 2023] aims to mitigate these issues. Novel PET reconstruction methods [Kurz et al., 2016, Reader et al., 2020, Xie et al., 2021, Hashimoto et al., 2024] could also help improve image quality. Additionally, in-beam PET, which is less affected by washout-induced signal degradation, can offer higher image accuracy [Parodi et al., 2008, Dendooven et al., 2015, Ferrero et al., 2018, Fiorina et al., 2021, Tashima et al., 2023, Kraan et al., 2024b]. In the next chapter, a preliminary validation study of the method using data acquired with in-beam PET will be presented, which represents the most promising form of in vivo treatment verification during beam delivery in modern carbon ion therapy.

7

Phantom validation with in-beam PET data

This chapter aims to validate the analytical approach with in-beam PET data of a PMMA phantom, providing a foundation for further translation to real patient cases involving in-beam PET. The experimental PET data were acquired at QST Chiba by Prof. Yamaya's group using the OpenPET system (see Section 3.3.1 for more details about the OpenPET system), and their data are analyzed in this work.

In Section 7.1, the PMMA experiments previously performed at QST Chiba are first presented. The analytical prediction of PED in PMMA based on the MC simulated IDD provided by QST is described. Besides, the β^+ activity calculation from PED in the case of in-beam PET is presented. Section 7.2 presents the outcomes of the validation process, including comparisons between analytical predictions and experimental PET measurements. Finally, Section 7.3 summarizes the main findings and outlines perspectives for future developments.

7.1 Material and methods

7.1.1 Experimental setup

The irradiated PMMA box phantom has dimensions of 150 mm (width) × 90 mm (height) × 150 mm (beam direction). It was positioned in the scanner FOV with the beam aligned along the z-axis. The isocenter position and the geometry setup in side, beam's-eye, and top views are illustrated in Figure 7.1.

The phantom was irradiated with a single spill, and the *mesh2* ripple filter [Tanaka et al., 2022] was applied in the beamline. This aluminum ripple filter broadens the Bragg peak of a monoenergetic beam longitudinally, following a normal distribution with a mean water-equivalent thickness t of 5.4 mm and a standard deviation σ of 1.5 mm [Tanaka and Inaniwa, 2024]. The irradiation was performed using a ^{12}C ion pencil beam with a nominal

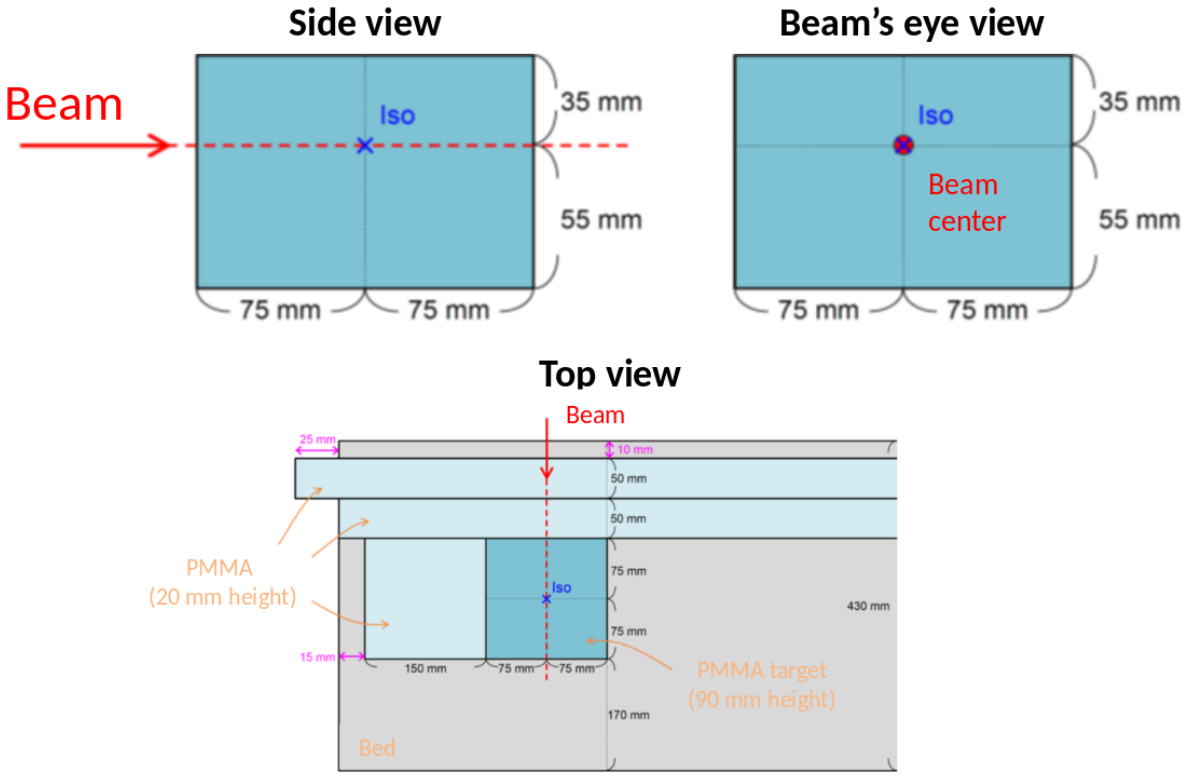

Figure 7.1: The PMMA phantom setup in side, beam's-eye, and top views, courtesy of Prof. Taiga Yamaya, QST Chiba, Japan.

energy of 255.7 MeV/n. Six irradiation configurations were investigated, as summarized in Table 7.1.

Table 7.1: Irradiation cases. The "Un-scanned" configuration corresponds to a single pencil beam (spot) irradiation, whereas in the other cases ion beams were scanned with a spot spacing of 2 mm to produce uniform square fields of the specified dimensions at the isocenter plane. The dose in each case refers to the physical dose at the Bragg peak.

Irradiation cases	**Particle number**	**Beam-on time [ms]**
Un-scanned 1.5 Gy	7.54×10^6	16
Un-scanned 3 Gy	1.51×10^7	34
2x2 cm^2 1.5 Gy	9.14×10^7	213
2x2 cm^2 3 Gy	1.83×10^9	426
4x4 cm^2 1.5 Gy	3.31×10^8	777
4x4 cm^2 3 Gy	6.62×10^8	1553

The OpenPET measurements were initiated prior to beam irradiation to ensure full

acquisition coverage. For data analysis, however, only the measurements acquired from the end of irradiation to 600 s post-irradiation were used. Five reconstruction time frames were generated: 0–60 s, 60-120 s, 60-300 s, 300–600 s and 0–600 s. Image reconstruction was performed at QST using list-mode maximum a-posteriori expectation maximization (MAPEM) reconstruction algorithm [De Pierro, 1995] based on the median root prior (MRP) [Alenius and Ruotsalainen, 1997] with 80 iterations [Tashima, 2024]. The final 3D PET images consisted of 540 × 480 × 480 voxels with an isotropic voxel size of 1.5 mm.

7.1.2 Analytical calculation of PED in PMMA under experimental conditions

As presented in Section 4.2, the analytical calculation of PED requires the dose distribution of the irradiation as well as the associated beam and phantom information. In contrast to patient treatments (cf. Section 6.1.2), the PMMA experiments employed only a single beam energy. Consequently, the dose of all beam spots exhibit the same characteristic shape, namely, the same longitudinal Bragg curve (differing only by scaling factors corresponding to the number of primary particles in each spot). Therefore, the dose distribution of a single spot in PMMA is sufficient for the analytical calculation of the PED. This dose distribution, simulated and provided by QST, was first laterally integrated to obtain the IDD curve in PMMA, and subsequently converted into the reference-material-equivalent depth (hereafter referred to as the QST IDD) using Eq. (4.12) (see Figure 7.2). Moreover,

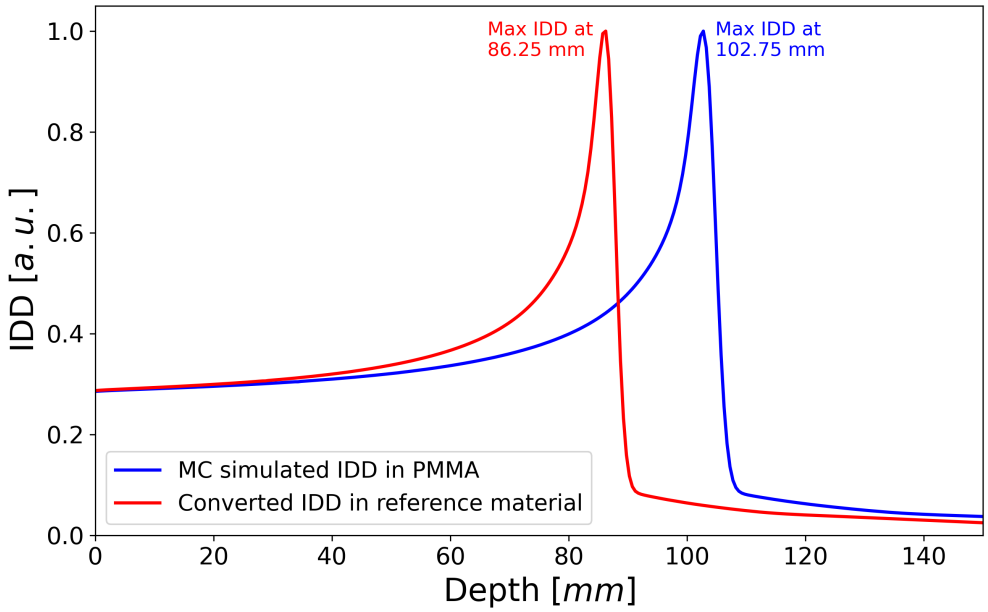

Figure 7.2: IDD curves in PMMA and in the reference material after conversion from a ^{12}C-ion pencil beam with initial nominal energy of 255.7 MeV/n. The blue and red lines represent the simulated IDD in PMMA and the converted IDD in the reference material, respectively.

the presence of the ripple filter along the beam path reduces the initial beam energy and modulates the particle range, resulting in a shallower and broader Bragg peak compared to a purely monoenergetic beam without ripple filter. Since the analytical algorithm is designed for monoenergetic (or quasi-monoenergetic) IDDs, a range-modulation procedure is applied to account for this effect in the analytical calculation, as detailed below.

Starting from a previously validated monoenergetic IDD in the reference material, a series of IDDs shifted in depth by 0.5 mm increments toward shallower depths is first generated, continuing until the rising edge of the QST IDD is reached. By fitting the QST IDD, the weights associated with these shifted IDDs are determined such that their weighted superposition reproduces the measured curve. The resulting weights are then normalized so that their sum equals one.

The reference IDD used for this procedure was obtained by a MC simulation of a monoenergetic ^{12}C-ion pencil beam at 250 MeV/n, as described in Section 4.1. Figure 7.3 shows the normalized QST IDD, the validated reference IDD, and the initial set of 22 shifted curves. Based on the preliminary fitting result, this set was reduced to 11 shifted curves with shifts from 1 mm to 6 mm, excluding those with negligible weights. The final weights are listed in Table 7.2. Figure 7.4 shows that the reconstructed IDD obtained as the weighted sum of the selected shifted curves matches the QST IDD with good agreement.

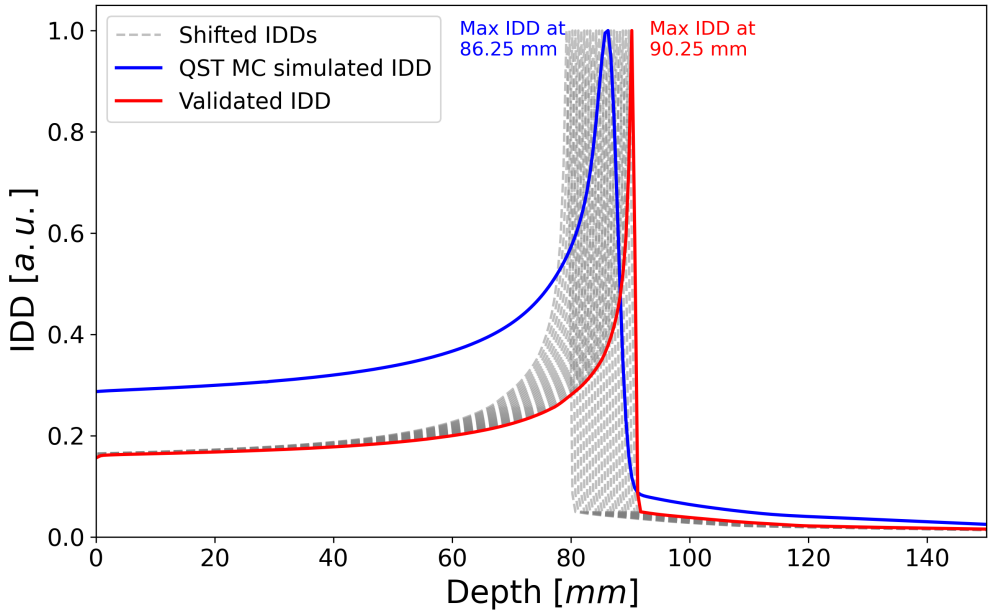

Figure 7.3: Normalized IDDs in the reference material. The blue line represents the IDD curve obtained from a ^{12}C-ion pencil beam with an initial nominal energy of 255.7 MeV/n, with the ripple filter effect applied. The red line represents the validated IDD curve obtained from a ^{12}C-ion pencil beam with an initial nominal energy of 250 MeV/n. The dashed lines represent the shifted curves, generated from the validated IDD curve with a step size of 0.5 mm.

Table 7.2: Weights of the shifted curves obtained from the fitting process.

Shifted Curves	Weights	shifted curves	Weights
Curve 1	0.0659	Curve 7	0.1511
Curve 2	1.0685	Curve 8	0.0887
Curve 3	0.1205	Curve 9	0.0787
Curve 4	0.1052	Curve 10	1.0635
Curve 5	0.1698	Curve 11	0.0323
Curve 6	0.1358		

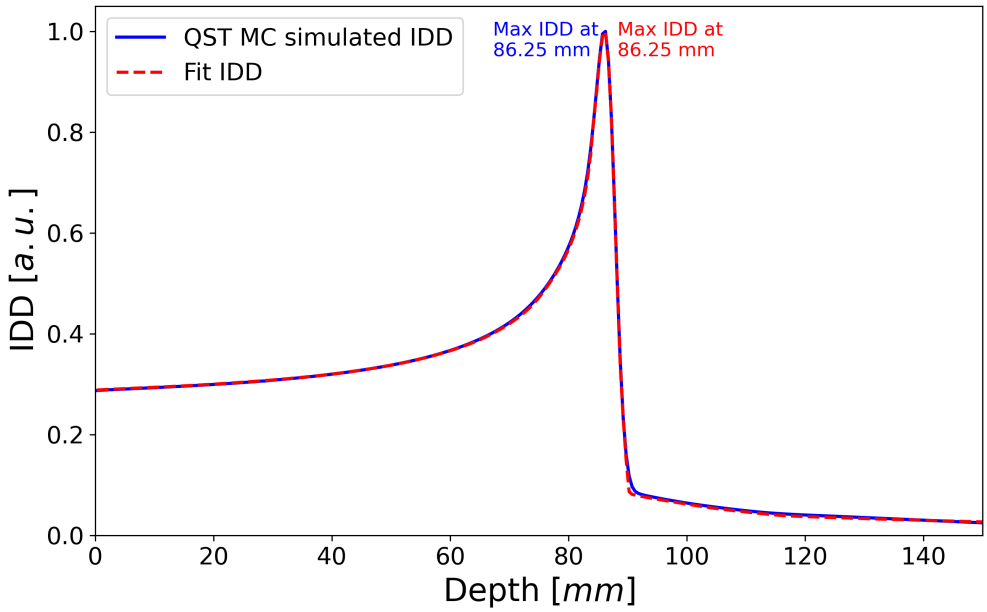

Figure 7.4: Normalized IDDs in the reference material. The blue line represents the QST IDD curve obtained from a ^{12}C-ion pencil beam with an initial nominal energy of 255.7 MeV/n, with the ripple filter applied. The red dashed line represents the normalized reconstructed IDD curve as the weighted sum of the selected shifted curves, with weights obtained from the fitting process.

Once the shifted IDDs and their weights were obtained, the PED corresponding to each IDD was calculated by the analytical approach. To reconstruct the PED corresponding to the QST IDD (i.e., a single beam spot), these PEDs of the shifted IDDs were summed according to their weights. The beam of a single spot and phantom parameters used in the analytical approach are summarized in Table 7.3.

Table 7.3: Beam and phantom parameters

Material characteristics			
	Water	Reference Material	PMMA *
Mean excitation energy [eV]	78	88.48	74.66
Electron density [10^{23}cm^{-3}]	3.34	4.71	3.87
Geometry characteristics			
Nb of voxels (x-axis)	Nb of voxels (y-axis)	Nb of voxels (z-axis)	Voxel size [mm]
150	90	150	1
Beam characteristics			
Mean beam energy [MeV/n]	Position	Initial size [mm]	Div. coef. in air
255.7	(75, 55, 0)	2.625 **	0.00333 ***

Note: * The SPR of PMMA relative to water equals 1.165 and is used to calculate the mean excitation energy for PMMA based on Eq. (4.13).
** The initial beam size used in the analytical method is assumed to be identical in the x and y directions and is taken as the average of the experimental σ_x and σ_y at the entrance surface (75 mm upstream of the isocenter).
*** The beam divergence coefficient in air is averaged over the experimental values in the x and y directions.

7.1.3 β^+ activity calculation for in-beam PET

In general, in-beam PET acquisition begins at the start of ion beam irradiation and continues for some time after the end of the treatment. During irradiation, the pulsed beam delivery is divided into cycles, each consisting of a beam-on phase (spill), during which the beam is active and PEs are continuously produced, and a beam-off phase (pause), during which only radioactive β^+ decay occurs. The resulting in-beam PET images can correspond to the spatial distribution of all β^+ decays occurring within a selected time window during the overall measurement period. To predict the PET image for a given time window, the activity as a function of time for each isotope is first calculated for every spill and pause. The time-dependent activity is then integrated over the selected acquisition time window to obtain the corresponding 3D decay distribution for each isotope. Finally, the decay distributions of all isotopes are summed, followed by the convolution with a Gaussian filter of 10 mm FWHM to account for the smoothing of the imaging process when forming the final PET image.

The following assumptions are adopted when calculating the activity:

- The annihilation position coincides with the location where the PEs come to rest.
- Temporal fluctuations in beam energy, position, and intensity during beam-on phases are neglected.
- A constant PE production rate K_j during the beam-on phases is assumed:

$$K_j = \frac{PE_j}{t_f - t_i} \tag{7.1}$$

  Where PE_j is the total number of isotope j generated during the beam on-phase, and t_i, t_f are its start and end time. Initially, the number of PEs in the phantom is zero, and since the analytical framework provides the number of each PE produced per primary particle, PE_j is obtained by multiplying this normalized value by the number of primaries delivered during this beam-on phase.

- For the PMMA phantom, biological washout effects occurring in living tissues are not considered, so that only the physical decay is modeled.

The activity $A_j(t)$ for each isotope j is calculated using the expressions in Eq. (7.2), with beam-on and beam-off phases treated separately [Parodi et al., 2001]. During the beam-on phase, the formulation accounts for both β^+ decay and the continuous production of PEs, whereas in the beam-off phase only the decay term is included.

$$\begin{cases} A_j(t) = A_j(t_i)e^{-\lambda_{phys,j}(t-t_i)} + \frac{PE_j}{t_f - t_i}(1 - e^{-\lambda_{phys,j}(t-t_i)}) & (1) \\ A_j(t) = A_j(t_i)e^{-\lambda_{phys,j}(t-t_i)} & (2) \end{cases} \tag{7.2}$$

Where j denotes the isotope species; t_i and t_f are the initial and final time of each phase, respectively (with t_i of one phase corresponding to t_f of the previous one); $A_j(t_i)$ is the residual activity at the beginning of the current phase (equal to the activity at t_f of the previous phase); In (1), the first term represents the decay of pre-existing PEs, while the second term accounts for their production during the beam-on phase, assuming a constant production rate as defined in Eq. (7.1).

The 3D decay distribution for each isotope during each phase is then obtained by integrating the corresponding activity:

$$D_j(t_i, t_f; x, y, z) = \int_{t_i}^{t_f} A_j(t)\, dt \tag{7.3}$$

- For beam-on phase:

$$D_j = A_j(t_i)\frac{1 - e^{-\lambda_{phys,j}(t_f - t_i)}}{\lambda_{phys,j}} + \frac{PED_j(x,y,z)}{t_f - t_i}\left[(t_f - t_i) - \frac{1 - e^{-\lambda_{phys,j}(t_f - t_i)}}{\lambda_{phys,j}}\right] \tag{7.4}$$

- For beam-off phase:

$$D_j = A_j(t_i)\frac{1 - e^{-\lambda_{phys,j}(t_f - t_i)}}{\lambda_{phys,j}} \tag{7.5}$$

Since all reconstruction time frames corresponded to the post-irradiation (beam-off) phase, the decay distributions were calculated using Eq. (7.5), where the t_i and t_f denote the start and end times of the respective time frame. Finally the total decay distribution (i.e., the expected annihilation photon counts) was obtained by summing the decay contributions from all considered PEs and was subsequently compared with the measurements.

All six PMMA experiments were performed using a single spill, and the beam-on phase lasted at most 1.553 s among the experiments. Therefore, for square irradiation fields composed of multiple beam spots, it can be assumed that the production of PEs by these beam spots happens at nearly the same time. After the PET image for a single spot was determined, the PET images for square irradiation fields were obtained straightforwardly by applying geometric translations of the single-spot PET and summing the contributions from all spots.

7.1.4 Isotope-dependent scaling of analytical PED predictions

When applying the analytical method to compute the PET images (laterally integrated depth counts) in the 0–60 s time window for the six scenarios, the predicted results were found to be remarkably higher than the corresponding measurements (see Figure 7.5). Since the decay within the 0–60 s window is dominated by short-lived PEs, such as ^{10}C and ^{15}O, this indicates substantial discrepancies between the analytically predicted yields of these isotopes and the experimental yields.

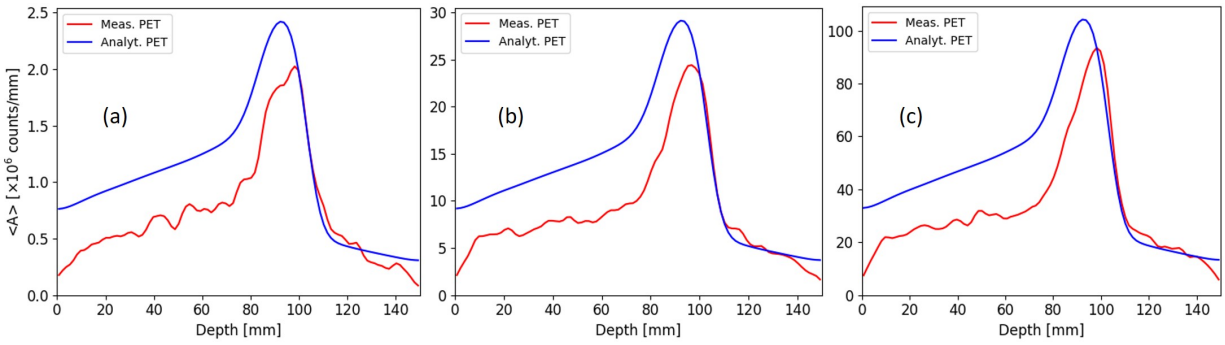

Figure 7.5: (a-c) show the total number of decays per depth within the 0-60 s window of the irradiation cases "Un-scanned 3 Gy", "2x2 cm^2 3 Gy" and "4x4 cm^2 3 Gy", respectively. The measured profiles are in red and the analytical profiles are in blue.

To further correct these deviations in the analytically predicted PE yields, QST provided additional MC-simulated PED in PMMA for single-spot irradiations at the same beam

energy [Sun et al., 2025], which replicated as closely as possible to the experiments using the MC code PHITS [Sato et al., 2024]. Based on these data, isotope-dependent scaling factors were derived and applied to the analytical predictions to improve agreement with the simulated results. Figure 7.6 shows the QST MC–simulated IDPEDs, the original analytical IDPEDs, and the analytical IDPEDs after applying the scaling factors. The scaled analytical IDPEDs were subsequently used for all following analytical predictions.

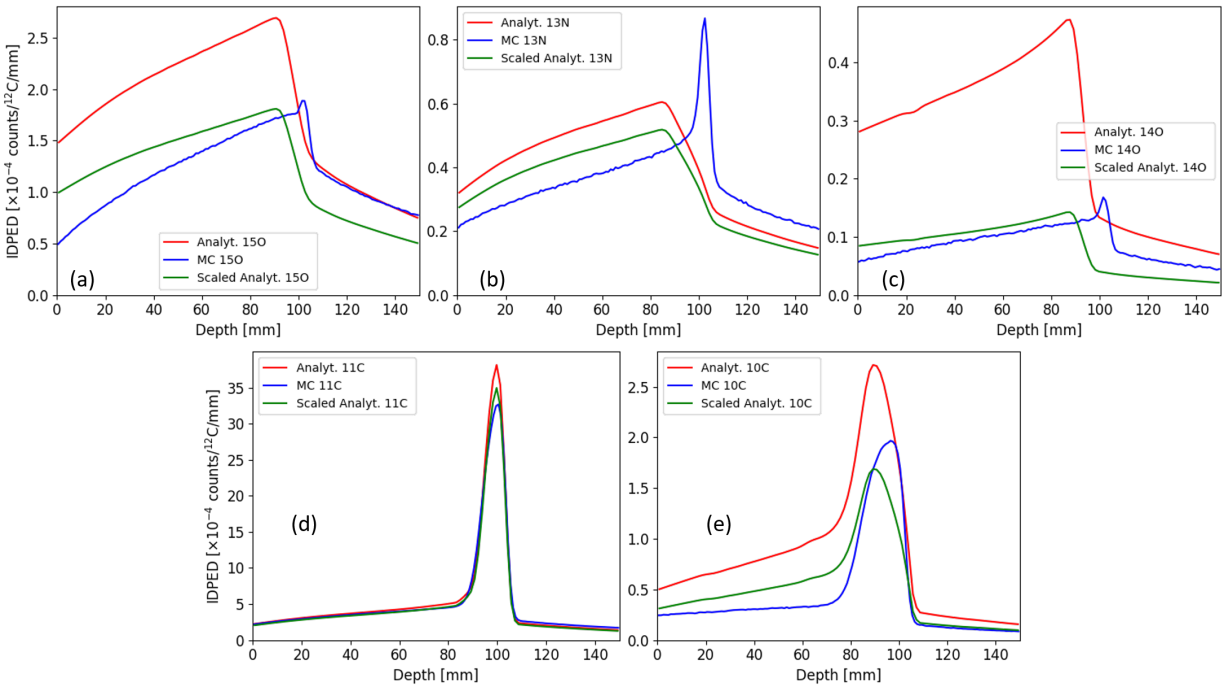

Figure 7.6: (a-d) show the IDPEDs of the five PEs, ^{15}O, ^{13}N, ^{14}O, ^{11}C and ^{10}C. The QST MC simulated profiles are shown in blue, the original analytical profiles in red and the scaled analytical profiles in green. Pronounced discrepancies are observed between the analytically predicted and QST MC–simulated yields for ^{15}O, ^{14}O, and ^{10}C.

7.2 Results

Since the 3 Gy cases provides higher statistics than the 1.5 Gy cases, resulting in lower measurement noise, only the 3 Gy results are presented in this section. For clarity, the activity results presented in this section refer to the total number of decays; for convenience, the term “activity” is used throughout.

Figure 7.7 presents the measured and analytically predicted (with scaling) laterally integrated depth counts for the un-scanned single spot, the 2x2 cm^2 and the 4x4 cm^2 irradiation fields for the measurement time frames of 0–60 s, 60-120 s, 60-300 s, 300–600 s and 0–600 s. Among the five time frames, the largest discrepancies between the predicted and measured results are observed in the 0–60 s interval. In this early time window, the

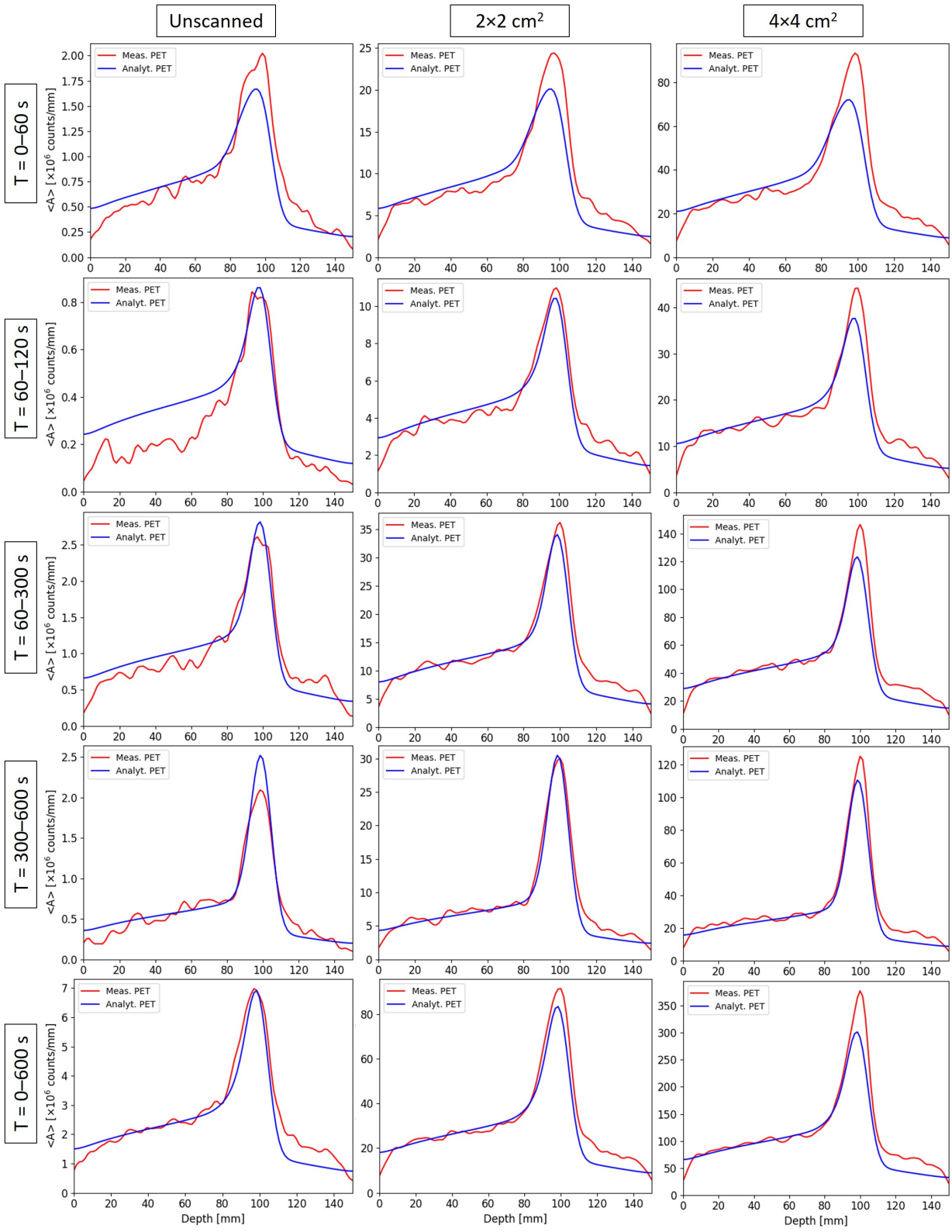

Figure 7.7: The measured (red curves) and analytical (blue curves) laterally integrated activity distributions at the measurement time frames of 0-60 s (1st row), 60-120 s (2nd row), 120-300 s (3rd row), 300-600 s (4th row) and 0-600 s (5th row) of the un-scanned (1st column), 2x2 cm^2 (2nd column), and 4x4 cm^2 (3rd row) irradiation fields.

formation of the activity peak is dominated by the contribution of ^{10}C. As shown in Figure 7.5(e), even after applying a scaling factor to match the analytically predicted $\text{IDPED}_{^{10}C}$ to the MC-simulated result, notable differences remain in both the peak amplitude and the peak position. This explains why the activity prediction exhibits the larger deviation from the measurement in the 0–60 s and time frames. As the time frames shift to later intervals, the agreement between predictions and measurements improves, since the contribution of ^{11}C becomes increasingly dominant.

To quantitatively assess the agreement between the predicted and measured curves in Figure 7.7 in terms of range and overall shape, the differences of the R80 values (shifts) and the NRMSE values (see Section 5.1.2) were calculated. The R80 values were determined after applying a linear interpolation and resampling with a finer bin size of 0.01 mm to estimate the sub-voxel depth position corresponding to 80% of the maximum activity. The error of R80 was estimated by combining contributions from the refined bin size and the error introduced by linear interpolation, which arises from the curvature of the original depth-IDPED curve between data points. For comparisons between measured and analytically predicted distributions, uncertainties were propagated in quadrature. The results are reported in Table 7.4.

Table 7.4: Corresponding shifts (= $\text{R80}_{Meas.}$-$\text{R80}_{Analyt.}$) and NRMSE values for the measured and analytically predicted laterally integrated activity profiles for each irradiation case and each time frame.

		Un-scanned	**2x2 cm^2**	**4x4 cm^2**
0-60 s	Shifts [mm]	-1.34 ± 0.04	-2.00 ± 0.04	-2.04 ± 0.04
	NRMSE [%]	9.19	9.27	10.12
60-120 s	Shifts [mm]	-1.63 ± 0.05	-0.79 ± 0.04	-1.39 ± 0.06
	NRMSE [%]	13.66	6.46	7.35
60-300 s	Shifts [mm]	-2.00 ± 0.05	-1.26 ± 0.05	-1.06 ± 0.04
	NRMSE [%]	7.35	5.81	6.47
300-600 s	Shifts [mm]	-0.85 ± 0.05	-0.97 ± 0.04	-0.72 ± 0.04
	NRMSE [%]	6.36	4.07	4.69
0-600 s	Shifts [mm]	-1.17 ± 0.05	-1.22 ± 0.04	-0.93 ± 0.03
	NRMSE [%]	6.50	6.20	6.95

Higher NRMSE values are observed for the un-scanned case and for the earliest time frame (0–60 s). The larger discrepancies in the 0–60 s interval are mainly attributable to the inaccurate prediction of the $\text{IDPED}_{^{10}C}$, which also leads to longitudinal shifts of approximately 2 mm. As the time frames progress to later intervals, the agreement between prediction and measurement improves, and the corresponding shifts decrease to around

1 mm for the major cases. This trend is consistent with the increasing dominance of longer-lived PE ^{11}C, which is predicted more reliably by the analytical approach and is reflected in the reduced NRMSE values of around 6%.

To assess the agreement between the predicted and measured activity distributions perpendicular to the beam direction (z-axis), the 1D lateral (x) and vertical (y) profiles were evaluated in both the build-up plateau and the peak region for the time frames of 60-300 s and 0-600 s, as shown in Figure 7.8. To reduce the statistical noise, the build-up plateau region was selected between 15 and 36 mm in depth and averaged along the z-axis to obtain a planar activity distribution. Similarly, the peak region was defined between 90 and 100.5 mm and averaged along the z-axis. The lateral (x) profiles were then obtained by integrating the planar activity distributions along the vertical (y) direction for each x-position, while the vertical (y) profiles were derived by integrating the 2D distributions along the lateral (x) direction for each y-position.

Table 7.5 summarizes the FWHM values of the measured and analytical profiles shown in Figure 7.8. The error of FWHM was estimated by the curvature of the original profiles between data points. In the peak region, the differences between measurements and analytical predictions are below 1.5 mm (corresponding to one voxel) for all the cases nd for both time frames. In the plateau region, the differences were slightly larger but remained below 3.0 mm (two voxels), which can be attributed to the lower counting statistics of the measurements in this region.

7.3 Discussion

In this chapter, the analytical approach was validated for the first time using in-beam PET data acquired in a PMMA phantom provided by QST Chiba with their in-house OpenPET system. Initial calculations revealed obvious discrepancies between predicted and measured activity distributions in the early 0–60 s time frame. A detailed analysis showed that these deviations primarily originated from inaccurate analytical predictions of the experimental yields of short-lived PEs, in particular ^{10}C and ^{15}O. To mitigate this effect, isotope-dependent scaling factors were introduced, using MC-simulated yields provided by QST as reference. After applying these corrections, good agreement was achieved for most cases in terms of both range and lateral profiles, especially in later time frames. In particular, the range shifts were below 2 mm for the majority of cases, demonstrating that the analytical approach can reliably reproduce activity distributions measured in in-beam PET scenarios in carbon ion therapy.

Nevertheless, larger discrepancies persisted in the earliest time frame (0–60 s), as reflected by larger range shifts and higher NRMSE values. In addition to the lower measurement statistics of this short acquisition window, these discrepancies can be mainly attributed to limitations in the prediction of short-lived PEs. The limitations in predicting short-lived PEs could not be revealed in the earlier validations with PET measurements from HIT because the corresponding isotopes had largely decayed by the time of offline PET acquisition. Although scaling factors were applied to correct their yields, the spatial ranges

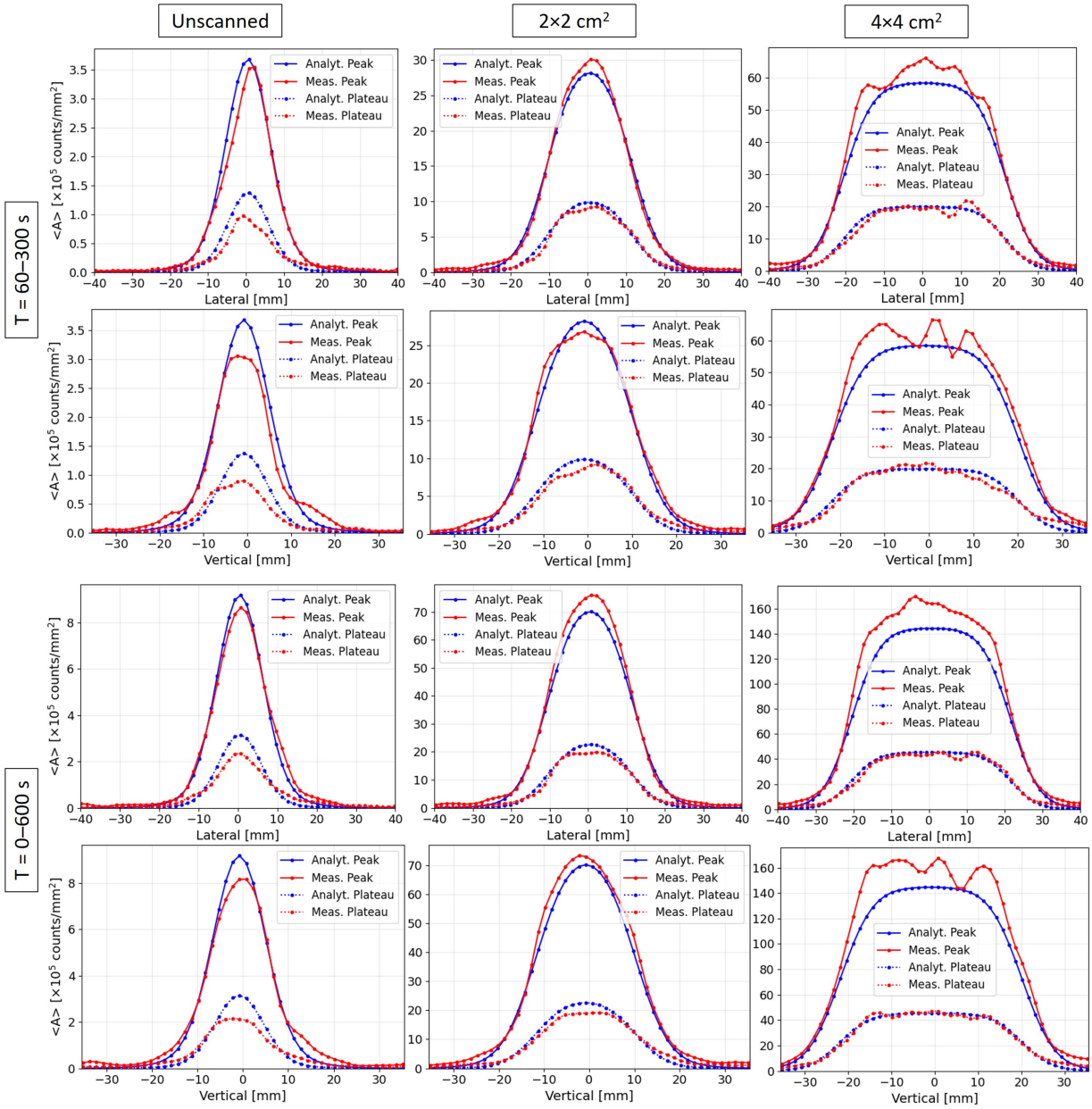

Figure 7.8: Lateral and vertical profiles of measured (red curves) and analytical (blue curves) activity distributions at the peak region (solid lines) and build-up plateau region (dotted lines) for the time frames of 60-300 s and 0-600 s for the un-scanned (1st column), 2x2 cm^2 (2nd column), and 4x4 cm^2 (3rd column) irradiation fields.

Table 7.5: Corresponding FWHM and the FWHM differences for the measured and analytically predicted lateral and vertical activity profiles.

		Un-scanned	2x2 cm^2	4x4 cm^2
T = 60-300 s, Plateau				
Lateral	Meas. [mm]	12.30 ± 0.10	23.20 ± 0.04	38.79 ± 0.03
	Analyt. [mm]	12.81 ± 0.04	22.84 ± 0.01	41.78 ± 0.00
	Diff. [mm]	0.51 ± 0.11	-0.36 ± 0.04	2.99 ± 0.03
Vertical	Meas. [mm]	15.20 ± 0.03	23.07 ± 0.03	39.06 ± 0.04
	Analyt. [mm]	12.80 ± 0.04	22.84 ± 0.01	41.98 ± 0.00
	Diff. [mm]	-2.39 ± 0.05	-0.23 ± 0.03	2.92 ± 0.04
T = 60-300 s, Peak region				
Lateral	Meas. [mm]	12.96 ± 0.04	21.93 ± 0.02	41.32 ± 0.03
	Analyt. [mm]	13.92 ± 0.03	23.30 ± 0.01	42.02 ± 0.00
	Diff. [mm]	0.95 ± 0.05	1.37 ± 0.03	0.71 ± 0.03
Vertical	Meas. [mm]	14.04 ± 0.10	24.41 ± 0.05	41.58 ± 0.04
	Analyt. [mm]	13.91 ± 0.03	23.30 ± 0.01	42.02 ± 0.00
	Diff. [mm]	-0.12 ± 0.10	-1.11 ± 0.05	0.44 ± 0.04
T = 0-600 s, Plateau				
Lateral	Meas. [mm]	13.67 ± 0.06	23.10 ± 0.01	40.77 ± 0.10
	Analyt. [mm]	12.76 ± 0.04	22.80 ± 0.01	41.97 ± 0.00
	Diff. [mm]	-0.91 ± 0.07	-0.30 ± 0.02	1.20 ± 0.10
Vertical	Meas. [mm]	15.42 ± 0.07	24.32 ± 0.01	40.06 ± 0.10
	Analyt. [mm]	12.76 ± 0.04	22.80 ± 0.01	41.97 ± 0.00
	Diff. [mm]	-2.66 ± 0.08	-1.52 ± 0.02	1.91 ± 0.10
T = 0-600 s, Peak region				
Lateral	Meas. [mm]	14.55 ± 0.04	22.77 ± 0.03	41.66 ± 0.03
	Analyt. [mm]	13.90 ± 0.03	23.24 ± 0.01	42.00 ± 0.00
	Diff. [mm]	-0.65 ± 0.05	0.47 ± 0.03	0.35 ± 0.03
Vertical	Meas. [mm]	14.76 ± 0.05	23.97 ± 0.06	41.95 ± 0.04
	Analyt. [mm]	13.89 ± 0.02	23.23 ± 0.01	42.00 ± 0.00
	Diff. [mm]	-0.87 ± 0.05	-0.74 ± 0.06	0.05 ± 0.04

of the corresponding IDPEDs remained unchanged (see Figure 7.6). As inaccuracies in the predicted ranges of short-lived PEs directly affect the early activity distribution, this limitation has a pronounced impact on the PET signal shortly after irradiation.

It should be noted that the analytical model was calibrated using MC simulations performed with the Geant4 toolkit and was extensively validated against MC results in various scenarios in previous chapters, where good agreement was observed. Consequently, the remaining discrepancies between measured and analytically predicted activity distributions are likely related to limitations in the underlying nuclear reaction models and cross-section data implemented in Geant4, particularly for light fragment production. This interpretation is consistent with the findings of Chacon et al. [2024], who reported similar deviations and attributed them to deficiencies in Geant4-based descriptions of light fragment yields.

Recent work by Sun et al. [2025] from QST Chiba performed PHITS simulations of monoenergetic carbon-ion beams in PMMA, and reported excellent agreement with the OpenPET measurements, achieving range errors (ΔR80) within 2 mm for both short and long time frames. Compared to their study, the longitudinal activity profiles obtained in the present work show less favorable agreement with measurements, although the range prediction capability remains comparable, with shifts also within 2 mm. Moreover, the high-quality MC results reported by Sun et al. [2025] highlight a potential pathway for further improving the analytical approach. In particular, using PHITS-simulated IDPEDs in the reference material or experimental yields from measurements to refine the parameters of the analytical modeling functions could substantially enhance the prediction accuracy for short-lived PEs.

The analytical approach demonstrated computational efficiency and potential for fast, near real-time prediction of PED and in-beam PET activity distributions. However, the current validation was restricted to the homogeneous PMMA phantom and monoenergetic ion beam. Future work should extend the validation to heterogeneous phantoms and patient-specific geometries. Prior to such studies, further refinement of the model parameters based on improved MC simulations or directly on experimental measurement data will be required.

8

Conclusion and outlook

Cancer remains one of the leading causes of morbidity and mortality worldwide. Among the available treatment modalities, radiotherapy plays a central role, and particle therapy has emerged as a highly promising approach due to its superior dose conformity and normal-tissue sparing capabilities. In particular, carbon ion therapy offers distinct physical and biological advantages over conventional photon therapy, including a sharp Bragg peak, reduced lateral scattering, and an increased relative biological effectiveness. These characteristics enable highly conformal dose delivery, especially for radioresistant and deeply seated tumors. However, the same properties also make carbon ion therapy highly sensitive to range uncertainties, which may compromise treatment accuracy and clinical outcome.

Positron emission tomography (PET)–based monitoring is currently the most widely used approach for in vivo range verification in carbon ion therapy. By comparing a predicted β^+ activity distributions (derived from predicted positron emitter distributions (PED)) to the measured PET data, the delivered treatment can be verified. The central objective of this thesis was the development and comprehensive validation of an analytical framework for predicting PED and β^+ activity distributions in carbon ion therapy, with the aim of enabling a fast, accurate, and clinically applicable computational method to support range verification.

Chapter 4 provides a detailed description of the development of the analytical framework. A 1D analytical method takes a reference laterally integrated depth dose (IDD) as input and predicts the corresponding reference laterally integrated depth positron emitter distribution (IDPED). Subsequently, a pencil beam algorithm (PBA) based framework incorporating the material information and Gaussian-modeled lateral PED parameters is used to extend the 1D reference IDPED into 3D PED in real media.

The 1D analytical approach originates from a filtering method initially developed for proton therapy, which converts dose profiles into 1D PED [Parodi and Bortfeld, 2006]. A key advantage of this method is its energy independence, meaning that the corresponding

PED can be predicted directly from arbitrary dose profiles without explicit knowledge of the beam energy [Parodi and Bortfeld, 2006]. However, when the filtering method to is applied to carbon ion therapy, this property no longer holds, as the energy dependence of PE production becomes more complex [Hofmann et al., 2019]. Nevertheless, the filtering approach remains capable of accurately predicting key positions of the PED, such as the distal fall-off position. By introducing energy-dependent modeling functions in combination with the filtering approach, a 1D analytical method was developed to predict IDPED from IDD for carbon ions and was preliminarily validated by [Hofmann et al., 2019]. Subsequent validation using patient data by Vasic et al. [2024] revealed its limitation in handling highly heterogeneous geometries. In addition, the original formulation considered only two positron emitters (PEs), ^{11}C and ^{15}O, whereas other relevant isotopes should also be taken into account. To address these limitations, Chapter 4 introduced several improvements to the original 1D approach, including the consideration of additional PE channels, refined modeling functions, and a novel mapping strategy to better account for longitudinal heterogeneity effects in projectile PED. Besides, another contribution of Chapter 4 is the development of the 3D PED calculation framework. By drawing an analogy to the PBA widely used for 3D dose calculation, an analytical method for predicting 3D PED was proposed for the first time. This framework integrated the improved 1D analytical model with medium and beam information, enabling the prediction of full 3D PED using 3D dose distributions as input.

In Chapter 5, the analytical framework was first validated by in-silico studies using Monte Carlo (MC) simulations as the reference standard. A slab phantom with longitudinal heterogeneity was initially employed to validate the longitudinal heterogeneity correction implemented in the analytical approach. The range shifts between the analytically calculated and the MC-simulated IDPEDs were below 0.8 mm, and the corresponding normalized root mean square error (NRMSE) values were smaller than 4%, confirming the validity of the longitudinal heterogeneity correction. Another slab phantom with both longitudinal and lateral heterogeneity was employed to validate the lateral heterogeneity correction. In this configuration, the upper and lower halves of a single pencil beam traversed two distinct parts of the phantoms with different material compositions. Submillimeter shifts were observed between MC simulations and analytical predictions for all cases, however, noticeable discrepancies appeared in the distal region of the PED. This finding highlights an intrinsic limitation of the ray-casting method employed for lateral heterogeneity correction, as particle scattering induces lateral blurring, whereas the ray-casting approach accounts for heterogeneities in a straight-line propagation manner. It should be noted that such extreme configurations where a single pencil beam traverses tissues with pronounced lateral heterogeneity across its cross section are unlikely to occur in realistic clinical scenarios. This was further confirmed by subsequent validation studies using anatomical geometries from four patient cases, in which the limitations of the ray-casting method were found to be negligible. Gamma analysis comparing the MC-simulated and analytically predicted PED yielded passing rates above 99% for the 2%/2 mm criteria, and the IDPED shifts remained below 1 mm for all cases. Overall, these in-silico studies demonstrated good agreement between analytical predictions and MC results in terms of both range and PED across a

variety of irradiation configurations.

In Chapter 6, the analytical method was validated under real clinical conditions by comparing its predictions with both MC simulations and offline PET measurements for four patient cases (one brain tumor, one head/neck tumor, one liver tumor, and one pelvic tumor) treated at the Heidelberg Ion Therapy Center (HIT). MC simulations were carefully tuned to reproduce the HIT MC framework, which serves as the clinical gold standard and underlies the treatment planning system (TPS) at HIT, enabling the MC simulations of this work to serve as a reliable reference for evaluating the analytical predictions. The comparison between analytically predicted and MC-simulated activity distributions demonstrated good agreement, with mean longitudinal shifts below 0.5 mm and mean NRMSE values below 2%, confirming that the analytical method accurately predicts PED in terms of both range and amplitude. The analytical predictions were then compared with measured PET data. The longitudinal shifts maps were evaluated and investigated with respect to published work. For the brain and head&neck cases, the analytical results agreed well with earlier findings, and the observed mean most-likely-shift (MLS) values fell well within commonly applied clinical safety margins. The liver case exhibited range shift patterns and a mean MLS value closely matching previously published results. For the pelvic case, larger and more scattered range deviations were observed, however, these were not associated with pronounced continuous over-range regions and are likely influenced by higher image noise due to low counting statistics and potential uncertainties in the biological washout model.

Overall, Chapter 6 demonstrates that the analytical approach achieves clinically relevant range prediction accuracy while offering a substantial gain in computational speed compared to full MC simulations in the considered clinical scenarios. These findings support its potential use for offline PET-based treatment verification and motivate further investigation with in-beam PET which is less affected by washout-induced signal degradation and also more sensitive to a wider range of PEs, including short-lived ones.

Chapter 7 presents a preliminary validation of the analytical approach using in-beam PET data acquired in a polymethylmethacrylate phantom at the National Institutes for Quantum Science and Technology (QST) Chiba with the in-house OpenPET system and provided for this work. In the initial analysis, large discrepancies between the predicted and measured activity distributions were observed in early measurement time frames. A detailed analysis showed that these deviations originate primarily from inaccuracies in the predicted yields and ranges of short-lived isotopes. The introduction of isotope-dependent scaling factors, derived from MC simulations provided by QST, significantly improved the agreement with experimental data. As a result, the range shifts were below 2 mm for the majority of cases, demonstrating that the analytical approach can reliably reproduce activity distributions measured in in-beam PET scenarios in carbon ion therapy.

Beyond the specific validation studies presented in this thesis, the analytical framework offers several intrinsic advantages. Compared to MC simulations, the method provides predictions at least 40 times faster, making it compatible with clinical workflows. Moreover, it is based on the traditional pencil beam algorithm and employs a data structure similar to that commonly used in TPS, making its integration into an analytical TPS feasible. Analogous to the continued role of PBA for dose calculation in the era of GPU-accelerated MC

techniques, the proposed framework is expected to remain valuable as a rapid, robust, and physically motivated verification tool. Its reliance on dose-based filtering and range-related features further supports applicability across different facilities and beam configurations, making it a pragmatic and scalable solution that bridges accuracy, computational efficiency, and clinical usability.

Importantly, the remaining limitations of the analytical predictions for short-lived isotopes indicate intrinsic uncertainties in the underlying nuclear reaction models and cross-section data in the Geant4 simulations that were used to generate the reference dataset, rather than deficiencies of the analytical framework itself. The findings therefore highlight the need for further improvements in the modeling of short-lived PEs. In this context, the ongoing and planned collaboration with QST Chiba provides a unique opportunity to further validate and refine the analytical framework using additional PHITS MC simulations or in-beam PET data acquired with the OpenPET under well controlled conditions in relevant homogeneous phantoms. Moreover, validation using real clinical in-beam PET data is planned to be performed in a forthcoming study building upon this thesis work and could be performed on the basis of the ongoing pilot clinical trial with the unique OpenPET system at QST Chiba [Tashima et al., 2024]. Together, these efforts are expected to enable validation under real clinical conditions and to guide the translation of the analytical approach into routine clinical practice.

Acknowledgements

This thesis would not have been possible without the support and guidance of many people.

First and foremost, I would like to express my deepest gratitude to my supervisor, Prof. Dr. Katia Parodi. From the very beginning of my PhD application to the completion of this thesis nearly five years later, every important milestone along this journey has been inseparable from her support, guidance, and encouragement. All the achievements I have made during this period are deeply rooted in her patient supervision. I am also very grateful for her financial support, which allowed me to focus better on my research. Her rigorous academic attitude, sharp scientific thinking, and profound knowledge have set an example for my future career. It is truly my great honor to have her as my PhD supervisor, and I sincerely appreciate that she chose me as her PhD student. This has been my great fortune.

I would like to express my special thanks to Dr. Marco Pinto, my second supervisor. At the early stage of my PhD, he provided me with tremendous support, and we had frequent and in-depth discussions on many details of the algorithm implementation. With his help, I was able to smoothly enter the middle stage of my PhD and gradually develop the ability to conduct research independently. Similar to Prof. Parodi, he has been involved in the supervision of my PhD project and the review of my publications, witnessing every step of my progress. I have benefited greatly from his guidance.

I would like to thank Prof. Dr. Julia Bauer and Dr. Thomas Tessonnier for all their help and support in my research. Prof. Bauer provided me with patient data from HIT and always gave detailed answers whenever I encountered problems. Dr. Tessonnier carefully explained to me the usage of phase space data. Their support made a remarkable contribution to my work on validating the analytical approach using offline PET data from HIT.

I would also like to thank Prof. Dr. Taiga Yamaya and his team at QST Chiba, including Dr. Hideaki Tashima, for providing in-beam PET data and valuable technical details. I am equally grateful to Prof. Dr. Taku Inaniwa and his team for providing MC simulation data. Thanks to their support, the validation of the analytical approach using in-beam PET data could be successfully carried out.

I would also like to thank the other members of my PhD defense committee, in addition to my supervisor Prof. Parodi: PD Dr. George Dedes for serving as the reviewer and for the additional effort devoted to reviewing my thesis; Prof. Dr. Marco Riboldi for serving as the chairperson; Prof. Dr. Otmar Biebel for serving as the additional examiner; and Prof. Dr. Barbara Ercalano for serving as the substitute. I sincerely appreciate their time

and willingness to participate in my defense.

I would like to thank all members of the Department of Medical Physics in Garching for providing a friendly and supportive research environment, including Ze, Lianren, Beatrice, Maxin, and many others. In particular, I would like to thank my confidante Dr. Zhuojie Sui. Our lunchtime conversations were among the few moments each day when I could truly relax. Having a close friend in the same workplace is like having a "comrade-in-arms", and our friendship has given me precious strength to move forward.

I would also like to thank all the friends I met in Munich, Yan, Jiao, Yue, De, Ke, Julian, Christian, and especially Dr. Minqi Liao, who brought a lot of color to my life during this long journey.

I gratefully acknowledge the financial support from the China Scholarship Council (CSC) and LMU, which made this research possible.

Finally, I would like to thank my mother Yan Hu (if I have any intelligence, it must come from her), my father Yinhe Du, and my 15-minute older twin brother Tianyu Du, for their love, understanding, and unwavering support throughout this challenging but rewarding journey. I would also like to thank myself for my courage in facing the unknown and for my persistence throughout this journey. I have truly done a good job.

Bibliography

Proton delivery system conventions, 2021. Taken from the .decimal dosimetry user guide, `https://apps.dotdecimal.com/doku.php?id=dosimetry:userguide:proton_delivery_system_conventions`, accessed on 17.07.2025.

S. Agostinelli, J. Allison, K. a. Amako, J. Apostolakis, H. Araujo, P. Arce, M. Asai, D. Axen, S. Banerjee, G. Barrand, et al. GEANT4—a simulation toolkit. *Nuclear instruments and methods in physics research section A: Accelerators, Spectrometers, Detectors and Associated Equipment*, 506(3):250–303, 2003.

G. Akamatsu, H. Tashima, S. Takyu, H. G. Kang, Y. Iwao, M. Takahashi, E. Yoshida, and T. Yamaya. Design consideration of compact cardiac TOF-PET systems: a simulation study. *Physics in Medicine & Biology*, 66(7):074002, 2021.

S. Alenius and U. Ruotsalainen. Bayesian image reconstruction for emission tomography based on median root prior. *European journal of nuclear medicine*, 24(3):258–265, 1997.

U. Amaldi, S. Braccini, and P. Puggioni. High frequency linacs for hadrontherapy. *Reviews of Accelerator Science and Technology*, 2(01):111–131, 2009.

C. Ammar, K. Frey, J. Bauer, C. Melzig, S. Chiblak, M. Hildebrandt, D. Unholtz, C. Kurz, S. Brons, J. Debus, et al. Comparing the biological washout of β^+-activity induced in mice brain after 12C-ion and proton irradiation. *Physics in Medicine & Biology*, 59(23): 7229, 2014.

F. Attanasi, A. Knopf, K. Parodi, H. Paganetti, T. Bortfeld, V. Rosso, and A. Del Guerra. Extension and validation of an analytical model for in vivo PET verification of proton therapy—a phantom and clinical study. *Physics in Medicine & Biology*, 56(16):5079, 2011.

F. H. Attix. *Introduction to radiological physics and radiation dosimetry*. John Wiley & Sons, 2008.

D. L. Bailey, M. N. Maisey, D. W. Townsend, and P. E. Valk. *Positron emission tomography*, volume 2. Springer, 2005.

V. Balakin, A. Bazhan, A. Pryanichnikov, A. Shemyakov, et al. Updated status of proton synchrotrons for radiation therapy. *Proc. RuPAC*, 21:120, 2021.

J. Bauer, D. Unholtz, F. Sommerer, C. Kurz, T. Haberer, K. Herfarth, T. Welzel, S. E. Combs, J. Debus, and K. Parodi. Implementation and initial clinical experience of offline PET/CT-based verification of scanned carbon ion treatment. *Radiotherapy and Oncology*, 107(2):218–226, 2013.

J. Bauer, F. Sommerer, A. Mairani, D. Unholtz, R. Farook, J. Handrack, K. Frey, T. Marcelos, T. Tessonnier, S. Ecker, B. Ackermann, M. Ellerbrock, J. Debus, and K. Parodi. Integration and evaluation of automated Monte Carlo simulations in the clinical practice of scanned proton and carbon ion beam therapy. *Physics in Medicine & Biology*, 59(16): 4635, jul 2014.

J. Berthold, J. Pietsch, N. Piplack, C. Khamfongkhruea, J. Thiele, T. Hölscher, G. Janssens, J. Smeets, E. Traneus, S. Löck, et al. Detectability of anatomical changes with prompt-gamma imaging: First systematic evaluation of clinical application during prostate-cancer proton therapy. *International Journal of Radiation Oncology* Biology* Physics*, 117(3): 718–729, 2023.

S. Bertschi, K. Stützer, J. Berthold, J. Pietsch, J. Smeets, G. Janssens, and C. Richter. Potential margin reduction in prostate cancer proton therapy with prompt gamma imaging for online treatment verification. *Physics and Imaging in Radiation Oncology*, 26:100447, 2023.

H. Bethe. Zur theorie des durchgangs schneller korpuskularstrahlen durch materie. *Annalen der Physik*, 397(3):325–400, 1930.

M. G. Bisogni, A. Attili, G. Battistoni, N. Belcari, N. Camarlinghi, P. Cerello, S. Coli, A. Del Guerra, A. Ferrari, V. Ferrero, et al. INSIDE in-beam positron emission tomography system for particle range monitoring in hadrontherapy. *Journal of medical imaging*, 4(1): 011005–011005, 2017.

F. Bloch. Bremsvermögen von Atomen mit mehreren Elektronen. *Zeitschrift für Physik*, 81 (5):363–376, 1933.

T. Böhlen, F. Cerutti, M. Chin, A. Fassò, A. Ferrari, P. G. Ortega, A. Mairani, P. R. Sala, G. Smirnov, and V. Vlachoudis. The FLUKA code: developments and challenges for high energy and medical applications. *Nuclear data sheets*, 120:211–214, 2014.

D. Bolst, G. A. Cirrone, G. Cuttone, G. Folger, S. Incerti, V. Ivanchenko, T. Koi, D. Mancusi, L. Pandola, F. Romano, et al. Validation of Geant4 fragmentation for heavy ion therapy. *Nuclear Instruments and Methods in Physics Research Section A: Accelerators, Spectrometers, Detectors and Associated Equipment*, 869:68–75, 2017.

D. Borys, J. Baran, K. Brzeziński, J. Gajewski, N. Chug, A. Coussat, E. Czerwiński, M. Dadgar, K. Dulski, K. V. Eliyan, et al. ProTheRaMon—a GATE simulation framework for proton therapy range monitoring using PET imaging. *Physics in Medicine & Biology*, 67(22):224002, 2022.

F. Bray, M. Laversanne, H. Sung, J. Ferlay, R. L. Siegel, I. Soerjomataram, and A. Jemal. Global cancer statistics 2022: Globocan estimates of incidence and mortality worldwide for 36 cancers in 185 countries. *CA: a cancer journal for clinicians*, 74(3):229–263, 2024.

C. A. Burnham, S. Aronow, and G. L. Brownell. A hybrid positron scanner. *Physics in Medicine & Biology*, 15(3):517, 1970.

T. Ceccotti, A. Lévy, H. Popescu, F. Réau, P. d'Oliveira, P. Monot, J. Geindre, E. Lefebvre, and P. Martin. Proton acceleration with high-intensity ultrahigh-contrast laser pulses. *Physical review letters*, 99(18):185002, 2007.

A. Chacon, S. Guatelli, H. Rutherford, D. Bolst, A. Mohammadi, A. Ahmed, M. Nitta, F. Nishikido, Y. Iwao, H. Tashima, et al. Comparative study of alternative Geant4 hadronic ion inelastic physics models for prediction of positron-emitting radionuclide production in carbon and oxygen ion therapy. *Physics in Medicine & Biology*, 64(15): 155014, 2019.

A. Chacon, H. Rutherford, A. Hamato, M. Nitta, F. Nishikido, Y. Iwao, H. Tashima, E. Yoshida, G. Akamatsu, S. Takyu, et al. A quantitative assessment of Geant4 for predicting the yield and distribution of positron-emitting fragments in ion beam therapy. *Physics in Medicine & Biology*, 69(12):125015, 2024.

R. A. Chandra, F. K. Keane, F. E. Voncken, and C. R. Thomas. Contemporary radiotherapy: present and future. *The Lancet*, 398(10295):171–184, 2021.

K. Choi, S. B. Mein, B. Kopp, G. Magro, S. Molinelli, M. Ciocca, and A. Mairani. FRoG—a new calculation engine for clinical investigations with proton and carbon ion beams at CNAO. *Cancers*, 10(11):395, 2018.

W. Chu, B. Ludewigt, and T. Renner. Instrumentation for treatment of cancer using proton and light-ion beams. *Review of Scientific Instruments*, 64(8):2055–2122, 1993.

S. E. Combs, J. Bauer, D. Unholtz, C. Kurz, T. Welzel, D. Habermehl, T. Haberer, J. Debus, and K. Parodi. Monitoring of patients treated with particle therapy using positron-emission-tomography (PET): the MIRANDA study. *BMC cancer*, 12:1–6, 2012.

M. Conti and B. Bendriem. The new opportunities for high time resolution clinical TOF PET. *Clinical and Translational Imaging*, 7(2):139–147, 2019.

B. Dai, M. E. Daube-Witherspoon, S. McDonald, M. E. Werner, M. J. Parma, M. J. Geagan, V. Viswanath, and J. S. Karp. Performance evaluation of the PennPET explorer with expanded axial coverage. *Physics in Medicine & Biology*, 68(9):095007, 2023.

A. R. De Pierro. A modified expectation maximization algorithm for penalized likelihood estimation in emission tomography. *IEEE transactions on medical imaging*, 14(1):132–137, 1995.

J. Deasy. A proton dose calculation algorithm for conformal therapy simulations based on molière's theory of lateral deflections. *Medical Physics*, 25(4):476–483, 1998.

T. R. DeGrado, T. G. Turkington, J. J. Williams, C. W. Stearns, J. M. Hoffman, and R. E. Coleman. Performance characteristics of a whole-body PET scanner. *Journal of Nuclear Medicine*, 35(8):1398–1406, 1994.

P. Dendooven, H. Buitenhuis, F. Diblen, P. Heeres, A. Biegun, F. Fiedler, M. Van Goethem, E. Van der Graaf, and S. Brandenburg. Short-lived positron emitters in beam-on PET imaging during proton therapy. *Physics in Medicine & Biology*, 60(23):8923, 2015.

S. Dowdell, C. Grassberger, G. Sharp, and H. Paganetti. Interplay effects in proton scanning for lung: a 4D Monte Carlo study assessing the impact of tumor and beam delivery parameters. *Physics in Medicine & Biology*, 58(12):4137, 2013.

T. Du, J. Bauer, K. Parodi, and M. Pinto. An analytical approach to predict 3D positron emitter distribution in carbon ion therapy. *Physics in Medicine and Biology*, 2025.

J. Dudouet, D. Cussol, D. Durand, and M. Labalme. Benchmarking Geant4 nuclear models for hadron therapy with 95 MeV/nucleon carbon ions. *Phys. Rev. C*, 89:054616, 2014.

M. Durante and J. S. Loeffler. Charged particles in radiation oncology. *Nature reviews Clinical oncology*, 7(1):37–43, 2010.

M. Durante and H. Paganetti. Nuclear physics in particle therapy: a review. *Reports on Progress in Physics*, 79(9):096702, 2016.

T. Elsässer, W. K. Weyrather, T. Friedrich, M. Durante, G. Iancu, M. Krämer, G. Kragl, S. Brons, M. Winter, K.-J. Weber, et al. Quantification of the relative biological effectiveness for ion beam radiotherapy: direct experimental comparison of proton and carbon ion beams and a novel approach for treatment planning. *International Journal of Radiation Oncology* Biology* Physics*, 78(4):1177–1183, 2010.

M. Engelsman, E. Rietzel, and H. M. Kooy. Four-dimensional proton treatment planning for lung tumors. *International Journal of Radiation Oncology* Biology* Physics*, 64(5): 1589–1595, 2006.

W. Enghardt, P. Crespo, F. Fiedler, R. Hinz, K. Parodi, J. Pawelke, and F. Poenisch. Charged hadron tumour therapy monitoring by means of PET. *Nuclear Instruments and Methods in Physics Research Section A: Accelerators, Spectrometers, Detectors and Associated Equipment*, 525(1-2):284–288, 2004.

E. Feldmeier, T. Haberer, M. Galonska, R. Cee, S. Scheloske, and A. Peters. The first magnetic field control (B-train) to optimize the duty cycle of a synchrotron in clinical operation. *Proceedings of IPAC2012, New Orleans, Louisiana, USA*, 2012.

V. Ferrero, E. Fiorina, M. Morrocchi, F. Pennazio, G. Baroni, G. Battistoni, N. Belcari, N. Camarlinghi, M. Ciocca, A. Del Guerra, et al. Online proton therapy monitoring: clinical test of a Silicon-photodetector-based in-beam PET. *Scientific reports*, 8(1):4100, 2018.

E. Fiorina, V. Ferrero, F. Pennazio, G. Baroni, G. Battistoni, N. Belcari, P. Cerello, N. Camarlinghi, M. Ciocca, A. Del Guerra, et al. Monte Carlo simulation tool for online treatment monitoring in hadrontherapy with in-beam PET: a patient study. *Physica medica*, 51:71–80, 2018.

E. Fiorina, V. Ferrero, G. Baroni, G. Battistoni, N. Belcari, N. Camarlinghi, P. Cerello, M. Ciocca, M. De Simoni, M. Donetti, et al. Detection of interfractional morphological changes in proton therapy: A simulation and in vivo study with the INSIDE in-beam PET. *Frontiers in Physics*, 8:578388, 2021.

J. Flanz, S. Durlacher, M. Goitein, A. Levine, P. Reardon, and A. Smith. Overview of the MGH-Northeast Proton Therapy Center plans and progress. *Nuclear Instruments and Methods in Physics Research Section B: Beam Interactions with Materials and Atoms*, 99 (1-4):830–834, 1995.

D. B. Flint, S. J. Bright, C. McFadden, T. Konishi, D. K. Martinus, M. Manandhar, M. B. Kacem, L. Bronk, and G. O. Sawakuchi. An empirical model of carbon-ion relative biological effectiveness based on the linear correlation between radiosensitivity to photons and carbon ions. *Physics in Medicine & Biology*, 69(24):245011, 2024.

P. Fossati, S. Molinelli, N. Matsufuji, M. Ciocca, A. Mirandola, A. Mairani, J. Mizoe, A. Hasegawa, R. Imai, T. Kamada, et al. Dose prescription in carbon ion radiotherapy: a planning study to compare NIRS and LEM approaches with a clinically-oriented strategy. *Physics in Medicine & Biology*, 57(22):7543, 2012.

M. C. Frese, K. Y. Victor, R. D. Stewart, and D. J. Carlson. A mechanism-based approach to predict the relative biological effectiveness of protons and carbon ions in radiation therapy. *International Journal of Radiation Oncology* Biology* Physics*, 83(1):442–450, 2012.

K. Frey, J. Bauer, D. Unholtz, C. Kurz, M. Krämer, T. Bortfeld, and K. Parodi. TPSPET—A TPS-based approach for in vivo dose verification with PET in proton therapy. *Physics in Medicine & Biology*, 59(1):1, 2013.

K. Frey, D. Unholtz, J. Bauer, J. Debus, C. H. Min, T. Bortfeld, H. Paganetti, and K. Parodi. Automation and uncertainty analysis of a method for in-vivo range verification in particle therapy. *Physics in Medicine & Biology*, 59(19):5903, sep 2014.

J.-J. Gaimard and K.-H. Schmidt. A reexamination of the abrasion-ablation model for the description of the nuclear fragmentation reaction. *Nuclear Physics A*, 531(3-4):709–745, 1991.

Z. Gao, X. Zhang, Y. Zhang, Y. Ju, L. Chen, H. Ge, F. Ma, Z. Chen, and W. Yang. Benchmarking GEANT4 nuclear models for light fragments of 80.5 MeV/u carbon ions bombarding heavy-metal targets. *Physical Review C*, 107(6):064618, 2023.

J. Góra, S. Grosshagauer, P. Fossati, M. Mumot, M. Stock, M. Schafasand, and A. Carlino. The sensitivity of radiobiological models in carbon ion radiotherapy (CIRT) and its consequences on the clinical treatment plan: Differences between LEM and MKM models. *Journal of Applied Clinical Medical Physics*, 25(7):e14321, 2024.

S. Grosshagauer, P. Fossati, M. Schafasand, A. Carlino, K. Poljanc, T. Radakovits, M. Stock, E. Hug, P. Georg, M. Pelak, et al. Organs at risk dose constraints in carbon ion radiotherapy at MedAustron: Translations between LEM and MKM RBE models and preliminary clinical results. *Radiotherapy and Oncology*, 175:73–78, 2022.

E. H. Grubbé. Priority in the therapeutic use of X-rays. *Radiology*, 21(2):156–162, 1933.

T. Haberer, J. Debus, H. Eickhoff, O. Jäkel, D. Schulz-Ertner, and U. Weber. The Heidelberg ion therapy center. *Radiotherapy and Oncology*, 73:S186–S190, 2004.

E. C. Halperin. Particle therapy and treatment of cancer. *The Lancet Oncology*, 7(8): 676–685, 2006.

F. Hashimoto, Y. Onishi, K. Ote, H. Tashima, A. J. Reader, and T. Yamaya. Deep learning-based PET image denoising and reconstruction: a review. *Radiological physics and technology*, 17(1):24–46, 2024.

R. B. Hawkins. A microdosimetric-kinetic model for the effect of non-Poisson distribution of lethal lesions on the variation of RBE with LET. *Radiation research*, 160(1):61–69, 2003.

Y. Hayakawa, J. Tada, N. Arai, K. Hosono, M. Sato, T. Wagai, H. Tsuji, and H. Tsujii. Acoustic pulse generated in a patient during treatment by pulsed proton radiation beam. *Radiation Oncology Investigations*, 3(1):42–45, 1995.

L. He, M. Bachhammer, F. Balling, S. Biswas, L. Doyle, S. Gerlach, I. Hofrichter, M. Kharbedia, J. Liese, M. De Marco, et al. Stable high-energy proton acceleration with water-leaf targets driven by intense laser pulses. *Physical Review Research*, 7(2):023190, 2025.

A. Helm and C. Fournier. High-LET charged particles: radiobiology and application for new approaches in radiotherapy. *Strahlentherapie und Onkologie*, 199(12):1225–1241, 2023.

S. Helmbrecht, W. Enghardt, K. Parodi, B. Didinger, J. Debus, D. Kunath, M. Priegnitz, and F. Fiedler. Analysis of metabolic washout of positron emitters produced during carbon ion head and neck radiotherapy. *Medical Physics*, 40(9):091918, 2013.

S. Helmbrecht, M. Priegnitz, W. Enghardt, H. Rohling, and F. Fiedler. Application of a yield approach for the prediction of positron emitter distributions produced during therapeutic carbon-ion beam irradiation. *IEEE Transactions on Nuclear Science*, 63(1): 61–69, 2016.

G. T. Herman. Image reconstruction from projections. *Real-Time Imaging*, 1(1):3–18, 1995.

V. L. Highland. Some practical remarks on multiple scattering. *Nuclear Instruments and Methods*, 129(2):497–499, 1975.

Y. Hishikawa, K. Kagawa, M. Murakami, H. Sakai, T. Akagi, and M. Abe. Usefulness of positron-emission tomographic images after proton therapy. *International Journal of Radiation Oncology* Biology* Physics*, 53(5):1388–1391, 2002.

T. Hofmann, A. Fochi, K. Parodi, and M. Pinto. Prediction of positron emitter distributions for range monitoring in carbon ion therapy: an analytical approach. *Physics in Medicine & Biology*, 64(10):105022, 2019.

F. Horst, W. Adi, G. Aricò, K.-T. Brinkmann, M. Durante, C.-A. Reidel, M. Rovituso, U. Weber, H.-G. Zaunick, K. Zink, and C. Schuy. Measurement of PET isotope production cross sections for protons and carbon ions on carbon and oxygen targets for applications in particle therapy range verification. *Physics in Medicine & Biology*, 64(20):205012, oct 2019.

W. C. Hsi, D. J. Indelicato, C. Vargas, S. Duvvuri, Z. Li, and J. Palta. In vivo verification of proton beam path by using post-treatment PET/CT imaging. *Medical physics*, 36 (9Part1):4136–4146, 2009.

H. M. Hudson and R. S. Larkin. Accelerated image reconstruction using ordered subsets of projection data. *IEEE Transactions on Medical Imaging*, 1994.

J. Hüfner, K. Schäfer, and B. Schürmann. Abrasion-ablation in reactions between relativistic heavy ions. *Physical Review C*, 12(6):1888, 1975.

N. Hünemohr, H. Paganetti, S. Greilich, O. Jäkel, and J. Seco. Tissue decomposition from dual energy CT data for MC based dose calculation in particle therapy. *Medical Physics*, 41(6Part1):061714, 2014.

ICRU. Report no. 30. Technical report, International Commission on Radiation Units and Measurements, Bethesda, MD, 1979.

ICRU. Stopping Powers for Electrons and Positrons, 1984.

ICRU. *Fundamental quantities and units for ionizing radiation*. International commission on radiation units and measurements, 1998.

A. B. Idrissi, G. Borghi, A. Caracciolo, C. Riboldi, M. Carminati, M. Donetti, M. Pullia, S. Savazzi, F. Camera, and C. Fiorini. First experimental verification of prompt gamma imaging with carbon ion irradiation. *Scientific Reports*, 14(1):25750, 2024.

H. Ikawa, M. Shinoto, M. Koto, T. Masuda, T. Inaniwa, H. Takiyama, T. Isozaki, S. Yamada, and H. Ishikawa. Dose-averaged LET escalation with multi-ion therapy for head and neck cancers: a phase I study protocol for a prospective, open-label, single-arm, single-centre trial (MULTI-ION-HN-I). *BMJ open*, 15(10):e098151, 2025.

T. Inaniwa, N. Kanematsu, Y. Hara, T. Furukawa, M. Fukahori, M. Nakao, and T. Shirai. Implementation of a triple Gaussian beam model with subdivision and redefinition against density heterogeneities in treatment planning for scanned carbon-ion radiotherapy. *Physics in Medicine & Biology*, 59(18):5361, 2014.

M. Ito, J. S. Lee, S. I. Kwon, G. S. Lee, B. Hong, K. S. Lee, K.-S. Sim, S. J. Lee, J. T. Rhee, and S. J. Hong. A four-layer DOI detector with a relative offset for use in an animal PET system. *IEEE Transactions on Nuclear Science*, 57(3):976–981, 2010a.

M. Ito, J. S. Lee, M.-J. Park, K.-S. Sim, and S. J. Hong. Design and simulation of a novel method for determining depth-of-interaction in a PET scintillation crystal array using a single-ended readout by a multi-anode PMT. *Physics in Medicine & Biology*, 55(13): 3827, 2010b.

Y. Iwata. Sc gantry at NIRS and new devlopment in SC magnets for gantreis & sychrotorn, 2016.

O. Jäkel. The relative biological effectiveness of proton and ion beams. *Zeitschrift für Medizinische Physik*, 18(4):276–285, 2008.

S. Jan, G. Santin, D. Strul, S. Staelens, K. Assié, D. Autret, S. Avner, R. Barbier, M. Bardies, P. Bloomfield, et al. GATE: a simulation toolkit for PET and SPECT. *Physics in Medicine & Biology*, 49(19):4543, 2004.

C. Z. Jarlskog and H. Paganetti. Risk of developing second cancer from neutron dose in proton therapy as function of field characteristics, organ, and patient age. *International Journal of Radiation Oncology* Biology* Physics*, 72(1):228–235, 2008.

X. Jia, J. Schümann, H. Paganetti, and S. B. Jiang. GPU-based fast Monte Carlo dose calculation for proton therapy. *Physics in Medicine & Biology*, 57(23):7783, 2012.

Z. Jiang, L. Sun, W. Yao, Q. J. Wu, L. Xiang, and L. Ren. 3D in vivo dose verification in prostate proton therapy with deep learning-based proton-acoustic imaging. *Physics in Medicine & Biology*, 67(21):215012, 2022.

K. C. Jones, W. Nie, J. C. Chu, J. V. Turian, A. Kassaee, C. M. Sehgal, and S. Avery. Acoustic-based proton range verification in heterogeneous tissue: simulation studies. *Physics in Medicine & Biology*, 63(2):025018, 2018.

T. Kanai, M. Endo, S. Minohara, N. Miyahara, H. Koyama-Ito, H. Tomura, N. Matsufuji, Y. Futami, A. Fukumura, T. Hiraoka, et al. Biophysical characteristics of HIMAC clinical irradiation system for heavy-ion radiation therapy. *International Journal of Radiation Oncology* Biology* Physics*, 44(1):201–210, 1999.

N. Kanematsu. Semi-empirical formulation of multiple scattering for the Gaussian beam model of heavy charged particles stopping in tissue-like matter. *Physics in Medicine & Biology*, 54(5):N67, 2009.

N. Kanematsu, M. Komori, S. Yonai, and A. Ishizaki. Dynamic splitting of Gaussian pencil beams in heterogeneity-correction algorithms for radiotherapy with heavy charged particles. *Physics in Medicine & Biology*, 54(7):2015, 2009.

A. M. Kellerer. *Linear energy transfer*, volume 16. 1970.

S. Kinouchi, T. Yamaya, H. Tashima, E. Yoshida, F. Nishikido, H. Haneishi, and M. Suga. Simulation design of a single-ring OpenPET for in-beam PET. In *2011 IEEE Nuclear Science Symposium Conference Record*, pages 3481–3483. IEEE, 2011.

A.-C. Knopf, K. Parodi, H. Paganetti, T. Bortfeld, J. Daartz, M. Engelsman, N. Liebsch, and H. Shih. Accuracy of proton beam range verification using post-treatment positron emission tomography/computed tomography as function of treatment site. *International Journal of Radiation Oncology* Biology* Physics*, 79(1):297–304, 2011.

A. Kraan, G. Battistoni, N. Belcari, N. Camarlinghi, G. Cirrone, G. Cuttone, S. Ferretti, A. Ferrari, G. Pirrone, F. Romano, et al. Proton range monitoring with in-beam PET: Monte Carlo activity predictions and comparison with cyclotron data. *Physica Medica*, 30(5):559–569, 2014.

A. C. Kraan, M. Moglioni, G. Battistoni, D. Bersani, A. Berti, P. Carra, P. Cerello, M. Ciocca, V. Ferrero, E. Fiorina, et al. Using the gamma-index analysis for inter-fractional comparison of in-beam PET images for head-and-neck treatment monitoring in proton therapy: A Monte Carlo simulation study. *Physica Medica*, 120:103329, 2024a.

A. C. Kraan, F. Susini, M. Moglioni, G. Battistoni, D. Bersani, P. Carra, P. Cerello, A. De Gregorio, V. Ferrero, E. Fiorina, et al. In-beam PET treatment monitoring of carbon therapy patients: Results of a clinical trial at CNAO. *Physica Medica*, 125:104493, 2024b.

G. Kraft, U. Arndt, W. Becher, D. Schardt, H. Stelzer, U. Weber, and T. Archinal. Heavy ion therapy at GSI. *Nuclear Instruments and Methods in Physics Research Section A: Accelerators, Spectrometers, Detectors and Associated Equipment*, 367(1-3):66–70, 1995.

C. Kurz, J. Bauer, D. Unholtz, D. Richter, K. Herfarth, J. Debus, and K. Parodi. Initial clinical evaluation of PET-based ion beam therapy monitoring under consideration of organ motion. *Medical Physics*, 43(2):975–982, 2016.

Y. Kusano, T. Kanai, S. Yonai, M. Komori, N. Ikeda, Y. Tachikawa, A. Ito, and H. Uchida. Field-size dependence of doses of therapeutic carbon beams. *Medical Physics*, 34(10): 4016–4022, 2007.

J. Lascaud, P. Dash, H.-P. Wieser, R. Kalunga, M. Würl, W. Assmann, and K. Parodi. Investigating the accuracy of co-registered ionoacoustic and ultrasound images in pulsed proton beams. *Physics in Medicine & Biology*, 66(18):185007, 2021.

S. Lehrack, W. Assmann, D. Bertrand, S. Henrotin, J. Herault, V. Heymans, F. Vander Stappen, P. G. Thirolf, M. Vidal, J. Van de Walle, et al. Submillimeter ionoacoustic range determination for protons in water at a clinical synchrocyclotron. *Physics in Medicine & Biology*, 62(17):L20, 2017.

Z. Li, Y. Wang, Y. Yu, K. Fan, L. Xing, and H. Peng. Machine learning approaches for range and dose verification in proton therapy using proton-induced positron emitters. *Medical physics*, 46(12):5748–5757, 2019.

J. Lindhard, M. Scharff, and H. E. Schiøtt. *Range concepts and heavy ion ranges*, volume 33. Munksgaard Copenhagen, 1963.

C. Liu, Z. Li, W. Hu, L. Xing, and H. Peng. Range and dose verification in proton therapy using proton-induced positron emitters and recurrent neural networks (RNNs). *Physics in Medicine & Biology*, 64(17):175009, 2019.

A. Lühr, J. Toftegaard, I. Kantemiris, D. C. Hansen, and N. Bassler. Stopping power for particle therapy: the generic library libdedx and clinically relevant stopping-power ratios for light ions. *International Journal of Radiation Biology*, 88(1-2):209–212, 2012.

P. Lysakovski, B. Kopp, T. Tessonnier, S. Mein, A. Ferrari, T. Haberer, J. Debus, and A. Mairani. Development and validation of monteray, a fast Monte Carlo dose engine for carbon ion beam radiotherapy. *Medical Physics*, 51(2):1433–1449, 2024.

C. C. Ma and T. Lomax. *Proton and carbon ion therapy*. CRC press, 2012.

S. Ma, Z. Hu, K. Ye, X. Zhang, Y. Wang, and H. Peng. Feasibility study of patient-specific dose verification in proton therapy utilizing positron emission tomography (pet) and generative adversarial network (gan). *Medical physics*, 47(10):5194–5208, 2020.

A. Mairani, S. Mein, E. Blakely, J. Debus, M. Durante, A. Ferrari, H. Fuchs, D. Georg, D. R. Grosshans, F. Guan, et al. Roadmap: helium ion therapy. *Physics in Medicine & Biology*, 67(15):15TR02, 2022.

C. Mancini-Terracciano, M. Asai, B. Caccia, G. Cirrone, A. Dotti, R. Faccini, P. Napolitani, L. Pandola, D. Wright, and M. Colonna. Preliminary results coupling "Stochastic Mean Field" and "Boltzmann-Langevin One Body" models with Geant4. *Physica Medica*, 67: 116–122, 2019.

S. McGowan, N. Burnet, and A. Lomax. Treatment planning optimisation in proton therapy. *The British journal of radiology*, 86(1021):20120288–20120288, 2013.

K. McNamara, A. Schiavi, D. Borys, K. Brzezinski, J. Gajewski, R. Kopeć, A. Rucinski, T. Skóra, S. Makkar, J. Hrbacek, D. C. Weber, A. J. Lomax, and C. Winterhalter. GPU accelerated Monte Carlo scoring of positron emitting isotopes produced during proton therapy for PET verification. *Physics in Medicine & Biology*, 67(24):244001, dec 2022.

S. Mein, C. Klein, B. Kopp, G. Magro, S. Harrabi, C. P. Karger, T. Haberer, J. Debus, A. Abdollahi, I. Dokic, et al. Assessment of RBE-weighted dose models for carbon ion therapy toward modernization of clinical practice at HIT: in vitro, in vivo, and in patients. *International Journal of Radiation Oncology* Biology* Physics*, 108(3):779–791, 2020.

T. Merlin, S. Stute, D. Benoit, J. Bert, T. Carlier, C. Comtat, M. Filipovic, F. Lamare, and D. Visvikis. CASToR: a generic data organization and processing code framework for multi-modal and multi-dimensional tomographic reconstruction. *Physics in Medicine & Biology*, 63(18):185005, 2018.

C.-H. Min, C. H. Kim, M.-Y. Youn, and J.-W. Kim. Prompt gamma measurements for locating the dose falloff region in the proton therapy. *Applied physics letters*, 89(18), 2006.

C. H. Min, X. Zhu, B. A. Winey, K. Grogg, M. Testa, G. El Fakhri, T. R. Bortfeld, H. Paganetti, and H. A. Shih. Clinical application of in-room positron emission tomography for in vivo treatment monitoring in proton radiation therapy. *International Journal of Radiation Oncology* Biology* Physics*, 86(1):183–189, 2013.

A. Miyatake and T. Nishio. Application of activity pencil beam algorithm using measured distribution data of positron emitter nuclei for therapeutic sobp proton beam. *Medical Physics*, 40(9):091709, 2013.

H. Mizuno, T. Tomitani, M. Kanazawa, A. Kitagawa, J. Pawelke, Y. Iseki, E. Urakabe, M. Suda, A. Kawano, R. Iritani, et al. Washout measurement of radioisotope implanted by radioactive beams in the rabbit. *Physics in Medicine & Biology*, 48(15):2269, 2003.

M. Moglioni, A. C. Kraan, G. Baroni, G. Battistoni, N. Belcari, A. Berti, P. Carra, P. Cerello, M. Ciocca, A. De Gregorio, et al. In-vivo range verification analysis with in-beam PET data for patients treated with proton therapy at CNAO. *Frontiers in Oncology*, 12:929949, 2022.

G. Moliere. Theorie der streuung schneller geladener teilchen i. einzelstreuung am abgeschirmten coulomb-feld. *Zeitschrift für Naturforschung A*, 2(3):133–145, 1947.

S. Muraro, G. Battistoni, and A. Kraan. Challenges in Monte Carlo simulations as clinical and research tool in particle therapy: a review. *Frontiers in Physics*, 8:567800, 2020.

NEMA. Digital imaging and communications in medicine (DICOM) part 3: Information object definitions. *NEMA PS*, pages 3–3, 2009. URL `https://dicom.nema.org/medical/Dicom/2018d/output/chtml/part03/sect_C.8.8.25.6.html`.

S. P. Nischwitz, J. Bauer, T. Welzel, H. Rief, O. Jäkel, T. Haberer, K. Frey, J. Debus, K. Parodi, S. E. Combs, et al. Clinical implementation and range evaluation of in vivo PET dosimetry for particle irradiation in patients with primary glioma. *Radiotherapy and Oncology*, 115(2):179–185, 2015.

T. Nishio, A. Miyatake, T. Ogino, K. Nakagawa, N. Saijo, and H. Esumi. The development and clinical use of a beam ON-LINE PET system mounted on a rotating gantry port in proton therapy. *International Journal of Radiation Oncology* Biology* Physics*, 76(1): 277–286, 2010.

H. Paganetti. Range uncertainties in proton therapy and the role of Monte Carlo simulations. *Physics in Medicine & Biology*, 57(11):R99, 2012.

H. Paganetti, A. Niemierko, M. Ancukiewicz, L. E. Gerweck, M. Goitein, J. S. Loeffler, and H. D. Suit. Relative biological effectiveness (RBE) values for proton beam therapy. *International Journal of Radiation Oncology* Biology* Physics*, 53(2):407–421, 2002.

K. Parodi and W. Assmann. Ionoacoustics: A new direct method for range verification. *Modern Physics Letters A*, 30(17):1540025, 2015.

K. Parodi and T. Bortfeld. A filtering approach based on Gaussian-powerlaw convolutions for local PET verification of proton radiotherapy. *Physics in Medicine & Biology*, 51(8): 7089–7106, 2006.

K. Parodi, W. Enghardt, and T. Haberer. In-beam PET measurements of β^+ radioactivity induced by proton beams. *Physics in Medicine & Biology*, 47(1):21, 2001.

K. Parodi, A. Ferrari, F. Sommerer, and H. Paganetti. Clinical CT-based calculations of dose and positron emitter distributions in proton therapy using the FLUKA Monte Carlo code. *Physics in Medicine & Biology*, 52(12):3369, may 2007a.

K. Parodi, H. Paganetti, E. Cascio, J. B. Flanz, A. A. Bonab, N. M. Alpert, K. Lohmann, and T. Bortfeld. PET/CT imaging for treatment verification after proton therapy: a study with plastic phantoms and metallic implants. *Medical physics*, 34(2):419–435, 2007b.

K. Parodi, H. Paganetti, H. A. Shih, S. Michaud, J. S. Loeffler, T. F. DeLaney, N. J. Liebsch, J. E. Munzenrider, A. J. Fischman, A. Knopf, et al. Patient study of in vivo verification of beam delivery and range, using positron emission tomography and computed tomography imaging after proton therapy. *International Journal of Radiation Oncology* Biology* Physics*, 68(3):920–934, 2007c.

K. Parodi, T. Bortfeld, and T. Haberer. Comparison between in-beam and offline positron emission tomography imaging of proton and carbon ion therapeutic irradiation at synchrotron-and cyclotron-based facilities. *International Journal of Radiation Oncology* Biology* Physics*, 71(3):945–956, 2008.

K. Parodi, A. Mairani, S. Brons, J. Naumann, M. Krämer, F. Sommerer, and T. Haberer. The influence of lateral beam profile modifications in scanned proton and carbon ion therapy: a Monte Carlo study. *Physics in Medicine & Biology*, 55(17):5169, aug 2010.

K. Parodi, A. Mairani, S. Brons, B. G. Hasch, F. Sommerer, J. Naumann, O. Jäkel, T. Haberer, and J. Debus. Monte Carlo simulations to support start-up and treatment planning of scanned proton and carbon ion therapy at a synchrotron-based facility. *Physics in Medicine & Biology*, 57(12):3759, may 2012.

K. Parodi, A. Mairani, and F. Sommerer. Monte Carlo-based parametrization of the lateral dose spread for clinical treatment planning of scanned proton and carbon ion beams. *Journal of radiation research*, 54(1):i91–i96, 2013.

K. Parodi, T. Yamaya, and P. Moskal. Experience and new prospects of PET imaging for ion beam therapy monitoring. *Zeitschrift für Medizinische Physik*, 33(1):22–34, 2023.

J. Pawelke, W. Enghardt, T. Haberer, B. Hasch, R. Hinz, M. Kramer, E. Lauckner, and M. Sobiella. In-beam PET imaging for the control of heavy-ion tumour therapy. *IEEE Transactions on nuclear science*, 44(4):1492–1498, 1997.

E. Pedroni, R. Bacher, H. Blattmann, T. Böhringer, A. Coray, A. Lomax, S. Lin, G. Munkel, S. Scheib, U. Schneider, et al. The 200-MeV proton therapy project at the Paul Scherrer Institute: Conceptual design and practical realization. *Medical Physics*, 22(1):37–53, 1995.

E. Pedroni, S. Scheib, T. Böhringer, A. Coray, M. Grossmann, S. Lin, and A. Lomax. Experimental characterization and physical modelling of the dose distribution of scanned proton pencil beams. *Physics in Medicine & Biology*, 50(3):541, 2005.

J. Perl, J. Shin, J. Schümann, B. Faddegon, and H. Paganetti. TOPAS: an innovative proton Monte Carlo platform for research and clinical applications. *Medical Physics*, 39 (11):6818–6837, 2012.

L. Piacentini, L. Dassa, D. Perini, A. Ratkus, T. Torims, and S. Uberti. Design of a 6-supports exactly constrained supporting system for superconducting magnets and its application to rotating gantries for cancer therapy. *Meccanica*, 59(12):2203–2226, 2024.

M. Pinto, K. Kröniger, J. Bauer, R. Nilsson, E. Traneus, and K. Parodi. A filtering approach for PET and PG predictions in a proton treatment planning system. *Physics in Medicine & Biology*, 65(9):095014, 2020.

G. Poludniowski, N. M. Allinson, and P. Evans. Proton radiography and tomography with application to proton therapy. *The British journal of radiology*, 88(1053):20150134, 2015.

F. Pönisch, K. Parodi, B. G. Hasch, and W. Enghardt. The modelling of positron emitter production and PET imaging during carbon ion therapy. *Physics in Medicine & Biology*, 49(23):5217, 2004.

G. A. Prenosil, H. Sari, M. Fürstner, A. Afshar-Oromieh, K. Shi, A. Rominger, and M. Hentschel. Performance characteristics of the Biograph Vision Quadra PET/CT system with a long axial field of view using the NEMA NU 2-2018 standard. *Journal of nuclear medicine*, 63(3):476–484, 2022.

M. Priegnitz, F. Fiedler, D. Kunath, K. Laube, and W. Enghardt. An experiment-based approach for predicting positron emitter distributions produced during therapeutic ion irradiation. *IEEE Transactions on Nuclear Science*, 59(1):77–87, 2012.

PTCOG. Particle therapy centers, 2026. URL `https://www.ptcog.site/`.

M. Qi, Q. Yang, X. Chen, and J. D. L. Yang. Fast calculation of Monte Carlo ion transport code. *Journal of Physics: Conference Series*, 1739(1):012030, 2021.

N. Qin, M. Pinto, Z. Tian, G. Dedes, A. Pompos, S. B. Jiang, K. Parodi, and X. Jia. Initial development of goCMC: a GPU-oriented fast cross-platform Monte Carlo engine for carbon ion therapy. *Physics in Medicine & Biology*, 62(9):3682, 2017.

A. J. Reader, G. Corda, A. Mehranian, C. da Costa-Luis, S. Ellis, and J. A. Schnabel. Deep learning for PET image reconstruction. *IEEE Transactions on Radiation and Plasma Medical Sciences*, 5(1):1–25, 2020.

S. Ren, Y. Yang, and S. R. Cherry. Effects of reflector and crystal surface on the performance of a depth-encoding PET detector with dual-ended readout. *Medical physics*, 41(7):072503, 2014.

C. Richter, G. Pausch, S. Barczyk, M. Priegnitz, I. Keitz, J. Thiele, J. Smeets, F. Vander Stappen, L. Bombelli, C. Fiorini, et al. First clinical application of a prompt gamma based in vivo proton range verification system. *Radiotherapy and Oncology*, 118(2): 232–237, 2016.

I. Rinaldi, S. Brons, O. Jäkel, B. Voss, and K. Parodi. Experimental investigations on carbon ion scanning radiography using a range telescope. *Physics in Medicine & Biology*, 59(12):3041, 2014.

E. Roncali and S. R. Cherry. Application of silicon photomultipliers to positron emission tomography. *Annals of biomedical engineering*, 39(4):1358–1377, 2011.

L. Rossi, A. Ballarino, D. Barna, E. Benedetto, C. Calzolaio, G. Ceruti, E. De Matteis, A. Echeandia, T. Ekelof, S. Farinon, et al. A European collaboration to investigate superconducting magnets for next generation heavy ion therapy. *IEEE Transactions on Applied Superconductivity*, 32(4):1–7, 2022.

K. Sato, S. Yamada, H. Ogawa, K. Kawachi, N. Araki, A. Itano, M. Kanazawa, A. Kitagawa, T. Kohno, M. Kumada, et al. Performance of HIMAC. *Nuclear Physics A*, 588(1):c229–c234, 1995.

T. Sato, Y. Iwamoto, S. Hashimoto, T. Ogawa, T. Furuta, S.-I. Abe, T. Kai, Y. Matsuya, N. Matsuda, Y. Hirata, et al. Recent improvements of the particle and heavy ion transport code system–PHITS version 3.33. *Journal of Nuclear Science and Technology*, 61(1): 127–135, 2024.

Y.-h. Sato, D. Sakata, D. Bolst, E. C. Simpson, S. Guatelli, and A. Haga. Development of a more accurate Geant4 quantum molecular dynamics model for hadron therapy. *Physics in Medicine & Biology*, 67(22):225001, 2022.

B. Schaffner and E. Pedroni. The precision of proton range calculations in proton radiotherapy treatment planning: experimental verification of the relation between CT-HU and proton stopping power. *Physics in Medicine & Biology*, 43(6):1579, 1998.

B. Schaffner, E. Pedroni, and A. Lomax. Dose calculation models for proton treatment planning using a dynamic beam delivery system: an attempt to include density heterogeneity effects in the analytical dose calculation. *Physics in Medicine & Biology*, 44(1): 27, 1999.

J. Schauer, H.-P. Wieser, Y. Huang, H. Ruser, J. Lascaud, M. Würl, A. Chmyrov, M. Vidal, J. Herault, V. Ntziachristos, et al. Proton beam range verification by means of ionoacoustic measurements at clinically relevant doses using a correlation-based evaluation. *Frontiers in Oncology*, 12:925542, 2022.

J. Schauer, H.-P. Wieser, J. Lascaud, Y. Huang, M. Vidal, J. Herault, V. Ntziachristos, G. Dollinger, and K. Parodi. Range verification of a clinical proton beam in an abdominal phantom by co-registration of ionoacoustics and ultrasound. *Physics in Medicine & Biology*, 68(12):125009, 2023.

M. Schillo, A. Geisler, A. Hobl, H. Klein, D. Krischel, M. Meyer-Reumers, C. Piel, H. Blosser, J.-W. Kim, F. Marti, et al. Compact superconducting 250 mev proton cyclotron for the PSI PROSCAN proton therapy project. In *AIP Conference Proceedings*, volume 600, pages 37–39. American Institute of Physics, 2001.

U. Schneider, E. Pedroni, and A. Lomax. The calibration of CT hounsfield units for radiotherapy treatment planning. *Physics in Medicine & Biology*, 41(1):111, 1996.

W. Schneider, T. Bortfeld, and W. Schlegel. Correlation between CT numbers and tissue parameters needed for Monte Carlo simulations of clinical dose distributions. *Physics in Medicine & Biology*, 45(2):459, feb 2000.

M. Scholz, A. Kellerer, W. Kraft-Weyrather, and G. Kraft. Computation of cell survival in heavy ion beams for therapy: the model and its approximation. *Radiation and environmental biophysics*, 36(1):59–66, 1997.

J. Schwaab, S. Brons, J. Fieres, and K. Parodi. Experimental characterization of lateral profiles of scanned proton and carbon ion pencil beams for improved beam models in ion therapy treatment planning. *Physics in Medicine & Biology*, 56(24):7813, 2011.

M. Seidel. Cyclotrons and fixed field alternating gradient accelerators. *arXiv preprint arXiv:2105.04477*, 2021.

S. Seifert, G. Van der Lei, H. T. Van Dam, and D. R. Schaart. First characterization of a digital SiPM based time-of-flight PET detector with 1 mm spatial resolution. *Physics in Medicine & Biology*, 58(9):3061, 2013.

L. A. Shepp and Y. Vardi. Maximum likelihood reconstruction for emission tomography. *IEEE transactions on medical imaging*, 1(2):113–122, 2007.

M. Siggel, P. Ziegenhein, S. Nill, and U. Oelfke. Boosting runtime-performance of photon pencil beam algorithms for radiotherapy treatment planning. *Physica Medica*, 28(4): 273–280, 2012.

M. Singh. A review of digital PET-CT technology: comparing performance parameters in SiPM integrated digital PET-CT systems. *Radiography*, 30(1):13–20, 2024.

M. Soukup, M. Fippel, and M. Alber. A pencil beam algorithm for intensity modulated proton therapy derived from Monte Carlo simulations. *Physics in Medicine & Biology*, 50(21):5089, 2005.

B. A. Spencer, E. Berg, J. P. Schmall, N. Omidvari, E. K. Leung, Y. G. Abdelhafez, S. Tang, Z. Deng, Y. Dong, Y. Lv, et al. Performance evaluation of the uEXPLORER total-body PET/CT scanner based on NEMA NU 2-2018 with additional tests to characterize PET scanners with a long axial field of view. *Journal of Nuclear Medicine*, 62(6):861–870, 2021.

R. D. Stewart, D. J. Carlson, M. P. Butkus, R. Hawkins, T. Friedrich, and M. Scholz. A comparison of mechanism-inspired models for particle relative biological effectiveness (RBE). *Medical Physics*, 45(11):e925–e952, 2018.

J. Sun, T. Masuda, H. Tashima, C. Toramatsu, A. Hamato, T. Yamaya, S. Tanaka, K. Kasamatsu, S. Mein, and T. Inaniwa. In-beam range determination using an OpenPET system for helium, carbon, oxygen, and neon ion beams. *Physics in Medicine & Biology*, 70(22):225005, 2025.

S. Surti and J. S. Karp. Advances in time-of-flight PET. *Physica medica*, 32(1):12–22, 2016.

W. Sweet. Localization of brain tumors with positron emitters. *Nucleonics*, 11:40–45, 1953.

H. Takei, R. Imai, T. Masuda, K. Aoki, T. Nakaji, Y. Nomura, A. Inomata, Y. Suzuki, and T. Inaniwa. Possibility of increasing linear energy transfer in multi-ion radiotherapy for bone and soft tissue sarcomas. *Medical Physics*, 52(9):e18097, 2025.

S. Tanaka and T. Inaniwa. Method for fabricating a mesh ripple filter for charged-particle therapy. *Physics in Medicine & Biology*, 69(14):145009, 2024.

S. Tanaka, T. Inaniwa, and S. Matsuba. Development of ripple filter composed of metal mesh for charged-particle therapy. *Physics in Medicine & Biology*, 2022.

H. Tashima. The first clinical study of openpet in carbon-ion therapy. In *Report on PET Imaging Physics Research*, pages 37–42. National Institutes for Quantum Science and Technology, Chiba, Japan, 2024. URL `https://www.qst.go.jp/uploaded/attachment/39799.pdf`.

H. Tashima, T. Yamaya, E. Yoshida, S. Kinouchi, M. Watanabe, and E. Tanaka. A single-ring OpenPET enabling PET imaging during radiotherapy. *Physics in Medicine & Biology*, 57(14):4705, 2012.

H. Tashima, E. Yoshida, N. Inadama, F. Nishikido, Y. Nakajima, H. Wakizaka, T. Shinaji, M. Nitta, S. Kinouchi, M. Suga, et al. Development of a small single-ring OpenPET prototype with a novel transformable architecture. *Physics in Medicine & Biology*, 61(4): 1795, 2016.

H. Tashima, E. Yoshida, Y. Iwao, H. Wakizaka, A. Mohammadi, M. Nitta, A. Kitagawa, T. Inaniwa, F. Nishikido, A. B. Tsuji, et al. Development of a multiuse human-scale single-ring OpenPET system. *IEEE Transactions on Radiation and Plasma Medical Sciences*, 5(6):807–816, 2020.

H. Tashima, C. Toramatsu, A. Mohammadi, Y. Iwao, N. Inadama, H. Kang, G. Akamatsu, M. Tajiri, H. Mizuno, M. Koto, et al. Bench-to-Clinical Transfer of OpenPET: First In-Beam Test in a HIMAC Treatment Room. In *2023 IEEE Nuclear Science Symposium, Medical Imaging Conference and International Symposium on Room-Temperature Semiconductor Detectors (NSS MIC RTSD)*, pages 1–1. IEEE, 2023.

H. Tashima, C. Toramatsu, A. Hamato, Y. Iwao, G. Akamatsu, H. Kang, F. Nishikido, M. Tajiri, H. Mizuno, M. Koto, et al. First Patient Study of In-Beam OpenPET for Range Verification in Carbon-Ion Therapy. In *2024 IEEE Nuclear Science Symposium (NSS), Medical Imaging Conference (MIC) and Room Temperature Semiconductor Detector Conference (RTSD)*, pages 1–1. IEEE, 2024.

M. M. Ter-Pogossian, M. E. Phelps, E. J. Hoffman, and N. A. Mullani. A positron-emission transaxial tomograph for nuclear imaging (PETT). *Radiology*, 114(1):89–98, 1975.

T. Tessonnier, T. Marcelos, A. Mairani, S. Brons, and K. Parodi. Phase space generation for proton and carbon ion beams for external users' applications at the Heidelberg Ion Therapy Center. *Frontiers in Oncology*, 5, 2016.

E. Testa, M. Bajard, M. Chevallier, D. Dauvergne, F. Le Foulher, N. Freud, J. M. Létang, J. Poizat, C. Ray, and M. Testa. Dose profile monitoring with carbon ions by means of prompt-gamma measurements. *Nuclear Instruments and Methods in Physics Research Section B: Beam Interactions with Materials and Atoms*, 267(6):993–996, 2009.

F. Tommasino, E. Scifoni, and M. Durante. New ions for therapy. *International journal of particle therapy*, 2(3):428–438, 2015.

C. Toramatsu, E. Yoshida, H. Wakizaka, A. Mohammadi, Y. Ikoma, H. Tashima, F. Nishikido, A. Kitagawa, K. Karasawa, Y. Hirano, et al. Washout effect in rabbit brain: in-beam PET measurements using 10C, 11C and 15O ion beams. *Biomedical Physics & Engineering Express*, 4(3):035001, 2018.

C. Toramatsu, A. Mohammadi, H. Wakizaka, H. Sudo, N. Nitta, C. Seki, I. Kanno, M. Takahashi, K. Karasawa, Y. Hirano, et al. Measurement of biological washout rates depending on tumor vascular status in 15O in-beam rat-PET. *Physics in Medicine & Biology*, 67(12):125006, 2022.

C. Toramatsu, A. Mohammadi, H. Wakizaka, N. Nitta, Y. Ikoma, C. Seki, I. Kanno, and T. Yamaya. Tumour status prediction by means of carbon-ion beam irradiation: comparison of washout rates between in-beam PET and (dce-mri) in rats. *Physics in Medicine & Biology*, 68(19):195005, 2023.

D. W. Townsend, M. Wensveen, L. G. Byars, A. Geissbuhler, H. J. Tochon-Danguy, A. Christin, M. Defrise, D. L. Bailey, S. Grootoonk, A. Donath, et al. A rotating PET scanner using BGO block detectors: design, performance and applications. *Journal of Nuclear Medicine*, 34(8):1367–1376, 1993.

N. Tsoulfanidis. *Measurement and detection of radiation*. CRC press, 2021.

M. Umezawa, R. Fujimoto, T. Umekawa, Y. Fujii, T. Takayanagi, F. Ebina, T. Aoki, Y. Nagamine, K. Matsuda, K. Hiramoto, et al. Development of the compact proton beam therapy system dedicated to spot scanning with real-time tumor-tracking technology. In *AIP Conference Proceedings*, volume 1525, pages 360–363. American Institute of Physics, 2013.

V. Vasic, K. Parodi, and M. Pinto. Evaluating an analytical prediction algorithm of positron emitter distributions in patient data for PET monitoring of carbon ion therapy: A simulation study. *Applied Radiation and Isotopes*, 213:111479, 2024.

M. Vretenar and E. Benedetto. New accelerator designs: NIMMS. *Health and Technology*, 14(5):945–955, 2024.

H. Wan Chan Tseung, J. Ma, and C. Beltran. A fast GPU-based Monte Carlo simulation of proton transport with detailed modeling of nonelastic interactions. *Medical Physics*, 42(6Part1):2967–2978, 2015.

L. S. Waters, G. W. McKinney, J. W. Durkee, M. L. Fensin, J. S. Hendricks, M. R. James, R. C. Johns, and D. B. Pelowitz. The MCNPX Monte Carlo radiation transport code. In *AIP conference Proceedings*, volume 896, pages 81–90. American Institute of Physics, 2007.

R. Wickert, T. Tessonnier, M. Deng, S. Adeberg, K. Seidensaal, L. Hoeltgen, J. Debus, K. Herfarth, and S. Harrabi. Radiotherapy with helium ions has the potential to improve both endocrine and neurocognitive outcome in pediatric patients with ependymoma. *Cancers*, 14:5865, 11 2022.

R. R. Wilson. Radiological use of fast protons. *Radiology*, 47(5):487–491, 1946.

Y. Xie, E. H. Bentefour, G. Janssens, J. Smeets, F. Vander Stappen, L. Hotoiu, L. Yin, D. Dolney, S. Avery, F. O'Grady, et al. Prompt gamma imaging for in vivo range verification of pencil beam scanning proton therapy. *International Journal of Radiation Oncology* Biology* Physics*, 99(1):210–218, 2017.

Z. Xie, T. Li, X. Zhang, W. Qi, E. Asma, and J. Qi. Anatomically aided PET image reconstruction using deep neural networks. *Medical physics*, 48(9):5244–5258, 2021.

T. Yabe, M. Nitta, M. Yamaguchi, M. Pinto, N. Kawachi, and K. Parodi. Patient CT-based simulation study of secondary-electron-bremsstrahlung imaging for range verification in proton therapy: comparison with prompt gamma and PET imaging for simplified proton pencil beam and SOBP irradiation scenarios. *Physics in Medicine & Biology*, 70(11): 115003, 2025.

M. Yamaguchi, Y. Nagao, K. Ando, S. Yamamoto, T. Toshito, J. Kataoka, and N. Kawachi. Secondary-electron-bremsstrahlung imaging for proton therapy. *Nuclear Instruments and Methods in Physics Research Section A: Accelerators, Spectrometers, Detectors and Associated Equipment*, 833:199–207, 2016.

M. Yamaguchi, Y. Nagao, K. Ando, S. Yamamoto, M. Sakai, R. K. Parajuli, K. Arakawa, and N. Kawachi. Imaging of monochromatic beams by measuring secondary electron bremsstrahlung for carbon-ion therapy using a pinhole x-ray camera. *Physics in Medicine & Biology*, 63(4):045016, 2018.

T. Yamaya, T. Inaniwa, S. Minohara, E. Yoshida, N. Inadama, F. Nishikido, K. Shibuya, C. F. Lam, and H. Murayama. A proposal of an open PET geometry. *Physics in Medicine & Biology*, 53(3):757, 2008.

M. L. Yap, E. Zubizarreta, F. Bray, J. Ferlay, and M. Barton. Global access to radiotherapy services: have we made progress during the past decade? *Journal of global oncology*, 2 (4):207–215, 2016.

E. Yoshida, H. Tashima, H. Wakizaka, F. Nishikido, Y. Hirano, N. Inadama, H. Murayama, H. Ito, and T. Yamaya. Development of a single-ring OpenPET prototype. *Nuclear Instruments and Methods in Physics Research Section A: Accelerators, Spectrometers, Detectors and Associated Equipment*, 729:800–808, 2013.

E. Yoshida, H. Tashima, G. Akamatsu, Y. Iwao, M. Takahashi, T. Yamashita, and T. Yamaya. 245 ps-TOF brain-dedicated PET prototype with a hemispherical detector arrangement. *Physics in Medicine & Biology*, 65(14):145008, 2020.

X. Yu, X. Zhang, H. Zhang, H. Peng, Q. Ren, J. Xu, Q. Peng, and S. Xie. Requirements of scintillation crystals with the development of PET scanners. *Crystals*, 12(9):1302, 2022.

Y. Yu, P. Qi, and H. Peng. Feasibility study of 3D time-reversal reconstruction of proton-induced acoustic signals for dose verification in the head and the liver: A simulation study. *Medical physics*, 48(8):4485–4497, 2021.

J. Zhang, P. Maniawski, and M. V. Knopp. Performance evaluation of the next generation solid-state digital photon counting PET/CT system. *EJNMMI research*, 8(1):97, 2018.

J. Zhang, Y. Lu, Y. Sheng, W. Wang, Z. Hong, Y. Sun, R. Zhou, and J. Cheng. A comparative study of two in vivo PET verification methods in clinical cases. *Frontiers in Oncology*, 11:617787, 2021.

X. Zhu, S. España, J. Daartz, N. Liebsch, J. Ouyang, H. Paganetti, T. R. Bortfeld, and G. El Fakhri. Monitoring proton radiation therapy with in-room PET imaging. *Physics in Medicine & Biology*, 56(13):4041, 2011.